University of Nottingham

Advanced Materials Research Group

Design and operation of a metal hydride reactor within a thermochemical energy store for use in concentrated solar power

---

Supervisors:

Author:

Marcus J. Adams

Prof. David Grant

Prof. Gavin Walker

Dr. Alastair Stuart

A thesis submitted for the degree of

Doctor of Philosophy

January 25, 2021

Abstract

This thesis covers the design of a metal hydride reactor within a thermo-chemical energy store for use in concentrated solar power (CSP). Thermo-chemical energy storage has been explored to improve on existing sensible heat technologies, potentially enabling fulfilment of CSP thermal energy storage cost targets, where metal hydrides have emerged as a TCES front-runner. This work introduces a unifying model for both the hydrogenation and dehydrogenation kinetics of MgH_2, through the Site Availability Model (SAM). The model expands on Langmuir's site theory, in which a site can also be unavailable or available to react. This "unavailability" is governed by the site availability driving force, incorporating ideas such as site de-activation and strain/relaxation, which is influenced by temperature and pressure. These phenomena are proposed for both hydrogenation and dehydrogenation. In addition, SAM assumes the rate determining step is at the surface, where both hydrogenation/dehydrogenation assume a spherical surface, with dehydrogenation including the concept of particle fragmentation.

The models developed, SAM:DR and SAM:ACR:SC:F, were successful in representing the kinetics of Mg hydrogenation and MgH_2 dehydrogenation respectively of a small 0.2g sample, for all conditions tested. This includes conditions at close and moderately far from equilibrium for Mg hydrogenation. The SAM was also successfully applied to a 154g magnesium sample, providing confidence that the derived rate laws exhibit intensive characteristics, and assurance that the models can be used for larger scale reactor design. The implications of the thesis demonstrate the advancement in reactor design for metal hydride thermo-chemical energy storage to enable larger scale reactor designs.

N.B. COVID-19 did not majorly impact the project completion, however it did disrupt the experiments on the large lab-scale reactor (chapter 6). The duration of the delay was approximately 3-4 months. It would have been desirable to run more tests and explore ways to achieve a higher operating temperature. In general, it was possible to fulfil the aims and objectives of this thesis.

Acknowledgements

I would like to thank David Grant and Gavin Walker for providing me with the opportunity and guidance to carry out the research presented in this thesis.

I would also like to thank Priyen Mistry, Alastair Stuart and Kandavel Manickam, for providing valuable assistance and help during my PhD, especially during the early years, where they imparted their knowledge on metal hydrides and good laboratory practice.

Finally, a special mention to Alastair Stuart, Karl Booker and Jordan Bradley, for dedicating their time on helping me get the large lab-scale rig operational, with many tedious hours cleaning flanges and pipes, lubricating and tightening joints, and general niggling issues that seemed like a never-ending game of ‘whack-a-mole’.

Contents

List of Figures

List of Tables

Table 1: Nomenclature with example section cross references

Symbol	Description	Typical units	Symbol	Description	Typical units
$\mathbf{A}$ or A	Component $\mathbf{A}$ (4.3.2) or frequency factor (A) (2.2) or area (A) (3.3.3.1)	- s^{-1} m^{-2}	u	Velocity (4.3.6) or arbitrary parameter in FEM explanation (see app. A.3)	$m\ s^{-1}$ -
$\mathbf{A} \cdot \mathbf{M}$	Bound $\mathbf{A}$ site		V	Volume	m^{-3}
$\mathbf{B}$ or B	Component $\mathbf{B}$ (5.3.6) or baffle spacing (B) (3.3.3.1)	- m	$\hat{V}$	Molar volume	$m^{-3}\ mol^{-1}$
C	Concentration	$mol\ m^{-3}$	$\mathbf{v}$	Vacancy	-
c_p	Specific heat capacity	$J\ kg^{-1}\ K^{-1}$	X	Fractional conversion	-
d	Diameter	m	x	Hydride fraction (4.3.5) or neutral charged (4.3.7)	-
D	Diffusion coefficient	$m^2\ s^{-1}$	x,y and z	Cartesian coordinate system (3.3.3.1)	-
E	Activation energy	$J\ mol^{-1}$	y	Empirical parameters for bound (defect) pressure	-
F	Fragmentation factor	-	Z	Compressibility	-
f_0	Outer fouling factor	$m^{-2}\ K\ W^{-1}$	SSA	Specific surface area	m^{-1}
G	Gibbs free energy	$J\ mol^{-1}$	RSA	Reactive surface area	m^{-1}
H	Enthalpy or (Free energy - Ising model)	$J\ mol^{-1}$ (J or eV only 2.2.2.3)	wt_m	Maximum weight percent	-
$\mathbf{H}$	Hydrogen site	-	wt	Weight percent	-
H-H	Hydrogen interactions	-	Nu	Nusselt number	-
h	Heat transfer coefficient	$W\ m^{-2}\ K^{-1}$	Re	Reynolds number	-
h_{ij}	Interaction energy between site i and j (2.2.2.3)	-	Pr	Prandtl number	-
I_D	Intrinsic defects	-	α	Solid solution phase (2.1) or absorpivity (1.2)	-
J	Molar flux (4.3.6) or solar flux (only 1.2)	$mol\ m^{-2}$ $W\ m^{-2}$	β	Hydride phase (2.1) or ($1/(k_B T)$ only 2.2.2.3)	- (J or eV)
K	Equilibrium constant	-	δ	Deviation from stoichiometry	-
k or (k_B)	Rate constant (2.2) or Boltzmann constant (only 2.2.2.3)	s^{-1} ($J\ K^{-1}$)	ϵ	Porosity (4.3.6) or Emissivity (only 1.2) or Occupancy number (only 2.2.2.3)	-
L	Length	m	η	Efficiency	-
$\mathbf{M}$ or M	Metal site $\mathbf{M}$ (4.3.2) or Molecular weight (M) (4.3.6)	- $g\ mol^{-1}$	γ	Surface energy flux	$J\ m^{-2}$
m	Mass	kg	ι	Heating rate for the Kissinger method	$T\ s^{-1}$
N	Moles	mol	κ	Sestek-Berggren parameters	s^{-1} or -
n	Reaction order (2.3.1) or Nearest neighbours (2.2.2.3) or Fragmentation order (5.4.4)	-	λ	Thermal conductivity	$W\ m^{-2}\ K^{-1}$
P	Pressure	bar	μ	Viscosity	Pa s
$\hat{p}$	Partition function	-	ν_m	Vibration frequency of metal lattice	Hz
Q	Heat duty	$W\ m^{-3}$ or W	ω	Product to reactive reactant volume ratio	-
R	Universal gas constant or R-squared statistical measure	$J\ mol^{-1}\ K^{-1}$ -	Ω	Empirical variable in SAM:EM	-
R_0	Particle/sphere radius	m	ϕ	Dimensionless pressure term for determining a PCI equation	-
R_c	Core radius	m	ψ	Basis function describing FEM (app. A.3)	-
r	Reaction rate	$mol\ m^{-3}\ s^{-1}$	ρ	Density	$kg\ m^{-3}$
S	Entropy	$J\ mol^{-1}\ K^{-1}$	σ_s σ_D	Sorption site availability Desorption site availability	-
T	Temperature	K or °C	$\sigma_{0.5}$	Over-pressure	-
t	Time	s	σ_{rad}	Stefan Boltzmann constant	$W\ m^{-2}\ K^{-1}$
t^*	Reaction completion time	s	τ	Tortuosity	-
t_{cr}	Nucleation time for metal phase	s	θ	Normalised hydride fraction	-
t_p	Precipitate growth time	s	θ'	Normalised metal fraction	-
t_c	Characteristic time	s	θ_s	Surface coverage	-
U	Overall heat transfer coefficient	$W\ m^{-2}\ K^{-1}$	ζ	Dummy variable - relaxation pressure	-

Chapter 1

Introduction

1.1 Global ambitions to combat climate change

Throughout history, the earth's climate has fluctuated due to factors mainly out of human control, such as variations in solar radiation from the sun due to the change in the Earth's orbit, to plate tectonics and volcanic eruptions. However, human impact on the environment is commonly referred to as global warming, where 97% of climate scientists agree *"that climate-warming trends over the past century are very likely due to human activities"*. [83]

These human activities grew significantly from the birth of the industrial revolution and the burning of fossil fuels primarily releasing carbon dioxide into the atmosphere. Carbon dioxide is a greenhouse gas, where an increase in greenhouse gases cause warming of the Earth. [83]. Logically, a push towards carbon neutrality or net zero, is necessary to reduce the effect of global warming. Net zero is achieved through either eliminating carbon emissions, instigating carbon removal such as offsetting, or a combination of both.

Another element to fossil fuels is the release of harmful emissions, such as carbon monoxide, nitrous oxides, and particulates. These substances can amplify the risk associated with pollution-related diseases, including respiratory infections. Globally, air pollution is estimated to cause around 7 million deaths each year, making it the world's largest single environmental health risk.

[96] Further, as the economic ramifications from COVID-19 materialises, the world looks for a path out. The International Energy Agency (IEA) report states that as the world stands still, the demand for oil, gas, and coal has fallen, while the demand for renewables remains constant. [4] With global renewable energy supply expected to grow by 5% in 2020, the current climate has enabled a favourable opportunity for sustainable energy solutions; through the adoption of green hydrogen/ammonia and renewable energy technologies, to be at the central heart of any economic stimulus package. In effect, the dual ambition in achieving net zero and eradicating air pollution can be accomplished.

This is no easy task, the world's total final consumption in 2017 was 9717 Mtoe, of which 41% was oil, 15.5% natural gas, 10.5% coal and 18.9% electricity. And regarding renewable electricity generation in 2017, nuclear generated 10%, hydro 16% and non-hydro 9%, combining to a 35% share. To achieve considerable reduction in carbon emissions, non-hydro sources need to increase significantly, where the key renewable resource driving the increase in non-hydro based supply is through harnessing solar energy. [35]

1.2 The potential of solar energy

Converting sunlight into a usable form is well established, such technologies available are solar photovoltaics (PV), solar thermal electricity and solar heating and cooling. Solar PV is experiencing rapid growth, where in 2018 there was 585 TWh of global capacity, and is on track to meet the 2030 International Energy Agency (IEA) targets of 3268 TWh. This is mainly due to low operating costs and falling prices. In comparison, electricity generation through concentrated solar power (CSP) holds a much smaller share with 13.4 TWh. Currently, CSP growth is not on track to reach the target of 184 TWh by 2030. However, the IEA recommends focusing on the value of thermal storage to attract investment in CSP [36].

Focusing on CSP, an indication of a suitable location for a CSP plant is through the measurement of direct normal irradiation (DNI). DNI is measured on a surface perpendicular to the direct sunbeam and affected by cloud cover. Below a DNI of 2 kWh m^{-2} day^{-1}, the electricity generation is 0 [47]. This rules out the United Kingdom, however there are plenty of suitable countries. From figure 1.1, the Atacama Desert in Chile (11 kWh m^{-2} day^{-1}), south Namibia and western South Africa (8.8 kWh m^{-2} day^{-1}), south west USA (8.5 kWh m^{-2} day^{-1}), western Australia (8.2 kWh m^{-2} day^{-1}), the Tibetan region of China (8 kWh m^{-2} day^{-1}) and the Sinai Peninsula in Egypt (7.8 kWh m^{-2} day^{-1}) are amongst the most attractive locations globally considering DNI only.

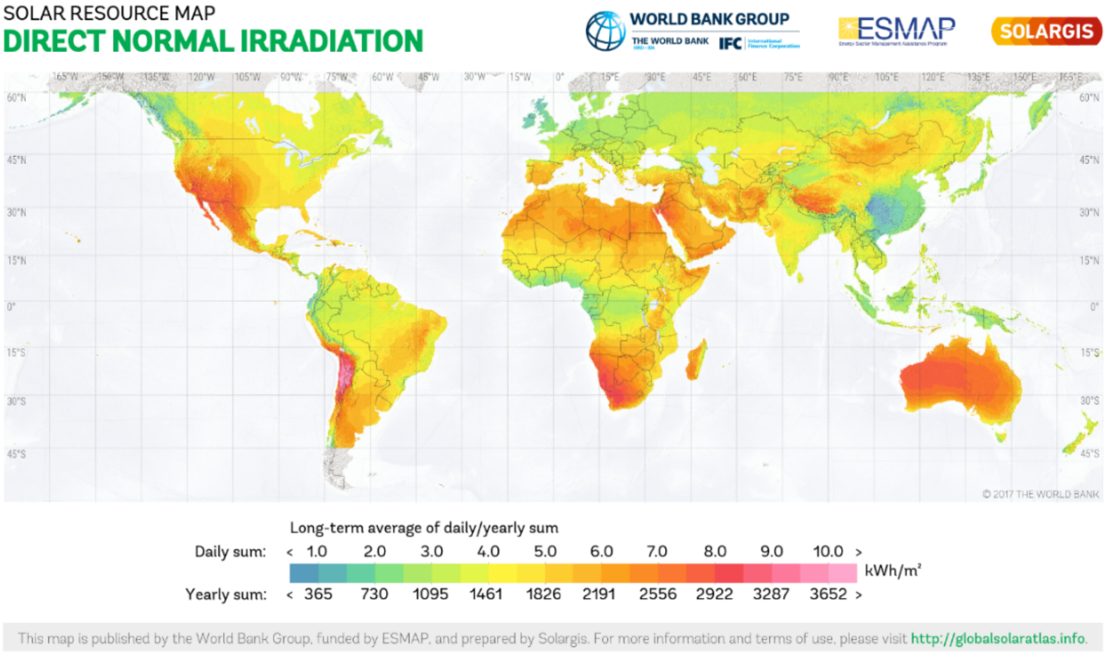

Figure 1.1: World map of direct normal irradiation (DNI) in 2017. [87]

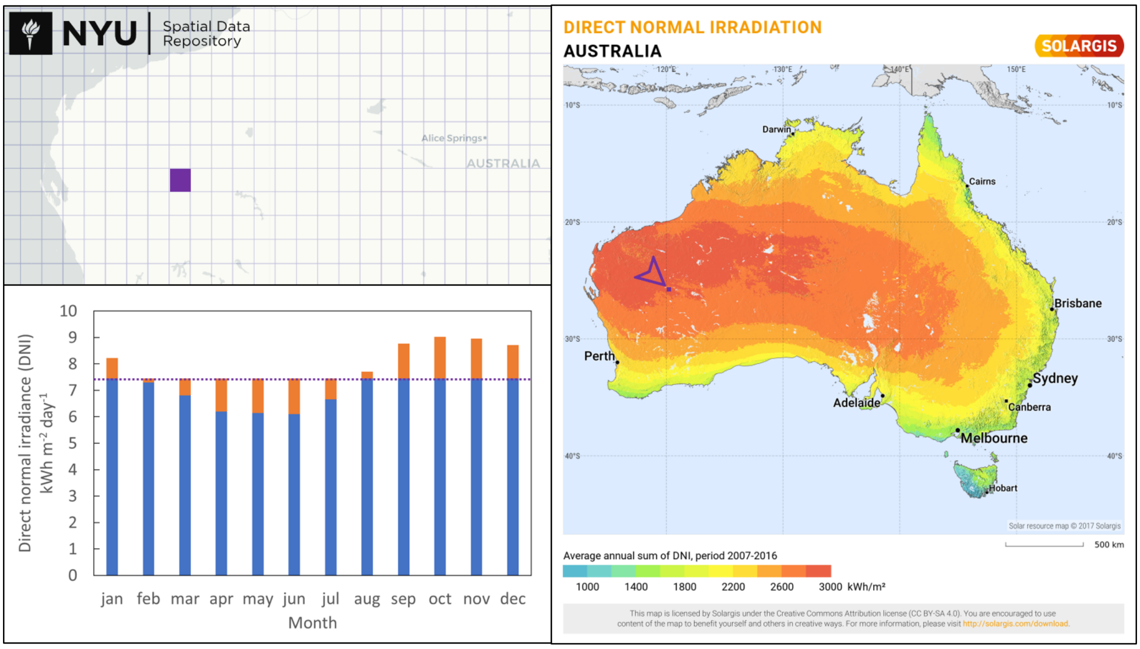

Figure 1.2: Yearly variation in direct normal irradiation of a typical CSP spot in Western Australia, with an average DNI of approximately 7.4 kWh m^{-2} day^{-1} [87, 66]

Another aspect with solar energy is that it varies daily and also, monthly. Dealing with the daily fluctuations can be managed through incorporating thermal energy storage. Figure 1.2 illustrates the change in DNI throughout the year in a suitable CSP plant location situated in Western Australia, where logically, there is additional output from the solar field during the summer and a reduction in the winter. The operating temperature of CSP plants depends on the type of collector technology used. The collector technologies can be split into two types, linear based or point-focus. Point-focus systems, such as solar towers, can typically reach higher overall efficiencies, mainly due to higher operating temperatures. Figure 1.2 illustrates the different technologies associated with linear and point-focus systems. When combining all suitable efficiencies, the overall efficiency indicates a suitable operating temperature range depending on the local solar flux concentrated 'C' times. Hence, the higher the value of C, the bigger, or more concentrated the collector. To calculate the overall efficiency:

$$\eta_{overall} = (\eta_{optical})(\eta_{transport})(\eta_{conversion})(\eta_{receiver})(\eta_{storage}) \tag{1.1}$$

$\eta_{optical}$ = The optical efficiency is defined as the amount of energy that reaches a solar collector, divided by the energy coming from the solar source. The optical efficiency for all systems was assumed to be 0.95. Losses include all reflectivity and flux spillage losses up to when radiation enters the receiver. [48]

$\eta_{transport}$ = The thermal losses within pipework and heat exchangers. For linear systems it is assumed a slightly lower $\eta_{transport}$ of 88% and 90% for point focus systems.

$\eta_{storage}$ = Thermal losses from the storage units. For this analysis, no storage is assumed

$\eta_{conversion}$ = The conversion efficiency is based on the second law of thermodynamics, where it is assumed the CSP plant operates at 70% from the maximum thermodynamic efficiency.

$$\eta_{conversion} = 0.7(\eta_{Carnot}) = 0.7(1 - T_L/T_H) \tag{1.2}$$

Where T$_H$ = hot source temperature and T$_L$ = heat sink temperature (assume ambient).

$\eta_{receiver}$ - The receiver efficiency is the useful converted energy over the input energy. Losses include reflective losses from the receiver and radiative, conductive and convective losses. [48]

$$\eta_{receiver} = (\dot{Q}_{absorbed} - \dot{Q}_{loss})/\dot{Q}_{input} \tag{1.3}$$

Assuming losses are dominated by radiative losses (suitable assumption at high temperature) thus,

$$\dot{Q}_{loss} = A_{rad}\,\epsilon_{rad}\,\sigma_{rad}\,T_H^4 \tag{1.4}$$

where A_{rad} = radiating surface area (m^2), ϵ_{rad} = emissivity factor, σ_{rad} = Stefan-Boltzmann constant (W m^{-2} K^{-4}) and T = temperature (K). Subscript "rad" for radiative. The absorbed heat flux is,

$$\dot{Q}_{absorbed} = \eta_{optical}\,\alpha_{rad}\,J_{rad}\,C_{rad}\,A_{rad} \tag{1.5}$$

where α_{rad} = absorptivity, J_{rad} = solar flux (W m^{-2}), and C_{rad} = concentration ratio. [48] Thus,

$$\eta_{receiver} = \eta_{optical}\alpha_{rad} - \frac{\epsilon_{rad}\,\sigma_{rad}T_H^4}{J_{rad}\,C_{rad}} \tag{1.6}$$

The solar flux (J_{rad}) and is based on an average daily DNI for a suitable area of 8.5 kWh m^{-2} day^{-1} = 354 W m^{-2}. The emissivity (ϵ_{rad}) is assumed as 0.8 [48] and absorptivity (α_{rad} = 0.9) for point-focus and 0.88 for linear systems. [47] Figure 1.3 shows that there is an optimum operating temperature for each CSP configuration. For instance, parabolic troughs and medium size point-focus systems can practically achieve a concentration ratio of 100, thus reaching an average efficiency of 20% within a moderate 300-400°C operating range. For large point-focus designs, such as a tower which concentrates the DNI by 1000 times, the optimum temperature is within the high range of 600-790°C delivering an average overall efficiency ≈ 30%, positioned as the target range for SunShot 2030 targets. However, there is an economic challenge at ≈ 600°C, whereby expensive nickel-based alloys are needed for steam turbine components [51]. Doubling the concentration ratio from 1000 to 2000, means operating temperatures in the region of 800-1000°C.

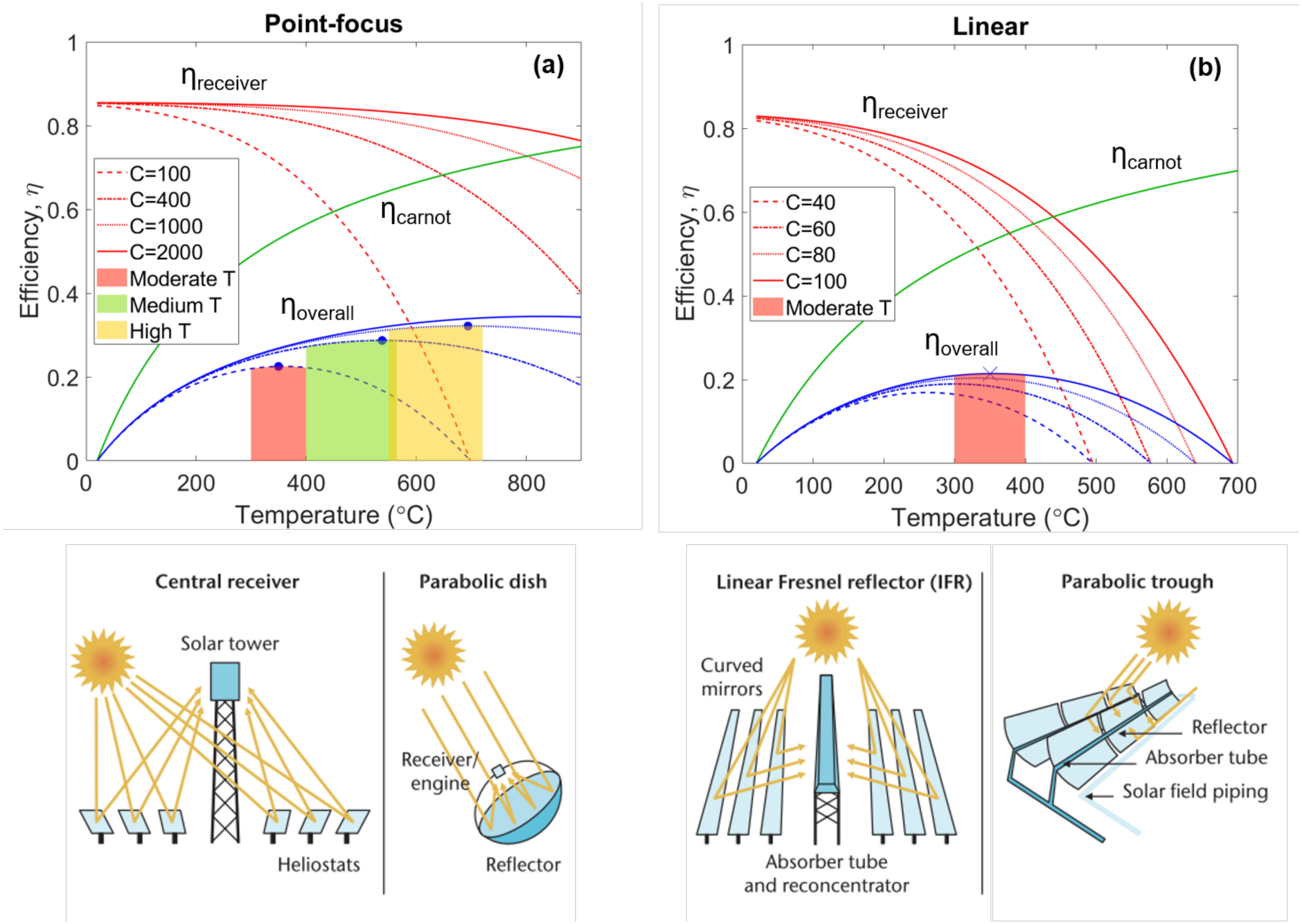

Figure 1.3: Plant efficiencies based on the average DNI of 8.5 kWh m^{-2} day^{-1}. (a) Point-focus systems such as Towers and Parabolic Dishes. (b) Linear systems such as Linear Fresnel reflectors and Parabolic troughs. Shaded areas are typical operating temperatures based on the concentration ratio. Images from [47]

1.3 Opportunity for CSP

According to the International Energy Agency (IEA), the current growth in CSP is not on track [34]. However, there is still opportunity for CSP playing a role in the global renewable energy mix. An advantage of CSP plants is the ability to utilise thermal energy storage (TES), allowing the energy to be used during demand periods [48, 99, 34].

Photovoltaics (PV) can also provide energy on demand when linked with energy storage such as PV to batteries (PV-B). As stated by the SunShot initiative (an American CSP research programme), when PV-B is considered next to CSP-TES, then the CSP-TES annualised net grid costs are attractive through realisation of the 2030 targets. The projected scenarios in 2050, based on the USA market are [63]:

1. 10% CSP-TES (of total installed capacity) if CSP-TES achieves its targets by 2030 while PV and batteries follow mid-cost trajectories.

2. 7% CSP-TES if CSP-TES achieves its targets by 2030 while PV follows low-cost trajectories and batteries mid-cost.

3. 1% CSP-TES if CSP-TES achieves its targets by 2030 while PV and batteries achieve low-cost trajectories

For CSP to reach these targets by 2030, a road map was devised by the National Renewable Energy Laboratory (NREL) based in the USA on three pathways, "molten salt", "falling particle" and "gas phase" [63, 56]. Although the direction and efficacy of these pathways is debatable, they cover all of the leading technologies in development with the potential to improve the economics of CSP. These pathways will be referred to when discussing competing technologies. When focusing on improving TES within CSP plants, the TES technologies are not independent, and any analysis should be aware that the TES system can affect the configurations and the associated challenges upstream and downstream of the TES.

1.4 DoE TES targets

The Unites States (USA), Department of Energy (DoE) sets targets for CSP-TES systems in order to achieve viability. These were taken on the 3/11/2019, and are as follows [21]:

1. **Improve heat transfer and thermal energy storage media TES materials.** All types of TES generally suffer from poor thermal conductivity and improving this will enhance performance. It will also allow less reactor space to be taken by heat transfer improvement architecture. Other general material improvements, such as energy density, volumetric density and resistance to degradation from cycling are also key to making TES more cost effective.
2. **Thermal energy storage (TES) cost $< \$15/\mathrm{kWh}_{th}$.** This cost includes installed and direct capital cost and does not include contingency and engineering, procurement & construction (EPC) indirect costs [55].
3. **Exergetic efficiency $> 95\%$.** Exergy analysis is useful for analysing a TES system as it includes factors such as how close the performance of a system approaches ideality and the supply thermal energy to the recovered thermal energy. Regarding, sensible and latent heat technologies, the storage duration then plays a part as the gap between supply temperature and recovery temperature increases with storage duration.
4. **Material degradation due to corrosion $< 15\ \mu$m/year.** This target is mainly for chlorine based molten salts as they are very corrosive in the liquid phase if oxygen and water are in the process stream. [63].

1.5 TES progress so far

At present, there are three types of thermal energy storage (TES) technologies which can be coupled to CSP plants. These are sensible heat, latent heat, and thermochemical energy storage (TCES) systems.

1.5.1 Sensible heat storage

1.5.1.1 Molten salts

Nitrate molten salts are a sensible heat technology, and the most common CSP-TES technology due to excellent life time (up to 10 000 cycles), good energy density and suitability for a Rankine cycle (up to 565°C). However, for a Brayton cycle ($\approx$ 720°C) chlorine/carbonate salts are required, leading to corrosion issues and significant cost increases. A Brayton cycle is an objective for CSP plants as higher efficiencies improve the economics. [67]

The current state of the art molten salt power tower uses a 60/40 wt% blend of sodium and potassium nitrate. The cold tank is held at 290°C and the hot tank is at 565°C. [63]

Various studies have been performed outlining the costs of nitrate salt systems at 565°C, and for systems at 720°C, carbonate and chlorine salts. The most comprehensive study was the Abengoa 2010 study, which was used to scale for the 720°C case and another was undertaken by Worley Parsons. The results are as follows [55]:

- TES direct cost for two-tank salt at 565°C = \$ 20 - 33 /kWh$_{th}$
- TES direct cost for two-tank salt ($MgCl_2$/KCl) at 720°C referenced from Abengoa 2010 = \$ 58 /kWh$_{th}$.
- TES direct cost for two-tank salt (Na/K/Li carbonate eutectic) at 720°C referenced from Abengoa 2010 = \$ 66 /kWh$_{th}$.

It is evident that all molten salt cases are above the TES target of \$ 15 /kWh$_{th}$ at both 565°C and 720°C scenarios.

1.5.1.2 Particulate solids

Another sensible heat technology, which is being advocated by researchers part of the SunShot project is using particulate solids. This uses ceramic/silica based particles as the heat transfer medium (HTM) with the silos (storage), particle heat exchanger (solid-sCO_2) and particle receiver integrated into the power tower. The HTM is raised to the receiver by a conveyor belt and falls through to the hot silo, into the particle heat exchanger and into the cold silo. The estimated cost of the TES system using insulated steel tanks was \$ 22/kWh$_{th}$ and \$ $<$ 15/kWh$_{th}$ using firebrick and concrete insulating materials.

Thus, this TES system has the potential to meet the cost target. The main challenge with this technology is not the storage system, but rather the integration of this system within the plant, such as the solid-sCO_2 heat exchanger (solid material on one side of the exchanger, supercritical carbon dioxide on the other), which is yet to be proven, or improving the HTM performance in the receiver. If achieved, particulate solids can be a feasible alternative to molten salts [55, 67].

1.5.2 Multiple loops in a CSP plant

Another approach is to use two separate loops within the CSP plant. One loop for the receiver-storage circuit, and the other for the power block. The receiver loop aims to use an inert fluid (e.g. CO_2, argon, helium) at conditions $\geq$720°C at the outlet of the receiver, 50-75 bar operating pressure and $\approx$ 550°C returning to the receiver. The power block is based on a (supercritical) sCO_2 Brayton cycle. The advantage of this approach allows potential decoupling of the TES technology, allowing for advanced energy storage methods, such as thermo-chemical energy storage. [55]

1.5.2.1 Latent heat systems

One of the technologies that has been considered with this approach is using latent heat systems. The materials are usually carbonates, fluorides or chlorides. Disadvantages with these systems are incongruent melting, sub-cooling and corrosion. Sub-cooling is undesired due to the unwanted shift in phase change temperature, aggravating the system. Encapsulating the PCM in a holding vessel reduces sub-cooling and corrosion but increases cost at scale-up. [67] A multi-tube heat exchanger has been estimated as the most competitive design at \$ 39/ kWh$_{th}$, above the 2030 target. [55]

1.5.2.2 Thermo-chemical energy storage (TCES)

Another candidate for a multiple loop system is thermo-chemical energy storage (TCES). In general, the main limitations with sensible and latent heat technologies are namely low energy densities (in comparison to TCES) and thermal losses, but are easier to design due to fewer complexities. [99] Table 1.1 summarises the advantages of thermo-chemical energy storage, compared to other TES technologies. The cost is the direct cost and is based on the recent estimates within the Generation 3 CSP road map report. For the TCES cost, the range is large due to the research being at a low maturity level.

From table 1.1, it is clear that TCES exhibits many advantages. It has larger volumetric and gravimetric energy densities, higher storage capacity and an unlimited storage period. Because of these inherent advantages, further research in TCES within CSP is a valid path in order to reach the DoE (USA Department of Energy) targets, specifically the target of \$15/kWh$_{th}$, with the potential to operate up to 720°C. Therefore, in the next section TCES candidates are explored, and the compatibility is discussed.

Table 1.1: Comparison of varying thermal energy storage technologies used in CSP plants.[99, 68]

Performance	Sensible thermal energy storage (STE)	Storage in phase change materials (PCM)	Thermo-chemical energy storage (TCES)
Storage capacity (kWh/t)	10-50	50-150	120-250
Cost (\$/kWh$_{th}$)	20-66 [84]	39-128 [55]	14-100
Energy density (volumetric density)	$\approx$ 50 kWh/m^3 of material	$\approx$ 100 kWh/m^3 of materials	$\approx$ 500 kWh/m^3 of reactant
Energy density (gravimetric density)	$\approx$ 0.02-0.03 kWh/kg of material	$\approx$ 0.05-0.1 kWh/kg of material	$\approx$ 0.5-1 kWh/kg of reactant
Storage period	Limited (thermal losses)	Limited (thermal losses)	Theoretically unlimited
Maturity	Industrial scale	Pilot scale	Lab/pilot scale
Complexity	Low	Medium	High

1.6 TCES system candidates

Although TCES has gained traction in interest over the past 5 – 10 years, it is in the early stages of development, with several key lab scale issues in need of resolving. These issues are the reaction kinetics, effective reactor design regarding heat and mass transfer and reducing loss of capacity with cycling [68, 99]. The leading TCES candidates are covered here, starting at the highest temperatures, followed by the candidates which show the most temperature versatility.

1.6.1 Steam methane reforming

The steam methane reformer (SMR) uses water and methane as the reactants at high temperatures (800-1000°C) to produce carbon monoxide and water endothermically. The SMR is linked to a methanator, i.e. the reverse reaction, producing the original reactants at lower temperatures of 350-700°C. The reaction is as follows. [48]

$$CH_4 + H_2O \rightleftharpoons CO + H_2$$

The products are cooled and stored at high pressure in a closed loop system. Further, the process generates side reactions, it suffers from poor reversibility, has catalyst issues (for methanation) and requires H_2 storage and CO storage. [68] In addition, this system operates at a receiver temperature that is too high at present and the recovery temperature is much lower than the receiver temperature.

1.6.2 Metal oxides

The other very high temperature candidate system is the metal oxide process. The process works by cycling between metal oxide in different oxidation states [74, 32],

$$MO_{2x+1} \rightleftharpoons MO + xO_2$$

where manganese is usually selected over other oxides (such as cobalt) due to lower material costs. [79] This system is of interest due to the oxygen being drawn from the air, negating the need for storage. The key issues with this system are the degradation with cycling. Binary metal oxides show promise with fast reaction kinetics, where Mn-oxide/Fe-oxide and Mn-oxide/Cu-oxide are potential candidates for CSP. These binary systems operate at 1000°C, so metal oxide TCES are very long term CSP options if plants reached such temperatures. [10] Table 1.2 summarises potential metal oxide candidates outlining useful data. The reaction time however is based for small samples on DSC/TGA and it will not necessarily relate to a typical prototype pilot scale reactor. In general, cycling incurs an increase in reaction time, where binary metal oxides perform better, showing enhanced stability. [10]

Table 1.2: Key oxide candidates taken from [10]. Onset temperature, reaction time and enthalpy analysed by simultaneous DSC/TGA in atmospheric air.

Material	Reduction			Re-oxidation		
	T (°C)	Enthalpy (J/g)	Reaction time (min)	T (°C)	Enthalpy (J/g)	Reaction time (min)
Mn-oxide	940	230	6	-	-	72
Fe-oxide	1400	600	5	1374	560	5
Cu/(Cu+Mn) = 0.5	960	167	5	930	120	6
Mn/(Fe+Mn) = 0.67	1000	233	7	900	162	9

From a current perspective however, the operating temperatures are above the ideal temperatures ≈ 720°C and for current plants up to 565°C. At present, all industrial scale systems utilise the Rankine cycle and super-heated steam for the power block, where the typical temperature ranges are shown in table 1.3.

Table 1.3: CSP design conditions/features in current and future target scenarios. The data for troughs and towers are based on current commercially proven systems [46, 55]

	Parabolic Trough	**Solar Tower**	**Sunshot target**
Operating solar field temperature (°C)	290-400	290-565	Receiver > 720
Power block and fluid	Rankine, superheated steam @ 380°C and 100 bar	Rankine, superheated steam 540°C and 100-160 bar	Brayton CO_2 @ 720°C and 200 bar
Heat transfer fluid	synthetic oil, water/steam, molten salt	Water/steam, molten salt	Molten salt (with low melting T), helium, argon, supercritical CO_2, particles
Storage system	Indirect two-tank molten salt (293-393°C)	Direct two-tank molten salt (290-565°C)	14h capacity

1.6.3 Ammonia reaction

One system that can operate within this temperature range is the reversible dissociation of ammonia.

$$NH_3 \rightleftharpoons N_2 + H_2$$

The dissociation of ammonia operates from 400-700°C, while the ammonia synthesis operates at 360-550°C using Haldo-Topsoe reactors. Other advantages are that there are no side reactions, a common storage volume can be used for H_2, N_2 and liquid NH_3 at ambient temperature and there is over 100 years of industrial experience to call upon [19]. The disadvantages however are the operating pressures and nature of the equilibrium curves. Typically, to dissociate NH_3, 700°C and 100 bar will give 90% conversion, whereas NH_3 synthesis at 400°C and 200 bar gives 60% conversion [19]. This means although the receiver can supply temperatures up to 700°C, the power generation temperature is throttled by the conversion limitations of NH_3. Ideally, it is desirable for a power block that operates close to the receiver temperature, along with a high temperature power generation loop enabling a high Carnot efficiency. However, a new catalyst has emerged for ammonia cracking at 400°C-450°C using lithium imide, which can cause researchers to re-visit this technology [50].

1.6.4 Hydration/dehydration of metal oxides

Another explored system is reacting steam with metal oxides. Pardo et al. reviewed many TCES candidates, including hydrides, carbonates, ammonia, redox systems and organic processes, and concluded that hydration systems were the most promising. They recommended the calcium system based on the follow equation.

$$Ca(OH)_2 \rightleftharpoons CaO + H_2O$$

The dehydration reaction (from receiver) operates at 420-450°C while the hydration (supplying power block) operates at 83 to 338°C. Advantages of this system include low operating pressure (1-2 bar), good reversibility, no by-products, no catalyst requirements and competitive material prices. However, prototypes have been expensive \$ 45 kWh_{th}^{-1}, with capacity tested up to only

100 cycles. Further, the system suffers from poor thermal conductivity, (albeit can be improved through good reactor design) and the operating temperatures limit the versatility. Again, from table 1.3 above, it is desirable for a system that can operate through trough and towers systems.

1.6.5 Hydride systems

Hydrides have the capability to operate at current commercial plant temperatures (290 to 565°C i.e. nitrate salts) and also at higher temperatures ($\geq$720°C). For instance, suitable materials are MgH_2 (practical 360-450°C), $MgFeH_2$ (practical 450-510°C) and $NaMgH_3$ (theoretical 382-683°C) [51, 84]. The practical term refers to the operating range useful work can be extracted from the heat of reaction. The partial addition of fluorine has been shown to help stabilise metal hydrides and improve cycling capabilities. For example, a $Mg(H_{0.85}F_{0.15})_2$ system can cycle at 80°C higher than bulk MgH_2 [97]. For very high temperature systems, (700-800°C) calcium based hydrides have been identified, such as Ca_5Si_3, $Ca_4Mg_4Fe_3H_{22}$ or $CaNH + CaH_2$ although the theoretical H_2 capacity is within 1-2.5 wt% [51]. In addition, $MgH_2 \rightleftharpoons Mg + H_2$ can reliably thermally cycle between 360°C-450°C. Thus, the receiver and power block can be within similar temperature ranges. The main disadvantage for hydride based TCES systems is what to do with the hydrogen. Two solutions for this are compression in underground gas storage and storage in a low temperature metal hydride (LTMH), such as $NaAlH_4$. [16, 95, 84]. The debate of which system is best is still ongoing, however Sheppard and Buckley performed a techno-economic study of various promising hydrides (e.g. MgH_2, Mg_2FeH_6, $NaMgH_3$, $NaMgH_2F$ and NaH) with underground gas storage and determined a specific installed cost range from \$13.7 to 26.7 kWh_{th}^{-1}. Thus, these calculations indicate hydride-compressed underground gas storage may reach DoE thermal energy storage costs targets. This paper also assumed a bulk density of 0.7, which if raised, can significantly reduce the number of reactors. In addition, they mentioned utilising the sensible heat of hydrogen to perform work allows potential for further cost reduction of the system [84].

Returning attention to MgH_2, a test system based on this material can be applied to current commercial plants as a suitable technological entry point. As a binary hydride, it is the simplest type of hydride, thus the kinetics will be (in theory) easier to interpret and validate in a prototype reactor. Furthermore, the material cost is an attractive €2.9 kWh_{th}^{-1} with a good thermal energy density of 962 kWh_{th} m^{-3} and a practical thermal storage of 2389 kJ kg^{-1} [51]. These suitable numbers enable MgH_2 to be a promising material for ≈ 400°C CSP TCES. A disadvantage of this material is centred around the thermal conductivity as the hydrogenation and dehydrogenation reaction rate are dependent on the rate of heat transfer. However, this effect can be minimised through including additives, such as exfoliated natural graphite and a catalyst (such as TiB_2) [18]. The other key obstacle surrounding magnesium based hydrides are the understanding of the reaction kinetics. For any reactor to reach commercial scale, a sufficient rate equation grounded on physical principles is required so that there is confidence in the design with scale-up. This objective is the backbone of the thesis.

As detailed in the next chapter, a suitable model both for magnesium hydrogenation and magnesium hydride dehydrogenation arguably has yet to be developed. Therefore, chapter 2 discusses the literature regarding generic and hydride reaction engineering models, which form the main theme of objectives.

1.7 Aims and objectives

1.7.1 Aims

The principal aim of this PhD is to build a unifying model that blends established concepts of reaction engineering, combined with thinking within the metal hydride community and novel ideas, to create a framework to which it could be applied to the reaction kinetics of metal hydrogenation and hydride dehydrogenation.

Through this, this work aims to apply the model to larger scale designs, and aid how one could envisage a metal hydride TCES in a commercial capacity. In parallel, this PhD aims to continue the work on 154 g magnesium reactor, a TCES prototype using thermal oil. The goal is to gather good quality data to test the derived model.

1.7.2 Objectives

1. Develop a model for magnesium hydrogenation suitable for scale up. (chapter 4)
2. Develop a model for magnesium hydride dehydrogenation suitable for scale up. (chapter 5)
3. Validate this model with experimental data at small (0.2 g) and large (154 g) lab-scale sample sizes. (chapter 4, 5 and 6)
4. Develop a TCES magnesium hydride prototype and explore the challenges associated with this technology. (chapter 6)

Chapter 2

Background

2.1 Overview of metal hydrides

Hydrides are compounds containing hydrogen anions which are bonded to a less electronegative element. The thermodynamics of hydride formation are described using pressure-composition-isotherms (abbreviated to either PCT or PCI). Starting with a definition of the change in Gibbs energy (ΔG) (J mol^{-1}) of a system,

$$\Delta G = \Delta H - T\Delta S$$

where ΔH (J mol^{-1}), ΔS (J K^{-1} mol^{-1}) and T (K) are the change in enthalpy, entropy of the system and temperature respectively. The Gibbs energy at a specified standard state can also be expressed in terms of the equilibrium constant K_{eq} as,

$$\Delta G^{\ominus} = -RTln(K_{eq})$$

with R (J K^{-1} mol^{-1}) being the universal gas constant. Equating the two equations and assuming standard conditions, results in the common (integrated) van't Hoff equation.

$$ln(K_{eq}) = -\frac{\Delta_R H}{RT} + \frac{\Delta_R S}{R} \tag{2.1}$$

In equation 2.1, $\Delta_R H$ and $\Delta_R S$ are the reaction enthalpy and entropy respectively. At a given temperature at equilibrium, the hydrogen gas pressure will equate to the hydrogen bound equilibrium pressure ($P_{H_2} = P_{eq}$) (bar). Also, the equilibrium constant is equal to the hydrogen fugacity, where the real gas behaviour is accounted for with a suitable equation of state. In general however, for brevity, it is usually noted that $K_{eq} = P_{eq}/P_0$, where P_0 is the reference pressure (usually 1 bar). If hydrogen is introduced in stages (an aliquot) at constant temperature, where equilibrium is reached for each stage, then the pressure at each stage can be plotted against the increasing reacted fraction. This plot is a pressure-temperature-composition (PCI) isotherm. Figure 2.1 shows a plot of a typical PCI. An isotherm is characterised by the solid red line on the left chart, with (typically) three distinct phases. The first phase is where hydrogen is in solid solution (α) with the metal. The bulk of the reaction occurs during the co-existence phase ($\alpha + \beta$), which is sometimes represented by a flat plateau (depending on the metal), where the β phase is the hydride phase. At a high hydrogen to metal ratio (H/M) the system is exclusively β phase. With increasing temperature, the PCI rises and if the temperature rises past the critical temperature (T_c), the co-existence phase ends. From equation 2.1, a plot of $ln(P_{eq})$ against $1/T$ allows one to determine $\Delta_R H$ and $\Delta_R S$ as shown in the right chart of figure 2.1. For hydrogenation $\Delta_R H < 0$ (i.e. exothermic) and $\Delta_R S < 0$ (fewer ways of arranging the energy of the system), while during dehydrogenation, $\Delta_R H > 0$ and $\Delta_R S > 0$.

The enthalpy term determines the strength of the metal hydrogen bond, while the entropy term mainly describes the change from molecular hydrogen into bound hydrogen. In addition, as the Gibbs energy is a measure of the system's spontaneity, the temperature a system is in equilibrium can be determined. At equilibrium $\Delta G = 0$ thus,

$$T\,(1\,bar) = \frac{\Delta H}{\Delta S} \tag{2.2}$$

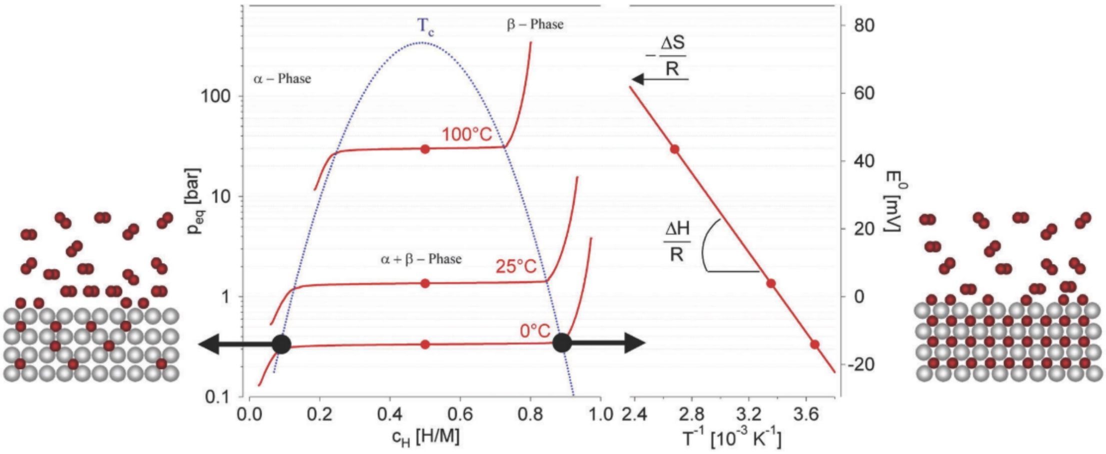

Figure 2.1: PCT for hydrogen hydrogenation (forward reaction) for a typical inter-metallic compound. [100]

Therefore, if a Mg, H_2 and MgH_2 (bulk) system were at 1 bar, and $\Delta_R H =$ -75.0 kJ mol^{-1} and $\Delta_R S =$ -135.6 J mol^{-1} K^{-1} [97], the temperature (1 bar) would be 280°C. Thus, the dehydrogenation of magnesium hydride would be spontaneous at temperatures greater than 280°C. Also, if it is assumed the formation of a binary hydride, i.e. $M + H_2 \rightleftharpoons MH_2$, as M and H_2 are elements, the enthalpy change of formation is equal to the enthalpy change of reaction.

In general, bulk solid powder usually exhibits a small surface area. However, reduction of the particle size to nano-scale results in a large proportion of the atoms at the surface. Part of the enthalpy would be stored as an excess surface energy, reducing the energy released during hydriding and de-hydriding. This results in a modified Van't Hoff relation, [78]

$$ln(P_{eq}) = -\frac{\Delta H'}{RT} - \frac{\Delta_R S^{\ominus}}{R} \quad \text{where} \quad \Delta H' = \Delta H + \frac{3\hat{V}_M \Delta_{M\rightarrow MH_2}}{R_0} \tag{2.3}$$

The right side of $\Delta H'$ in equation 2.3 is based on a non-porous sphere, where the specific surface area (SSA) of a sphere $= 3/R_0$ ($R_0 =$ radius of sphere). $\hat{V}$ is the molar volume of the respective component ($M =$ metal, $MH_2 =$ metal hydride). The term $\Delta_{M\rightarrow MH_2}$ (being a function of radius R_0 and surface energy flux γ) is denoted as, [78]

$$\Delta_{M\rightarrow MH_2}(\gamma, R_0) = \left[\gamma_{MH_2}(R_0)\left(\frac{\hat{V}_{MH_2}}{\hat{V}_M}\right)^{\frac{2}{3}} - \gamma_M(R_0)\right] + E_{ads} \tag{2.4}$$

An additional energy term E_{ads} is included to account for the discrepancy in surface energy reduction between the metal and hydride phases [78]. Equation 2.3 states increasing the surface area (to very small particle size) can alter the enthalpy of reaction, which is related to the reaction thermodynamics. For magnesium particles however, a minimum of 15 nm particle size is predicted based on repulsive energy calculations [20].

Moreover, Bérubé et al. noted the effect of excess enthalpy and strain at the grain boundary due to a rise in surface energy. This effect would become more pronounced with nano-size particles (for Mg $<$ 5 nm) as a larger number of atoms reside in the grain boundary, further reducing the enthalpy. This effect also increases the specific heat capacity and is related to the materials bulk modulus. [78]

The use of chemical destabilisation has been commonly reported in the literature, where a new component is introduced that reacts with the metal to form an intermediate species. In principal, instead of cycling between $M + H_2 \rightleftharpoons MH_2$, the addition of a de-stabiliser can cycle between the intermediate species and a hydride, such as $MA_x + H_2 \rightleftharpoons MH_2 + xA$. There are many destabilising systems, yet the common example is the magnesium hydride/silicon system [93],

$$MgH_2 + Si \rightleftharpoons \frac{1}{2}Mg_2Si + H_2$$

The dehydrogenation reaction is de-stabilised, resulting in a reduced enthalpy of reaction, as the endothermic dehydrogenation of magnesium hydride is counteracted by the exothermic formation of magnesium silicide. Thus, the overall equation can be split into two half equations,

$$MgH_2 \rightarrow Mg + H_2 \qquad \Delta_f H = 75\,kJ/mol \tag{2.5}$$

$$Mg + Si \rightarrow \frac{1}{2}Mg_2Si \qquad \Delta_f H = -39\,kJ/mol \tag{2.6}$$

Giving a enthalpy of reaction of 36 kJ/mol. Subsequently, the T(1 bar) is reduced but with a sacrifice in gravimetric hydrogen density. Further, the reversibility is challenging due to the difficulty in returning the Mg_2Si into its elements [93, 39].

Switching attention to the kinetics, metal hydride reaction kinetics are not entirely understood. Züttel explained the reaction pathway of hydrogen from molecular hydrogen to within the metal lattice (hydrogenation). To begin, a hydrogen molecule attaches to the metal surface via physisorption at about 0.2 nm from the metal surface. The required energy is $E \approx 10$ kJ mol^{-1}. As it gets closer, hydrogen dissociates and is chemisorbed to form a hydrogen metal bond (≈ 50 kJ/mol H_2). Once chemisorbed, the hydrogen has high mobility and can interact with each other, where the hydrogen can jump into the subsurface layer and diffuse into interstitial sites through the metal sublattice. [100]

The reaction pathway for metal hydrogenation outlined by Züttel [100] does not describe which stage of the reaction mechanism is rate determining. This is because this question is much in debate. One of the aims of this thesis is to contribute answering this pressing question, as metal hydride systems cannot truly be utilised until sufficient physical reaction mechanisms are established. Thus, the next section covers the essentials of current ideas surrounding the essentials of reaction kinetics, surface reactions and ultimately how these have been applied to the hydrogenation of metals and the dehydrogenation of metal hydrides.

2.2 General reaction kinetics

2.2.1 Homogeneous reactions

The reaction kinetics are an essential part of designing any chemical reactor, which is expressed algebraically as a rate law/equation. Homogeneous reactions are in general the simplest to derive, therefore this system is used to show the basics of reaction kinetics, and illustrate the terminology used in this thesis. Firstly, as a metal hydride reactor is a batch reactor, the mole balance is in the form [28],

$$-r_A = \frac{1}{V}\frac{dN_A}{dt} = kf(C) \tag{2.7}$$

The above equation states that the rate of disappearance of component **A** (r_A, mol m^{-3} s^{-1}, negative sign for reducing and subscript A) is related to the volume (V, m^3) and the derivative of the moles of **A** with respect to time (dN_A/dt, mol s^{-1}), and the product of the rate constant (k, s^{-1}) and some concentration dependent function $f(C)$ (mol m^{-3}) [28, 43].

For the reaction **A** → Product, the rate law for the rate of disappearance of **A** can be written as,

$$-r_A = kC_A \tag{2.8}$$

Equating 2.7 and 2.8, knowing that the concentration of component **A** is $C_A = N_A/V$ (N = moles, V = volume) and defining a fractional conversion as $X_A = 1 - C_A/C_{A_0}$ (C_{A_0}= initial concentration of A) gives,

$$-r_A = -\frac{dC_A}{dt} = kC_{A_0}(1 - X_A) \tag{2.9}$$

To calculate k, equation 2.1 can be differentiated with respect to T (K) giving another form of the van't Hoff equation.

$$\frac{d\,ln\,K_{eq}}{dT} = \frac{\Delta_R H^{\ominus}}{RT^2} \tag{2.10}$$

As the equilibrium constant is $K_{eq} = k_1/k_{-1}$ (where k_1 and k_1 are the rate constants of the forward and backward reaction respectively), then equation 2.10 can be rewritten as [76],

$$\frac{d\,ln\,k_1}{dT} - \frac{d\,ln\,k_{-1}}{dT} = \frac{E_1}{RT^2} - \frac{E_{-1}}{RT^2} \tag{2.11}$$

where E is the energy to drive the respective reaction (subscript 1 = forward, -1 = backward). Van't Hoff then argued that the first and second terms on each side can be equated [76],

$$\frac{d\,ln\,k_1}{dT} = \frac{E_1}{RT^2} \qquad\qquad \frac{d\,ln\,k_{-1}}{dT} = \frac{E_{-1}}{RT^2} \tag{2.12}$$

If one then focuses on either the forward or backward reaction independently, (for brevity, the subscripts are subsequently dropped) and if E is assumed independent of temperature and integrated, this gives,

$$ln\,k = -\frac{E}{RT} + \text{constant} \tag{2.13}$$

$$k(T) = A\,exp\left(-\frac{E}{RT}\right) \tag{2.14}$$

where equation 2.14 is the Arrhenius equation. Where A (typically s^{-1}) is the frequency/pre-exponential factor and E (J mol^{-1}) is the activation energy [28].

The common method to test a rate equation is through applying linear least squares on an integrated rate equation. In this thesis, this is referred to as the **integral method**. The rate equation is integrated and re-arranged into a linear format. If the experimental data is directly proportional to the integrated rate law (i.e. a straight line), then the fit is considered satisfactory. If equation 2.9 above is written in terms of conversion only thus, $dX_A/dt = k(1-X_A)$ and integrated from 0 to X_A and from 0 to t; this gives,

$$-ln(1 - X_A) = kt \tag{2.15}$$

A plot of $-ln(1 - X_A)$ versus t would test a first order rate equation, with the rate constant k being the gradient. [43] From taking the natural logarithm of the Arrhenius equation,

$$ln(k) = ln(A) - \frac{E}{RT} \tag{2.16}$$

The activation energy E and frequency factor A can be determined by isothermal experimental data collected at different temperatures, where a plot of the rate constants against temperature can be performed using equation 2.16 [43].

2.2.2 Heterogeneous reactions

Gas-solid reactions are heterogeneous reactions. Much of this area concentrates on catalytic reactions due to its industrial importance, with an influential example being the ammonia reaction $N_2 + 3H_2 \rightleftharpoons 2NH_3$ on an iron based catalyst. The common approach to model solid catalysed reactions is through the work of Irving Langmuir (and then Hougen & Watson) [53]. For this reason, the essentials of Langmuir's work are covered, to help understand the potential links to metal hydride kinetics.

2.2.2.1 Langmuir isotherm

If an elementary reaction is assumed to be in dynamic equilibrium, then the adsorption reaction is based on the net rate of adsorption.

$$\mathbf{A} + \mathbf{M} \rightleftharpoons \mathbf{M} \cdot \mathbf{A}$$

This is where the rate of attachment is equal to the rate of detachment. The rate of attachment of component **A** to an active site (**M**) is proportional to the number of collisions that these molecules make with a surface active site per second. As such, the collision rate is proportional to component **A**'s partial pressure (P_A). As **A** only adsorbs to vacant sites, not occupied ones, it must also be proportional to the concentration of vacant sites (C_v). Thus, the rate of attachment (subscript A) is proportional to the product of P_A and C_v [28].

$$r''_A = k_A P_A C_v \tag{2.17}$$

Assuming the rate of detachment is first order, the rate of detachment (subscript -A) will be proportional to component **A** attached to the surface.

$$r''_{-A} = k_{-A} C_{M \cdot A} \tag{2.18}$$

With reaction rate (r) superscript $''$ denoting a surface reaction rate units, mol m^{-2} s^{-1}. Further note that with the rate equation expressed in flux form, the rate constant k_A and k_{-A} have units of m s^{-1}). As $r_A = r_{-A}$ (dynamic equilibrium), then

$$k_A P_A C_v = k_{-A} C_{M \cdot A} \tag{2.19}$$

Defining an equilibrium constant as $K_A = k_A/k_{-A}$, incorporating the site balance where $C_T = C_v + C_{M \cdot A}$ then,

$$K_A P_A (C_T - C_{M \cdot A}) = C_{M \cdot A} \tag{2.20}$$

and including the surface coverage θ_s, as $\theta_s = C_{M \cdot A}/C_T$ and rearranging to make θ_s the subject,

$$\theta_s = \frac{K_A P_A}{1 + K_A P_A} \tag{2.21}$$

Equation 2.21 above is commonly referred to as the Langmuir Isotherm [28], where Brunauer denoted this type of isotherm as a type 1 isotherm [53]. The pressure of component **A** over the surface is related to the concentration of **A** through the gas law ($P_A = Z C_A R T$, where Z = compressibility). Other essential assumptions of the Langmuir isotherm are [53]:

- The gas adsorbs on identical sites on a homogeneous surface.

- The gas adsorbs via a single layer (a monolayer) and once all sites are filled, maximum capacity is reached.

- Once the gas adsorbs, it is immobile.

- There are no interactions between adjacent adsorbed molecules. This results in a constant heat of adsorption, and thus this parameter does not change with surface coverage.

2.2.2.2 Langmuir-Hinshelwood mechanism

The theory defining the isotherm above can be applied to determine the rate of gas-on-surface reactions. For example, with the reaction,

$$\mathbf{A} \rightarrow \text{Product}$$

whereby component **A** is (1) absorbed to an active site, (2) converted to product and finally (3) desorbed to free the site; the net rate of adsorption (r''_{AP} - units [mol m^{-2} s^{-1}]) is taken from equation 2.19, thus

$$r''_{AP} = k_{AP}C_A(1-\theta_s) - k_{-AP}\theta_A$$

with the desorption rate dependent on the surface coverage of **A** only. The surface coverage (θ_s) is the sum of sites covered by **A** and Product (subscript P),

$$\theta_s = \theta_A + \theta_P \tag{2.22}$$

and as the reaction step at the surface (2) is assumed rate determining (Langmuir-Hinshelwood mechanism), a dynamic equilibrium for both **A** and Product can be assumed.

$$K_A C_A(1-\theta_s) = \theta_A \tag{2.23}$$

$$K_P C_P(1-\theta_s) = \theta_P \tag{2.24}$$

Equating equation 2.23 and 2.24 into 2.22 allows the creation of the isotherm equation.

$$\theta_s = K_A C_A(1-\theta_s) + K_P C_P(1-\theta_s) \tag{2.25}$$

$$\theta_s = \frac{K_A C_A + K_p C_p}{1 + K_A C_A + K_p C_p} \tag{2.26}$$

If the forward reaction dominates the backward reaction, one can assume $k_{AP} \gg k_{-AP}$ and thus $r''_{AP} = k_{AP}C_A(1-\theta_s)$. Substitution of the isotherm equation (2.26) into the rate equation to eliminate θ_s gives,

$$r''_{AP} = k_{AP}C_A\left[1 - \frac{K_AC_A + K_pC_p}{1 + K_AC_A + K_pC_p}\right] = \frac{k_{AP}C_A}{1 + K_AC_A + K_pC_p} \tag{2.27}$$

Most experimental data of gas reactions catalysed on a solid surface can be represented accurately using a Langmuir-Hinshelwood mechanism [53]. The result of 2.27 shows a fundamental difference to a simple homogeneous reaction ($r_A = k_AC_A$) in that equation 2.27 contains a resistance term and thus the equation is in the form, [43]

$$\text{Rate} = \frac{\text{(Kinetic term)(driving force)}}{\text{resistance}} \tag{2.28}$$

another way to view this is that the resistance is site inhibition as components **A** and Product are blocking/occupying sites, so the reaction rate is reduced. To generate the surface reaction rate law above, an isotherm/PCI was used, in this case the Langmuir isotherm (to remove θ_s).

The above example is for the basic gas-solid reaction (**A** → Product). In general, surface reactions are more complex with intermediate states resulting in a non-elementary reaction, where the stoichiometry does match the kinetics [43]. Non-elementary reactions can be split into a series of elementary reaction steps.

$$\mathbf{M} + \mathbf{A} \underset{2}{\overset{1}{\rightleftharpoons}} \mathbf{A}_{ad} \tag{2.29}$$

$$\mathbf{A}_{ad} \underset{4}{\overset{3}{\rightleftharpoons}} \mathbf{B}_{ad} \tag{2.30}$$

$$\mathbf{B}_{ad} \underset{6}{\overset{5}{\rightleftharpoons}} \mathbf{B} + \mathbf{M} \tag{2.31}$$

In this sequence, component **A** adsorbs to a metal site **M** to create an adsorbed species $\mathbf{A}_{ad}$, reacts to form $\mathbf{B}_{ad}$ and then desorbs to release the site M and create product **B**. If $\mathbf{A}_{ad} \underset{4}{\overset{3}{\rightleftharpoons}} \mathbf{B}_{ad}$ is assumed rate determining, then the reaction rate would be [53],

$$r_{AB} = \frac{\left(\frac{k_1 k_3}{k_2}\right) P_A M_T - \left(\frac{k_6 k_4}{k_5}\right) P_B M_T}{1 + \left(\frac{k_1}{k_2}\right) P_A + \left(\frac{k_6}{k_5}\right) P_B} \tag{2.32}$$

where M_T is the total number of sites. From equation 2.32, there are many constants that need to be determined, which generally grow in number with more complicated mechanisms. This is an issue with long and complicated rate equations, whereby it can become problematic finding the right mechanism. A large number of parameters requires good quality and reproducible data. Thus, it is not acceptable to select mechanisms which fit the data well and state "this is the correct mechanism", as the difference in fit can fall within experimental error. Therefore, it is preferred to say "this type of reaction can be represented well by this mechanism".

2.2.2.3 The type V Isotherm

When the Langmuir Isotherm was derived it was mentioned that it falls within the scope of a type 1 isotherm. This classification was proposed by Brunauer who separated adsorption of gases onto solids into five general forms. Over the years a type VI was introduced [85]. A figure of the isotherms are shown in figure 2.2.

One can notice that the type V isotherm has an uncanny resemblance to the metal hydride PCI shown in figure 2.1, but with the axes swapped. The convention for hydrogen gas reacting with solids appears to have always had the pressure on the y-axis, and the molecules reacted on the x-axis.

As the path of hydrogen involves physisorption, chemisorption (two forms of adsorption) and a highly mobile hydrogen diffusing through to the bulk (essentially absorption); this has potentially contributed to the varied range of naming conventions regarding hydrogen reacting with solids. For the hydriding reaction, some researchers use absorption, others use sorption (thus both absorption and adsorption) and many use hydrogenation. For the dehydriding reaction desorption and dehydrogenation are used. For clarity, in this thesis:

- Hydriding reaction - Interchangeably use hydrogenation or sorption.
- Dehydriding reaction - Interchangeably use dehydrogenation or desorption.

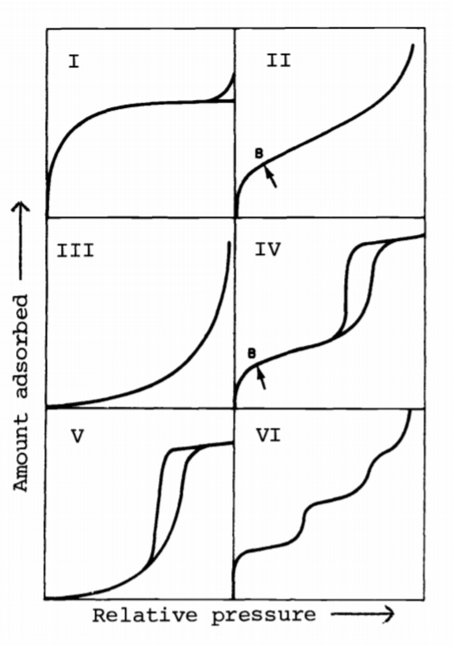

Figure 2.2: 6 types of adsorption isotherms first proposed by Brunauer with the addition of type VI as classified by IUPAC. [85]

Type I - Representative of micro-porous solids having relatively small external surface. (e.g. zeolites) Maximum uptake governed by accessible micro-pore volume rather than by the internal surface area. [85]

Type II - This isotherm represents unhindered monolayer to multilayer adsorption, and is represented well by the BET isotherm. Obtained with non-porous or macro-porous adsorbent. Point B indicates where multilayer coverage begins. [85]

Type III - Representative of systems which increase in capacity as adsorbate nucleates on the surface and then enters a significant growth phase. [53]

Type IV - Similar to type II, i.e. monolayer to multilayer coverage. The hysteresis is due to capillary condensation taking place in mesopores. [85]

Type V - Sing (1982) stated Type V is similar to type III in that the adsorbent—adsorbate interaction is weak compared with the adsorbate—adsorbate interactions [53, 85, 81]. Type VI - This isotherm typically represents stepwise multilayer adsorption occurring on a uniform non-porous surface [85].

Focusing on the type V isotherm, models have been developed to represent them. A common model is the lattice gas model. This model can:

- Represent adsorbate-adsorbate (H-H) interactions for commensurate layers. A commensurate layer is an ordered array of distinct lattice sites [53].
- Also, it predicts the arrangement for the adsorbed layer.

The lattice gas model starts with the same assumptions as the Langmuir Adsorption Model. I.e. component **A** can adsorb onto unoccupied sites to give an adsorbed species,

$$\mathbf{A} + \mathbf{M} \rightleftharpoons \mathbf{M} \cdot \mathbf{A} \tag{2.33}$$

The lattice gas model however accounts for each possible arrangement of the adsorbate and the effect of the local interactions between adjacent adsorbed molecules. This means the adsorbate arrangement is considered in creating the isotherms. From a physical perspective, the lattice gas model considers that at a given coverage, variations in surface atom arrangement would influence the nearest neighbour interactions and thus have different energies.

To do this, statistical mechanics are employed. Derivation is shown in Masel (1996), and the key results are summarised here [53]. Assuming there is only one type of adsorption site, the partition function for all arrangements of the adsorbed layer ($\hat{p}$) is,

$$\hat{p} = \sum_{n} exp(\beta\ E_n) \tag{2.34}$$

where E_n is the expectation value of the free energy (energy of lattice gas) when the layer is in arrangement n and $\beta = 1/(k_B T)$; k_B = boltzmann constant and T = temperature). For site i an occupancy number of $\epsilon_i = 0$ is empty and $\epsilon_i = 1$ is occupied. Assuming there are only direct H-H interactions with pairwise additive potential and only two-body interactions then,

$$-H_n = H_0 + H_1 \sum_{i} \epsilon_i + \frac{1}{2} \sum_{i,j} h_{ij} \epsilon_i \epsilon_j \tag{2.35}$$

H_0 = free energy of surface with no adsorbate
H_1 = free energy of adsorbed molecule
h_{ij} = interaction energy between molecules on site i and j. $+h_{ij}$ = attractive interaction, $-h_{ij}$ = repulsive interaction.

The second term in equation 2.35 represents free energy change with coverage. The third term represents the variation in free energy with changing adsorbate arrangement. To solve these equations, the Monte Carlo method can be used to generate the adsorption isotherms. Figure 2.3 shows the result of the Monte Carlo method. It is evident, the isotherms display similar characteristics to an ideal metal hydride PCI but with the axes swapped (e.g. 2-phase region, overall shape and critical point etc.).

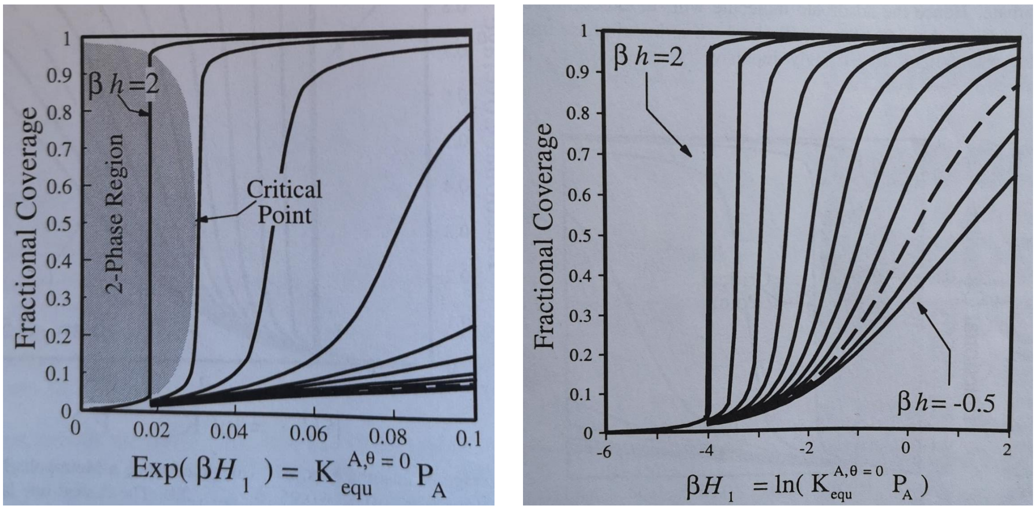

Figure 2.3: Graphs of the solved Metropolis/Monte Carlo algorithm on a 40x40 lattice. These are taken directly from Masel [53] ($\beta = 1/k_BT$). (Left) This graph shows close resemblance to a traditional PCI, but with the axes flipped. Highlighted is the two-phase region, critical point, and subsequent transition away from a flat plateau. (Right) Replot with $ln(K_{eq}P_A)$. Attractive interactions show a flat plateau, while repulsive interactions show a slope.

The solution from the Monte Carlo method does not provide an analytical solution. The simplest approximation that does give an analytical solution is the Bragg-Williams approximation, where the H-H interactions are considered in an average sense. The end result gives the following equation 2.36:

$$\theta = \frac{1}{1 + exp(-\beta H_1 - 0.25\beta h n_n \theta)} \tag{2.36}$$

Equation 2.36 is essentially a sigmoid function $f(x) = 1/(1 + e^{-x})$, where H_1 is the independent variable. The $(0.25\beta h n_n \theta)$ term alters the trajectory of the function, where h is the average interaction energy and n_n is the number of nearest neighbours at a given site.

2.2.2.4 Fluid-particle reactions

In the previous sections, the material covered involves gas reacting at a surface (typically a catalyst surface) whereas in this section, the scenario is a gas coming in contact with a solid, **reacting with it** and producing a product,

$$\mathbf{A}(\text{gas}) + \text{b}\mathbf{B}(\text{solid}) \rightarrow \text{Product (solid)} \tag{2.37}$$

where b is the stoichiometric ratio. This is similar to the metal hydrogenation reaction, however this reaction usually involves volume expansion. For $Mg + H_2 \rightarrow MgH_2$ the expansion is in the region of 20-30% [70]. The shrinking core model (SCM) is a fluid-particle reaction model based on a constant particle size. In this model, the reaction occurs at the pellet surface. At the beginning, the reaction starts at the outer skin, with the reaction front moving inwards as the reacting "core shrinks" until the core is fully reacted. This model can be applied to varying pellet shapes, such as spheres, cylinders or flat plates [43].

Section A.4 shows the derivations of the shrinking core equations in the differential form (see figure 2.4), which is not shown in [43], and also in the integral form (also see figure 2.4), which is originally shown in [43]. Figure 2.4 shows a summary of the rate equations depending on which step is rate determining. For instance, if the surface chemical reaction is rate determining, then model (3) is used. These models have been commonly used to represent metal hydrogenation [61, 60, 59].

$$A(fluid) + bB(solid) \rightarrow Solid\ product$$

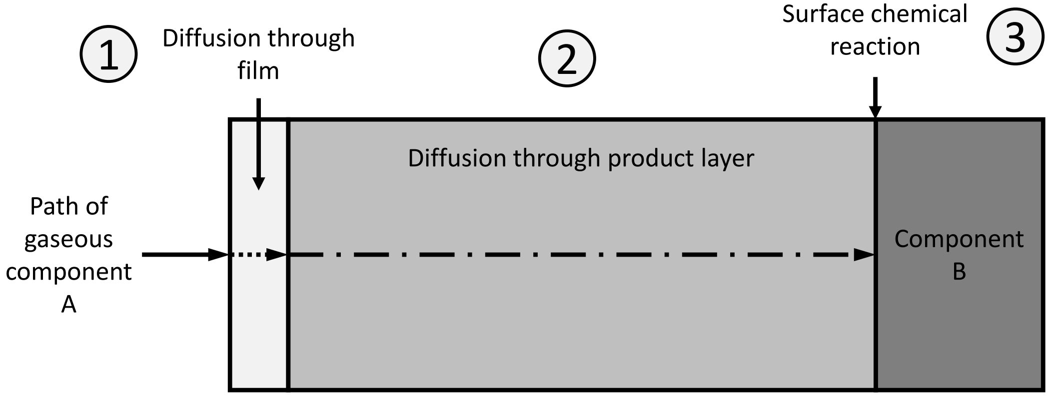

Combining resistances in series

① + ② + ③

$$t_{total} = t_{film} + t_{product} + t_{reaction}$$

$$-\frac{1}{4\pi R_c^2}\left(\frac{dN_B}{dt}\right) = \frac{bC_A}{\frac{1}{k_g} + \frac{R_0(R_0 - R_c)}{R_c} + \frac{R_0^2}{R_c^2 k"}}$$

Model	Differential form	Integral form
①	$\frac{-bSSA}{4\pi R_0^2}\frac{dN_A}{dt} = -r_A = bk_g(SSA)C_T(1 - X_B)$	$\frac{t}{t^*} = X_B$ or $kt = X_B$
②	$-\frac{dN_A}{dt}\frac{RSA}{4\pi R_0^2} = -r_A = \frac{D_e RSAC_T}{R_0}\frac{(1 - X_B)^{\frac{5}{3}}}{1 - (1 - X_B)^{\frac{1}{3}}}$	$\frac{t}{t^*} = 1 - 3(1 - X_B)^{\frac{2}{3}} + 2(1 - X_B)$
③	$-\frac{dN_A}{dt}\frac{RSA}{4\pi R_0^2} = -r_A = b(k"RSA)C_T(1 - X_B)^{\frac{5}{3}}$	$\frac{t}{t^*} = 1 - (1 - X_B)^{\frac{1}{3}}$

Figure 2.4: Shrinking core equations for a fluid-particle reaction. Based on a spherical surface, where the diagram is a 2D representation of a sphere. SSA = specific surface area, RSA = reactive surface area, R_0 = particle radius, R_c = shrinking core radius, X_B = fractional conversion of B, k_g = mass transfer coefficient, D_e = effective diffusion coefficient, k'' = effective velocity coefficient, t = time, t^* = completed time.

2.3 Magnesium hydrogenation kinetics

2.3.1 Diffusion, contracting volume and JMA models

Barkhordarian et al. investigated the magnesium hydrogenation reaction catalysed with Nb_2O_5 [8]. They summarised 7 models in the integrated form shown in table 2.1. The fractional conversion of B (X_B in previous sections) is equivalent to the normalised hydride fraction (θ). The normalised hydride fraction is the normalised fraction of hydride formed, i.e. when $t = 0$, θ=0 and $t = t^*$, θ=1. (t^* = time for complete reaction)

Table 2.1: Barkhordarian et al. equations used to fit their experimental sorption/hydrogenation data

Number	Integrated rate equation
1	$\theta = kt$
2	$[-ln(1-\theta)]^{\frac{1}{3}} = kt$
3	$[-ln(1-\theta)]^{\frac{1}{2}} = kt$
4	$1-[(1-\theta)]^{\frac{1}{3}} = kt$
5	$1-[(1-\theta)]^{\frac{1}{2}} = kt$
6	$1-\left(\frac{2\theta}{3}\right)-(1-\theta)^{\frac{2}{3}} = kt$

First, the terminology is addressed, as over the years, researchers have given differing names to the very similar mechanisms, and for some it is difficult to determine which interface one is referring to. The terminology and reaction steps are shown in figure 2.5, with also a comparison to the Site Availability Model (SAM) [1].

Many of the models in table 2.1 were developed/collated by Mintz. An important difference between Mintz and SAM is the where the hydrogen dissociates. Mintz assumes the hydrogen dissociates at the metal hydride surface, and then diffuses through as a hydrogen atom. The other distinction is the names given to respective boundaries. "Author"-"Terminology" is used for describing each model.

(1) $\theta = kt$: This equation was denoted by Barkhordarian et al. as a surface controlled reaction, whereas Yagi-Kunii refers to it as a gas film controlled reaction. As such, the "Mintz"-"Surface/Film" is identical to equation A.41. It is apparent magnesium hydrogenation does not

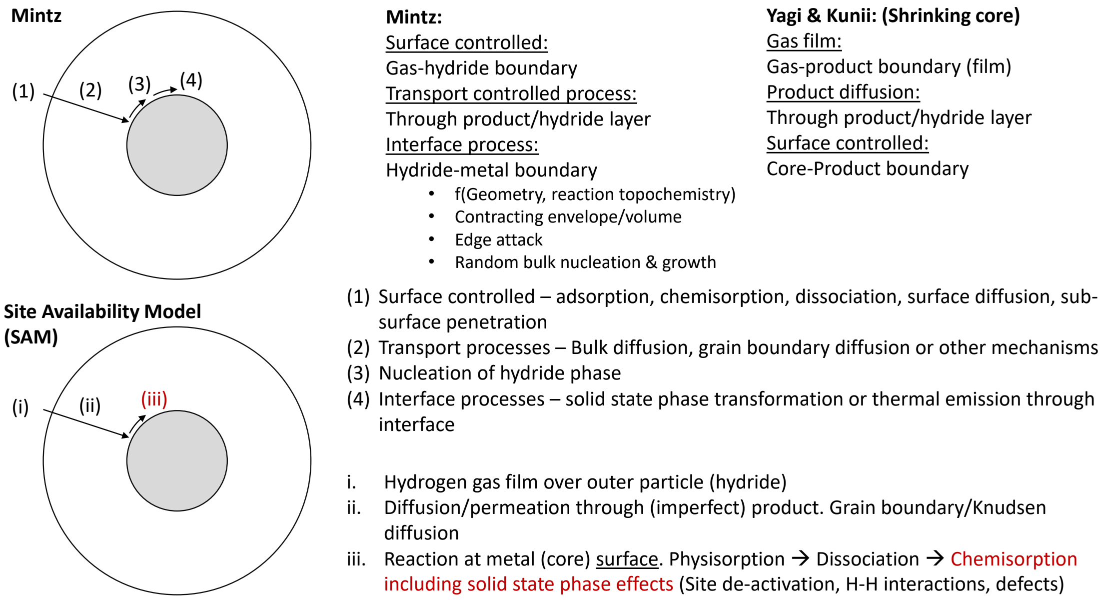

Mintz:
Surface controlled:
Gas-hydride boundary
Transport controlled process:
Through product/hydride layer
Interface process:
Hydride-metal boundary

- f(Geometry, reaction topochemistry)
- Contracting envelope/volume
- Edge attack
- Random bulk nucleation & growth

Yagi & Kunii: (Shrinking core)
Gas film:
Gas-product boundary (film)
Product diffusion:
Through product/hydride layer
Surface controlled:
Core-Product boundary

(1) Surface controlled – adsorption, chemisorption, dissociation, surface diffusion, sub-surface penetration
(2) Transport processes – Bulk diffusion, grain boundary diffusion or other mechanisms
(3) Nucleation of hydride phase
(4) Interface processes – solid state phase transformation or thermal emission through interface

i. Hydrogen gas film over outer particle (hydride)
ii. Diffusion/permeation through (imperfect) product. Grain boundary/Knudsen diffusion
iii. Reaction at metal (core) surface. Physisorption → Dissociation → Chemisorption including solid state phase effects (Site de-activation, H-H interactions, defects)

Figure 2.5: Mintz terminology compared to the Yagi & Kunii shrinking core terminology. Also included is the reaction pathway outlined by Mintz and Bloch [60] and for comparison the Site Availability Model (SAM) [1]. The step in red is assumed the rate determining step for (SAM).

follow this as the uptake experimental data is not directly proportional to time.

Equations (2) to (6) in table 2.1 originated by Mintz & Bloch and are "Mintz-Bloch"-"Interface" processes, i.e. they are concerned with the hydride-metal boundary. (4) and (5) are identical to the A.51 and A.56 respectively (where $1/t^* = k$) and therefore have already been covered. Equations (2) and (3) however, are a nucleation and growth model which is based on the Johnson-Mehl-Avrami (JMA) equation. The JMA model assumptions are [5, 38]:

- Random and homogeneous nucleation over un-transformed material
- Constant growth velocity over reaction duration
- Growth occurs according to the geometry. i.e. if a sphere, the same rate in all directions.

The JMA models assumes there is a constant increase in concentration (C) of nuclei (dC/dt), $\dot{C}$, where they transform from A to B with an outward velocity u. Further, there are two time scales, where t is regular time and t_P is the precipitate growth time. t_P begins when nucleation occurs while precipitates are nucleating at different times t. The differential moles of nuclei (dN) during dt_P in a constant volume V is $dN = \dot{C}V dt_P$. Therefore, the differential volume of unrestricted growth (dV_u) is dV_u = Geometry x Generation,

$$dV_u = \left(\frac{4}{3}u^3(t-t_P)^3\right)(\dot{C}Vdt_P) \tag{2.38}$$

Where for a sphere the volume $= \frac{4}{3}\pi R_0^3$ and the radius $R_0 = u(t-t_P)$. If equation 2.38 is integrated from $t_P = 0$ to $t_P = t$ and V_u from 0 to V_u this gives,

$$V_u = \frac{\pi}{3}\dot{C}Vu^3t^4 \tag{2.39}$$

Introducing the normalised hydride fraction (θ) that has transformed as $\theta = V_B/V$, so the fraction not reacted yet $= 1 - V_B/V$. The differential volume of V_B is proportional to dV_u and $1 - V_B/V$,

$$dV_B = \left(1 - \frac{V_B}{V}\right)(dV_u) \tag{2.40}$$

Integration from 0 to V_B and 0 to V_u and some algebra gives

$$-Vln(1-\theta) = V_u = \frac{\pi}{3}\dot{C}Vu^3t^4 \tag{2.41}$$

$$[-ln(1-\theta)]^{(1/4)} = \left(\frac{\pi\dot{C}u^3}{3}\right)^{(1/4)} t \tag{2.42}$$

$$[-ln(1-\theta)]^{(1/4)} = k_{CD}t \tag{2.43}$$

Which is in the form of $[-ln(1-\theta)]^{(1/n)} = kt$ as indicated in table 2.1 where n indicates the growth based on the geometry, or reaction order. Note the geometry would also alter the rate constant k and the rate concentration of nuclei $\dot{C}$ is dependent on temperature. The advantage of the JMA equation is that the parameter n changes the shape of curve, giving versatility to the rate law. When $n = 1$, the rate law is equivalent to a first order reaction. However, there are three criticisms, one is that the model is based on an extended volume concept, which means a shrinking surface is not accounted for (of course this is acceptable if there is not one), another is that there is no pressure dependency, but it is known that metal hydrides kinetics are $f(P)$, and that there are two time scales. Therefore, getting the JMA equation into a differential equation to be solved via Runge Kutta's methods for example is difficult. Further, the JMA equation can be re-arranged to the following equation,

$$\theta = 1 - exp(-(k_{CD}t)^n) \tag{2.44}$$

This is the common JMAK form of the Avrami equation. This can be rearranged into the following linear format,

$$ln(-ln(1-\theta)) = ln(k_{CD}) + n\, ln(t) \tag{2.45}$$

Thus, a plot of $ln(-ln(1-\theta))$ and $ln(t)$ gives $n =$ slope and $ln(k_{CD}) =$ intercept. One of the issues with this is that applying natural logarithm on an already integrated rate equation will suppress the discrepancies and make the fit look more satisfactory and therefore, potentially misleading.

The last equation covered (6) by Barkhordarian et al. is the Carter-Valensi expression, used by Mintz and Zeiri [61]. The "Carter"-"Interface-Diffusion Controlled" model is for a contracting volume where the thickening product layer offers increasing resistance. The equation is as follows:

$$f(\theta) = \frac{\omega - [1 + (\omega - 1)\theta]^{2/3} - (\omega - 1)(1 - \theta)^{2/3}}{\omega - 1} = \frac{2k_D}{R_0^2}t \tag{2.46}$$

The model introduces ω, a product to reactive reactant volume ratio. If $\omega \to 1$ (i.e. very small volume expansion) then $(\omega - 1)\theta \ll 1$, and applying a series expansion of $(1 + (\omega - 1)\theta)^{2/3}$ gives,

$$f(\theta) = 1 - \frac{2}{3}\theta - [1 - \theta]^{2/3} = \frac{2k_D}{R_0^2}t \tag{2.47}$$

This reduced expression is an approximation whereby there is an unchanged particle size, and a Taylor series expansion to two θ terms only. Equation A.46 ("Yagi"-"Diffusion") achieves the similar objectives to the "Carter-Valensi" expression, with a constant particle size and a rate determining product layer, but slightly differently as equation (A.45) assumes pseudo steady-state.

2.3.2 The pressure term

The disadvantage of the above rate laws is they do not cover for the phenomenon, regarding metal hydride kinetics, in which the reaction rate is improved by increasing the rate of heat removal during hydrogenation, and rate of heat input during dehydrogenation [88, 57, 2]. This is in direct contrast to exothermic reactions such as combustion. If combustion goes out of control, the reaction rate increases due to an increase in temperature, causing the temperature to rise further and hence a rapid increase in reaction rate. Thus, improving the rate of heat transfer **from** the system **slows** the reaction. But with metal hydrogenation (also exothermic), improving the rate of heat transfer **from** the system **accelerates** the reaction.

One of the ways researchers have included this phenomenon into the rate law is through a dimensionless pressure term. Ron experimented with many different pressure terms [80] but it was Mintz and Bloch [60, 59] who brought this line of thinking to the forefront after the work of Flanagan [26]. It was proposed that for a hydriding mechanism, which is controlled by a phase transformation step (metal-hydride boundary), the interface velocity u is,

$$u = L\,\nu_m\,exp\left(\frac{E_a}{RT}\right)ln\left(\frac{P_g}{P_{eq}}\right) \tag{2.48}$$

where L = distance from the interface boundary within which the transformation takes place (m), ν_m = vibrational frequency of metal lattice (Hz), E_a = activation energy of phase transformation (J mol^{-1}), P_g = working/gas pressure and P_{eq} = equilibrium pressure at working/local temperature (bar). It was assumed the reaction front velocity (u, m s^{-1}) was assumed proportional to dissociated hydrogen supersaturated in metal, and the supersaturation was proportional to the chemical potential driving force of dissociated hydrogen in solution (in equilibrium with hydrogen gas ($H_{2_{(g)}}$) at working pressure) and dissociated hydrogen in the product (in equilibrium with hydrogen gas ($H_{2_{(g)}}$) at equilibrium pressure P_{eq}) [26]. The $ln\left(\frac{P_g}{P_{eq}}\right)$ term was called the supersaturation factor. They pointed out that this model is based on macroscopic thermodynamic parameters (e.g. T, P) thus this assumption is valid for a large ensemble of atoms (i.e. bulk quantity calculations) [26]. Flanagan also noted the Gibbs energy driving force ($\Delta G'$) is dependent on strain energy (ΔG_{strain}), i.e.

$$\Delta G' = k\,ln\left(\frac{P_g}{P_{eq}}\right) - \Delta G_{strain} \tag{2.49}$$

Another result from equation 2.49 shows that if $\Delta G_{strain} = 0$ and the driving force $\Delta G' = 0$, then equilibrium has been reached, where $P_g = P_{eq}$. Commonly, most used rate equations with a dimensionless pressure term drop the strain energy term [64, 54, 12]. In the late 90s, Ron collated and experimented with varying dimensionless pressure terms. For hydrogenation these are shown below. All pressure terms satisfy the criteria that when $P_g = P_{eq}$, reaction has reached equilibrium. Ron's paper primarily focused on dehydrogenation, however the pressure terms used all had varying degrees of success with (1) and (5) most common, where P_{eq} = equilibrium pressure, P_g = gas pressure P_{00} = initial gas pressure.

1. $ln\left(\frac{P_g}{P_{eq}}\right)$
2. $P_g - P_{eq}$
3. $\frac{P_g - P_{eq}}{P_{00}}^{0.5}$
4. $(P_g - P_{eq})^{0.5}$
5. $\frac{P - P_{eq}}{P_{eq}}$
6. $\left(\frac{P_g}{P_{eq}}\right)^a$ a = constant

2.3.3 Other models

Other commonly used models are the ones by developed by Chou and Xu [14]. The equations were expressed in the form of 'characteristic reaction time' $= t_c$. For the first case, it was assumed a reaction at a spherical particle surface giving,

$$\theta = 1 - \left(1 - \frac{t}{t_c}\right)^3 \tag{2.50}$$

This is synonymous with the shrinking core as re-arranging to give t/t_c the subject (or kt) gives $1 - [(1-\theta)]^{\frac{1}{3}} = kt$. For the derived sub-cases (physisorption/ chemisorption/ surface penetration) the rate law is un-changed except for the characteristic reaction time, t_c (or k). The other case is based on the diffusion of hydrogen atoms through a hydride layer giving,

$$\theta = 1 - \left(1 - \sqrt{\frac{t}{t_c}}\right)^3 \tag{2.51}$$

$$\left(1 - [(1-\theta)]^{\frac{1}{3}}\right)^2 = kt \tag{2.52}$$

with equation 2.52 showing the 'Chou-Diffusion' model expressed in the form seen previously. The rate constant here is based on solid diffusion.

2.4 Magnesium hydride dehydrogenation kinetics

The amount of research on hydride dehydrogenation kinetics is infrequent in comparison to metal hydrogenation kinetics. In many cases, the dehydrogenation models are very similar to the hydrogenation models. In summary however, the reaction rate of metal hydride dehydrogenation is known to be influenced by the initial hydride/metal concentration, the mean particle size, additives and gas pressure [72].

2.4.1 JMAK model

The first model considered is the Avrami equation based on a nucleation & growth mechanism, where the derivation is based on the extended volume concept and yields the following integrated rate equation, [5]

$$\theta' = 1 - exp(-Kt^n) \tag{2.53}$$

Equation 2.53 can be modified into a linear format giving equation 2.54. If the experimental data is a straight line, the rate law is suitable.

$$ln(-ln(1-\theta')) = ln(K) + nln(t) \tag{2.54}$$

This equation has been covered previously for magnesium hydride dehydrogenation, however, in the dehydrogenation context equation 2.53 is based on the rate of metal growth, hence the use of the normalised metal fraction (θ').

2.4.2 Dehydrogenation models including pressure

One of the downsides regarding the JMAK model is that pressure effects are not included. Similar to some hydrogenation models, dimensionless pressure terms have been added to consider pressure effects. Researchers have used a generic form of a rate equation that has been applied to metal hydrides such as MgH_2 or $LaNi_5$. It is as follows:

$$\mathrm{d}\theta'/\mathrm{dt} = (\text{T term} = \text{Arrhenius})(\text{P term} = \text{A ratio})(\text{Concentration term})$$

Where θ' = normalised metal fraction, T = temperature (K) and P = pressure (bar). For instance,

1. Dehydrogenation of MgH_2 by Chaise, Rango and Marty

$$\frac{d\theta'_{20}}{dt} = \left(2Aexp\left(-\frac{E}{RT}\right)\right)\left(ln\frac{P_{eq}}{P_g}\right)\left(\frac{\theta'_{20}}{(-ln\,\theta'_{20})^{0.5}}\right) \tag{2.55}$$

   Where E = 130 kJ/mol, $A = 1 \times 10^{10}$ 1/s. θ'_{20} is the normalised metal fraction up to a period of 20 minutes [12].

2. Dehydrogenation of $LaNi_{4.7}Al_{0.3}$ by Mayer, Groll and Supper, essentially a first order rate equation [54].

$$\frac{d\theta'_{20}}{dt} = Aexp\left(-\frac{E}{RT}\right)\left(\frac{P_{eq}-P_g}{P_{eq}}\right)(1-\theta') \tag{2.56}$$

Concentrating on the pressure term, Ron summarised many pressure terms used for the dehydrogenation of AB_2 hydrides. Some representation of pressure is crucial within the rate equation as changing the pressure difference $(P_{eq} - P_g)$ will alter the reaction rate. Perejón et al. demonstrated this with DSC measurements of MgH_2 at 10 bar and 20 bar. It was apparent that for all heating rates, the peak and onset temperatures were lower at 10 bar, indicating that the fastest dehydrogenation kinetics occur when the pressure difference is maximised [72].

The pressure terms summarised by Ron for dehydrogenation are shown below [80]. They all mathematically represent a positive driving force when $P_{eq} > P_g$ and when $P_{eq} \rightarrow P_g$ the pressure term approaches zero and thus the reaction approaches equilibrium, except with (5), $(P_{eq}/P_g)^a$, which tends to 1 (a = constant). It was not entirely clear with its representation, but it may have attempted to represent the effects of over-pressure (higher gas to equilibrium pressure ratio) on the reaction rate.

1. $|P_{eq} - P_g|/P_{atm}$, P_{atm} = 1 atm
2. $ln(P_{eq}/P_g)$
3. $(P_{eq} - P_g)/P_{eq}$
4. $P_{eq} - P_g$
5. $(P_{eq}/P_g)^a$

A physical explanation of the pressure term is in section 2.3.2, where Mintz and Bloch identified that the pressure term may be a super-saturation factor, whereby it tracks the amount of hydrogen super-saturated within the lattice [60].

To empirically determine the pressure term, Ron devised an experimental procedure by systematically applying them independently. First, quasi-isobaric and isothermal experiments were performed. By assuming the material exhibits a flat plateau and the bulk of the experiment operates across this region, then $P_{eq} \approx$ constant and thus the pressure term is constant. This allows integration of the rate law and then the pressure term can be determined through plotting the pressure term at $\theta = 0.5$ against time. A straight line would indicate a suitable pressure term. For instance, Ron found that $(P_{eq} - P_g)/P_{eq}$ for $\mathrm{FeTi_{0.8}Ni_{0.2}}$ worked well [80].

2.4.3 Sestak-Berggren equation

In another approach, Perejon et al. adopted the Sestak-Berggren equation,

$$f(\theta) = \kappa_1 (1-\theta)^{\kappa_2} \theta^{\kappa_3} \tag{2.57}$$

Equation 2.57 is commonly used to model solid state reactions. κ_1 is a constant equivalent to the rate constant k (governed by Arrhenius) and κ_2 and κ_3 are empirical constants, covering for physical mechanistic changes. They used this equation on DSC MgH_2 dehydrogenation data at far from equilibrium, in order to minimise pressure effects. They found their data was represented by $f(\theta) = (1-\theta)^{0.83}\,\theta^{0.745}$, which yielded a sigmoid profile [72].

2.4.4 Model by Maad et al.

Experimental data of magnesium nickel hydride (Mg_2NiH_2) collected by Hsu et al. was used by Maad, Askri & Nasrallah to generate the following rate equation.

$$r = k \frac{P_g - P_{eq}}{P_{eq}} (1 - exp(-\theta)) \tag{2.58}$$

The pressure term within equation 2.58 would give a negative answer for dehydrogenation, which causes the rate term to be negative. With the rate laws displayed in this paper, the convention is to place the negative sign next to the r, to note formation or disappearance of the respective component. Thus, the rate law should be multiplied by -1, or swapping the pressure term to $P_{eq} - P_g$. Plotting this rate equation also gives a first order equation.

2.4.5 Model by Evard, Gabis and Yartys

Evard, Gabis and Yartys derived a model for dehydrogenation of MgH_2 [24]. Evidence from DSC data indicated that dehydrogenation from partial hydrogenation produced a decrease in the onset temperature and a broadening of the peaks. The explanation was based on islands of metal reactant available on the surface enabling it to act as a dehydrogenation channel. In other words, dehydrogenation only starts to occur when a nucleus of metal materialises. Further, through analysing an optical microscopy image of an etched metallographic section, the magnesium reaction front expanded outwards into the magnesium hydride. In effect, it was proposed that a shrinking core mechanism is not valid for MgH_2 dehydrogenation. It was also suggested that a diffusion mechanism (diffusion length) does not primarily influence the reaction rate. The resultant rate equation is established on an outward reaction front based on a time dependent particle radius in a two step process.

$$R_0(t) = \begin{cases} 0, \ \ t < t_{cr} \\ \\ \pi R_0^2, \ \ t \geq t_{cr} \end{cases}$$

$$\frac{dR_0}{dt} = \begin{cases} 0, \ \ t < t_{cr} \\ \\ \frac{R_0^{t^*}}{2R_0^{t^*} - R_0(t)} \frac{kC_s^{eq2}}{C_h - C_s^{eq}}, \ \ t \geq t_{cr} \end{cases}$$

Where k is governed by the Arrhenius equation, $C_s^{eq} = H_2$ concentration in solution phase in equilibrium with the hydride phase, C_h = hydride concentration and $R_0^{t^*}$ is the completed spherical particle radius. t_{cr} is the nucleation time for the metal phase. Two disadvantages are that the discontinuity of the rate equation has to be accounted for when modelling, and a pressure dependence term is not included.

In view of the literature covered, the following points should be considered when exploring the metal hydride dehydrogenation reaction.

- Representation of the reaction occurring at the surface, noting that the magnesium may evolve via expanding into the hydride.
- A representation of the pressure effects, and the nature of these effects when close and far from the equilibrium pressure.
- A physical mechanism, based on a chemical reaction, which governs the sigmoidal concentration profile.

2.5 Hydride reactor designs: for CSP applications

2.5.1 General design intent

In this section, past papers into metal hydride reactor design are reviewed, where many prototypes have been built/simulated to test metal hydride TCES reactors. In general, many aims for heat exchanger design apply to these reactors. These are shown in the list below [86]. Meeting these design deliverables will aid minimising reactor costs.

- Design with established fabrication techniques
- Easily cleaned
- Fit within current design procedures
- Good mechanical layout, such that withstanding pressure swing is possible (around 0 - 50 bar)
- Reasonable heat transfer area to small volume ratio

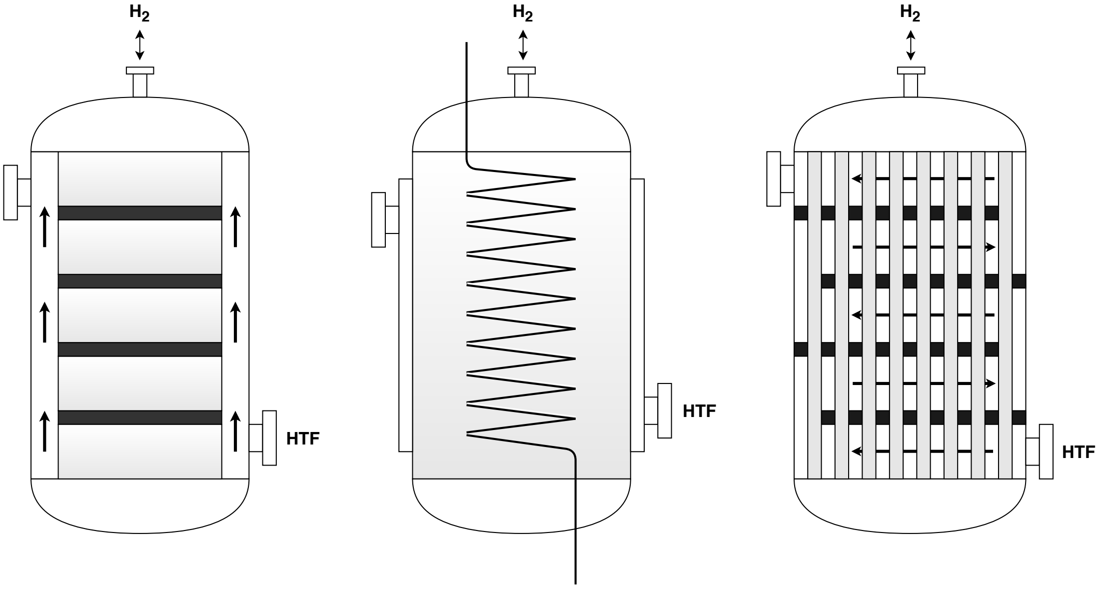

Figure 2.6: Typical layout designs for TCES reactors for CSP applications. (Left) Double pipe with fins. (Middle) Jacketed vessel with internal helical fins. (Right) Shell and tube with hydride in tubes. HTF = heat transfer fluid.

2.5.2 Current reactor designs

2.5.2.1 Double pipe reactors

A double pipe reactor is the simplest type, where they are usually applied to low heat loads and high pressure systems. A multi-tube reactor is a variation with higher heat transfer area. [65] Patil and Gopal simulated a double pipe arrangement with the powder in the inner tube. It was found that including the resistance of the tube wall within the overall heat transfer coefficient improves the model [71]. Bao et al. explored a multi-tube arrangement with the powder within the shell. It was concluded a high bed effective thermal conductivity and the inclusion of contact resistance is essential [7]. Kukkapalli and Kim also simulated a double pipe variation with the inner pipe holding the HTF with metal fins penetrating into the shell. It deduced fins an effective method to increasing the reaction rate and recommended exploring an optimal fin geometry [41, 6, 44]. Figure 2.6 illustrates a double pipe arrangement with the use of lateral fins.

2.5.2.2 Jacketed reactor

Another category of reactor is a jacketed vessel. These types of reactors employ a helical type heat transfer arrangement around the external wall, encapsulating the reactor in a "jacket". Figure 2.6 illustrates a potential jacketed reactor. A helical coil could also be added internally. The heat transfer is usually greater due to the centrifugal effect, where these reactors are for average heat duties or low HTF flow rates with higher velocity [65]. Feng et al. simulated a metal hydride bed with an internal coil. One conclusion was that there were regions that did not react at regions near the wall [25] with a coil to reactor diameter ratio of 1:2. The proposed solution was to remove these parts from the reactor bed, losing fill volume. It was concluded this reactor design is suitable for MH TCES reactors. Note, that the simulation was based on a lab scale size of inner diameter = 5 cm and length = 20 cm reactor, and not commercial scale. Dong et al. developed an internal helical coil exchanger/reactor for 30 g of MgH_2 with TiB_2 and expanded natural graphite (ENG) additives using H_2O as the HTF [18]. Although the HTF flow rate was small (2-5 ml/min) the inclusion of HTF gave a uniform temperature distribution and a sufficient reaction rate was achieved. A change in bed temperature was also observed. However, the temperature of the outlet H_2O was not provided. A coil wrapped around a porous tube was used for the hydrogen inlet and coil support.

2.5.2.3 15kg Steam Mg/Ni TCES reactor

Bogdanovic et al. developed a much larger prototype (15 kg of MgH_2 doped with Ni) using a jacketed vessel concept, where water was vaporised to saturated steam in the outer spiral and then superheated as it passed through the internal helical coil. A central sintered metal tube was used for the hydrogen inlet and exit. Both a high temperature hydride coupled to either a compressed hydrogen store or a low temperature hydride was tested (code 5800 - $Ti_{0.98}Zr_{0.02}V_{0.43}Fe_{0.09}Cr_{0.05}Mn_{1.2}$). [11]

It was demonstrated that when the store was linked to compressed hydrogen tanks, operating under a constant hydrogen pressure, a constant steam outlet temperature throughout at $\approx 80\%$ of the reaction was delivered. Whereas delivery of hydrogen under a varied flow rate (30 to 5 bar) resulted in a gradual temperature decrease in the steam outlet (≈ 50°C) across the reaction. It was stated that the system efficiency can further be improved through a sensible heat store between the high temperature store and hydrogen gas store, to preheat the hydrogen during hydrogenation. Another variation could be a heat exchanger positioned before the reactors, which can preheat the HTF prior to entering the reactors using hot hydrogen. Further, when the steam generator was cut open, the following observations were made [11]:

1. The MgH_2 formed a ductile highly porous substance, in which the vessel container walls withstood the additional pressure due to expansion.
2. The powder had expanded to a tight fit around the inner coil
3. Due to a vertical arrangement, the density was higher at the steam generator base. This varied from 0.7 to 1.15 g cm^3. It was concluded that this had no effect on the reaction kinetics. Positioning the reactor in the horizontal position would minimise this issue.
4. As the density and thus the storage capacity varied by up to 30%, optimising the filling bulk density can significantly reduce cost.

2.5.2.4 Shell and tube reactors

Considering shell and tube reactors, Urbanczyk et al. developed a thermo-chemical heat storage system with 5 kg of Mg_2FeH_6 using molten salt as the heat transfer fluid. The fill density was 1.085 g cm^{-3} and the powder was capped with sea sand and glass wool. The reactor was intended to operate up to 550°C, where in preliminary tests, they achieved an efficiency of 31.5%, due to flow instability and insufficient insulation [92]. Figure 2.6 is an example of a shell and tube.

2.5.2.5 Reactor design summary

At present, an effective reactor design for metal hydride TCES at commercial scale has not been identified. However, it is clear heat transfer architecture is required in order to improve the reaction rate, but the level of improvement required, has not been determined. A horizontal orientation will enable a uniform bulk density, where an optimum bulk density should be explored.

Chapter 3

Experimental & simulation methods

3.1 Sievert's apparatus

A Sievert's apparatus was used to monitor the de/hydrogenation reaction over time for the small 0.2g magnesium samples. This is achieved through measuring the pressure change over time within a fixed volume, with the reactor cell (holding the sample) kept at a constant temperature. The pressure change can be used to determine the amount (of reactant) reacted. The experimental data gathered was used to analyse the kinetic behaviour of magnesium hydrogenation and magnesium hydride dehydrogenation, and used to test existing models and develop new ones. Once suitable validation of models has been achieved, it can then be tested to larger sample sizes. The equivalent volume method was used when operating and interpreting the data from the Sievert's apparatus (this method is described in section A.1.1). In this section, the magnesium activation and cycling experimental conditions are covered.

3.1.1 0.2g magnesium activation and cycling conditions

The magnesium used was atomised Mg powder (26 μm) by SFM - FluorsidGroup Company (a picture is shown in figure A.14 in the appendix. Most of the magnesium (in 5 kg barrels) was stored in a metal container in a outside store. This metal container used a metal clamp mechanism to improve the seal. A smaller Kilner clip-top glass jar was used to store magnesium in the laboratory.

There were two samples used. For both samples, the capacity recovered by the fourth cycle. The general cycling procedure was as follows - morning (8-9am), dehydrogenation at respective condition, 9am-1pm hydrogenation at respective condition. Dehydrogenation (1pm-2pm), then hydrogenation (2-6pm). Sometimes, a single dehydrogenation and hydrogenation cycle was performed in one day, if time could not allow two. The pressure was dropped to +0.5 bar above the plateau at the respective temperature before leaving the apparatus overnight. The aim was to maintain the sample in the hydrogenated state overnight, and minimise the time the sample is in the metal state at temperature. This was to minimise sintering. The sample history is shown in table 3.1.

Table 3.1: Magnesium activation and cycling sample history (in chronological order) for 0.2g sample 4 (S004) and 0.2g sample 5 (S005) Sievert's experiments. PCI = pressure composition isotherm.

Hydrogenation				**Dehydrogenation**			
T (°C)	P (bar)	Duration	Runs	T (°C)	P (bar)	Duration (hours)	Extra info.
360	40	2-3 days	4	360	<1 bar	To completion	Activation S004
360	16	4 h	3	360	<1 bar	1.4 h	Kinetics S004
360	25	4 h	3	360	<1 bar	1.2 h	Kinetics S004
360	32	4 h	3	360	<1 bar	1 h	Kinetics S004
360	40	4 h	3	360	<1 bar	1 h	Kinetics S004
330	8	4 h	3	360	<1 bar	(Not recorded)	Kinetics S004
330	12	4 h	3	360	<1 bar	(Not recorded)	Kinetics S004
330	16	4 h	3	360	<1 bar	(Not recorded)	Kinetics S004
330	20	4 h	3	360	<1 bar	(Not recorded)	Kinetics S004
360	-	2 weeks	1	360	<1 bar	0.8 h	PCI S004
380	-	2 weeks	1	380	<1 bar	0.3 h	PCI S004
			30				
360	40	2-3 days	4	360	<1 bar	To completion	Activation S005
345	11	4 h	3	360	<1 bar	(Not recorded)	Kinetics S005
380	24	4 h	3	380	<1 bar	0.4 h	Kinetics S005
400	36	4 h	3	400	<1 bar	0.2 h	Kinetics S005
			13				

3.1.2 Experimental issues

The Sievert's apparatus used a single pressure transducer with a range from 0 - 150 bar. Although this is suitable for the hydrogenation experiments, it creates a larger error for the dehydrogenation experiments. The original intention was to only measure hydrogenation, therefore there was a single Druck transducer, with a range from 0 - 150 bar. Thus, the measurements between 0 - 1 bar were not as accurate than if an additional low range sensor was used. Further, the Sievert's used did not have extra volume for dehydrogenation within the temperature controlled box, thus, some external tubing was used instead, and that the transducer required re-calibration. Manual linear re-calibration was performed to amend the pressure at 0 (it was known that the transducer still exhibited a linear profile). Figure 3.1 shows this. As such, the starting pressure for dehydrogenation is denoted as < 1 bar. Calculated from the transducer's error, measurements < 1 bar can be up to ± 0.1 bar. The pressure measurements range during dehydrogenation was $\approx 0.5 - 2.5$ bar.

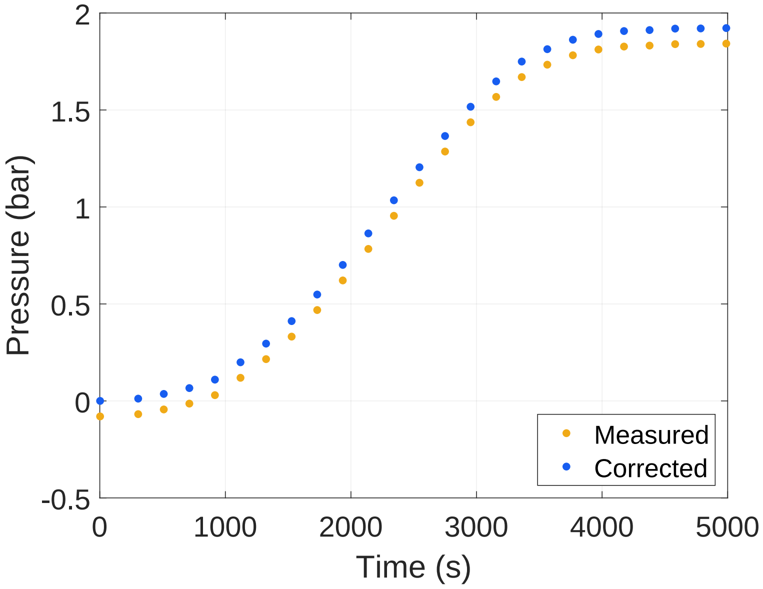

Figure 3.1: Experimental data for dehydrogenation at 360°C < 1 bar from a 360°C 25 bar hydrogenation.

3.1.3 Extra Sievert's information

For Sievert's experiments in chapters 4 and 5, high purity hydrogen (99.9999%) was used. The bulk density was 1000 kg m^{-3}, thus giving an assumed porosity of (1 - 1000/1740) $\approx$ 0.4 (1740 kg m^{-3} is the density of pure magnesium).

Kinetic runs were at several constant initial temperatures and at varying over-pressures. The over-pressure is a measure of how far the system is from equilibrium at a given temperature. The over-pressure is detailed further in section 4.1.1. It is assumed that when the over-pressure $= 0$, it is at equilibrium, when the over-pressure is ≤ 1, it is close to equilibrium, and when >1, the system is at far from equilibrium. The sample temperature was measured with a thermocouple in the sample.

The sample holder has a thick steel wall designed to act as a large thermal mass, dissipating heat through the steel domain, and minimise surrounding temperature fluctuations. The holder was made from stainless steel 316.

A thermocouple was placed 15mm from the edge of the inner wall (where sample is place, see figure 3.2) and the temperature was monitored throughout. It was observed to remain relatively steady at the set point. Thus, it was assumed that everywhere at 15mm from the edge of the sample was at this set point. This enabled a suitable boundary condition of constant temperature. Figure 3.2 illustrates this. The hydrogen enters and exits through the centre of the holder, whereby the height of the sample was calculated from the sample mass, density, and radius of the drilled hole.

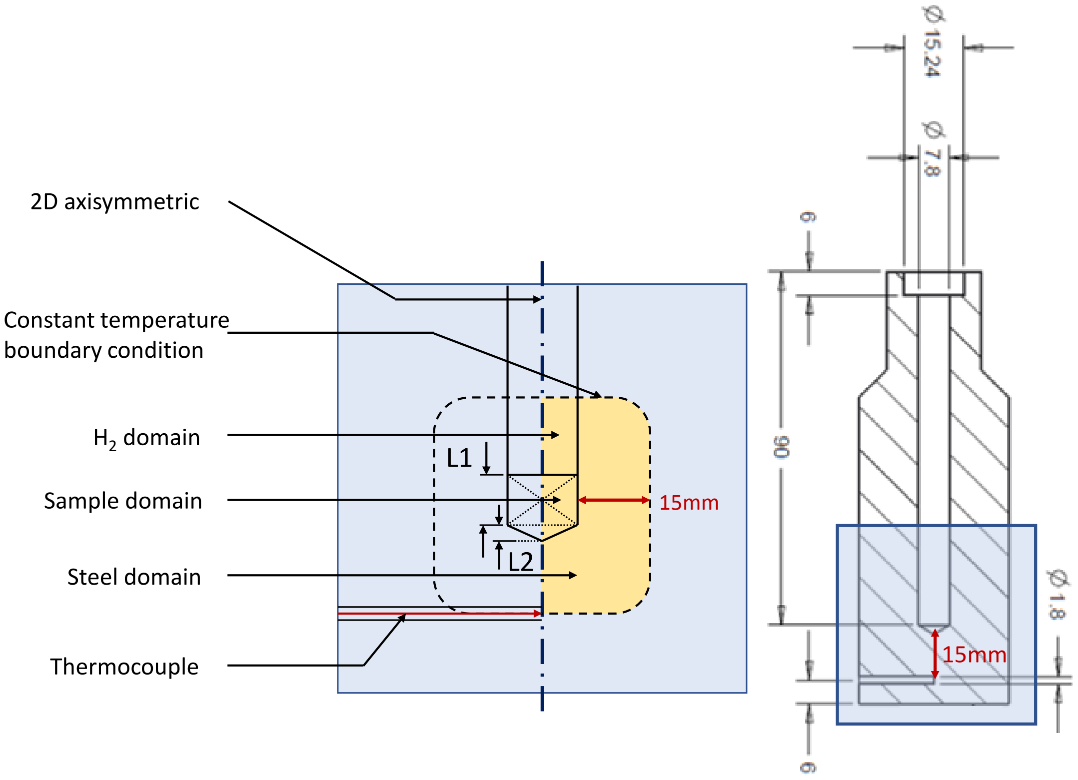

Figure 3.2: (a) 2D axi-symmetric geometry (yellow zone). Simplified to optimise simulation. (b) Schematic of sample holder: material used 316ss, measurements in mm. See figure A.7 for mesh.

3.1.3.1 Sample dimensions

The domain height was calculated by assuming the sample volume to be the sum of a cylinder and a cone. The conical end height (L_2) was assumed to be 20% of the main cylinder height (L_1) (see figure 3.2). The mass of sample was 0.2g, and assuming the metal hydride reaches maximum capacity (e.g. 7.66wt%), the mass of hydrogen at $t = t^*$ (t^* = completion time) is $m_{H_2}^{t^*}$,

$$m_{H_2}^{t^*} = \frac{wt_m m_{Mg}}{1 - wt_m} \tag{3.1}$$

where wt_m = maximum weight percent of sample and m_{Mg} = mass of magnesium/sample.

Time	Status	Mass	Density	Volume
At $t = 0$	100% magnesium	0.2 g	1740 kg/m^3 [13]	0.1145 cm^3
At $t = t^*$	100% magnesium hydride	0.2166 g	1450 kg/m^3 [58]	0.1494 cm^3

To model this problem, the sample domain must increase with time. This would increase computation complexity, as the sample would need re-meshing after each time step. Also, the kinetics have assumed no volume expansion. As such, it was necessary to work with an average porous matrix density (ρ_p) and thus a pseudo value for L_1 and L_2, equating to an effective sample domain volume (V_{d_e}). Taking a simple average density of Mg and MgH$_2$ gives a $\rho_p = 1590$ kg/m^3. V_{d_e} is calculated by considering the maximum uptake of hydrogen,

$$V_{d_e} = \frac{m_{Mg} + m_{H_2}^{t^*} x_m}{\rho_p (1 - \epsilon_b)} \tag{3.2}$$

where ϵ_b is the bed porosity and x_m is the volume averaged maximum hydride fraction. This is the hydride fraction determined from experimental data.

3.2 Large lab-scale reactor

The aim of a metal hydride thermo-chemical energy store (TCES) is un-conventional. A metal hydride TCES requires equal importance of the utility and reactor section, where the "product" is the conditions of the heat transfer fluid supplied by the duty of the chemical reaction. This section looks at the commissioning and operation of a metal hydride TCES, detailing the experimental and assembling procedure. The purpose of this reactor is to test the models developed for the small 0.2g sample, and apply them to a larger 154g sample, in a more realistic setting using a heat transfer fluid.

3.2.1 Reactor design

A metal hydride TCES was in development at the University of Nottingham, prior to the start of this PhD. The reactor was based on a double pipe heat exchanger, but with a variation whereby the hot oil spirals around the reactor bed (helical flow, see figure 3.4). The outer flow was made with a copper wire wrapped around the inner chamber/cylinder. The second cylinder was then inserted over the assembly with an interference fit.

The inclusion of the wire/baffles results in the fluid flowing between the wires/baffles as a duct, increasing the length of time the oil is exposed to the bed in comparison to a conventional double pipe reactor. A diagram of the reactor is shown in figure 3.3. As a double pipe heat exchanger is the easiest type of reactor to model, and one of the objectives was to simulate this reaction at large lab-scale, the decision was made to keep and use this reactor for experiments.

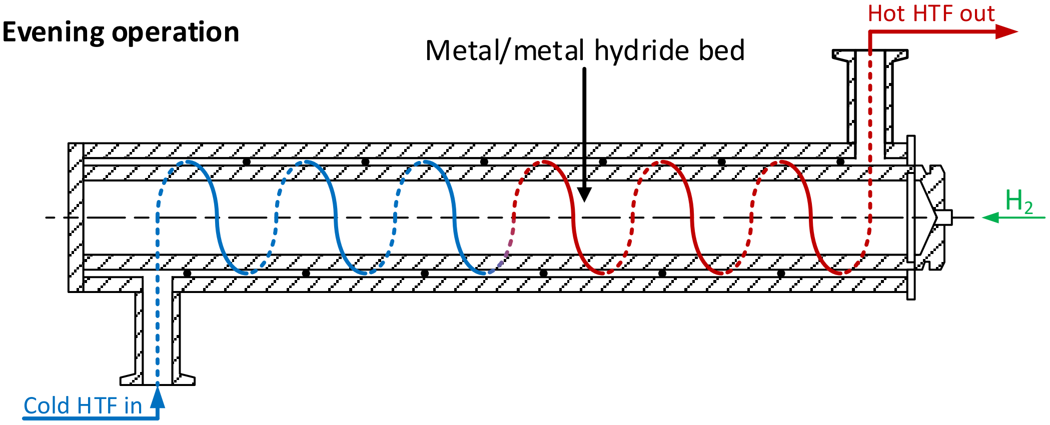

Figure 3.3: Illustration of the double pipe heat exchanger incorporating helical flow for the heat transfer fluid (HTF) (Drawing not to scale). Shown is the evening operation if coupled to a CSP plant, with the exothermic hydrogenation reaction transferring useful work to the fluid.

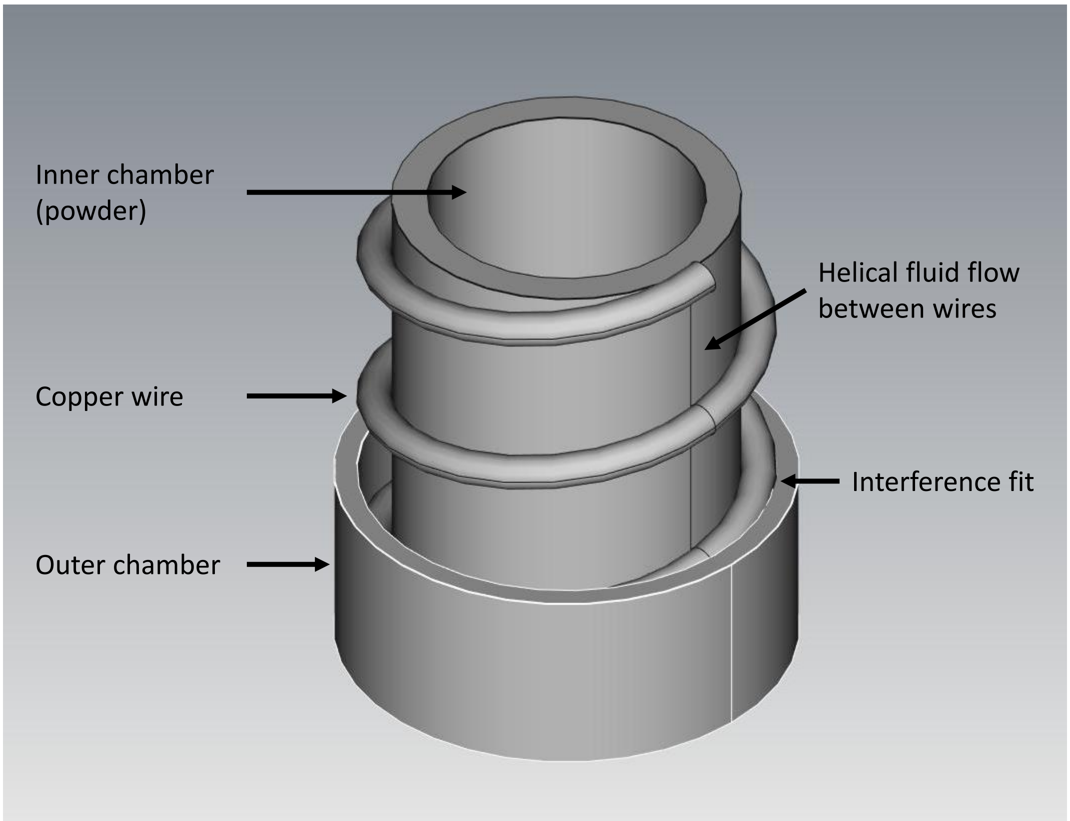

Figure 3.4: Visualisation of the helical fluid flow using copper wire/baffles in the modified double pipe reactor.

3.2.2 Process flow diagram

3.2.2.1 Hydrogen

Figure 3.5 shows the overall process for the (de)hydrogenation reaction. This rig utilises flow control with a continuous flow of hydrogen to supply the hydrogenation reaction and likewise a continuous removal of hydrogen for dehydrogenation. Explanation of the flow based calculations for de/hydrogenation are shown in the appendix, section A.2.

The flow is controlled manually by the needle valve (NV1), with two flow recorders (FR) in parallel. FR1 can measure between 0.5 to 25 nl/min accurately and FR2 can accurately measure 6 to 300 nl/min. For single reactor operation, using only FR1 is required. As flow recorders have a maximum operating temperature of 60°C, a passive air cooler is added upstream of the flow recorders when operating in dehydrogenation mode. This passive cooler is simply a serpentine shaped tube layout.

There are two pressure recorders in this process. One by the entrance of the gas regulators, and another at the entrance to the reactor vessel. It is necessary to record the pressure as well as flow readings, as this enables calculation of reaction uptake. It is also useful for the kinetics and safety. An analogue pressure gauge (PI) is in-between V12 and the reactor, to manually read the pressure if PR2 fails. A pressure relief valve (PRV) is set to relief at 38 barg. The PRV has a tolerance of approximately 5% to be within the design pressure of 40 bar.

Surface thermocouples are attached both to the entry pipe of each pressure recorder, labelled TR1 and TR2. This monitors the fluctuations in room temperature to improve accuracy of the uptake calculations. TR3 is a triple thermocouple assembly which measures the reactor centre-line temperature. One sensor is positioned in line with the thermal oil entry (TC1), another in line with the thermal oil outlet (TC3), and the final sensor positioned in the middle of the reactor (TC2). This provides the bed temperature profile through the vessel as the reaction progresses. This helps indicate how the reaction is performing. The buffer tank is added in order to minimise pressure fluctuations when operating in hydrogenation mode. A flashback arrestor is included to prevent the reverse flow of air into the system.

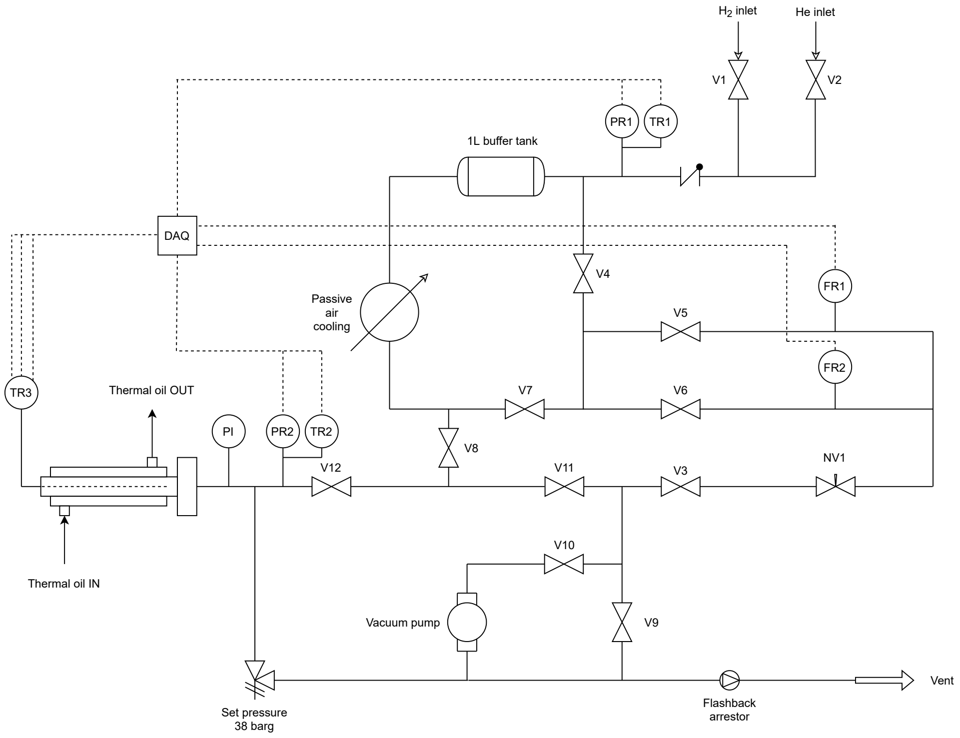

Figure 3.5: Process flow diagram of the gas fluid (hydrogen and helium) side. The DAQ (data acquisition) device records the pressure (PR), temperature (TR) and flow (FR) at the specified locations. PI is a pressure gauge. Valve (V) positions are closed/open depending on the mode of operation, with the needle valve (NV) providing additional flow control.

3.2.2.2 Hot oil

Figure 3.6 shows the thermal oil circuit. A flow indicator gives a manual reading of the flow through the hot oil circuit. Closing the bypass valve enables more flow through the reactor section. The meter is calibrated for Marlotherm SH at 330°C. TR4 monitors the thermal oil inlet temperature at the pipe surface and TR5 monitors the thermal oil outlet at the pipe surface. Two isolating valves enable the heater and reactor to be separated. The heater is a commercial heater by Tool Temp (TT-390) designed for use with Marlotherm SH up to 360°C, where there is automatic temperature control with a heating capacity of 16 to 24kW and an indirect cooling capacity of up to 90kW at 360°C. This model contains a pump with a seal-less magnetic drive. Marlotherm SH is a thermal oil sold by Global Heat Transfer (ght). The component is dibenzyltoluene with a temperature range from 250 - 350°C. The properties of the fluid are shown in the appendix A.4.

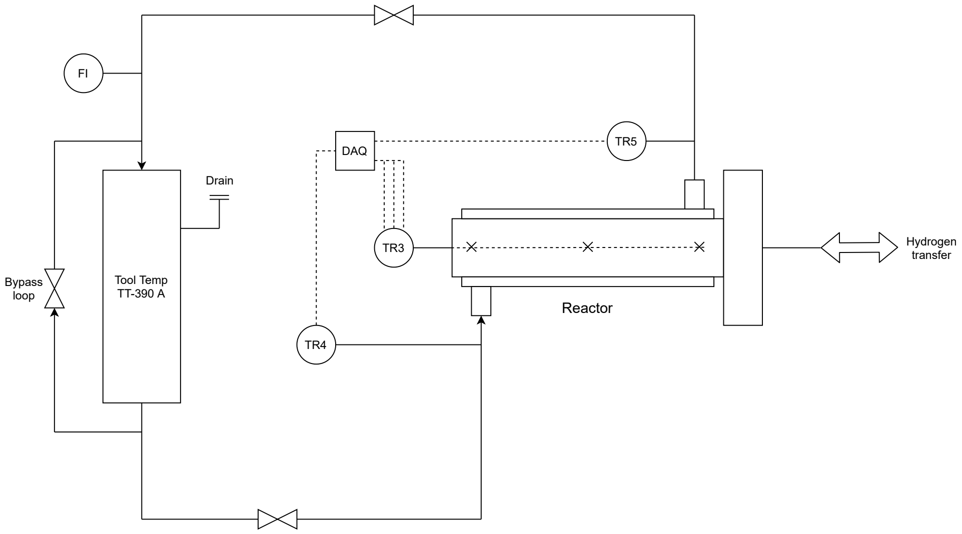

Figure 3.6: Thermal oil layout. Shown are the temperature recorders TR3, TR4 and TR5. They are the triple thermocouple assembly, heat transfer fluid (HTF) entry and exit respectively. The crosses indicate the approximate position within the reactor centreline. FI is a flow indicator, calibrated using Marlotherm SH at 330°C. The bypass loop controls the amount of fluid entering the reactor section. DAQ = Data acquisition software (National Instruments, CompactDAQ chassis)

3.2.3 Loading the reactor

The inside cylinder fill dimensions were 24.3 mm by 462.8 mm. This gave a total internal volume of 215 cm^3. There were 39 expanded natural graphite (ENG) fins/discs each with a depth of 0.12 cm with a radius of 1.215 cm inserted into the powder section. As the ENG fins exhibit a very high radial thermal conductivity, they aid in reducing the bed thermal resistance. This gave a total fin volume of 21.7 cm^3 and thus a fill volume of 193 cm^3.

Using a fully filled reactor of packing density 1 g cm^{-3} (supplied on the SFM Atoultra 200 spherical inert gas atomised Mg powder datasheet), gave a mass of 193 g. Allowing for 20% volume expansion gave 154 g. This amount was used to fill the reactor. Thus, the end bulk density was 154/193 = 0.8 g cm^{-3}.

The procedure to fill the reactor became more complicated as it was decided to retrofit the reactor with a thermocouple arrangement so the inside reactor profile could be measured. Figure 3.7 shows the arrangement of the thermocouple fitting. The filling assembly procedure was as follows:

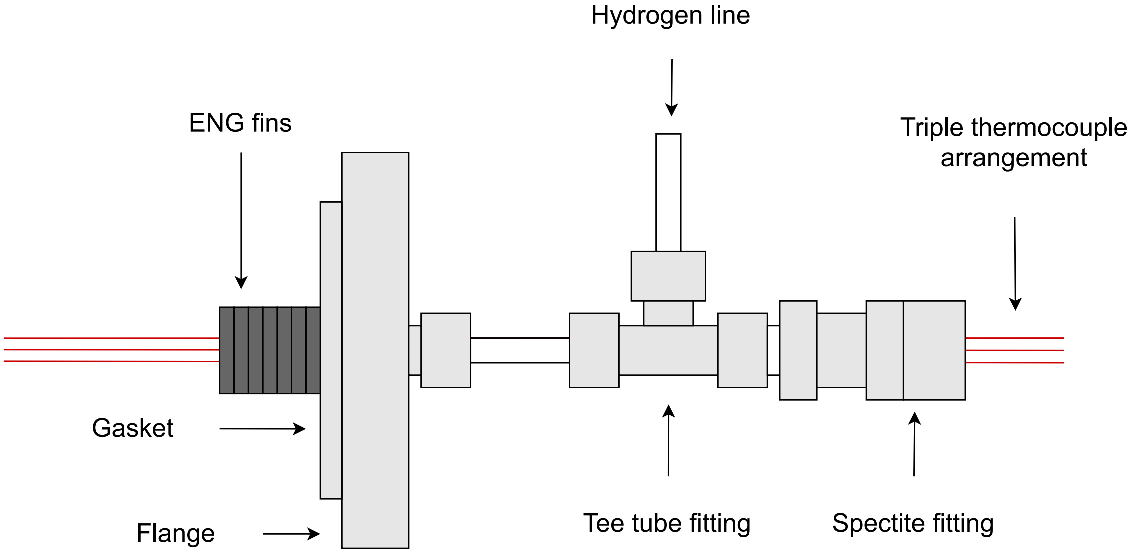

Figure 3.7: The tube fitting arrangement of the reactor hydrogen outlet. The spectite MF fitting was a triple hole PTFE fitting. The spectite fitting required a NPT to compression fitting adapter, and all other connections were compression fittings. The compression fitting to the flange was welded by the reactor manufacturer. This assembly is attached to reactor flange on the right shown in figure 3.8.

1. Graphite ENG fins were cut to size using a knife and a mudguard washer was used as a template. Each fin was checked to have a tight fitting to the cylinder wall. The centre point was marked and a 2 mm hole hand drilled. A circular file was then used to remove excess flakes resulting in a clean 2 mm diameter hole.

2. A tube fitting arrangement was assembled as per figure 3.7. The gasket and ENG fins were inserted over the thermocouples. The length of the thermocouples were adjusted to give the positions shown in figure 3.8. Three mineral insulated type K with pot seal thermocouples were used of diameter 1.5 mm and length of 1m, 0.75m and 0.5m each. The 1m sensor was the furthest from the hydrogen entry/exit flange and 0.5m sensor was closest to the flange. From the outlet of the spectite fitting, there was clearance of ≈ 30 cm before the pot seal and start of the plastic sheaved wiring. This resulted in approximately 30 cm between hot sections and electrically components. Due to the low specific heat capacity of air, the air

temperature around the electrical components was < 35°C.

3. An individual batch of magnesium was poured into the reactor. A fin was then inserted down the reactor, using the depth gauge. The depth gauge was a special made metal assembly, with the diagram shown in the appendix (A.13). A new batch of magnesium was poured in and another fin was inserted down the reactor. This cycle was repeated until full. There was 20 mm between each fin in a thermocouple region, and 10 mm gap everywhere else as shown in figure 3.8. The reactor was filled in a vertical position and then positioned horizontally. A hammer with a plastic end was hit at the points along the reactor to promote distribution in each respective section.

4. Once full, a ENG fin was added on top and then tightly packed with quartz wool. The wool was used to stop powder escaping into the pipework when under dehydrogenating conditions.

For details on connection assembly on reactors, flanges and fittings, see section A.6.

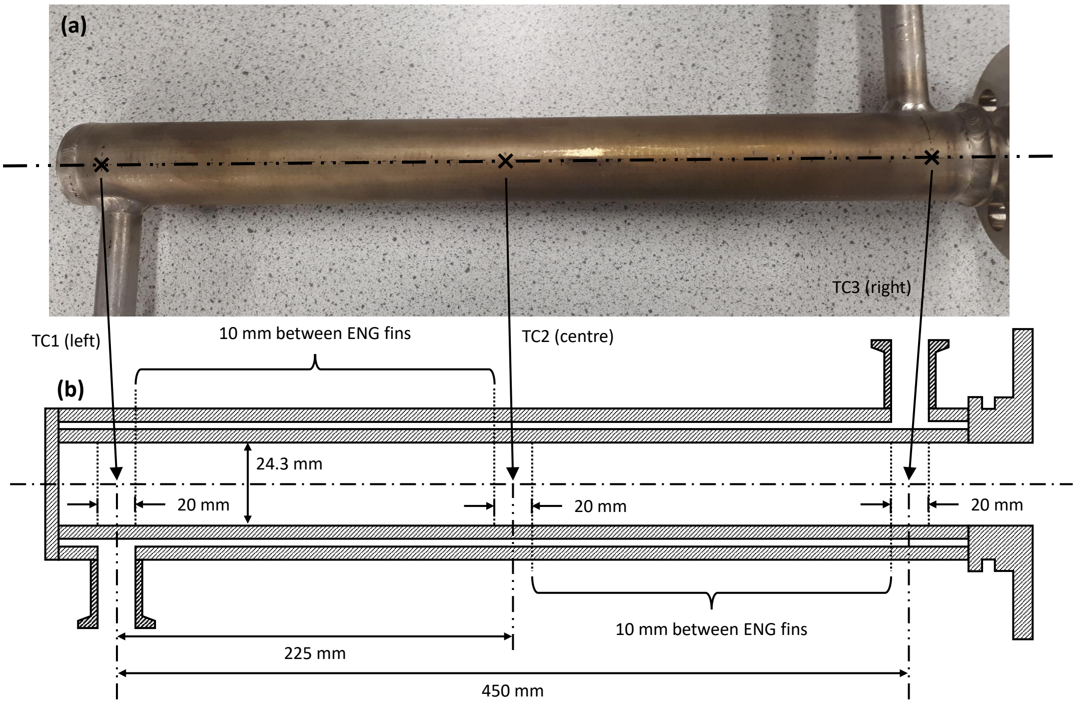

Figure 3.8: (a) Reactor and approximate location of thermocouples (TC). (b) Reactor diagram showing location of thermocouples and distance between each expanded natural graphite (ENG) fin.

3.2.4 Volume calibration

The method was to couple the reactor to an existing Sievert's of known manifold volume. At room temperature this filled reactor volume was then calculated. From knowing this volume, other volume segments were either calculated by $P_1V_1 = P_2V_2$ when attached to the large lab-scale hydrogen circuit, or by filling the RED segment with a fixed pressure and emptying it into another section (such as BLUE). The different segments are shown in figure 3.9. The effective reactor volume at temperature was calibrated when attached to the large lab-scale hydrogen circuit, rather than the Sievert's apparatus. All other segments are assumed to be at room temperature.

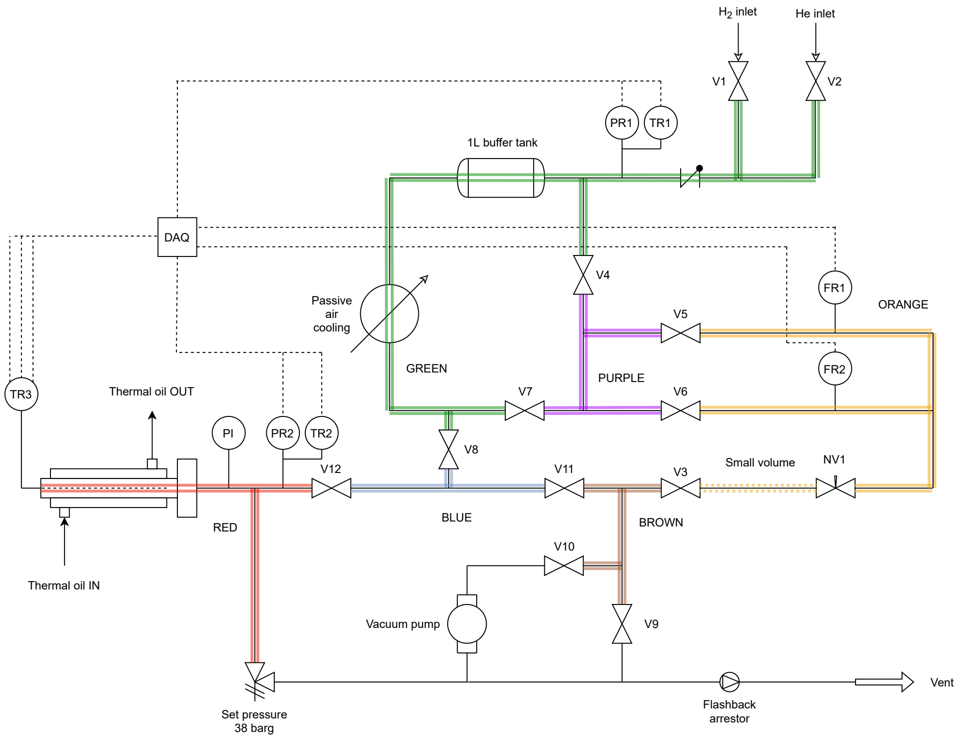

Figure 3.9: Process flow diagram (PFD) including the respective sections. The DAQ (data acquisition) device records the pressure (PR), temperature (TR) and flow (FR) at the specified locations. PI is a pressure gauge. Valve (V) positions are closed/open depending on the mode of operation, with the needle valve (NV) providing additional flow control.

3.2.5 Activation

For activation, the reactor was surrounded with heating tape. Heating tape was used for activation for the following reasons:

- I had past experience in using electrical heating for magnesium reactors and was comfortable using it.
- Originally, a large oven was purchased that could fit the reactors so they could be activated. However, once activated this meant disconnecting the reactor to air before reconnecting to the position for the hot oil circuit. It was decided to try and avoid this exposure to air.
- Although the hot oil circuit could have been used to activate the sample, there were troubles getting it assembled, therefore activation with tried and tested electrical tape was used to progress experiments.

An additional heating rope was wrapped around the flange as it was acting as a heat sink. For sufficient activation, a uniform temperature distribution was desirable. To test for a uniform distribution, the empty reactor was filled with sand before filling with magnesium, where the results are detailed in chapter 6. The setup was then replicated during magnesium activation. The activation operating procedures for hydrogenation and dehydrogenation are shown in figures 3.10 and 3.11 respectively. The heating tape was controlled using a proportional, integral, derivative (PID) Watlow EZ-zone controller, with the sensor between the tape and the outer reactor wall. The set-point (SP) of the tape and rope were set such that the average of the temperature readings inside of the reactor (TR3) were at 380°C (SP-tape = 387°C SP-rope = 390°C).

For hydrogenation, the initial reactor temperature and pressure was 380°C and 24 bar respectively. Initially, the reactor section was evacuated (isolated at V12) and the hydrogen manifold was set at 24 bar. V12 was opened to start hydrogenation and when the flow rate < 1 nL/min, the reaction was considered finished. For dehydrogenation, the conditions were 380°C and an operating pressure ≈ 1 bar. Initially, V12 was shut and the hydrogen manifold evacuated. V12 was then opened to start dehydrogenation and the vent line was opened sufficiently to hold a constant pressure. Once the mass flow dropped to around 0.8 nL/min, the vacuum pump was opened.

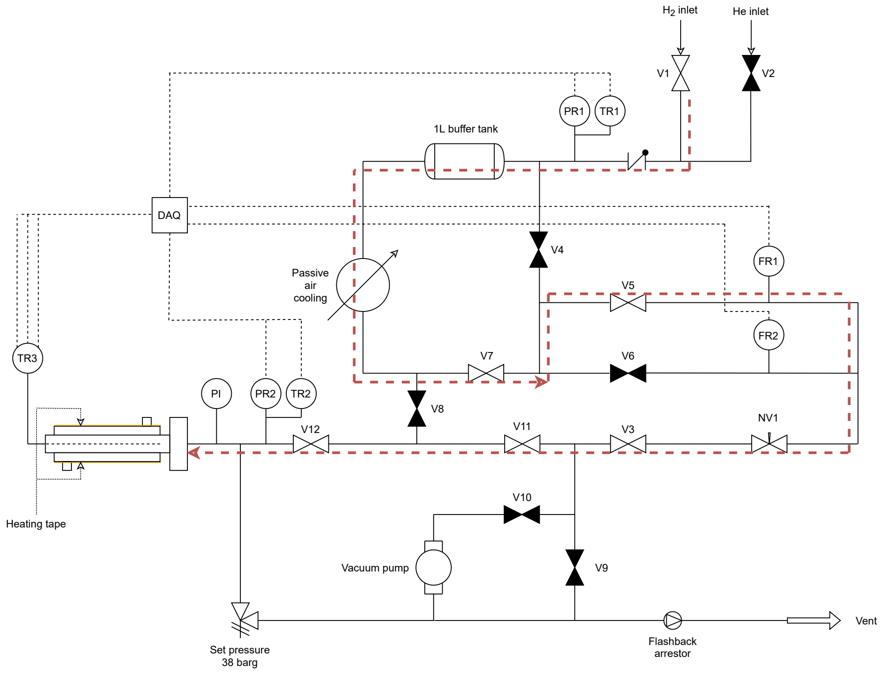

Figure 3.10: General operating procedure when activating reactor for hydrogenation. Valves in the closed position are filled black.

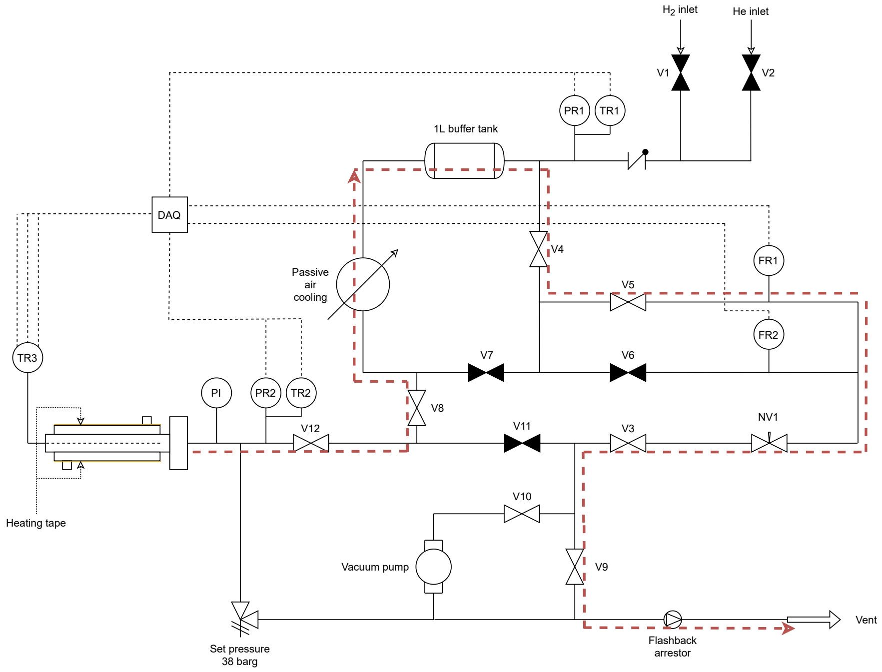

Figure 3.11: General operating procedure when activating reactor for de-hydrogenation. Valves in the closed position are filled black.

3.2.6 Preparing hot oil circuit

When the hot oil loop was operated for the first time or when the flow rate needed resetting, the bypass loop control valve was fully opened (figure 3.6). Then manual adjusting of the bypass control valve enabled the desired flow rate when at temperature. As the HTF viscosity changes with temperature, constant adjusting of the control valve is required during startup and shutdown. When transitioning from the heating tape to the hot oil circuit, the reactor was cooled to room temperature before removing the tape.

3.2.7 Experiments with Marlotherm SH

The operating procedure using Marlotherm SH for hydrogenation was the same for activation, except V3 was used as the isolation valve instead of V12. This was because a metal frame was erected around the rig for safety reasons, and V12 was positioned close to the thermal oil circuit. For dehydrogenation, as the reaction rate was slow and the pressure difference required maximising, the reactor was open to the vacuum pump for the duration of the reaction. The operating temperatures for hydrogenation were 302°C and 9 -14 barg and 302°C and -0.65 barg for dehydrogenation. The thermal oil flow rate was 6 nL/min. More information on this (and the influence of COVID-19 on experiments) is described in section 6.2.3 in chapter 6. The total reaction time for both reactions was fit around open laboratory times. As such, a hydrogenation was performed in the mid afternoon (1-3 hours reaction time), and a dehydrogenation was started at 5pm the same day, so that it finished around lunchtime the next day (25-30 hours reaction time). This was to avoid a scenario where the reactor would be in the metal state for long periods. Once heated to operating temperature, the thermal oil circuit was kept at temperature until experiments were completed.

3.3 COMSOL: Multi-physics software

COMSOL is a commercial software package that uses the finite element method to solve differential equations. COMSOL was used for modelling the chemical reactions in chapters 4, 5 and 6. In the appendix (A.3), the general physics interfaces in COMSOL are covered in relation to the kinetics of metal hydrides from a graphical user interface perspective, the basics around the finite element method, and parameters, variables and mesh used for simulations (figure A.7 and A.6). In this section the equations used to model metal hydride kinetics in a Sievert's apparatus (0.2g) and for the large lab-scale reactor (154g) are discussed.

3.3.1 Sievert's model

3.3.1.1 Governing equations

The mass balance is expressed in concentration form. The volume chosen is up to the user (and geometry), common volumes are reactor volume, void volume or a unit volume. As it is assumed that the time taken for the H_2 molecule to the get from the entrance of the reactor to the reactant surface is much faster than the hydride reaction, the external diffusion effects are neglected. Therefore, the equation reduces to,

$$-\frac{\partial C_A}{\partial t} = r_A \tag{3.3}$$

where C_A and r_A are the concentration and reaction rate of component A respectively. The Arrhenius equation calculates the effective specific rate constant k_e, using effective activation energy E_e and effective pre-exponential factor A_e, which accounts for the average reactive surface area (RSA).

$$k_e = A_e exp\left(-\frac{E_e}{RT}\right)$$

Due to the non-isothermal nature of the reaction, an energy balance is included. Conductive heat flux was expected to dominate, thus convective heat flux of hydrogen was neglected,

$$(\rho c_p)_e \frac{\partial T}{\partial t} + \nabla \cdot (-\lambda_e \nabla T) = -r\Delta_R H \tag{3.4}$$

where ρ = density, c_p = specific heat capacity, λ = thermal conductivity, $\Delta_R H$ = heat of reaction, and subscript e = effective. Equation 3.4 also assumes that there is a local thermal equilibrium, where the temperature of the fluid and solid are the same. Nasrallah et al. experimentally validated this assumption for a $LaNi_5$ system [37]. It is assumed that the local thermal equilibrum assumption is also valid for a magnesium hydride system.

3.3.1.2 Hydrogen gas properties

The specific heat capacity of H_2 and thermal conductivity of H_2, were governed by an empirical equation which was a $f(T,P)$, using data from NIST database at the system pressure ranges [42].

$$\lambda_{H_2}(T[K],P[bar]) = 4.805E^{-4}T + 3.983E^{-2} + 4.344E^{-5}P \tag{3.5}$$

Uncertainty = $\pm 2.698 \times 10^{-5}$ @ 1 bar, $\pm 8.347 \times 10^{-5}$ @ 50 bar

$$c_{p_{H_2}}(T[K],P[bar]) = 1.599E^{-6}T - 1.429E^{-3} + 5.231E^{-4}P + 14.83 \tag{3.6}$$

Uncertainty = $\pm 5.231 \times 10^{-4}$ @ 1 bar, $\pm 2.926 \times 10^{-3}$ @ 50 bar

The thermal conductivity and specific heat capacity of the porous matrix (λ_p & c_{p_p} respectively) were assumed to be a constant. c_{p_p} = 1545 J kg^{1} K^{1} [52, 1].

3.3.1.3 Effective thermal conductivity

In the simulations, the porous matrix thermal conductivity (λ_p) was selected as an input parameter to reach the desired value of λ_e. To determine the effective thermal conductivity, data provided by Albert et al. was extrapolated [3]. This data was for magnesium in a hydrogen atmosphere from 1-25 bar and 25, 100, 200 and 300°C. λ_e was found to be a function of pressure and temperature with a logarithmic type trend (fast initially, slow increase then on after). λ_e was also a function of the cycle number (no. 10/11 to 28/27 respectively), increasing 50% both for dehydrogenation and hydrogenation, attributed to cycling causing densification (hydrogenation) and powder re-arrangement (dehydrogenation), thus enhancing heat transfer paths [3]. Additionally, magnesium sintering may occur, also improving heat transfer [3, 97]. In addition, a dehydrogenated state hydride (i.e. metal) exhibits a higher effective thermal conductivity than hydrogenation at a given temperature and pressure. This was explained through increased electron transport in metallic particles [91]. At 410°C and 25 bar, hydrogenated state λ_e was measured as 1.1 W m^{-1} K^{-1} and dehydrogenated magnesium hydride 1.80 W m^{-1} K^{-1} after 18 cycles [3].

Extrapolation was difficult as the jump from 25 to 100 was large, but the 100-200 jump was smaller than 200-300°C. Equation 3.7 was generated digitising the data from [3], resulting in a residual sum of squares of 0.005. The results are shown in figure 3.12

$$0.0547\, ln(P) + 0.216 + 0.0757\, ln(T) + 0.000173 \tag{3.7}$$

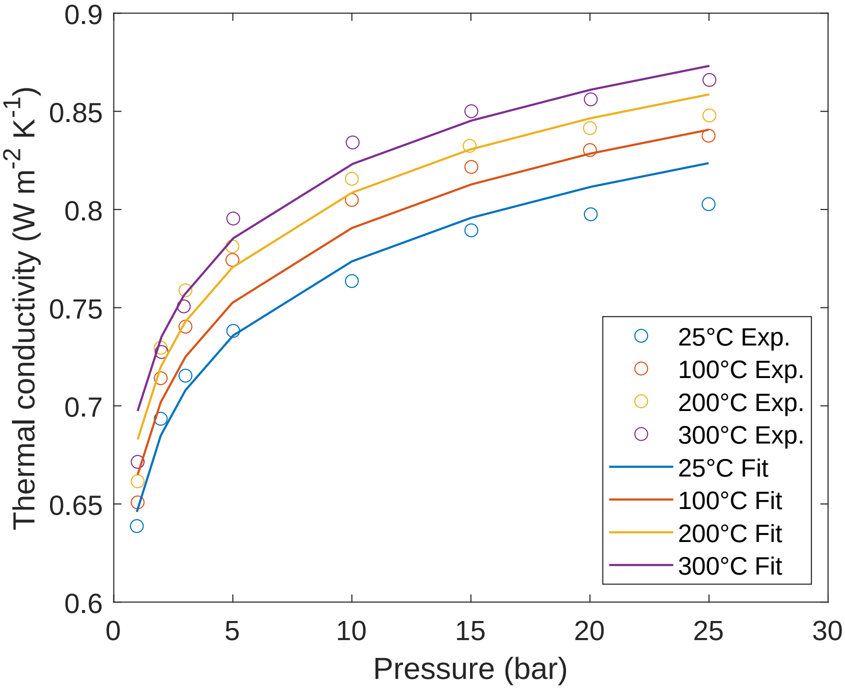

Figure 3.12: Equation 3.7 applied to experimental data from [3].

Using equation 3.7, for 330°C at 8-20 bar λ_e = 0.84-0.89 W m^{-1} K^{-1}, 360°C at 16-40 bar λ_e = 0.88-0.93 W m^{-1} K^{-1}, 380°C at 24 bar 0.91 W m^{-1} K^{-1}, and at 400°C at 32 bar 0.92 W m^{-1} K^{-1}. It was found that a change from 0.8-0.9 W m^{-1} K^{-1} resulted in little change to the reaction profile when compared to experimental data. This is expanded upon in section 4.5.6. Accordingly, a constant λ_e of 0.9 W m^{-1} K^{-1} was used for all hydrogenation simulations.

For dehydrogenation experiments, accurate λ_e values have less significance, as other parameters within the model that are regressed) (such as fragmentation and initial value of $C_{H \cdot M}$ - see section 5.3) offer similar changes to the reaction rate. The effective thermal conductivity in dehydrogenation simulations was $\lambda_e = 1.5$ W m^{-1} K^{-1}, which was calculated from a $\lambda_p = 2$ W m^{-1} K^{-1}.

3.3.2 Large lab-scale reactor simulation: activation

This section looks at how COMSOL was used to model the large lab-scale reactor. The large lab-scale reactor simulations used the same mass and energy balance as the Sievert's models (section 3.3.1.1) within the reaction domain (i.e. the metal/metal hydride). The differences came from the geometry and boundary conditions. Figure 3.13 shows the 2D-axisymmetric reactor geometry, which attempted to represent the dimensions and layout of the actual reactor, with the mesh shown in figure A.6.

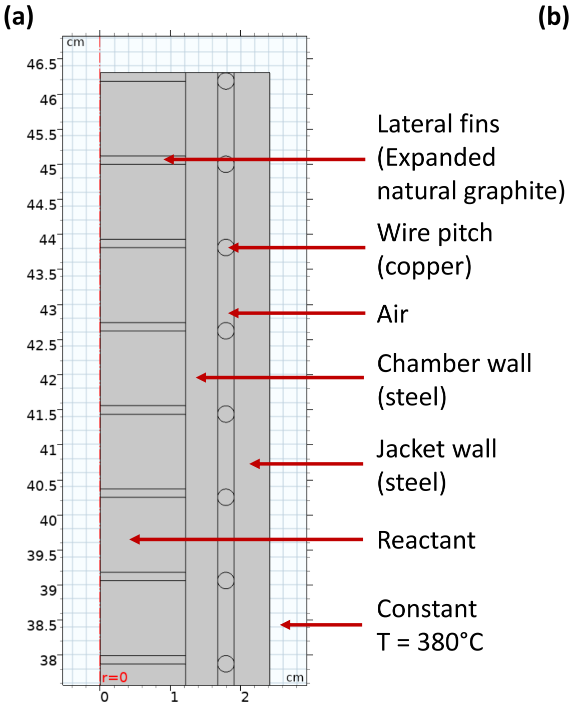

(b)

Information	Value
Mass of metal	154g
Reference H_2 content	7.66 wt%
Reference moles H	12.67 mol
Total Internal V	215 cm^3
Fin number	39
Wire pitch	6 or 39
Total fin volume	21.7 cm^3
Fill volume	193 cm^3
Bulk density	0.8 g/cm^3
Bed porosity	0.54
x_m (No P_{BD}) [6]	0.915
x_m (P_{BD}) [6]	0.955
x_m (No P_{BD}) [39]	0.915
x_m (P_{BD}) [39]	0.955

Figure 3.13: (a) COMSOL geometry of large lab-scale reactor during activation. Top of reactor shown only. Chamber ID = 24.3mm (1"NB), ENG fin depth = 1.2mm, chamber wall = 4.55mm, air/wire = 2.35 mm, jacket wall = 5.08 mm & length = 463 mm. (b) Data for this setup. ENG fins: $\lambda_e = 190$ W m^{-1} K^{-1}, $\rho = 1$ kg m^{-3}, $c_p = 900$ J kg^{-1} K $^{-1}$, x_m = maximum hydride fraction

Figure 3.13 shows the reaction domains sandwiched in-between lateral fins. This is followed by the chamber wall, then the section which would have HTF following through during hot oil operation (but stagnant air during activation using heating tape) and finally the outer/jacket wall, to where a constant temperature condition of 380°C was applied. There were two scenarios for each model tested, where the wire pitch was modified. The wire pitch was chosen as the air gap provides significant thermal resistance, thus changing the number of contact crossings (wire) can easily alter the thermal resistance, where the first scenario was a wire pitch of 39 (as per engineering drawing) and in the second scenario, 6. The change in wire pitch is an unrefined representation of the systems thermal resistance. As the site availability depends on the heat transfer rate, thermal resistance is essentially a variable. Modelling thermal resistance is challenging in this setup due to the following reasons:

- The reactor wire pitch in practice is a helical spiral. As its not possible to revolve a spiral in 2D axi-symmetry, a torus was used instead. Thus, the 39 wire pitch is not a true representation. Further, the wire was wrapped around the inner chamber wall, and then the outer cylinder was slot over in an interference fit, thus there was not perfect contact.

- A constant boundary temperature is assumed, but in reality this is hard to achieve using heating tape. The measured boundary temperatures at the "tape" and "rope" could not be used as they had to be higher to counter the heat losses. The boundary PID controller was set so that the reactor centre-line started on average at 380°C.

- The tape was not long enough to completely wrap around the reactor without leaving non-directly heated areas. Therefore, parts of the wall were cooler than parts in direct contact with the heater. A 3D simulation was generated, but due to a spiral shape and asymmetric distribution, symmetry was not possible, and this was abandoned as the simulation would be computationally expensive.

- The reactor heat losses were uneven. For instance, the flange acted as a heat sink, which was countered by the rope heater, and at the other end of the reactor, loose insulation was used. In comparison to the model, the ends of the reactor assumed an adiabatic boundary.

- The simulation assumes perfect thermal contact between the fins, wall and reactant material.

In reality, this is not a true representation as a certain amount of powder was inserted incrementally, followed by a fin, allowing expansion head-space. Then, it was positioned horizontally. Thus, there would have been a volume with a larger void space than other regions, and so this would have resulted in variations in thermal contact.

Therefore, the wire pitch was a regression parameter, whereby it was altered as an "effective" thermal resistance parameter, taking into account the issues described above.

3.3.3 Large lab-scale reactor simulation: hot oil

For the simulations that used thermal oil, the geometry and boundary conditions were modified to factor the different scenario. Figure 3.14 shows the geometry used for the large lab-scale reactor. For these simulations the heat transfer effect of the fluid was modelled using the overall heat transfer coefficient (U).

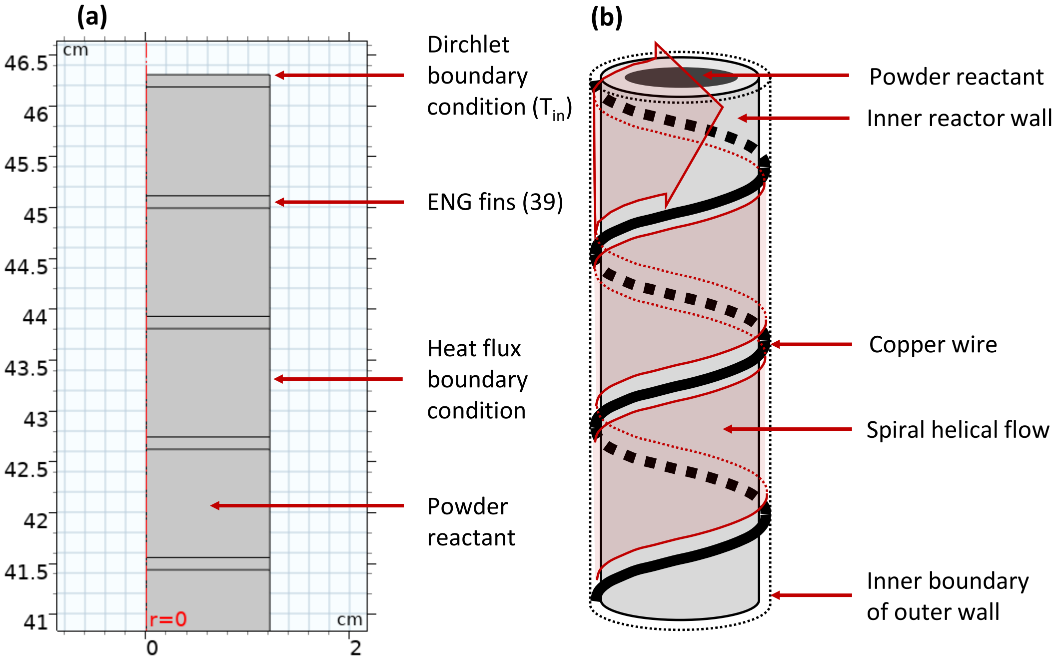

Figure 3.14: (a) 2D-axisymmetric geometry used for the 154g reactor. (b) Illustration of helical flow in an annulus, reactor.

3.3.3.1 Overall heat transfer coefficient

The method used to the model the heat transfer fluid (HTF) was through adding thermal resistances in series. Figure 3.15 shows this for a metal hydrogenation reaction. The resistance of the reactor bed is dominated by conduction, i.e. the bed effective thermal conductivity. At the edge of the bed, thermal contact between the powder and solid wall adds further resistance, as the contact is not perfect. Further, the wall adds resistance, as does the fouling layer of the HTF, liquid film and finally the inverse of the convective heat transfer coefficient at the tube outer wall.

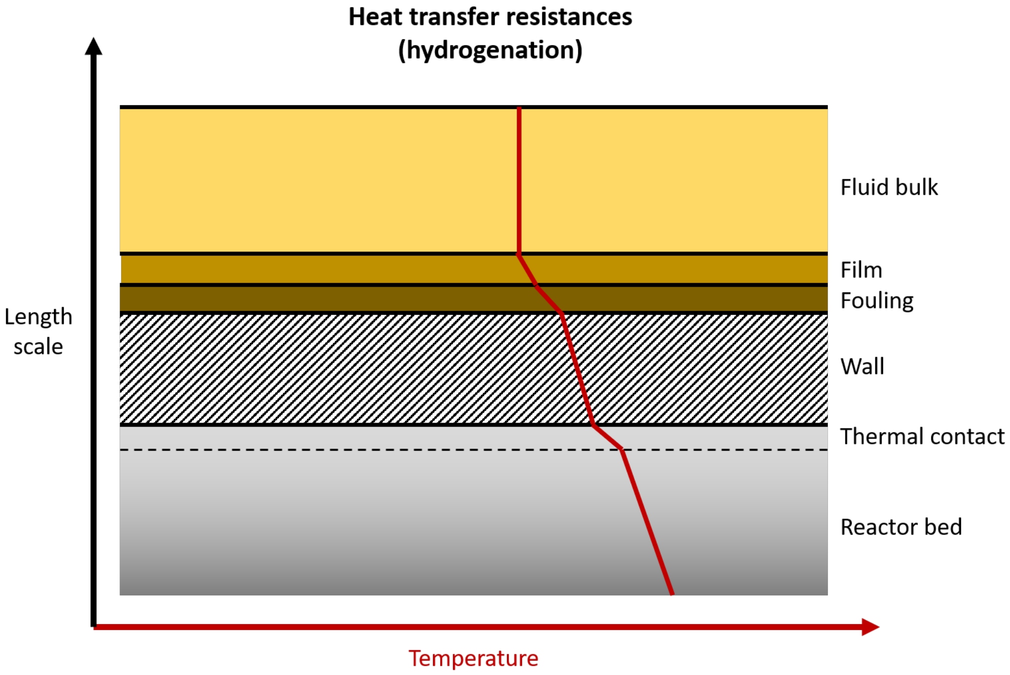

Figure 3.15: Idealised diagram of the heat transfer resistances during the metal hydrogenation reaction. It is assumed the other profiles are linear. The fluid bulk temperature is also considered to be constant at that point in-line (i.e. z and y direction) but changing in the x direction. The gradients are not representative, but are shown to display the differences between layers.

This can be summarised in terms of the overall heat transfer coefficient (U) as,

$$\frac{1}{U} = \frac{1}{h_o} + f_o + \frac{L_w}{\lambda} + \frac{1}{h_{tc}} + \frac{1}{h_b} \tag{3.8}$$

where the contact areas are equal, and h_o = outer heat transfer coefficient, f_0 = outer fouling factor, L_w = tube wall thickness, λ = tube material thermal conductivity, $1/h_{tc}$ = Arbitrary parameter to denote thermal contact resistance and $1/h_b$ = Arbitrary parameter for the reactor bed resistance. The heat load (Q) is,

$$Q = UA_{HT}(\Delta T) \tag{3.9}$$

where A_{HT} is the heat transfer area. A Dirchlet boundary condition is placed on a corner point (inlet temperature) and a "heat flux" boundary interface is used. An energy balance is applied on the boundary using equation 3.10,

$$\frac{\partial T_c}{\partial t} + c_{p_c}\dot{m}_c \cdot \nabla T_c = 2\pi R_I \, h(T - T_c) \tag{3.10}$$

where T_c = coolant temperature (K), R_I the internal radius (m), $\dot{m}_c$ = coolant flow rate (kg s^{-1}), c_{p_c} = coolant specific heat capacity (J kg^{-1} K^{-1}), h = convective heat transfer coefficient (W m^{-2} K^{-1}), and at the "heat flux" boundary, there is an inward heat flux of $-h(T - T_c)$.

3.3.3.2 Helical flow in an annulus

Ideally, an experimental correlation should be used to determine the convective heat transfer coefficient (h). In this case, an experimental correlation for h was not found and therefore, a numerically investigated correlation was used instead. Maakoul et al. first tested their simulation on a double pipe heat exchanger [22]. They used the following double pipe correlation from Petukhov,

$$Nu = 0.023 \, Re^{0.8} \, Pr^{\frac{1}{3}} \tag{3.11}$$

where Nu = Nusselt number, Re = Reynolds number and Pr = Prandtl number. Maakoul et al. then developed the following correlation for helical flow down an annulus with a Reynolds number $5982 \leq Re \leq 71785$ and baffle spacing $0.025 \; m \leq B \leq 0.1 \; m$ [22],

$$NuPr^{\frac{1}{3}} = 0.04572 \, Re^{0.6098}(1 + B)^{7.565} \tag{3.12}$$

Both equation 3.11 and 3.12 number use the hydraulic diameter. Between these ranges, a decrease in baffle spacing and rise in Reynolds number (velocity) results in a higher heat transfer coefficient relative to a standard double pipe arrangement. This increase in heat transfer comes at a cost of increased pressure drop.

Maakoul noted the cross-sectional area as $A_{cs} = 0.5B(d_o - d_i)$ and $Re = (\rho u d_o)/\mu$, where $B =$ baffle spacing (width), $d_o - d_i =$ annulus gap. However, here there is disagreement as the flow cross-sectional area can be estimated as a rectangular duct as shown in figure 3.14c and 3.16, therefore, $A_{cs} = B(d_o - d_i)$. Further, the hydraulic diameter (d_H) is assumed to be a fully filled rectangular duct,

$$d_H = \frac{4A_{cs}}{\text{wetted perimeter}} = \frac{2B(d_o - d_i)}{d_o - d_i + B} \tag{3.13}$$

with the Reynolds number as $Re = (\rho\, u\, d_H)/\mu$. Using these equations, figure 3.17 outlines an example calculation for finding the convective heat transfer coefficient for helical flow in an annulus based on the reactor "as built" dimensions as shown in figure 3.16.

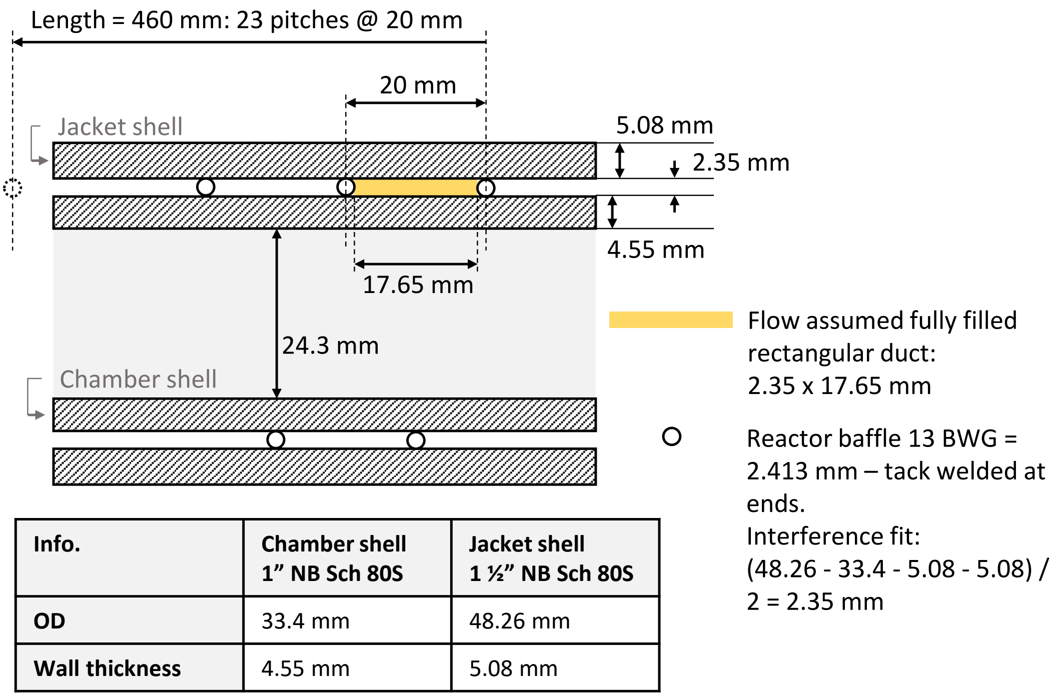

Info.	Chamber shell 1” NB Sch 80S	Jacket shell 1 ½” NB Sch 80S
OD	33.4 mm	48.26 mm
Wall thickness	4.55 mm	5.08 mm

▬ Flow assumed fully filled rectangular duct: 2.35 x 17.65 mm

○ Reactor baffle 13 BWG = 2.413 mm – tack welded at ends.
Interference fit:
(48.26 - 33.4 - 5.08 - 5.08) / 2 = 2.35 mm

Figure 3.16: Diagram outlining the dimensions of the fully filled rectangular duct. Dimensions taken from the reactor schematic. Nominal bore (NB) dimensions taken from [23]. BWG = Birmingham wire gauge, OD = outer diameter.

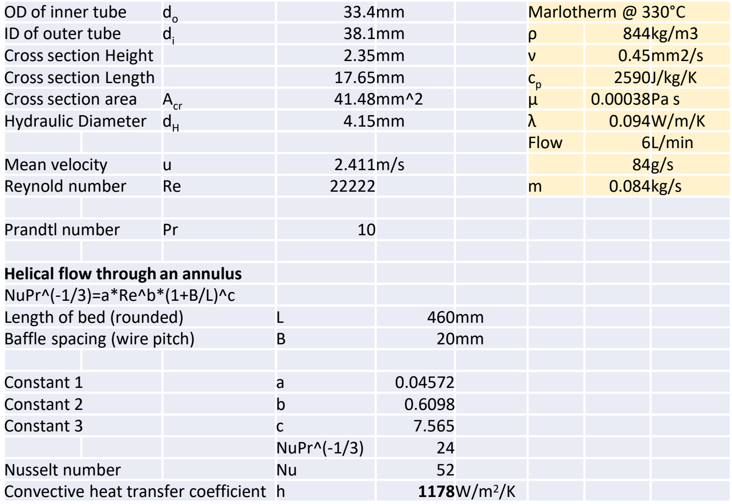

OD of inner tube	d_o	33.4mm		Marlotherm @ 330°C	
ID of outer tube	d_i	38.1mm		ρ	844kg/m3
Cross section Height		2.35mm		v	0.45mm2/s
Cross section Length		17.65mm		c_p	2590J/kg/K
Cross section area	A_{cr}	41.48mm^2		μ	0.00038Pa s
Hydraulic Diameter	d_H	4.15mm		λ	0.094W/m/K
				Flow	6L/min
Mean velocity	u	2.411m/s			84g/s
Reynold number	Re	22222		m	0.084kg/s
Prandtl number	Pr	10			
Helical flow through an annulus					
NuPr^(-1/3)=a*Re^b*(1+B/L)^c					
Length of bed (rounded)		L	460mm		
Baffle spacing (wire pitch)		B	20mm		
Constant 1		a	0.04572		
Constant 2		b	0.6098		
Constant 3		c	7.565		
		NuPr^(-1/3)	24		
Nusselt number		Nu	52		
Convective heat transfer coefficient		h	**1178**W/m²/K		

Figure 3.17: Calculation of the heat transfer coefficient using the Maakoul et al. correlation. Marlotherm data taken from the datasheet and dimensions from the schematic.

The cross sectional area (A_{cs}) of the duct for the 154g reactor was outside the range tested by Maakoul et al. In figure 3.18a, values of h based on Maakoul's tested range and our Marlotherm SH conditions were between 777-1039 W m^{-1} K^{-1}. Applying $L = 460$mm and altering baffle length for similar A_{cs} gave similar h values. For comparison, both cases are above the Petukhov correlation, at $h \approx 750$ W m^{-1} K^{-1}. As the 154g reactor is close to Maakoul's tested range it was decided to use this correlation. However, as it was not experimentally validated, there is little bonus covering extra detail of fouling, thermal contact and the Marlotherm SH film, thus a rounded convective heat transfer coefficient $h = 1000$ W m^{-1} K^{-1} was used.

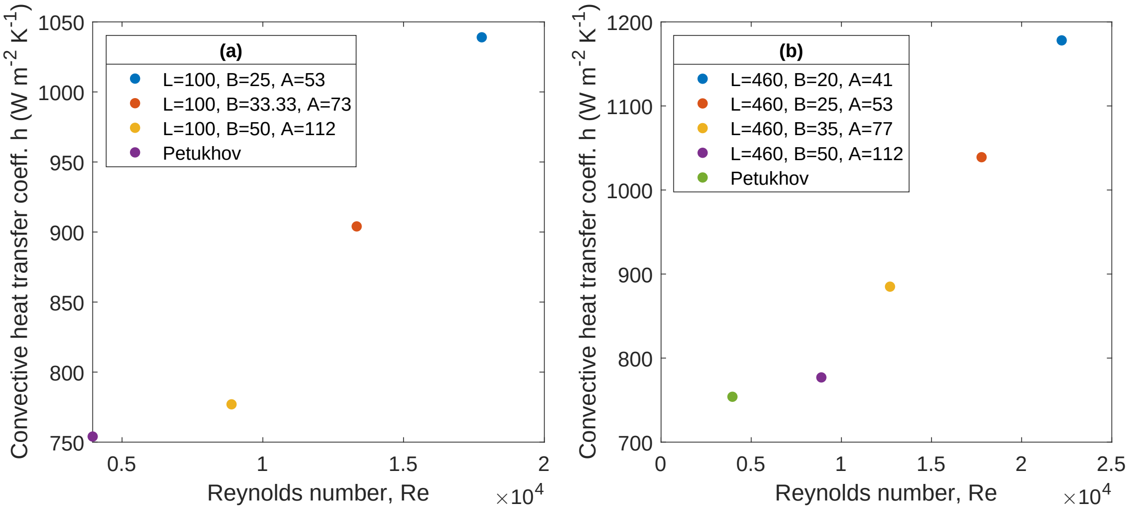

Figure 3.18: (a) Maakoul correlation based on their range tested (units L, B = mm, A = mm^2) (b) Maakoul correlation at 154g reactor length and varying baffle lengths. Both compared to Petukhov correlation.

Chapter 4

Hydrogenation kinetics

4.1 Experimental hydrogenation data

Magnesium hydrogenation experimental data was gathered on a manual Sievert's for a 0.2 g sample at varying initial gas pressures and temperatures. The results are shown in figure 4.1. One can see that the initial reaction rate increases with temperature (figure 4.1d). At 330°C and 360°C, an increase in gas pressure results in a faster initial reaction rate, but then decreases into a linear trend at high hydride fractions. This linear trend is more profound at higher temperatures (380°C and 400°C) as shown in figure 4.1c. Not only is there a noticeable change in the uptake profile/curve as the pressure increases at a given temperature, but there is also a reduction in capacity. Hydrogenation capacity tends to reduce as the temperature decreases, however the capacity at 380°C is lower than at 400°C at one over-pressure ($\sigma_{0.5}$), see equation 4.1.

4.1.1 Over-pressure

When a hydrogenation kinetic experiment is carried out, a degree of over-pressure is applied to help drive the reaction. The greater the gas pressure, the further the system is from the equilibrium pressure. When gathering the experimental data, the over-pressure ($\sigma_{0.5}$) was defined as,

$$\sigma_{0.5} = \frac{P(initial) - P(eq\,@\,\theta = 0.5)}{P(eq\,@\,\theta = 0.5)} \tag{4.1}$$

As stated above, a rise in the over-pressure causes a kinetic change, where this change is also influenced by the temperature. In this thesis, this kinetic change, is split into two sections, 'close to equilibrium', and 'far from equilibrium'. Although the results suggest this kinetic change is gradual, instead of a sudden transition; to aid structure to this thesis, 'close to equilibrium' refers to conditions when the over-pressure $\sigma_{0.5} = 1$ and initial sample temperatures are between 300-360°C. 'Far from equilibrium' is set as initial sample temperatures at 380°C and above at $\sigma_{0.5} \geq 1$, or 300-360°C at $\sigma_{0.5} > 1$.

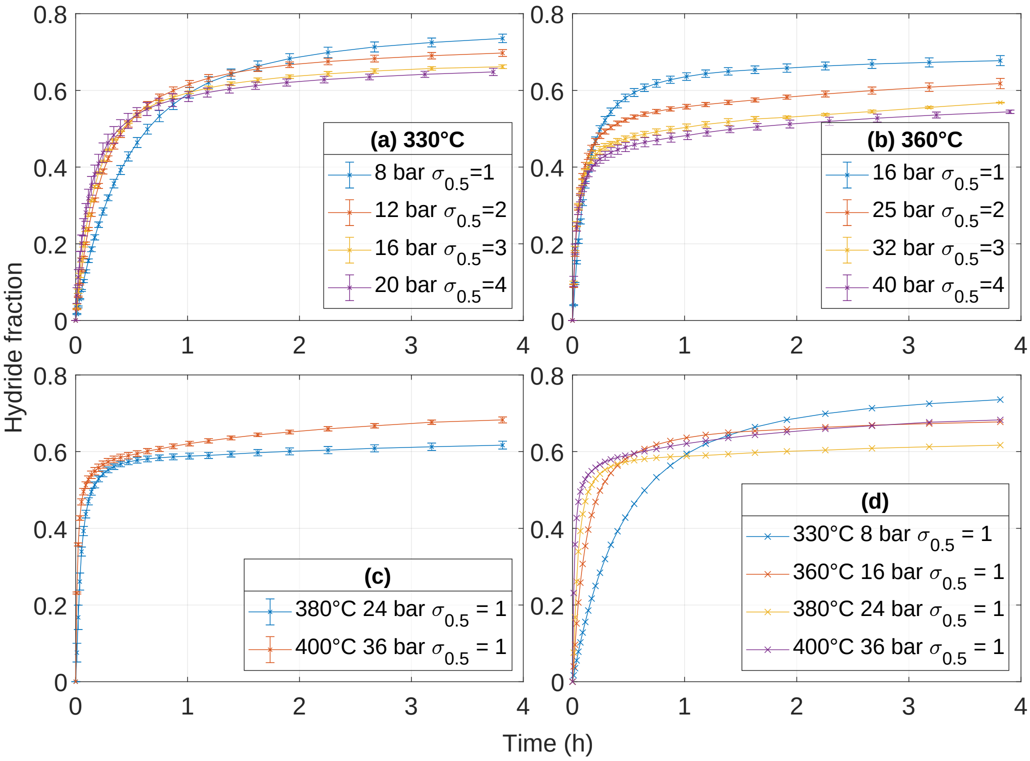

Figure 4.1: Hydrogenation of Mg experimental data using a Sievert's apparatus at varying initial temperatures and over-pressure. Experiments were performed in triplicates and the standard error is shown. (Conversion to wt% = x*7.66 for Mg)

4.2 Analysing previous rate laws

To test the rate laws developed by previous researchers, the magnesium hydrogenation data at 330°C shown in figure 4.1 was applied to the integrated rate laws covered in the chapter 2. A straight line indicates a good fit. The JMA rate law $-ln(1-\theta)^{\frac{1}{n}}$ is shown in figure 4.2. One can see that the best rate law is when $n = 1$ at 8 bar and it does not translate to higher pressures (4.2a), and the other rate laws at higher values of n are also insufficient (4.2b,c and d).

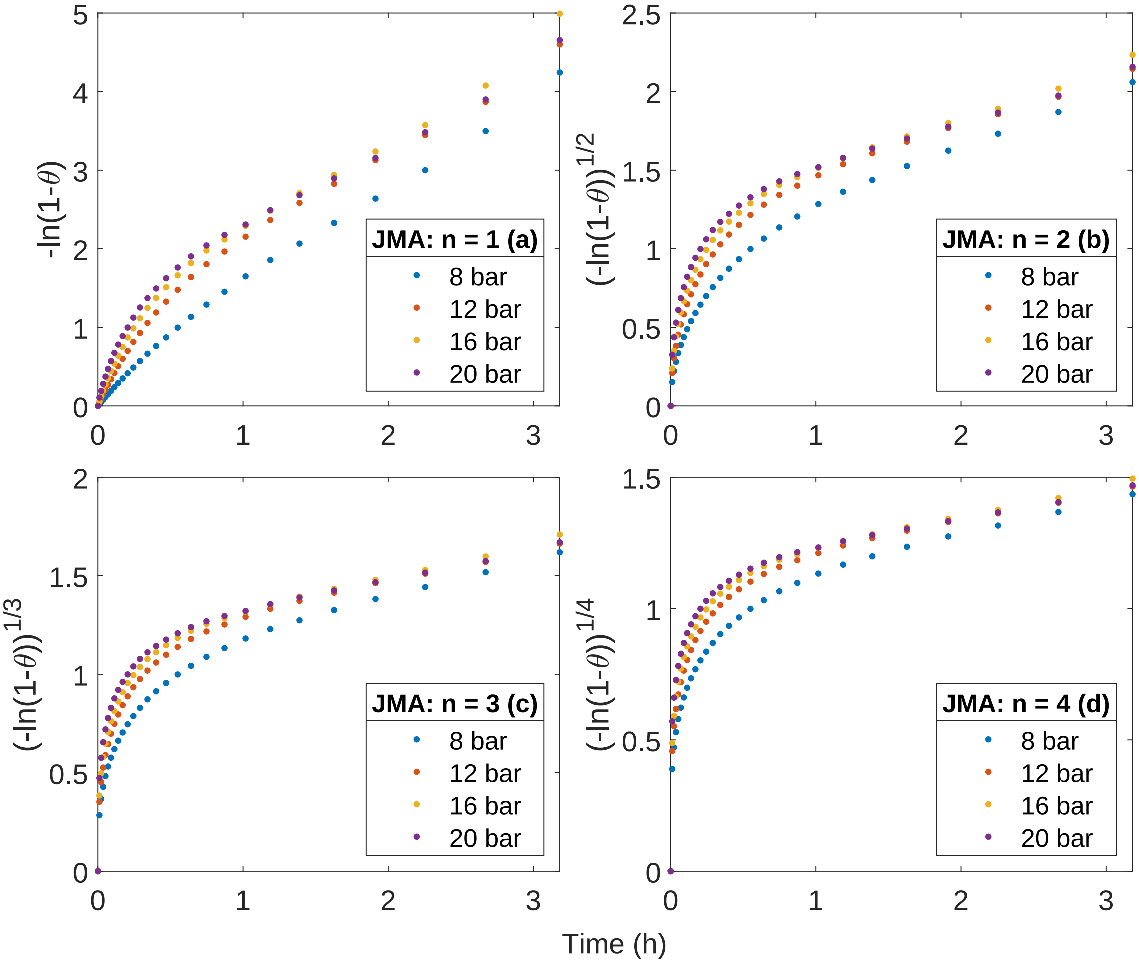

Figure 4.2: JMA integrated rate laws using experimental data at initial temperature of 330°C and varying initial gas pressures.

When the experimental data is applied to the shrinking core/contracting volume and diffusion limiting rate equations (figure 4.3), the fits are equally unsatisfactory and not linear. The Cater-Valensi equation [61] is unstable at higher pressures (figure 4.3a), whereas the SC:Diff Controlled [43] is more robust (figure 4.3d).

The next set of models tested were the models derived by Chou et al. (figure 4.4). The first

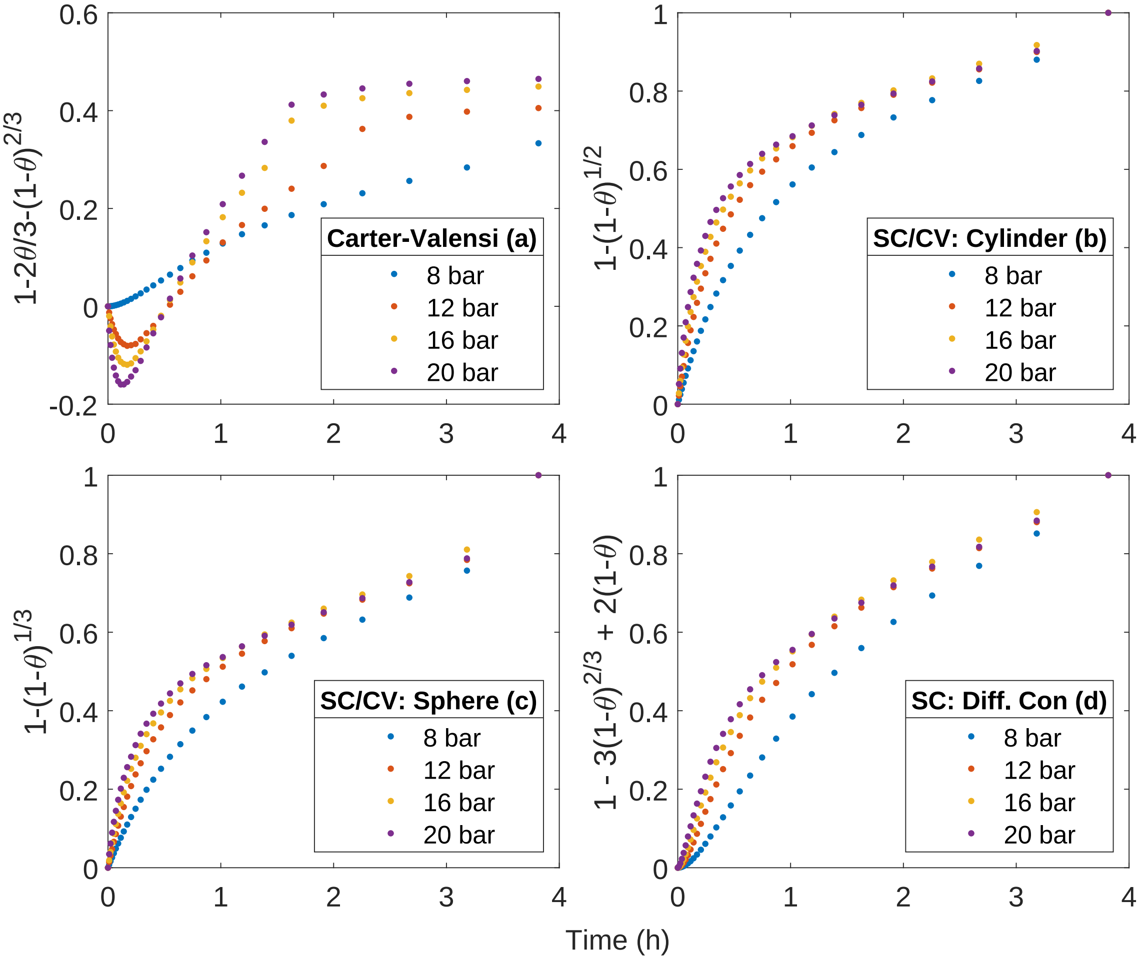

Figure 4.3: Shrinking core/contracting volume and diffusion controlled integrated rate laws using experimental data at initial temperature of 330°C and varying initial gas pressures

surface-based Chou model is synonymous with the shrinking core/contracting volume y-axis but the gradient term varies depending on the reacting mechanism (figure 4.4a). The diffusion-based Chou model is shown for all temperatures tested as this model displayed a reasonable fit at 330°C (figure 4.4b). The model runs into issues at higher temperatures and over-pressures however (figure 4.4c and d). It is evident that there are two straight line regions, where it can be tempting to draw two lines and designate the rapid gradient change to a phase change. This thesis argues to avoid such temptation, as the derived model mathematically states $(1-(1-\theta)^{(1/3)})^2$ is plotted on the y-axis with time (t) on the x-axis, and k or $1/t^*$ being the gradient. Therefore, the y-intercept goes through the origin and inserting a secondary straight line that has a y-intercept > 0 contravenes the rate law.

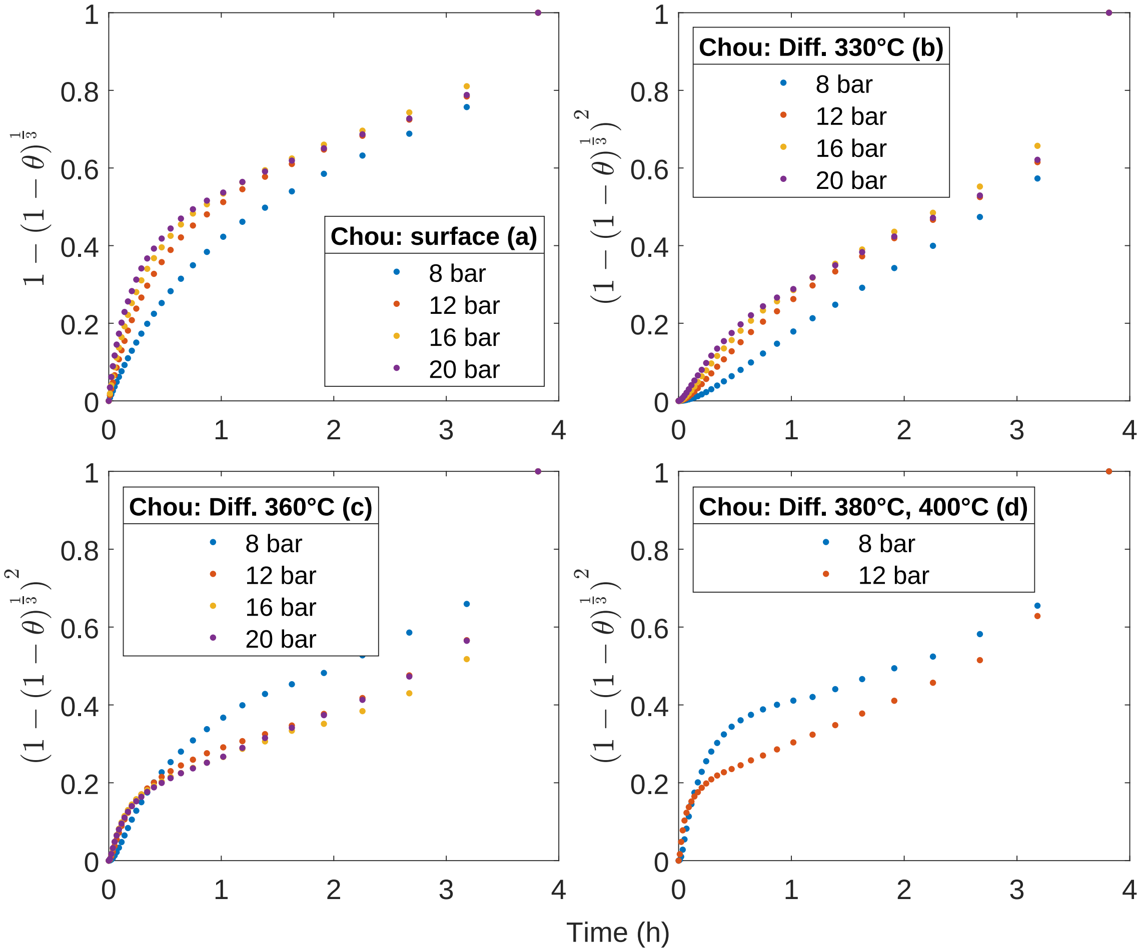

Figure 4.4: Application of the Chou model based on the contracting volume and diffusion mechanisms for all tested experimental conditions.

In summary, it is evident that all the common rate laws used within the metal hydride community do not sufficiently represent the kinetics of magnesium hydrogenation at 330°C and 360°C. As such, it was decided to derive a new model, based on the observations and clues provided by the experimental data.

4.3 The Site Availability Model (SAM)

4.3.1 Overview

In this section, work within the paper, written by the author of this thesis, "Modelling a kinetic deviation of the magnesium hydrogenation reaction at conditions close to equilibrium" [1] is recapped, and then expanded upon, by developing the Site Availability Model (SAM) through the use of non-stoichiometric defects to represent metal hydrogenation kinetics far from equilibrium.

4.3.2 General mechanism

The key theme of the SAM model is assuming a surface reaction. The site availability model builds from the assumptions of the Langmuir adsorption model (covered in [28]), but also includes a shrinking core approach (covered in Levenspiel [43]). A generic reaction is assumed where component **A** binds to component **M** to create a complex $\mathbf{M} \cdot \mathbf{A}$.

$$\mathbf{A} + \mathbf{M} \rightarrow \mathbf{M} \cdot \mathbf{A}$$

Assuming component **A** reacts at the metal surface, component **A** has to transport itself there. Therefore, the general mechanism for an idealised sphere can be summarised below and illustrated in figure 4.5.

1. Transport of **A** to surface
    (a) Initial permeation through the porous bed (external diffusion)
    (b) Diffusion through product layer (internal diffusion)
2. Dissociation at metal surface (currently ignored)
3. Adsorption reaction to shared complex and depletion of core. Once hydrogen has been chemisorbed, the hydrogen has high mobility as described by [100] in section 2.1.

Within this shrinking core approach, the particle size does not change, thus R_0 is a constant, whereas R_c is the radius of shrinking metal reactant or reaction front. If step 3 is selected, then this

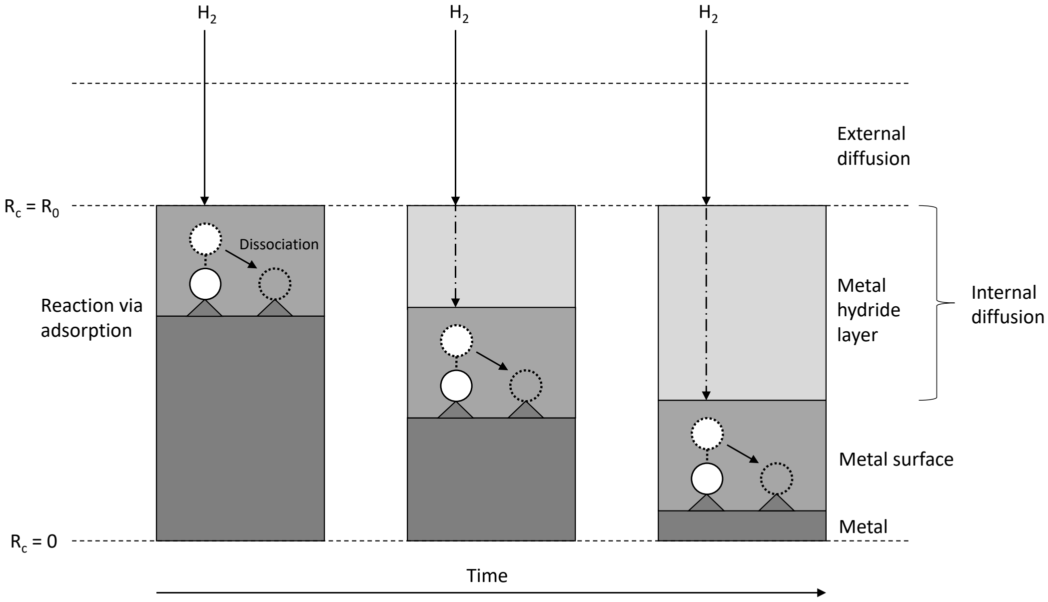

Figure 4.5: Proposed general mechanism of hydrogenation kinetics for Magnesium. This is a 2D cutout section of a sphere. R_0 is the radius of the sphere, R_c is the radius of shrinking metal reactant

is an adsorption reaction, thus the Langmuir adsorption model would be a sensible place to start. Table 4.1 details how a metal hydrogenation reaction is modified from conventional Langmuir with the modification of P_A with the site availability σ_s. The concept of site availability is introduced due to phenomenon regarding hydride reactions, detailed next.

4.3.3 Site de-activation

For H_2 hydrogenation to a metal to occur, the gas pressure (P_g) must be greater than the bound pressure (P_B). As the exothermic reaction invokes a rise in temperature, which causes the bound pressure P_B to rise and approach P_g; the driving force is reduced and so must the reaction rate.

Expanding on site theory, if the reaction rate must fall, the rate of a successful collision to an active site must decrease. Thus, it is assumed that the rise in temperature and subsequently the reduction in the "pressure driving force", must temporarily de-activate a site, even if that site is unoccupied/unavailable, to reduce the amount of successful collisions, and therefore reduce the reaction rate.

Within SAM, this theory is represented by the ratio of available sites to unavailable sites. As temperature is linked to the bound pressure, then across each time step, P_B indicates the unavailable sites. At the next time step, the change in $(P_g - P_B)$ will be an indication of sites that have become inactive across that time step. Therefore, the ratio that sites that are available to ones that are unavailable can be estimated by the site availability, σ_s. Thus, the "pressure driving force" can be viewed as a "site availability driving force".

$$\sigma_s \approx \frac{\text{Available sites}}{\text{Unavailable sites}} \approx \frac{P_g - P_B}{P_B} \tag{4.2}$$

As discussed in section 2, different pressure ratios have been applied to metal hydride reactions, however here an alternative physical meaning is proposed through site theory and probability. This concept of site availability is a key theme as this concept expands to relate ideas such as H-H interactions and defects imposed by the inclusion of hydrogen into the metal sub-lattice.

Table 4.1: Comparison between Langmuir (forward rate) [28] and using site availability

Langmuir (forward rate)	Site Availability Model (SAM)
The rate of attachment to an active site (M) is proportional to rate of collisions that A makes with active sites	Same
An active site is any unoccupied site.	An active site is a site that is unoccupied and available. (i.e. both unoccupied and available to react)
The collision rate to an active site is proportional to the pressure over the surface (P$_A$).	The collision rate to an active site is proportional to the (sorption) site availability (σ_s).
As A only adsorbs on active sites, it is proportional to concentration of active/vacant sites. (C$_v$)	Same
$r_{A \cdot M} = k'' P_A C_v$	$r_{A \cdot M} = k'' \sigma_s C_v$

4.3.4 Isotherm representation

At close to equilibrium conditions i.e. an imposed gas pressure not too far away from the equilibrium pressure (P_{eq}), the bound pressure (P_B) is assumed to be similar to bound equilibrium pressure determined through PCT measurements. Thus, $P_B \approx P_{eq}$. To model P_B, a semi-empirical equation has been developed to represent metal hydrogenation which is a function of temperature

(T) and normalised hydride fraction (θ). Starting with a basic sigmoidal function with θ as the dependent variable,

$$\theta = \frac{1}{1 + exp(-y_1\phi)} \tag{4.3}$$

For stability, the midpoint must pass through 0, and the vertical axis must start at 0 and end at 1. As such, the normalised hydride fraction suits the vertical axis, while for the horizontal axis, a dimensionless normalisation term, ϕ is introduced,

$$\phi = \frac{P_B - P_N}{P_N} \tag{4.4}$$

P_N is the normalisation pressure. For a typical PCI, this point would be where $\theta = 0.5$, often this position is the plateau pressure. Therefore, one can use the van't Hoff relation to determine the isotherm pressure at $\phi = 0$.

$$P_N = exp\left(\frac{\Delta_R H}{RT} - \frac{\Delta_R S}{R}\right) \tag{4.5}$$

With $\Delta_R H$ and $\Delta_R S$ enthalpy and entropy of reaction respectively, R = universal gas constant and T = temperature. Thus, this pressure is a normalisation point to which the equilibrium pressure can be determined at a given normalised hydride fraction and temperature. In effect, when $P_{eq} = 0$, $\phi = -1$, and when $P_{eq} = 2P_N$, $\phi = 1$. Rearranging 4.3 and substituting into 4.4 gives:

$$P_B = P_N\left(1 - \frac{1}{y_1}ln\left(\frac{1-\theta}{\theta}\right)\right) \tag{4.6}$$

On a practical point, note, equation 4.6 will return error values at $\theta = 0$ or at $\theta = 1$, so this needs to be avoided when modelling. Within a sigmoidal function, increasing y_1 will increase the ascent of the curve (equally resembling a flat plateau) and thus is called the growth parameter. If y_1 is constant, the curve will be symmetrical. To demonstrate the versatility of y_1, there are 3 examples of defining y_1 as $f(\theta)$; a constant growth rate, an exponential drop, and a bell-shaped curve (figure 4.6).

It is apparent that all phases can be influenced by defining an equation for y_1, as a function of θ. This approach is practical as the equation for y_1 can be a single custom polynomial (or a spline of the respective phases) by regressing to experimental data and therefore, each metal hydride will have a custom equation for y_1. Equation 4.6 can be modified for a metal hydride system that exhibits two separate growth phases,

$$\theta = \frac{1}{1 + y_2 exp(-y_1 \phi^3)} \tag{4.7}$$

And if rearranged to make the bound pressure the subject, this gives,

$$P_B = P_N \left(1 - \left[\frac{1}{y_1} ln \left(\frac{1-\theta}{y_2 \theta} \right) \right]^{\frac{1}{3}} \right) \tag{4.8}$$

Where 'y_2' is a constant which can shift the location of the normalisation point. The normalisation point is recommended to be half of the pressure at $\theta = 1$ (yellow), which is at $\theta = 0.5$, and then translate the normalisation point by modifying y_2 (orange), followed by regressing to experimental data by customising an equation for y_1 (blue).

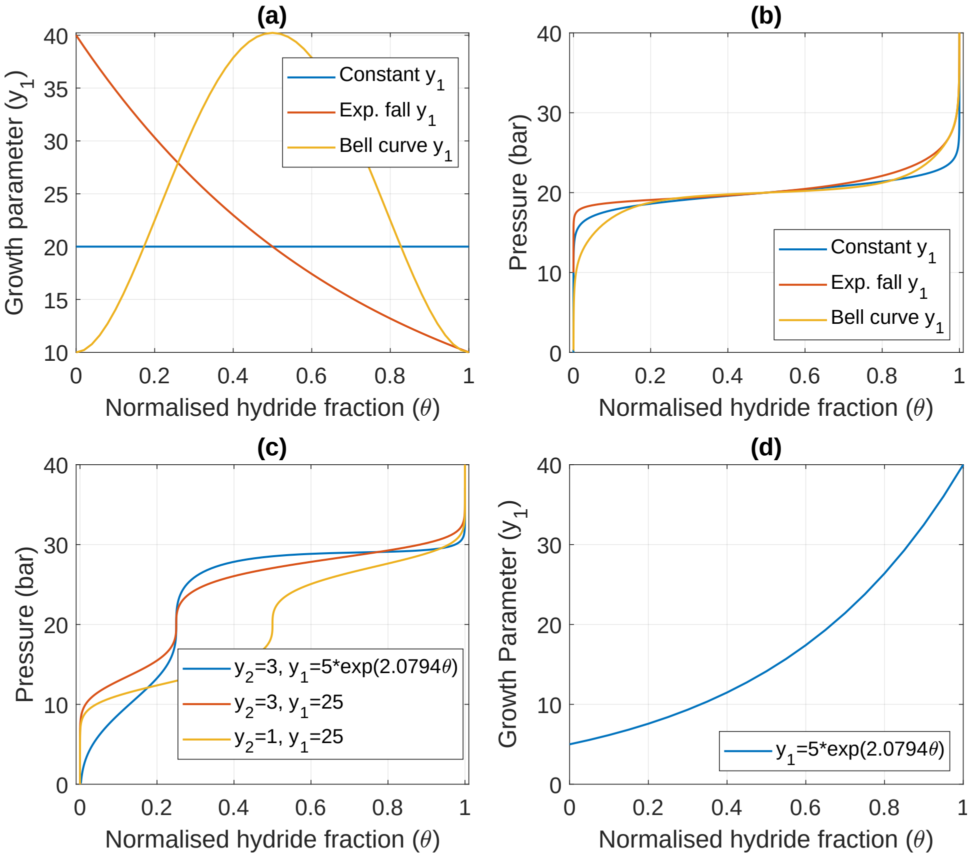

Figure 4.6: (a) Growth parameter y_1, (i) $y_1 = 20$, (ii) Exponential fall of y_1 from 40 to 10, (iii) Bell curve of y_1 from 10 to 40 and back to 10. (b) Subsequent PCI shapes based on eq. 4.6 using growth parameters in (a). (c) Two growth PCI shapes using eq. 4.8 and varying y_1 and y_2. (d) Illustration of y_2 based on equation in key.

4.3.5 Adsorption reaction

If dissociation is ignored, the rate of **A** forming $\mathbf{A} \cdot \mathbf{M}$ is directly proportional to the product of site availability (σ_s) and vacant sites (C_v), providing a fluid molecule can overcome the activation energy. Thus, if step 3 is considered the rate-determining step, the rate of forming $\mathbf{A} \cdot \mathbf{M}$ is (" denotes surface reaction),

$$r''_{A \cdot M} = k'' \sigma_s C_v \tag{4.9}$$

Units: $k'' =$ m s^{-1} & $r'' =$ mol m^{-2} s^{-1}. The concentration of vacant sites can be split into the concentration of available and vacant sites C_{Av-v}, and unavailable and vacant C_{Un-v}. Therefore, the concentration of total sites (C_T) is

$$C_T = C_{Un-v} + C_{Av-v} + C_{A \cdot M} \tag{4.10}$$

If C_T is also given by $C_T = C_{ref} x_m$, where C_{ref} is the reference concentration (taken as 7.66wt%) and x_m is the maximum capacity fraction at operating conditions, then the amount of unavailable & vacant sites at the end of the reaction would be represented through x_m. This means x_m is a regression parameter. Thus, the site balance can be simplified by

$$C_T = C_{Av-v} + C_{A \cdot M} \tag{4.11}$$

Where concentration of vacant sites $C_v = C_{Av-v}$. Further incorporating the normalised hydride fraction $\theta = C_{A \cdot M}/C_T$, gives a first order rate equation.

$$r''_{A \cdot M} = k'' \sigma_s C_T (1 - \theta) \tag{4.12}$$

If a hydride fraction is introduced $x = \theta x_m$, then the rate equation can be modified to,

$$r''_{A \cdot M} = k'' \sigma_s C_{ref} (x_m - x) \tag{4.13}$$

4.3.6 Including resistances

Within this thesis, resistances are expressed as mechanisms that hinder the reaction rate based on equation 4.12 above. These two mechanisms are denoted as diffusion resistance and surface resistance.

Therefore, this section includes step 1 of the reaction mechanism (diffusion resistance). However, as equation 4.12 is based in surface terms, understanding of the reaction surface is also required (surface resistance). For metal hydrogenation, the available reactive surface area will decrease with time. Likewise, a hydride product layer will form, which 'fresh' hydrogen would need to diffuse through before it can react with metal. To attempt to model these resistance effects, a shrinking core method has been used as discussed in section 2.2.2.4.

The diffusion of hydrogen through the bed (such as Darcy's law) has been neglected. This is due to the belief that the time required for hydrogen to diffuse and reach the pellet surface, would be much faster than the internal diffusion and surface kinetics. A constant bed porosity (ϵ_b) has also been assumed and thus particle sizes do not vary. As the reaction proceeds, a product layer forms, and thus the reactive surface area decreases.

In this model an important distinction is made compared with Gérard and Ono [30]. Here the assumption that any dissociation that occurs on the outside metal hydride surface and subsequent atomic diffusion to the inner metal surface is sufficiently small that it can be neglected. Instead the expansion of the metal hydride forms surface cracks, grain boundaries and defects in the structure allowing the permeation of molecular hydrogen direct to the inner metal surface via Knudsen diffusion as shown in figure 4.7.

Again, assuming a generic reaction whereby $\mathbf{A}+\mathbf{M} \rightleftharpoons \mathbf{A}\cdot\mathbf{M}$, with the resistance effects derived seperately, the following rate law can be developed. Note that the rate law (equation 4.12) is based on rate of accumulation of component **A** within the metal hydride. This rate equation is based on the rate of disappearance of component **A** in the gas (bulk) **that takes part in the reaction**. For example, if the pressure went from 20 - 18 bar, this rate law is based on the moles corresponding to the difference, 2 bar. For the surface reaction resistance,

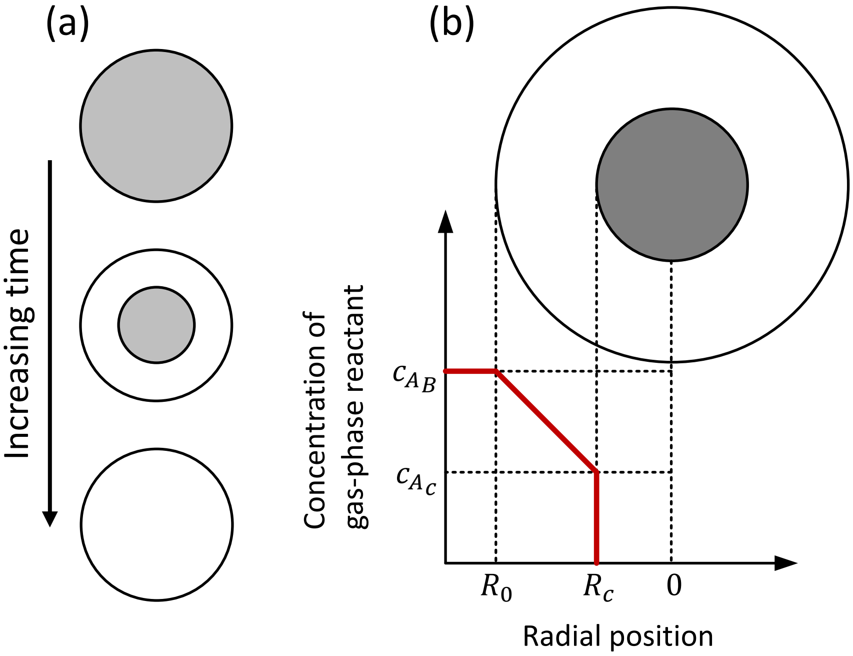

Figure 4.7: (a) Visualisation of the shrinking core over time, grey = metal, white = metal hydride (b) The concentration profile of the gas-phase reactant against the radial position within the reacting sphere/pellet

$$\text{Rate of disappearance of } \mathbf{A}_{(g)} = \text{Kinetics at surface}$$

written as a mole balance,

$$-\frac{dN_A}{dt} = k''(C_{A_c} - 0)\sigma_s \cdot 4\pi R_c^2 \tag{4.14}$$

C_{A_c} is the concentration of component **A** at the metal surface or shrinking core, N_A the moles of **A** and R_c is the shrinking core radius. As the rate determining mechanism is assumed at the surface, an increase in surface area would increase the reaction rate, where a common coarse method is to represent the specific surface area (SSA) within a 'velocity' rate constant of the reaction front (k''). This gives an effective rate constant ($k_e[s^{-1}] = SSA[m^2/m^3] \times k''[m\ s^{-1}]$),

$$k_e = A_e exp\left(\frac{E_e}{RT}\right) \tag{4.15}$$

However, if what matters does occur at the surface, then the reactant specific surface area is not a constant and will decrease. In this case, SSA is substituted with the variable, reactive surface area, (RSA) instead. As this would further complicate k_e, it is further assumed to use an average value of E_e (effective activation energy) and A_e (effective frequency factor) across the reaction duration (i.e. a constant). Thus, converting 4.14 into effective volume terms,

$$-\frac{dN_A}{dt}\cdot\frac{RSA}{4\pi R_c^2}=k''\cdot RSA\cdot C_{A_c}\sigma_s=k_eC_{A_c}\sigma_s \tag{4.16}$$

Where RSA is the reactive surface area, and if the pellet is assumed as a sphere this gives,

$$RSA=\frac{Reactive\,surface\,area}{volume\,of\,porous\,sphere}=\frac{4\pi R_{c_{av}}^2}{\frac{4}{3}\pi R_0^3}=\frac{3R_{c_{av}}^2}{R_0^3} \tag{4.17}$$

With $R_{c_{av}}$ being the average radius of the shrinking core. Upon rearranging,

$$C_{A_c}=-\frac{1}{4\pi R_c^2}\frac{RSA}{k_e\sigma_s}\frac{dN_A}{dt} \tag{4.18}$$

For the diffusion resistance,

Rate of disappearance of $\mathbf{A}_{(g)}$ = Rate of diffusion to reaction surface (Fick's law)

The mole balance in terms of **A** is,

$$-\frac{dN_A}{dt}=4\pi R^2J_A=4\pi R^2D_e\frac{dC_A}{dR} \tag{4.19}$$

where J_A (mol m^{-2}) is the molar flux of **A**and R (m) is the radius to be integrated over regarding the diffusion resistance. Converted into volume terms of R_c,

$$-\frac{dN_A}{dt}\cdot\frac{RSA}{4\pi R^2}=D_e\cdot RSA\cdot\frac{dC_A}{dR} \tag{4.20}$$

Applying the pseudo steady-state assumption of the concentration gradient from $R_0\rightarrow R_c$ and C_{A_B} to C_{A_c}, noting that the concentration gradient is positive and integrating across the product layer yields:

$$-\frac{dN_A}{dt}\cdot\frac{RSA}{4\pi}\int_{R_0}^{R_c}\frac{1}{R^2}dR = D_e \cdot RSA\int_{C_{A_B}}^{C_{A_c}} dC_A \tag{4.21}$$

$$-\frac{dN_A}{dt}\cdot\frac{RSA}{4\pi}\left[\frac{1}{R_0}-\frac{1}{R_c}\right] = D_e \cdot RSA(C_{A_c} - C_{A_B}) \tag{4.22}$$

C_{A_B} is the concentration of **A** in the bulk. All concentrations are linear and in series and thus the resistances can be combined (equate 4.18 and 4.22):

$$-\frac{dN_A}{dt}\cdot\frac{RSA}{4\pi}\left[\frac{1}{R_0}-\frac{1}{R_c}\right] = \frac{RSA^2}{4\pi R_C^2 k_e \sigma_s}\frac{dN_A}{dt} + RSA \cdot C_{A_B} \tag{4.23}$$

Rearranging gives:

$$-r_{A_B} = -\frac{dN_A}{dt}\cdot\frac{RSA}{4\pi R_0^2} = \frac{C_{A_B}\cdot RSA}{\frac{R_0^2 RSA}{R_c^2 k_e \sigma_s} + \frac{R_0}{D_e}\left(\frac{R_0 - R_c}{R_c}\right)} \tag{4.24}$$

In words, the rate equation considering resistance effects can be summarised as,

$$\begin{array}{c} \text{Rate of disappearance of M} \\ \text{based on effective pellet volume} \end{array} = \frac{\text{Driving force}}{\text{Surface resistance + Diffusion resistance}}$$

Thus, the surface resistance $= \frac{R_0^2 RSA}{R_c^2 k_e \sigma_s}$ and the diffusion resistance $= \frac{R_0}{D_e}\left(\frac{R_0 - R_c}{R_c}\right)$. In addition, the radius of the shrinking core can be defined as,

$$Fraction\, of\, A\, receding = \frac{Vol.\, of\, unreacted\, core}{Total\, vol.\, of\, particle} = \frac{\frac{4}{3}\pi R_c^3}{\frac{4}{3}\pi R_0^3} = \left(\frac{R_c}{R_0}\right)^3 = \frac{C_{A_B}}{C_{A_0}} \tag{4.25}$$

$$R_c = R_0\left(\frac{C_{A_B}}{C_{A_0}}\right)^{\frac{1}{3}} \tag{4.26}$$

Equation 4.24 was used as a direct rate equation to be used in COMSOL, with R_c being calculated with equation 4.26. As these equations are based on the moles of **A** disappearing from the bulk, and what is required is the moles of **A** within the forming hydride, a mole balance is used such that,

$$N_{A\cdot M} = N_{A_0} - N_{A_B} \tag{4.27}$$

where N_{A_0} is the (dummy) moles of the initial bulk $\mathbf{A}_{(g)}$, which is also the maximum uptake of

$\mathbf{A}_{(s)}$ within the hydride at the respective conditions. This means that $N_v = N_{A_B}$ and enables calculation of the normalised hydride fraction $\theta = N_{A \cdot M}/N_T$ (N_T = total moles) and the hydride fraction $x = N_{A \cdot M}/N_{ref}$ (see figure A.7 for the illustration of this). Note that if using the isotherm equation 4.6, it will not solve when $N_0 = N_{A_B}$ at $t = 0$, thus an estimated initial value of N_1 should be used just after $t = 0$.

To model the diffusion through the porous product layer, it is assumed that Knudsen diffusion, D_k, dominates, and that a pore is assumed to be a straight cylinder of pore radius, R_{PL}. The Knudsen diffusion is related to the mean speed of the component, u and mean path length, $\lambda = 2R_{PL}$, as a molecule collides with the wall more often than another molecule. [82, 77]. This is given by the following equation,

$$D_k = \frac{\lambda u}{3} = \frac{2}{3} R_{PL} \sqrt{\frac{8RT}{\pi M_A}} \tag{4.28}$$

Where M_A is the molecular weight of component $\mathbf{A}$. The effective diffusion coefficient D_e, where ϵ_{PL} and τ_{PL} are the porosity and tortuosity of the product layer is,

$$D_e = \frac{D_k \epsilon_{PL}}{\tau_{PL}} \tag{4.29}$$

4.3.7 Including non-stoichiometric defects

To recap from previous sections, Langmuir's original assumptions of a surface reaction were expanded upon, and the concept of site availability was introduced. The assumption stated that a site must be unoccupied and available for a reaction to occur. The availability of a site could be de-activated as the temperature increased and then re-activated as the temperature reduced. It was assumed that this unavailability was temporary and therefore, the hydrogen capacity of the sample should not be affected. The use of modelling $P_B \approx P_{eq}$ could potentially reduce the predicted capacity, but from modelling experimental data at higher over-pressures using equation 4.77, it falls short (figure 4.8d).

Applying theory from the site availability model, to maximise the hydrogenation reaction rate the site availability driving force should be maximised. As hydrogenation is exothermic the bound pressure will rise, reducing the site availability driving force by sites being temporarily turned off. Thus, it would be desirable to run the reaction isothermally as this would result in a bound pressure being similar to the equilibrium pressure (figure 4.8a). However, in most cases, it would be difficult to achieve true isothermal conditions, thus the bound pressure profile resembles figure 4.8b.

In order to further increase the site availability driving force, one might be tempted to then increase the gas pressure (P_g) in relation to the bound pressure (P_B). This ratio was defined as the system over-pressure. From experimental results shown in figure 4.8d, imposing a system over-pressure initially results in an increased reaction rate, followed by a noticeably altered mid-section and finally a reduced capacity, where this effect is profound for magnesium hydrogenation. The reality is in direct contradiction to the current theory of site availability so far as P_B (for a non-isothermal system) would follow the green dotted line in figure 4.8c, resulting in an incorrect hydride uptake profile (figure 4.8d). To address the change in uptake profile when there is an increase in system over-pressure, an expansion to the site availability model (SAM) is proposed with the inclusion of non-stoichiometric defects. The potential effect of non-stoichiometric defects is visually shown in figure 4.8, where the defects reduce the site availability driving force and ultimately reduce the hydrogen capacity.

Firstly, it is assumed the intrinsic point defects are Frenkel defects. At the pure stoichiometric composition, there are equal hydrogen vacancies and interstitials (i.e. $[\mathbf{H}_i'] = [\mathbf{v}_H^{\cdot}]$), while at reduced hydrogen activity (pressure), hydrogen vacancies dominate and at high hydrogen activity, hydrogen interstitials dominate. In shorthand notation, a Frenkel defect on the hydrogen sub-lattice can be written as equation 4.30.

$$\phi \rightleftharpoons \mathbf{H}_i' + v_H^{\cdot} \tag{4.30}$$

$$\mathbf{H}_H^x + \mathbf{v}_i^x + \frac{1}{2}H_{2_{(g)}} \rightleftharpoons \mathbf{H}_i' + \mathbf{v}_H^{\cdot} + \frac{1}{2}H_{2_{(g)}} \tag{4.31}$$

Where the neutral species is denoted ϕ. For a Frenkel defect, a hydrogen interstitial ($\mathbf{H}_i'$) and a hydrogen vacancy ($\mathbf{v}_H^{\cdot}$) can form, and likewise return to its neutral state. The longer notation (equation 4.31) includes the hydrogen gas and neutral interstitial and hydrogen sites. The "x" denotes neutral, whereas the apostrophe is negative (electron) and the dot is positive (hole). Equation 4.31 can be split into two equations depending on the hydrogen gas conditions thus,

$$\mathbf{v}_i^x + \frac{1}{2}H_{2_{(g)}} \overset{K_1}{\rightleftharpoons} \mathbf{H}_i' \tag{4.32}$$

$$\mathbf{H}_H^x \overset{K_2}{\rightleftharpoons} \mathbf{v}_H^{\cdot} + \frac{1}{2}H_{2_{(g)}} \tag{4.33}$$

Therefore, under high hydrogen pressure, the equilibrium constant (K_1) can be expressed as,

$$K_1 = \frac{[\mathbf{H}_i']}{[\mathbf{v}_i^x]\, P_{eq}^{\frac{1}{2}}} \tag{4.34}$$

with square brackets indicating the concentration of the respective site (normal or interstitial). If the concentrations were the number of species per mole of hydride then $[\mathbf{M}] = [\mathbf{H}] = 1$, then the concentration is the mole fraction. Further, as the number of vacant interstitials is very large in comparison to the number of filled interstitials, then $[\mathbf{v}_i^x] \approx 1$. Thus,

$$K_1 = x_{H_i'}\, P_{eq}^{-\frac{1}{2}} \tag{4.35}$$

Likewise, with reduced pressure conditions, the equilibrium constant is

$$K_2 = \frac{[\mathbf{v}_H^{\cdot}]\, P_{eq}^{\frac{1}{2}}}{[\mathbf{H}_H^x]} = x_{v_H^{\cdot}}\, P_{eq}^{\frac{1}{2}} \tag{4.36}$$

For a non-stoichiometric hydride, the deviation from stoichiometry (δ) can be defined as

$$\delta = x_{H_i'} - x_{v_H^{\cdot}} \tag{4.37}$$

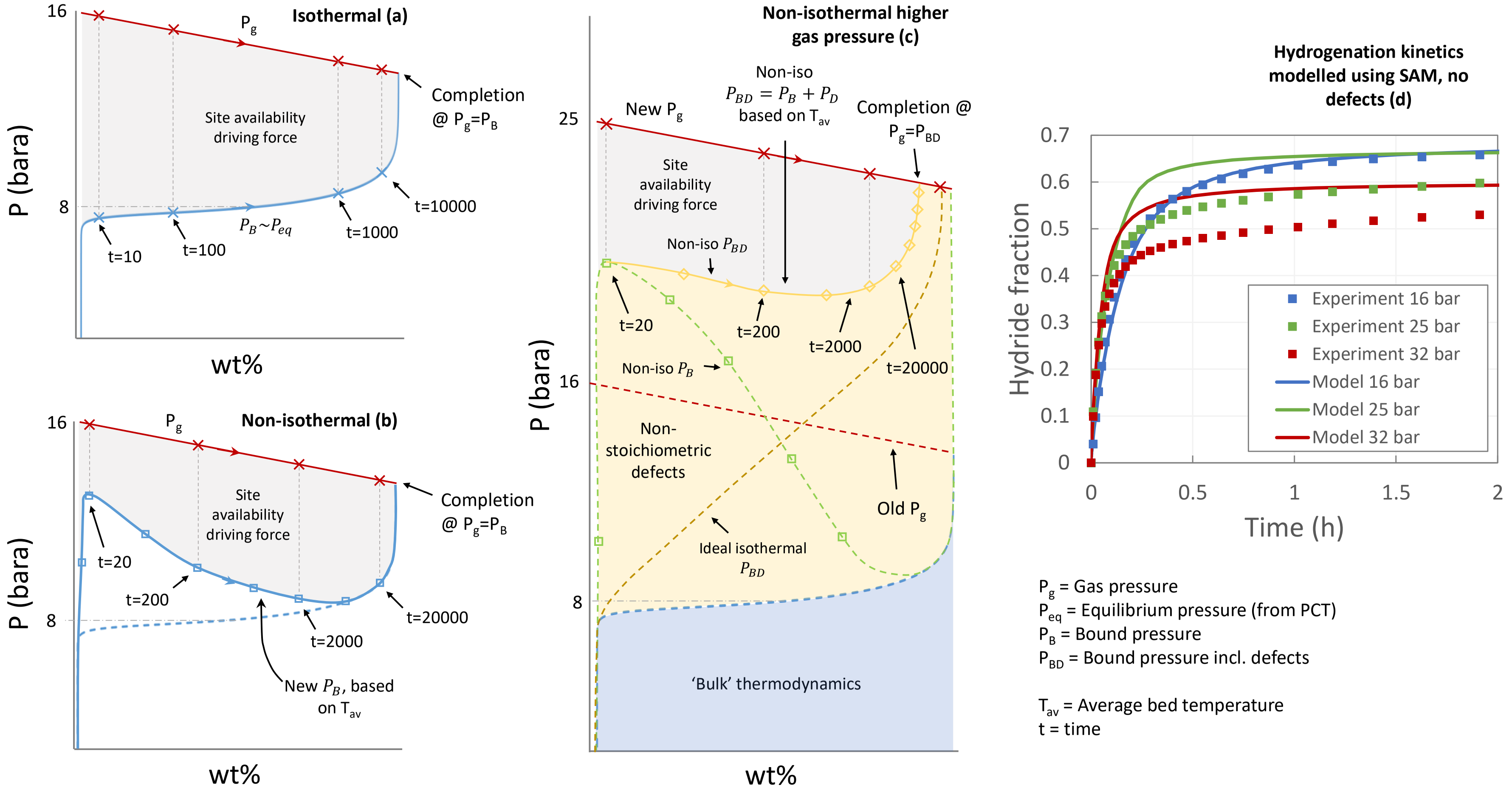

Figure 4.8: (a) General hydrogenation reaction under isothermal conditions in a Sievert's apparatus. (b) The proposed difference when reacting in non-isothermal conditions at close to equilibrium gas pressure. (c) The addition of defects with an increase in gas pressure during hydrogenation. (d) Hydrogenation kinetics of magnesium spheres (26 μ m) using a Sievert's apparatus and modelled using the (original) SAM rate law

One conclusion from this is that when $\delta = 0$, the intrinsic defects in the crystal structure (I_D) correspond to the stoichiometric composition. Following through the same deviation as outlined by Libowitz in [45], if equations 4.35 and 4.36 are substituted into 4.37,

$$K_1\, P_{eq} - \delta\, P_{eq}^{\frac{1}{2}} - K_2 = 0 \tag{4.38}$$

And solved via the quadratic formula gives,

$$P_{eq}^{\frac{1}{2}} = \frac{\delta \pm \sqrt{\delta^2 + 4K_1\, K_2}}{2K_1} \tag{4.39}$$

At the stoichiometric composition ($\delta = 0$) so,

$$K_1\, P_0^{\frac{1}{2}} = K_2\, P_0^{-\frac{1}{2}} \quad \therefore \quad P_0 = \frac{K_2}{K_1} \tag{4.40}$$

Likewise, the intrinsic disorder of a crystal I_D is defined as,

$$I_D \equiv x_{H_i'} \equiv x_{v_H^{\cdot}} \quad \therefore \quad I_D^2 = K_1 P_0^{\frac{1}{2}}\, K_2 P_0^{-\frac{1}{2}} = K_1 K_2 \tag{4.41}$$

And substituting I_D into equation 4.39, squaring and then dividing by P_0 results in the following,

$$\frac{P_{eq}}{P_0\,(\delta = 0)} = 1 + \frac{\delta^2 \pm \delta\sqrt{\delta^2 + 4\, I_D^2}}{2\, I_D^2} \tag{4.42}$$

The result of equation 4.42 is shown in figure 4.9. As the quadratic provides two solutions, it is for a theoretical hydride of composition $MH_{1\pm\delta}$, with the purple curve illustrating $MH_{1-\delta}$, for example. Turning attention to the positive solutions, the fraction of intrinsic defects heavily influences the pressure ratio for a given deviation from stoichiometry. Further, as the number of defects is minimised as the temperature approaches absolute zero, the intrinsic disorder is a function of temperature.

Primary defects such as Frenkel defects will maintain stoichiometric ratio as the concentration of cation **M** and anion **H** are effectively unchanged. To exhibit non-stoichiometry, while also main-

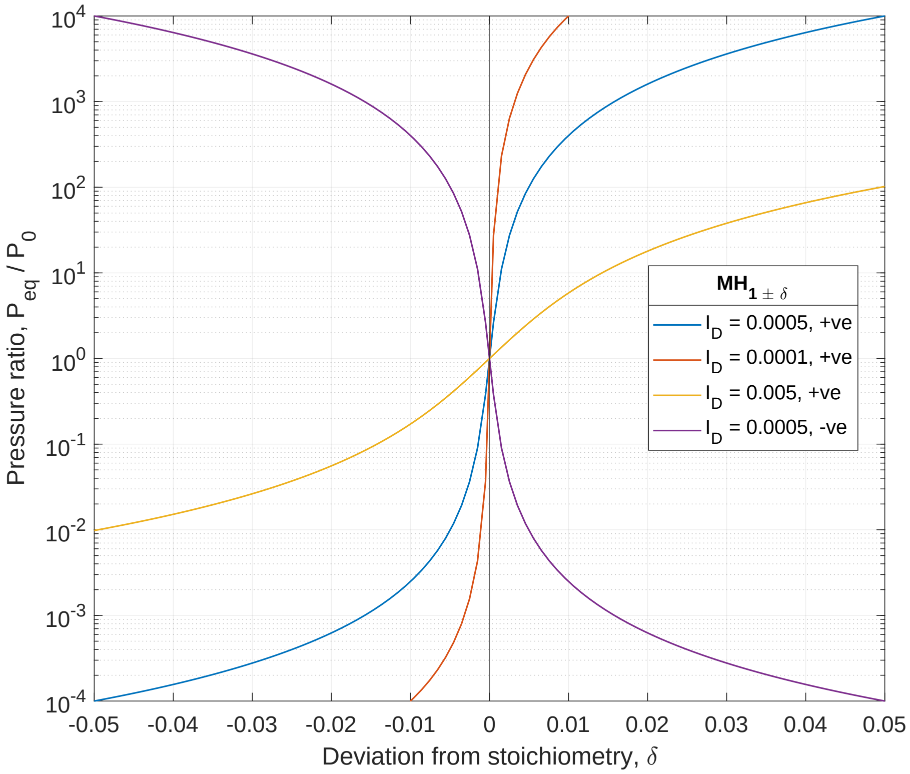

Figure 4.9: The theoretical relationship between the equilibrium pressure and small deviations from stoichiometry calculated from equation 4.42. "+ve" is the solution of the quadratic when $\pm = +$ and visa versa for the "-ve" solution.

taining charge balance, secondary defects occur. For a hydrogenation reaction, K_1 will dominate over K_2. This would either create a metal deficiency, or an anion excess. To balance an anion excess for example, the cation vacancies could contribute electrons to the conduction band. [90]

Expanding on Libowitz's work, if Frenkel defects are assumed dominant, the deviation from stoichiometry can be estimated by,

$$\delta = x_{H_i'} - x_{v_H^{\cdot}} \approx x_{H_i'} = K_1 \, P_{eq}^{\frac{1}{2}} \tag{4.43}$$

If this equation is squared,

$$P_{eq} = \frac{\delta^2}{K_1^2} \tag{4.44}$$

Rearrange and dividing by $P_0 = K_2/K_1$

$$\frac{P_{eq}}{P_0} = \frac{\delta^2}{K_1 K_2} = \left(\frac{\delta}{I_D(T)}\right)^2 \tag{4.45}$$

This expression implies that a large pressure ratio will result from a small degree of intrinsic disorder even with a very small deviation from stoichiometry. Returning to equation 4.35,

$$[\mathbf{H}_i'] = K_1 {P_{eq}}^{\frac{1}{2}} \tag{4.46}$$

and inserting the Gibbs energy gives,

$$\begin{aligned}
[\mathbf{H}_i'] &= exp\left(-\frac{\Delta G_1}{RT}\right) P_{eq}^{\frac{1}{2}} \\
&= exp\left(\frac{\Delta S_1}{RT}\right) exp\left(-\frac{\Delta H_1}{RT}\right) P_{eq}^{\frac{1}{2}} \\
&= A_1 exp\left(-\frac{\Delta H_1}{RT}\right) P_{eq}^{\frac{1}{2}}
\end{aligned} \tag{4.47}$$

Where ΔS_1 and ΔH_1 are the entropy and enthalpy of hydrogen interstitial formation. Equation 4.47 states that at high hydrogen (equilibrium) pressures and a given temperature, this will correspond to the concentration of hydrogen interstitials. Thus, under hydrogenating conditions $\delta \approx x_{H_i'}$, the deviation from stoichiometry can be approximated by,

$$\delta \approx A_1 exp\left(-\frac{\Delta H_1}{RT}\right) P_g^{\frac{1}{2}} \tag{4.48}$$

This states that at under hydrogenation conditions at a given local gas pressure and temperature, there will be defects corresponding to δ providing there is a formation enthalpy corresponding to ΔH_1 ($\delta \propto {P_{eq}}^{\frac{1}{2}}$). It is also assumed that at each time step, the defect reaction is at dynamic equilibrium at that given temperature and pressure ($P_{eq} = P_g$), resulting in non-stoichiometry forming. As the non-stoichiometry would increase alongside the reaction front, which is 'observed' via the normalised hydride fraction (θ), and if it is assumed the rate of accumulation of defects, $d\delta/dt$, is zero order with respect to θ ($d\delta/dt \propto k$), and equation 4.48 is integrated from 0 to δ and 0 and θ,

$$\delta = A_D \, P_g^{\frac{1}{2}} exp\left(-\frac{\Delta H_D}{RT}\right)\theta = k_D \theta \tag{4.49}$$

With subscript "D" referring to defect. If it is further assumed that P_0 is at 1 bar, then the defect pressure (P_D) can be calculated by substituting equation 4.49 into 4.45 which gives,

$$P_D = \left(\frac{k_D\theta}{I_D}\right)^2 \tag{4.50}$$

As the formation of defects would be an addition to the bound pressure of the bulk material, the bound pressure including defects (P_{BD}) can be determined by,

$$P_{BD} = P_B + P_D \tag{4.51}$$

And inserting the equation for both the bound pressure and defect pressure gives,

$$P_{BD} = P_N\left(1 - \frac{1}{y_1} ln\left(\frac{1-\theta}{\theta}\right)\right) + \left(\frac{k_D\theta}{I_D}\right)^2 \tag{4.52}$$

Where to recap the site availability is the ratio of available sites to ones that are unavailable,

$$\sigma_s = \frac{P_g - P_{BD}}{P_{BD}} \tag{4.53}$$

In effect, the addition of non-stoichiometry during hydrogenation imposes a defect pressure onto the system further suppressing the site availability driving force, thus reducing the reaction rate. In all, the rate equation is essentially unchanged except with the modification in how the site availability is calculated.

For completeness, the formation of defects must be endothermic as it must remove energy from the system to create the defect. Returning back to the original Frenkel defect equation,

$$\mathbf{H}_H^x + \mathbf{v}_i^x \rightleftharpoons \mathbf{H}_i' + \mathbf{v}_H^{\cdot} \tag{4.54}$$

the equilibrium constant for this reaction and subsequent enthalpy of formation of a Frenkel defect are as follows. It is assumed that there are small defect concentrations so $[\mathbf{H}_H^x] = [\mathbf{v}_i^x] = 1$.

$$K_F = \frac{[\mathbf{H}_i'][\mathbf{v}_H^{\cdot}]}{[\mathbf{H}_H^x][\mathbf{v}_i^x]} \quad \therefore \quad K_F = [\mathbf{H}_i'][\mathbf{v}_H^{\cdot}] \tag{4.55}$$

$$[\mathbf{H}_i'] = [\mathbf{v}_H^{\cdot}] = K_F^{\frac{1}{2}} = exp\left(\frac{\Delta_F S_F}{2R}\right) exp\left(-\frac{\Delta_F H_F}{2RT}\right) \tag{4.56}$$

Applying this into the energy balance would result in $Q = -Q_R + Q_D$ where Q_R is the heat generated from the reaction and Q_D is the heat sink of the defect generation. To get into units (W m^{-3}) the total defect concentration is included (C_D).

$$Q = -Q_R + Q_D = r_H(-\Delta_R H_{H_2}) + \frac{d\delta}{dt}\Delta_F H_F C_D \tag{4.57}$$

In general, the energy taken to create the defect should be much smaller than the reaction enthalpy, and can be ignored in the calulations.

4.3.8 Relaxation pressure (SAM:DR)

The concept of relaxation pressure has been developed to complement the defect pressure, where it was created by working backwards from analysing the reaction profile trends at high over-pressures and high temperatures. A discussion on the significance of this potential "reliefing" pressure is shown in section 4.6.4.4. At first, it is assumed that the hydride undergoes some change during the phase transition from $\alpha + \beta$ to β. It is assumed to follow a sigmoid shape, with this dummy variable ζ being a f(θ) (θ = normalised hydride fraction),

$$f(\zeta) = \frac{1}{1 + exp(-\theta)} \tag{4.58}$$

If it is further assumed that the resulting pressure (called the relaxation pressure $[P_R]$) is proportional to the dummy variable then,

$$P_R = k\frac{1}{1 + exp(-\theta)} \tag{4.59}$$

Using a logistic function, the sigmoid function can be manipulated to suit the needs of the user. This is similar to how the equation for the bound pressure (P_B) was developed. Following the procedure below,

1. Define the mid-point of the S curve as θ_{mid}, i.e. the middle point of the phase transition
2. Normalise the curve through $\frac{(\theta - \theta_{mid})}{\theta_{mid}}$
3. Insert a growth parameter of the S curve through y_3. To simplify, it is assumed constant.
4. And note the final pressure of P_R as $P_{R_{final}}$ then,

$$P_R = \frac{P_{R_{final}}}{1 + exp\left(-y_3 \frac{(\theta - \theta_{mid})}{\theta_{mid}}\right)}$$

If it is assumed that the final pressure term, $P_{R_{final}}$, is dictated by some energy term, which follows an Arrhenius type expression and the same pressure dependency as the defect pressure, i.e. ${P_g}^{0.5}$, then P_R can be written as,

$$P_R = \frac{A_R exp\left(\frac{-E_R}{RT}\right) {P_g}^{0.5}}{1 + exp\left(-y_3 \frac{(\theta - \theta_{mid})}{\theta_{mid}}\right)}$$

To incorporate P_R into the SAM model, the relaxation pressure will be opposing the defect pressure, so the total pressure (P_{BD}) $=$ Equilibrium/bound pressure (P_{eq}/P_B) $+$ Defect pressure (P_D) - Relaxation pressure (P_R).

$$P_{BD} = P_B + P_D - P_R \tag{4.60}$$

The outcomes of including P_D and P_R are shown in figure 4.10. One can see that when P_{R_1} is included in the model, then the isothermal P_{BD_1} curve exhibits a sloping plateau followed by a secondary plateau at high normalised hydride fractions (θ). This “secondary plateau” alters the shape of the uptake curve to display a linear profile at high hydride fractions. If P_R is more sensitive to temperature than P_D, then at higher temperatures the relaxation pressure starts to dominate and the secondary plateau transitions to a dip as shown by profile P_{BD_2} in figure 4.10. This extends the linear uptake profile at high hydride fractions, and also implies higher uptake capacities are reached (relative to P_{BD_1}).

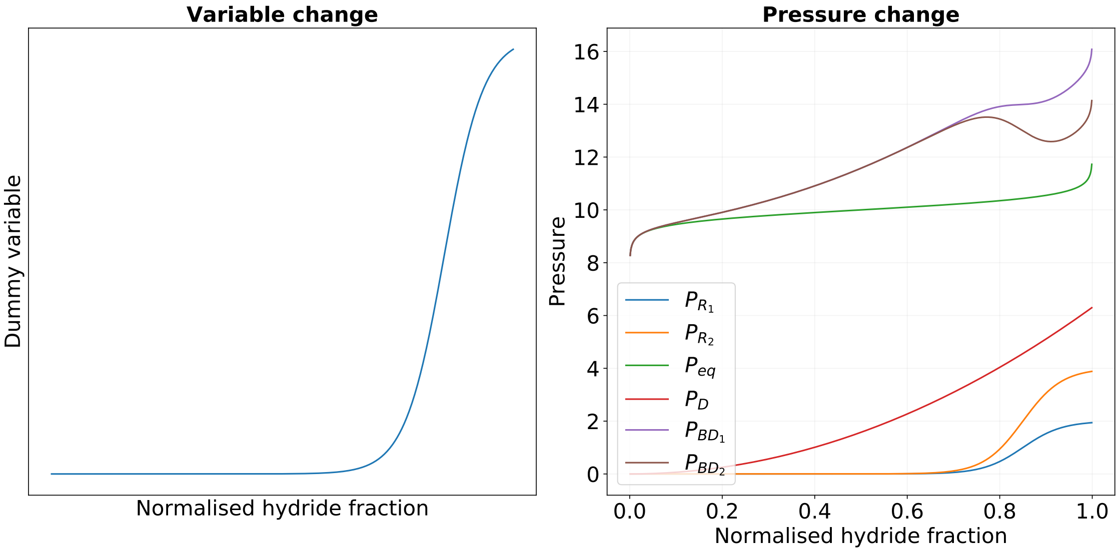

Figure 4.10: (Left) Assumed dummy variable change with normalised hydride fraction. (Right) Resultant changes in the pressure terms with normalised hydride fraction. Shown are P_{BD} with P_D and low P_R (P_{R_1}) and high P_R (P_{R2}).

4.4 Other extensions

4.4.1 Including an encasing shell (SAM:ES)

The derivation of the SAM-"encasing shell" (SAM:ES) rate equation is similar in approach to adding resistance in series, such that the concept of resistance in series is adopted, but an encasing shell is also included, in which dissociated hydrogen diffuses through solid hydride. It is assumed the action to dissociate hydrogen at the hydride surface in comparison to the diffusion step, is negligible to the reaction rate.

An illustration of the reaction progression is shown in figure 4.11, where the gaseous reactant (H_2) starts (at $t = 0$) with a bulk concentration of C_{A_0} and full unreacted identical spherical particles of constant radius R_0. Over time, the reacting core depletes producing a product which is assumed to be divided into two distinct layers, an encasing shell and porous layer.

Again, the rate equation is based on the gas that participates in the reaction, where the moles of gas reduces across the radius of the sphere due to the resistances in series. This implies that each section has a resistance effect, influencing the reaction rate and thus there is not a single rate determining step.

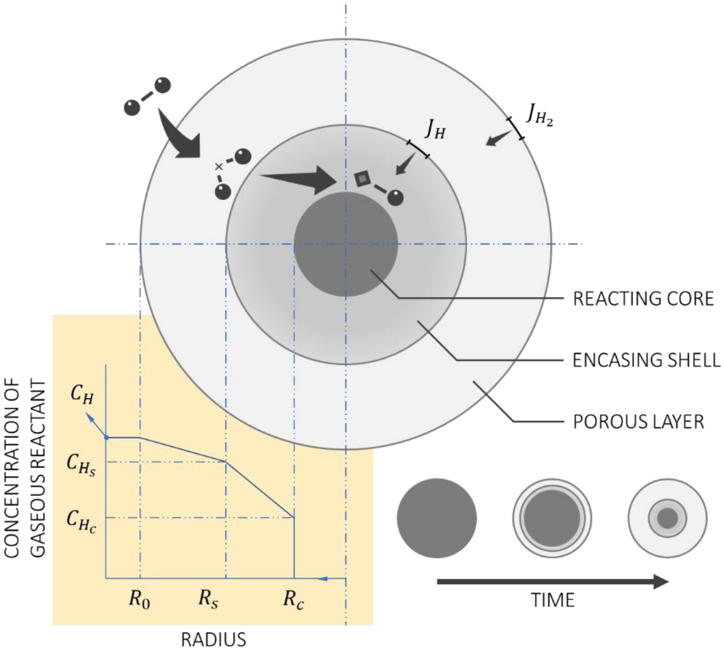

Figure 4.11: Shrinking core representation with addition of the encasing shell. J = flux, C = concentration, R = radius.

The derivation involves focusing on each section individually. For the porous layer, the moles of gas disappearing over time is related to the molar flux of H_2 through the surface area of that section:

$$-\frac{dN_{H_2}}{dt} = 4\pi R^2 J_{H_2} = 4\pi R^2 D_{k_e} \frac{dC_{H_2}}{dR} \tag{4.61}$$

The molar flux is represented by Fick's first law, where J_{H_2} and $\frac{dC_{H_2}}{dR}$ are positive (both C and R are reducing). D_{k_e} is the effective Knudsen diffusion coefficient. Applying $dC_{H_2} = 0.5\, dC_H$ and integrating from R_0 to R_s (applying the pseudo steady state approximation),

$$D_{k_e} \int_{C_H}^{C_{H_s}} dC_H = -\frac{dN_H}{dt} \cdot \frac{1}{4\pi} \int_{R_0}^{R_s} \frac{dR}{R^2} \tag{4.62}$$

Rearranging gives,

$$C_{H_s} = \frac{dN_H}{dt} \cdot \frac{1}{4\pi D_{k_e}} \left(\frac{1}{R_s} - \frac{1}{R_0} \right) + C_H \tag{4.63}$$

The **encasing shell** is similar, except equation 4.61 is integrated from R_s to R_c and use the solid diffusion coefficient D_s,

$$D_s \int_{C_{H_s}}^{C_{H_c}} dC_H = -\frac{dN_H}{dt} \cdot \frac{1}{4\pi} \int_{R_s}^{R_c} \frac{dR}{R^2} \tag{4.64}$$

Which gives,

$$D_s(C_{H_c} - C_{H_s}) = -\frac{dN_H}{dt} \cdot \frac{1}{4\pi} \left(\frac{1}{R_s} - \frac{1}{R_c} \right) \tag{4.65}$$

For the **reaction**, the moles of gas disappearing over time is equal to the reaction kinetics at the surface based on the expansion of Langmuir, which is the foundation of the SAM.

$$-\frac{dN_H}{dt} = k'' C_{H_c} \sigma_s 4\pi R_c^2 \tag{4.66}$$

$$C_{H_c} = -\frac{1}{4\pi R_c^2 k'' \sigma_s} \frac{dN_H}{dt} \tag{4.67}$$

Substituting 4.67 & 4.65 into 4.63 and re-arranging to be in the form of effective pellet volume gives,

$$-r_H = -\frac{dN_H}{dt} \frac{RSA}{4\pi R_0^2} = \frac{C_H RSA}{\frac{R_0^2}{D_{k_e}} \left(\frac{1}{R_s} - \frac{1}{R_0} \right) + \frac{R_0^2 RSA}{R_c^2 k_e \sigma_s} + \frac{R_0^2}{D_s} \left(\frac{1}{R_c} - \frac{1}{R_s} \right)} \tag{4.68}$$

Where the RSA and R_c are defined based on a sphere.

$$RSA = \frac{3R_c^2}{R_0^3} \tag{4.69}$$

$$R_c = R_0 \left(\frac{C_H}{C_T} \right)^{\frac{1}{3}} \tag{4.70}$$

Equation 4.68 is similar to 4.24, and it is clear that if the encasing shell did not form, so $R_s = R_c$, the solid diffusion resistance term $(R_0^2)/D_s(1/R_c - 1/R_s)$ would drop out and then the rate equation would return to 4.24 as before. It is assumed that the formation of the encasing shell is essentially identical to the formation of the porous layer, which would be proportional to the shrinking core.

$$R_s = R_{0_s} \left(1 - \left(\frac{C_H}{C_T} \right)^{\frac{1}{3}} \right) \tag{4.71}$$

The final radius of the encasing shell is assumed as $R_{0_s} = 0.33 R_0$. A sensitivity analysis was performed on the ratio (in this case 1/3), where it was found that changing it (from 0.05 to 0.5) did not influence the reaction rate, as the rate was mainly dominated by the magnitude of the solid diffusion coefficient. The solid diffusion coefficient is calculated based on a typical solid diffusion relation,

$$D_s = A_{sd}\, exp \left(\frac{E_{sd}}{RT} \right) \tag{4.72}$$

Where the solid diffusion coefficient D_s is a function of temperature, A_{sd} is the solid diffusion pre-exponential factor and E_{sd} is the solid diffusion activation energy. For SAM:ES, D_0 and E_{sd} are the key regression parameters.

4.4.2 Empirically modified (SAM:EM)

This model extends the SAM model by empirically broadening the site availability assumption (labelled SAM:EM), which is positioned within the surface resistance term.

One of the conclusions of section 4.5.3 in the results details that the diffusion resistance is negligible. In effect, the surface resistance is dominating. Therefore, equation 4.77 is used for this particular model.

The focus on the rate equation is the σ_s term, where the introduction of an over-pressure induces a physical change in the product formation and/or at the metal reactant surface, which is assumed represented by a change in bound pressure P_B. This is represented by an empirical parameter "Ω", as shown in 4.73, which is a polynomial being assumed a $f(\theta)$ only (e.g. $f(\theta) = -75.702\theta^6 + 180.01\theta^5 - 153.01\theta^4 + 58.068\theta^3 - 10.011\theta^2 + 1.0421\theta + 0.8003$). This modifies the site availability driving force resulting in a reduced reaction rate. This model enables a different angle to analyse the hydrogenation and dehydrogenation reactions (therefore used as analysis purposes only), where it is used for an accurate representation of P_{BD} ($P_{BD} = \Omega P_B$).

$$-r_{A_B} = k_e \left(\frac{P_g - \Omega P_B}{\Omega P_B} \right) C_T (1-\theta)^{\frac{5}{3}} \tag{4.73}$$

To help the reader understand unique work to this thesis, as often new ideas are intermixed with previous literature, table 4.2 has been created to aid clarification.

Table 4.2: Table outlining unique work within this thesis for the hydrogenation model and previous literature used.

Category	Langmuir/Site availability	Shrinking core	PCI representation	Resistances	Defects	Relaxation	Encasing shell
Previous work	Langmuir adsorption model common model for surface systems [28]. Dimensionless pressure term used in the reaction rate [54, 64]	Shrinking core reaction mechanisms are common models for solid particle reactions. [43] Applied to metal hydride reactions [8]	Many equations for PCI exist in the literature. These have not been covered in the thesis but an example of one is shown in [33].	Applying resistances in solid particle reactions is covered in [43].	Work by Libowitz [45] details the potential of non-stoichiometric defects on metal hydrides. Book by Swalin [90] expands on this. Paper on strain [69], and book by Masel [53] on H-H interactions.	No previous literature used.	Applying resistances in solid particle reactions is covered in [43].
New to this thesis	Allocated alternative meaning to the dimensionless pressure term – Site availability. Linked to Langmuir via site theory. Added ideas such as site de-activation.	Applied shrinking core with the site availability term and expressed in effective volume form (Eq. 4.79). The resultant equation, although from the same methodology gave a better fit than the equation in the literature (Eq. A.51).	Combined a standard sigmoid curve with a dimensionless pressure term, where the van't Hoff equation is at the sigmoid centre (eq. 4.6). When a power 1/3 was included arbitrarily (eq. 4.8) it gave two growth phrases.	This thesis applied the resistances method but included site availability. It was found to be surface resistance dominating. (assume hydrogen dissociates at metal surface)	This work was expanded upon, where it was applied to the site availability concept. Resulted in the defect pressure. Figure 4.8 shows the illustration of this. Highlighted the potential link to strain and H-H interactions.	Trial and error using the SAM:EM (eq. 4.73) rate law discovered the possibility that bound defect pressure (P_{BD}) may decrease at high weight percent. Developed the idea that the phase transition may allow bonds to relax after they have been strained.	Again applied the resistances method but included a solid diffusion region (hydride) + a Knudsen diffusion region

4.5 Results and discussion [close to equilibrium]

In this section equation 4.24 is applied to data at close to equilibrium (over-pressure $=$ 1) and at initial temperatures $\leq$ 360°C. The bound pressure (P_B) is assumed close to the equilibrium pressure (P_{eq}), thus y_1 is determined from equation 4.6 based on PCI data. The resistances are then compared and analysed.

4.5.1 Isotherm modelling

The calculated polynomial for y_1 from experimental magnesium hydrogenation PCI data found in the literature (between 300-390°C) [98] and used within COMSOL simulations is shown in equation 4.74. The paper calculated a ΔH $=$ -76.07 kJ mol^{-1} ± 1.21 and a ΔS $=$ -137.89 J K^{-1} ± 1.97. The values of ΔH and ΔS calculated by these authors are comparable to others [49, 89]. This equation sufficiently represents the plateau and β phase but does not include the α phase. This is because the total α-phase reaction time was less than 10 seconds, and thus could be omitted. The PCI, where y_1 was regressed using data at 300°C, was assumed not to be a function of temperature.

$$y_1 = -245.09\theta^4 + 310.95\theta^3 - 123.74\theta^2 - 12.268\theta + 73.943 \tag{4.74}$$

The depiction of y_1 with θ is shown in figure 4.12d, and the resultant calculation for P_{eq} from equation 4.6 is shown in figure 4.12c.

4.5.2 Kinetics

Using the equations outlined in previous sections, enabled the calculation of the hydride fraction as the reaction progressed, shown in Figure 4.12. The gas pressure experimental data was directly used within the rate equation. The calculated effective activation energy (E_e $=$ 172 kJ mol^{-1}, A_e $=$ 4.5×10^{11} s^{-1}) was within the error of one standard deviation to the values determined by DSC dehydrogenation under argon via Kissinger plots of the same magnesium batch (169± 9 kJ mol^{-1} and A $=$ 4.5 ×10^{11} s^{-1} (lower limit -1.8×10^{11} s^{-1} and upper limit +6.8×10^{11} [62]).

The experimentally determined value of E_e was used as the initial value. Then A_e was kept constant with E_e as a regression parameter within the COMSOL simulation. The reaction at 360°C has progressed further compared to 330°C and 345°C (of which no reaction reached completion) and results indicate that lower temperatures result in higher capacities at conditions close to equilibrium.

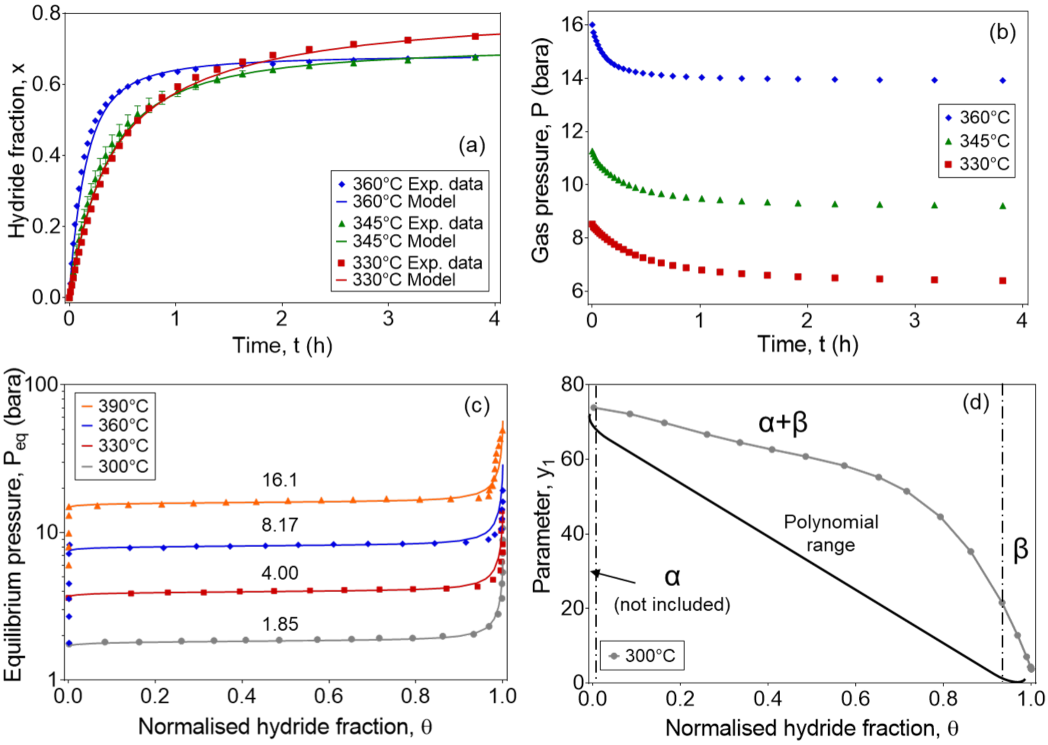

Figure 4.12: (a) Model results versus experimental uptake and initial pressure data at 1 overpressure. Averaged results of triplicates. (b) Experimental gas pressure data. (c) Equilibrium pressure fits of magnesium PCT's [98], (d) Regressed parameter y_1 @ 300°C

4.5.3 Diffusion and surface resistance

Equation 4.24 enables the resistances to be plotted independently. In the first case, the diffusion resistance is assumed to have a product layer porosity of 0.3 (expansion by 30%) with an assumed pore radius of 1 nm (figure 4.13a and b). In case two, the diffusion resistance is maximised by minimising the porosity and pore radius. Here, it is assumed a practical minimum of porosity = 0.1 and the pore radius = 0.5 nm (figure 4.13c and d) (2x the diameter of 1 hydrogen molecule) to give a maximum Knudsen diffusion of 10^{-8} m^2 s^{-1}. From Figure 4.13, the diffusion resistance does not exceed 8000 s m^{-1} for when the effective diffusion coefficient is maximised.

In comparison, the surface reaction resistance is in the order of 10^7 s m^{-1}. In effect, a small diffusion resistance implies that hydrogen diffusing through the hydride has little effect on limiting the kinetics, if based on Knudsen diffusion. However, one cannot eliminate the possibility that diffusion resistance becomes influential at far from equilibrium operating conditions, where the additional overpressure could change the process in how the hydride forms, minimising cracks and forming an encasing shell, i.e. no longer entirely Knudsen diffusion.

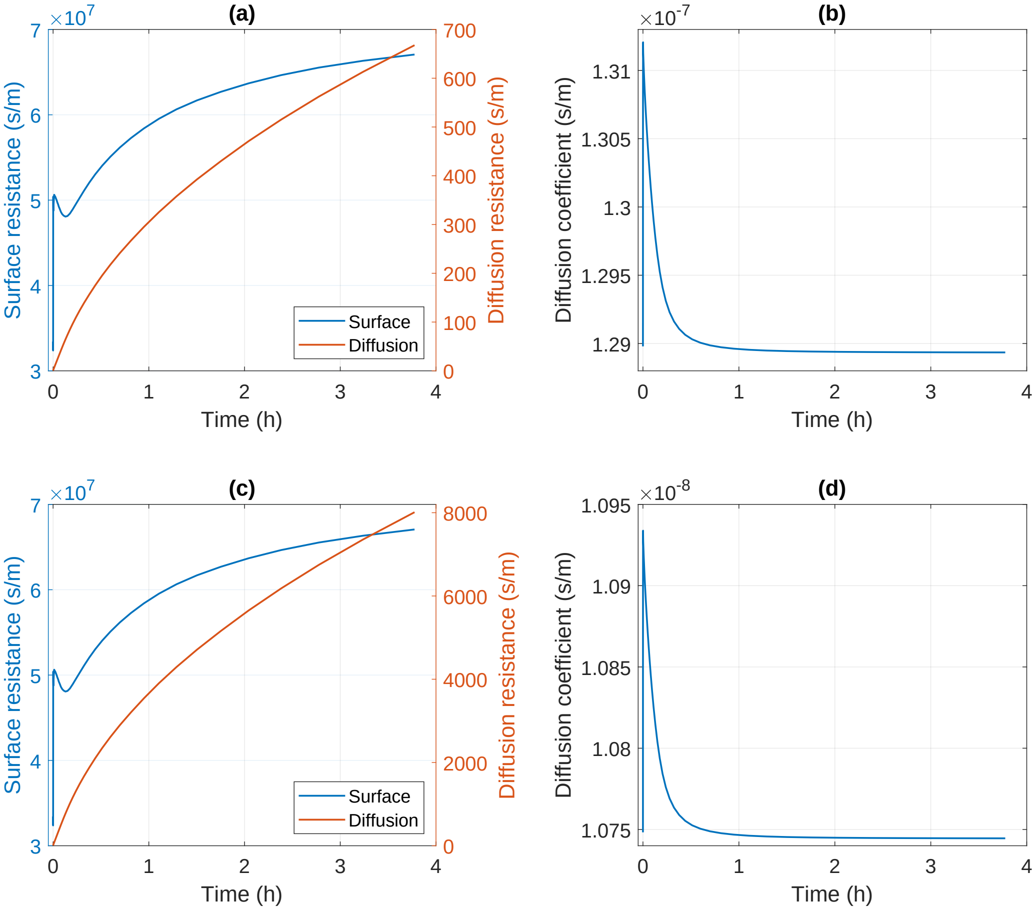

Figure 4.13: The averaged volume resistances and effective molecular diffusion coefficient. Initial conditions at 360°C & 16 bar ($\sigma_s \approx 1$) over the duration of 4 hours. (a,b) ϵ=0.3, Pore radius = 1 nm. (c,d) ϵ=0.1, Pore radius = 0.5 nm. The temporary improvement of the surface resistance is due to site re-activation.

4.5.4 Surface resistance

Consequently, if it is assumed that the diffusion resistance is negligible, equation 4.24 simplifies to equation 4.75:

$$-r_{A_B} = k_e \sigma_s C_{A_B} \left(\frac{R_c}{R_0}\right)^2 \tag{4.75}$$

If equation 4.75 is analysed at close to equilibrium conditions, the effective rate constant (k_e) dominates the reaction rate in comparison to $(R_c/R_0)^2$ and σ_s. As $k_e = k''\ RSA$ where $RSA = 3R_c^2/R_0^3$, an increase in RSA would increase k_e and thus raise the reaction rate, which is achieved by a reduction in particle size (R_0). This mathematically represents that reducing the particle size, increases the reaction rate. Further, as k_e dominates, maximising the RSA is crucial in achieving a very high reaction rate. If equation 4.75 is further simplified by substituting 4.26, this gives the result in terms of concentration only (4.76), and if expressed in terms of the normalised hydride fraction gives equation 4.77.

$$-r_{A_B} = k_e \sigma_s C_{A_B} \left(\frac{C_{A_B}}{C_T}\right)^{\frac{2}{3}} \tag{4.76}$$

$$-r_{A_B} = k_e \sigma_s C_T (1-\theta)^{\frac{5}{3}} \tag{4.77}$$

This result indicates that if there is a sufficient reduction in the RSA, feasibly a high wt% material, where the rate determining step is a reaction occurring at a surface of a sphere at conditions close to equilibrium, the reaction order is 5/3. If in contrast, the material is low wt%, where there is not a significant reduction in R_c, thus $\mathrm{R}_c/\mathrm{R}_0 \approx 1$; equation 4.75 simplifies to a first order rate equation (4.12) - similar to kinetics currently used for low wt% materials based on the work of Mayer and Groll [54] and popularised by Jemni and Nasrallah. [37] In effect, a low wt% material potentially contains a low total amount of available sites for hydrogen relative to the total surface, so the metal reactant does not shrink. In contrast, a high wt% material contains a high total amount of available sites, resulting in a shrinking metal reactant and therefore, the analysis indicates inclusion of the reacting surface is important when deriving a suitable rate equation for a high wt% material.

4.5.4.1 Integrated SAM rate law

In addition, if σ_s is assumed a constant, equation 4.76 is suitable for integration:

$$\frac{3}{2}\left(\left[\frac{C_T}{C_{A_B}}\right]^{\frac{2}{3}} - 1\right) = k_e \sigma_s t \tag{4.78}$$

And inserting $C_{A \cdot M} = C_T - C_{A_B}$ can give the integrated rate law in terms of normalised hydride fraction (θ),

$$\frac{3}{2}\left(\left[\frac{1}{1-\theta}\right]^{\frac{2}{3}} - 1\right) = k_e \sigma_s t \tag{4.79}$$

The integral method was tested using magnesium hydrogenation (at close to equilibrium) experimental data collected on a Sievert's apparatus. Using equation 4.78, the fits are reasonable (figure 4.14a) where the fitted curves R^2 values are 0.989, 1.000 and 0.987 for 360°C, 345°C and 330°C respectively. Using a value of $\sigma_s = 0.5$, the effective rate constant was determined (figure 4.14b) with a $R^2 = 0.981$ and a gradient = -14980 ±2085. This gives an effective activation energy E_e = 125 ±17 kJ mol^{-1}.

However, when calculating the reaction rate, what really matters is the accuracy of the effective rate constant (k_e). Crucially, this parameter is dependent on both the pre-exponential factor (A_e) and E_e. Thus, comparing both E_e and A_e would be more thorough. This is shown visually in 4.14d, where the value of k_e is similar for all three techniques used. In effect, even though E_e might be slightly displaced, the A_e can be tweaked to still give a reliable value of k_e for a good reaction rate representation.

This is shown in 4.14c, as E_e determined through the integral method was different by 50 kJ/mol to the DSC method (Kissinger plot), where this difference was adjusted by a change in the pre-exponential factor, resulting in a similar k_e value. The DSC measurements were of the same magnesium batch (26 μm atomised spheres from SFM - FluorsidGroup) but not the same sample, whereby the data is detailed in this paper [62]. It is noted that the activation energy determined through DSC experiments was for dehydrogenation experiments and not hydrogenation.

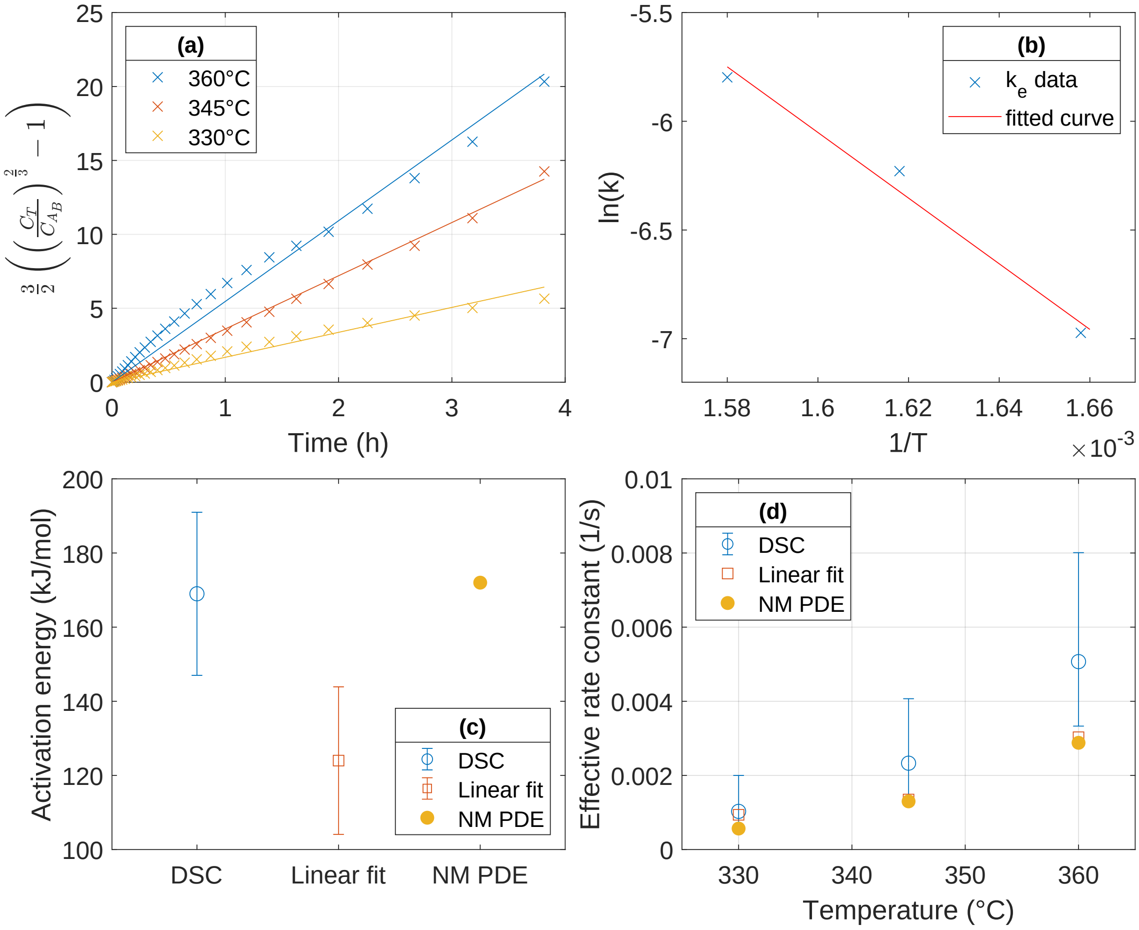

Figure 4.14: (a) Plot of equation 4.78 using Mg hydrogenation data from Sievert's experiments (b) Arrhenius plot to find the effective activation energy and pre-exponential factor (c) Variation in effective activation energy through different methods (d) Comparison of DSC, linear and NM PDE (numerical method partial differential equation) to calculating the effective rate constant

As mentioned previously, solving the differential equations using COMSOL was by assuming the same value of A_e determined through DSC, and modifying the effective activation energy. This resulted in a value of $E_e = 172$ kJ mol^{-1}, which is comparable to the effective activation energy determined through DSC measurements.

Regarding using linear least squares on an integrated rate law (noted integral method in this thesis), if including the assumption of the site availability, the accuracy of the calculated effective activation energy is dependent on the estimated value of σ_s as within equation 4.78, the gradient is $k_e\sigma_s$. Thus, a value of σ_s is required. Based on the average site availability curve, the average σ_s over the reaction was ≈ 0.5. This enabled calculation of k_e. It is important to mention that if only the integral method was used, the average site availability would need to be estimated and this would lead to an increase in error. The distribution/variance of the average site availability can be minimised by the following methods:

- Operating under isothermal conditions, thus P_B does not rise with temperature. Isothermal conditions are also essential to reliably assign a single rate constant (k) value at a given temperature, as $k(T)$.
- Operating under isobaric conditions so the gas pressure remains constant.
- Operate kinetics within the plateau of the bound pressure curve to further minimise change in P_B.

4.5.4.2 Surface resistance summary

The analysis indicates the integral method (therefore only solving the mole balance) has disadvantages when **completely** modelling H_2 hydrogenation of metals at close to equilibrium. Comparably, including an energy balance models the change in temperature (T) and therefore change in site availability (σ_s), which better represent the key changing parameters within the system.

4.5.5 Site availability

Analysing the site availability results of the 0.2 g sample, results in several key observations. To start with a general overview of σ_s, there are three key observations:

- If the initial bound pressure cannot be greater than the gas pressure, then site de-activation would limit the initial temperature spike. This indicates that with an enclosed system of exclusively hydrogen and metal, thermal runaway cannot occur even with a large inventory of hydrogen dumped on the solid reactant.
- If the temperature is linked to the bound pressure, which is related to the site availability; a rise in temperature increases site de-activation, where an improvement in heat transfer would improve site re-activation and thus increase the reaction rate.
- As the temperature spike occurs at the beginning of the reaction, site de-activation is only important initially. However, if the bed effective thermal conductivity is low, and/or with a inefficiently designed heat exchange system, site de-activation will be key.

Also, there is an apparent difference between the site availability across the domain. The wall region experiences relatively no site de-activation, where the conditions are relatively isothermal. When comparing to the middle of the domain, a significant proportion of sites become temporarily unavailable. This important observation implies that regions experiencing a higher rate of heat transfer will transition to slower phases sooner, such as the transition from $\alpha+\beta$ to β phase. Thus, one conclusion from this analysis suggests that for commercial scale reactor design, modelling localised phase transitions may be required for appropriate interpretation of the kinetics.

4.5.6 Effect of the effective thermal conductivity

Albert et al. measured the effective thermal conductivity of MgH_2 in a H_2 environment to be around 0.8 - 1.0 W m^{-1} K^{-1} depending on the temperature and pressure [3]. A parametric sweep was performed in COMSOL varying the effective thermal conductivity from 0.2 to 2 W m^{-1} K^{-1} and shown in figure 4.15. The model demonstrates the variation in the fitted curves with changing λ_e. The best fit occurs when assuming a constant λ_e of approximately 0.8 W m^{-1} K^{-1}, coinciding with the measured experimental data. At very low λ_e's, around 0.1-0.2 W m^{-1} K^{-1} the fit is fundamentally different, whereas the fitted curve trend appears to converge at higher λ_e's, from 1.6 - 2.0 W m^{-1} K^{-1}. However, this is for a 0.2 g magnesium sample in an approximately 3 mm radius cylinder. This is confirmed when considering that conductive resistance in one dimension is,

$$\text{Conductive resistance} = \frac{\Delta L}{\lambda} \tag{4.80}$$

then with ΔL (distance) = 3 mm, the conductive resistance becomes small at $\approx$ 2 W m^{-1} K^{-1}. If the conductive resistance is 0.0019 m^2 K^1 W (at bed effective thermal conductivity = 1.6 W m^{-1} K^{-1} @ 3 mm radius); considered the minimum for heat transfer to not hinder the reaction rate (for Mg 26 μm), then the same resistance at 20 mm radius needs an effective thermal conductivity of 10 W m^{-1} K^{-1} as illustrated in figure 4.15b, if the heat conduction is only/dominated in one dimension.

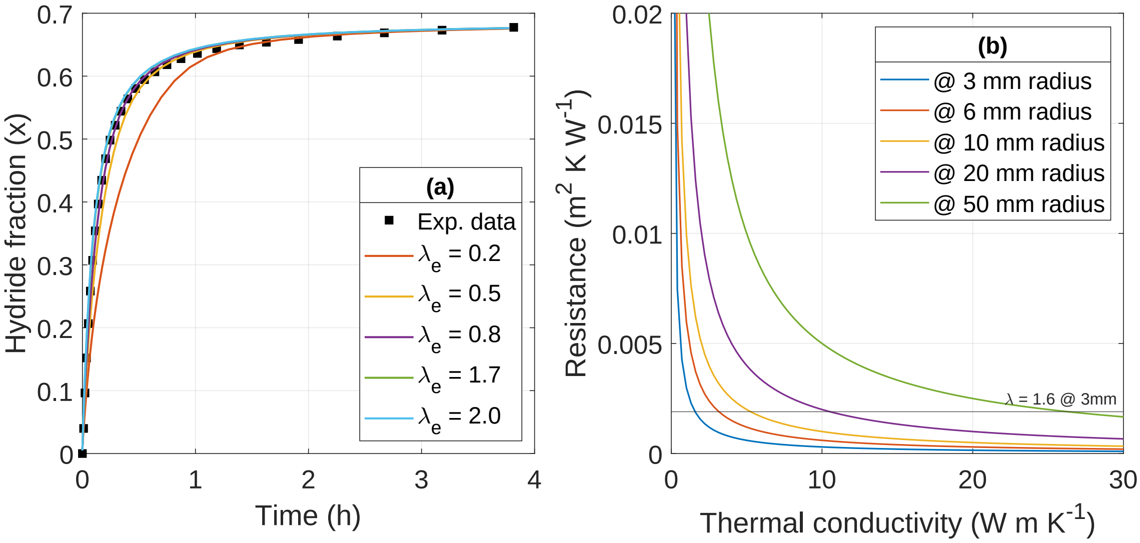

Figure 4.15: Parameter sweep modelled experimental data (conditions: 360°C 16 bar initial pressure) using different values of effective thermal conductivity.

4.6 Results and discussion [further from equilibrium]

4.6.1 Applying the original SAM (SAM) rate law

To further demonstrate that the SAM model (without extensions, i.e. non-stoichiometric defects or other mechanisms) loses significance at higher temperature and pressures, the SAM integrated rate equation $\frac{3}{2}\left(\frac{1}{1-\theta}\right)^{\frac{2}{3}}-1)=kt$ was applied to 330°C and 360°C at 1,2,3 and 4 over-pressures, and at 380°C & 400°C at 1 over-pressure as shown in figure 4.16. One can observe that the threshold appears to be around 360°C, where above 1 over-pressure, the trend is no longer linear. It is noted that for the fit to be reasonable, a R^2 value of approximately 0.985 is required. Further, at 330°C, an increase in pressure gives an increase in k, whereas at 360°C, an increase in pressure reduces k and the fit decreases. This gives evidence that the SAM model in the current form breaks down beyond 360°C and at higher pressures. It also demonstrates that there might be an 'over-temperature' alongside an over-pressure, whereby the increase in T and P are forcing a change in the kinetics. Unfortunately, not much else can be determined from the integral method. Therefore, the Finite Element Method is adopted using COMSOL, where sensitivities studies were performed on certain variables to understand their impact, or to fit to experimental data; incorporating theory of non-stoichiometric defects and other mechanisms.

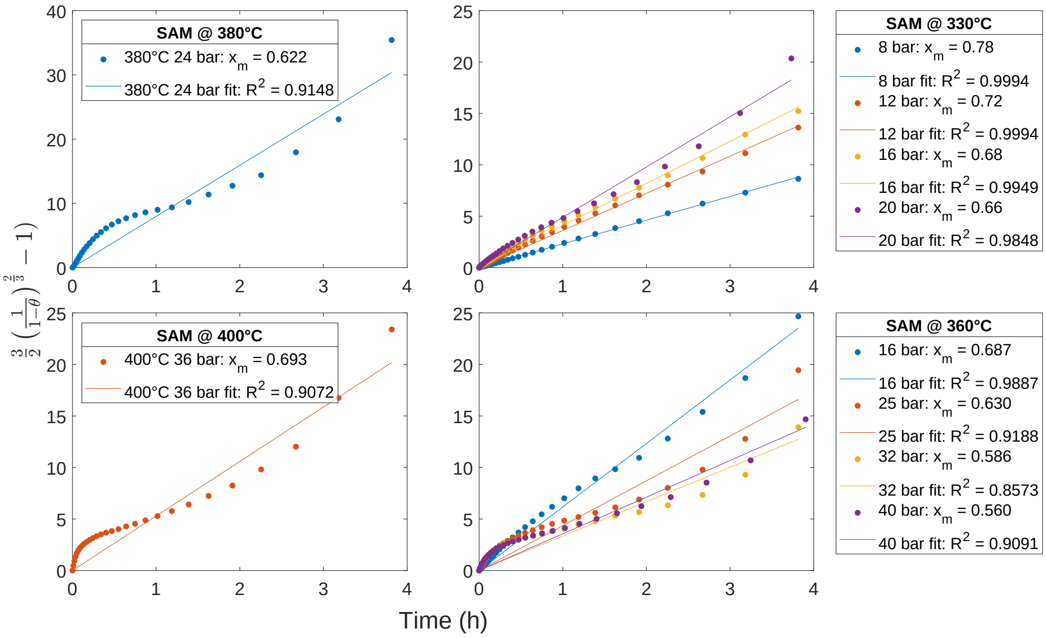

Figure 4.16: Use of the SAM integrated rate law for all hydrogenation conditions tested.

4.6.2 Applying other SAM extensions: 'Encasing Shell' (SAM:ES), 'Defects + Encasing Shell' (SAM:D+ES) and 'Empirically Modified' (SAM:EM)

4.6.2.1 Encasing shell extensions: SAM:ES and SAM:D+ES

One noticeable characteristic of magnesium hydrogenation at far from equilibrium is a linear uptake profile at high weight percent, as mentioned when the experimental data was examined at the start of this chapter. To try and represent this linear profile at high hydride fractions, the SAM:ES model was tested first (figure 4.17a & 4.17b). Here, both the surface and diffusion resistance are within 10^7, where the reaction profile is too slow initially (up to hydride fraction, $x = 0.57$) and then too fast from $x = 0.57$ to 0.61 (linear profile). When combining the defects and encasing shells into a single model, SAM:D+ES (figure 4.17c & 4.17d), the reaction profile again is too slow initially (up to $x = 0.57$) with an improved fit through $x = 0.57$ to 0.61. However, the linear uptake profile at high weight percents has not been achieved.

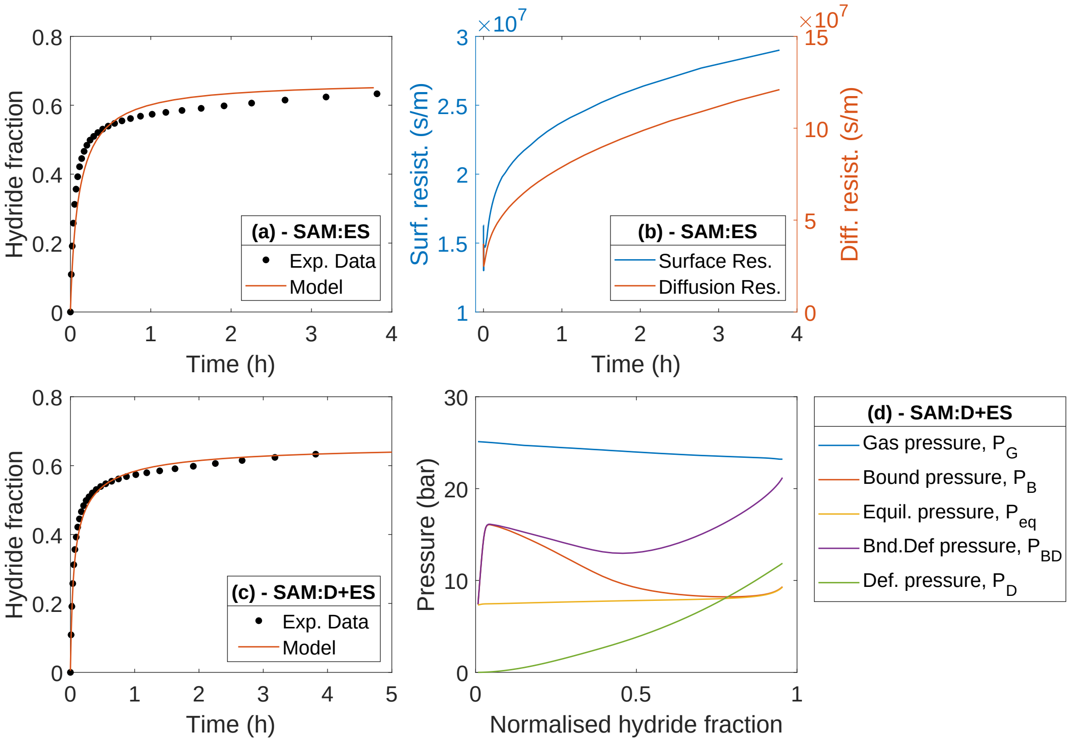

Figure 4.17: Models at initial conditions 360°C and 25 bar. (a) SAM:ES uptake profile (b) Surface & diffusion resistance profiles (c) SAM:D+ES uptake profile (d) SAM:D+ES pressure curves.

4.6.2.2 Empirically modified extension (SAM:EM)

The SAM:EM extension was then developed to try and improve the linear profile at high hydride fractions. It was found that the only way to achieve this shape, through the confines of the Site Availability Model, was by altering the isothermal bound pressure (P_B) curve such that a secondary plateau occurred at high hydride fractions for many of the conditions tested. It was also found that if the secondary plateau was transitioned to a 'hump' or a 'dip' ($\diamondsuit_1$ and $\diamondsuit_2$), the linear profile at high hydride fractions lengthened. Shown in figure 4.18 are the results of the SAM:EM extension at 360°C and 25/40 bar. The results of this observation led to the development of the 'relaxation' concept shown in the next section.

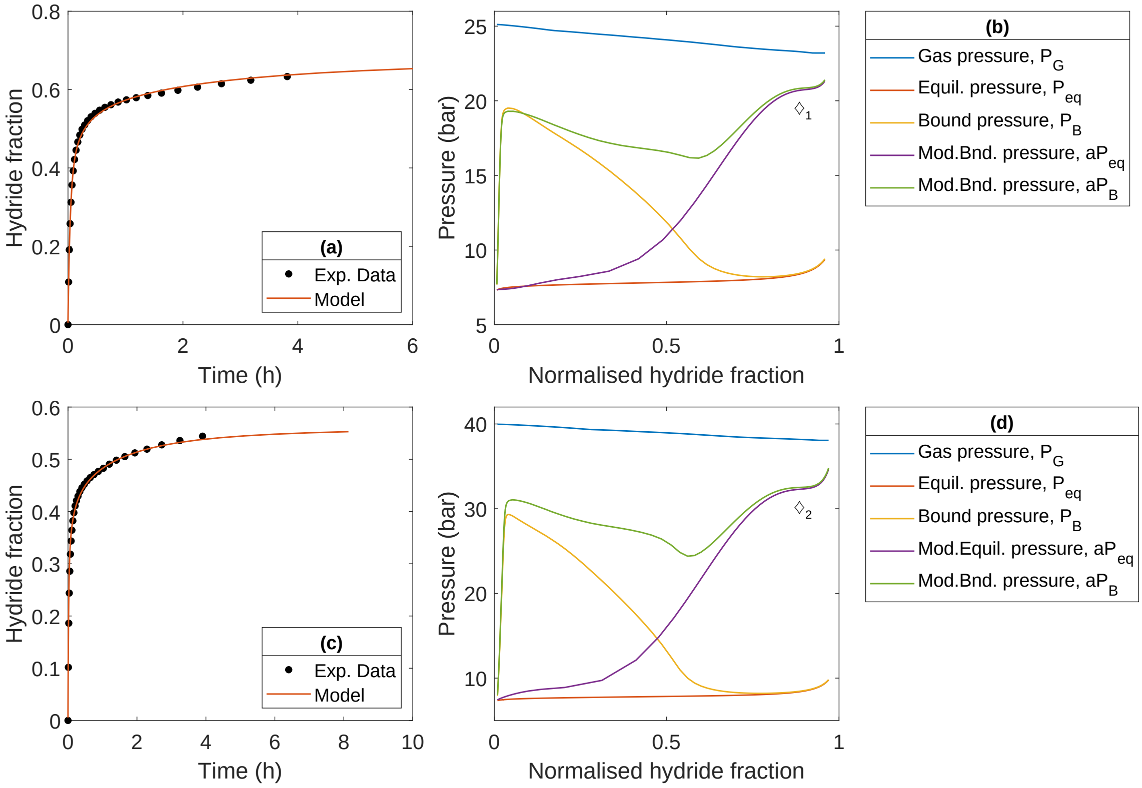

Figure 4.18: (a) and (b) SAM:EM extension applied to 360°C and 25 bar, showing uptake profiles and pressure curves. (c) and (d) SAM:EM extension applied to 360°C and 40 bar

4.6.3 Applying the SAM:Defects-Relax (SAM:DR) rate law

4.6.3.1 Assumptions of SAM:DR

To apply the SAM:DR model, some assumptions were made, due to key experimental data being hard to obtain or unavailable. For instance, obtaining the intrinsic defects parameter (I_D) requires reaching equilibrium of a PCI during the β phase at different temperatures. This was attempted for the 26 μm sample using an automated Sievert's apparatus. This sample was very slow (up to 1-1.5 months for one PCI) and on every experiment, the capacity reached above the theoretical maximum of 7.66 wt%. After trying to find fixes, and not happy with the results, it was decided not to pursue a experimental value of I_D further. Table 4.3 shows the values used for the SAM:DR model.

Table 4.3: Parameters used for each operating condition for the SAM:DR model. E_R and A_R are unit-less as the equation is empirical. y_1 (within equation 4.6) for Mg-MgH$_2$ was taken from the previous work on this model [1]

Temp. (°C)	**360**				**380**	**400**
Pres. (bar)	**16**	**25**	**32**	**40**	**24**	**32**
E_e (J/mol)	172 000	172 000	172 000	172 000	172 000	172 000
A_e (1/s)	$4.5\text{x}10^{11}$	$4.5\text{x}10^{11}$	$4.5\text{x}10^{11}$	$4.5\text{x}10^{11}$	$4.5\text{x}10^{11}$	$4.5\text{x}10^{11}$
x_m	0.91	0.67	0.58	0.57	0.62	0.71
ΔH_D (J/mol)	1730	1730	1730	1730	1730	1730
A_D (bar$^{-0.5}$)	0.001	0.001	0.001	0.001	0.001	0.001
I_D	0.0008	0.0008	0.0008	0.0008	0.00084	0.0009
E_R	34000	34000	34000	34000	34000	34000
A_R	886	886	886	886	886	886
θ_{mid}	0.9	0.9	0.9	0.9	0.9	0.9
y_3	20	20	20	20	20	20

E_e and A_e were taken as before from the original SAM model. They were measured through MgH$_2$ dehydrogenation measurements under Argon of the same magnesium batch but not sample. It is assumed the rate constant for dehydrogenation and hydrogenation are similar [62].

The maximum hydride fraction (x_m) for most cases was very similar to the estimated end point based on extrapolating from experimental data. The exception is at 360°C & 16 bar, which required a higher x_m value.

Grau-Crespo et al. combined ab initio calculations and statistical mechanics to determine MgH_2 can only accommodate a small concentration of hydrogen vacancies at conditions of practical interest [31]. Therefore, the intrinsic defects (I_D) was varied from 0.0008 to 0.0009 depending on the temperature. With this low assumed range of I_D, the maximum deviation in stoichiometry at the end of the reaction is 0.002 - 0.004. That is, the resultant hydride is virtually stoichiometric.

Assuming this provides more confidence with the value of I_D, then the rise in defect pressure (P_D) is largely governed by A_D and ΔH_D. Values were selected so that the change in P_D to the reaction rate was minimal at 330°C but significant at 360-400°C. The same procedure was used to determine A_R and E_R for the relaxation pressure P_R. The change from $\alpha + \beta$ to β was assumed at $\theta = 0.9$ and the growth in relaxation pressure (y_3) was set as 20 to give an ascent in relaxation pressure that influenced the site availability.

Further, it was assumed that the total concentration of defects was very small in relation to the bulk material, such that the heat removed from the system was small and thus omitted from the energy balance.

4.6.3.2 Results (SAM:DR)

The results on the SAM:DR model validated against Sievert's hydrogenation experimental data is shown in figure 4.19. There is negligible difference between the standard SAM model and SAM:DR extension at 360°C & 16 bar scenario. With the inclusion of defects, it is apparent a more effective fit is achieved at higher over-pressures and temperatures, although the SAM:DR extension is harder to model at 380°C & 400°C. In figure 4.19d, the isothermal P_{BD} curve exhibits an increasing ascent, followed by the forming of another plateau, due to the relaxation pressure P_R. This gives the P_{BD} curve (based on average bed temperature), which significantly lowers the site availability driving force than if P_B was used. This is shown in figure 4.19c, where the site availability using the SAM:DR extension is almost always less than one.

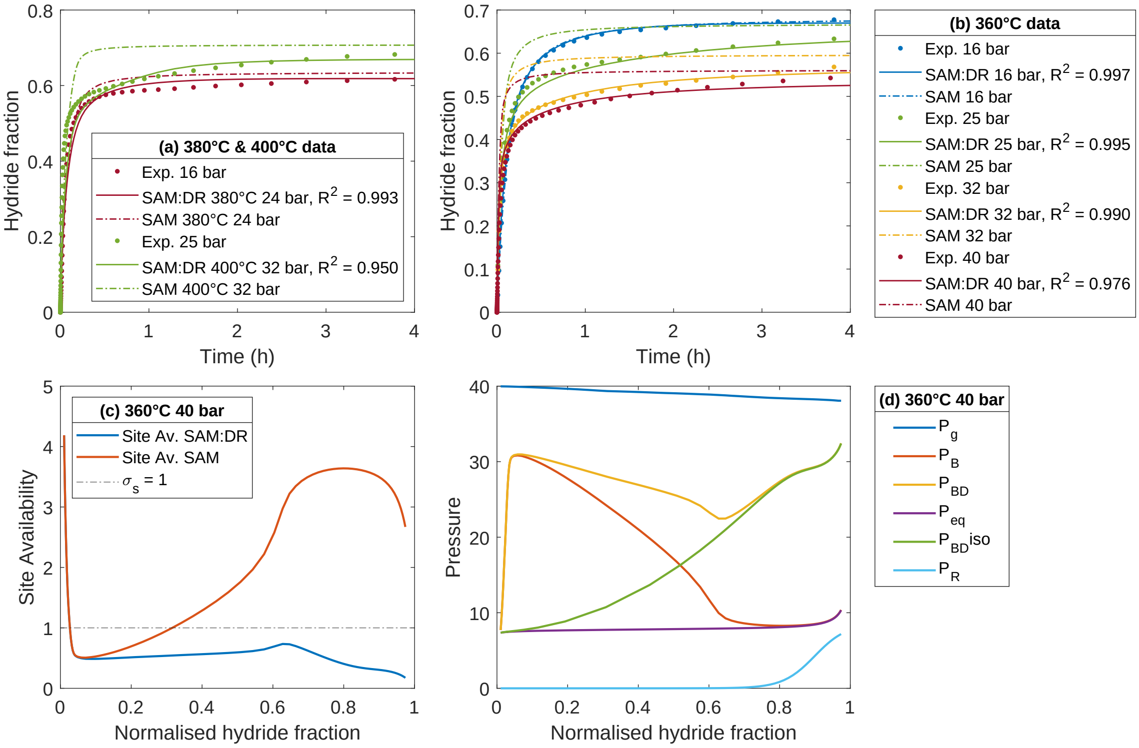

Figure 4.19: (a) Model validations for experimental data at 360°C and varying initial gas pressures. (b) Model validations at 380°C and 400°C. (c) Change in site availability by including defects and relaxation. (d) Pressure curves from model at 360°C and 40 bar initial pressure.

4.6.4 Discussion (SAM:DR)

4.6.4.1 Effect of SAM:DR model

The inclusion of the SAM:DR extension enables modelling of the linear portion of the uptake curve exhibited at high hydride fractions. The P_{BD} curve reduces the site availability driving force in comparison to the P_B curve, allowing the site availability to <1 for most of the reaction (figure 4.19), which strictly according to the site availability theory, is a requirement. σ_s is greater than 1 at the beginning due to the way the bound pressure is modelled at the α phase using equation 4.6. However, this portion is very fast so the influence on the uptake curve is negligible.

The SAM:DR extension at 380°C and 400°C is harder to fit. This may be due to two reasons. The first reason is that the intrinsic defects may be a stronger function of temperature above 380°C, so the initial temperature spike causes a greater drop in defect pressure than just assuming a constant I_D. This would then create a faster reaction rate at the beginning (up to 0.5 hours @ 380°C and 400°C). The other reason was using a manual iterative variable sensitivity analysis to find the defect+relax parameters was difficult, as such, getting a good fit at higher hydride fractions for all temperature + pressure cases was difficult to achieve.

4.6.4.2 Transferring to larger scale reactors

Including the defects + relaxation extension reduces the site availability driving force (SA-DF). The end effect of site de-activation does the same. If a large scale reactor was intentionally designed so that site de-activation dominates over the proposed defects + relaxation phenomenon, then in theory the defects + relaxation extension is not needed, as the SA-DF is dictated by site de-activation. This illustrates that from analysing the SAM:DR, for metal hydride CSP applications, some level of site de-activation could be desirable, thus chasing a super fast reaction rate may be a fallacy. In effect, the engineer would want some level of site de-activation to enable a constant bed temperature (governed by the van't Hoff equation), and also for a smoother reactor design process.

4.6.4.3 The intrinsic defects parameter

The intrinsic defects in the crystal structure (I_D) is a significant parameter when determining the magnitude of the defect pressure (P_D). When the intrinsic defects are small (nearly stoichiometric) the defect pressure is sensitive to I_D. A small change in I_D, assumed due to temperature, can influence P_D by 1-5 bar, thus considerably altering the reaction rate. This could in part explain the difficulty of magnesium hydride kinetics, due to it being virtually stoichiometric.

On the contrary, a moderate to large non-stoichoimetric alloy would exhibit a high degree of intrinsic defects, thus the resultant defect pressure is minimal. This may help to explain why defect+relax extensions have never been developed for low temperature non-stoichiometric alloys, because they were never needed.

4.6.4.4 The importance of strain

One of the ways to look at the importance of P_D and P_R is through observing hydrogen as a foreign atom entering the metal lattice (i.e. extrinsic defects). For the hydrogenation of Mg, H atoms enter into the interstitial sites of (hexagonal close packed) HCP crystal lattice and then the lattice rearranges to form the tetragonal structure of MgH_2.

The nature of this interaction is elastic (at temperatures of interest) and the lattice dilatation caused by interstitial H atoms is constant across the whole crystal, so attractive interactions are favoured. If the lattice is not free to expand upon H sorption, the interactions can become repulsive [69]. The Lattice Gas Model covered previously also described how positive/attractive interactions exhibited a flat slope (plateau), while negative/repulsive interactions caused the gradient of the slope to increase (sloping plateau). This is summarised in figure 4.20a.

Compared to the original Site Availability Model and site theory, attractive interactions correspond to a large site availability driving force. Whereas repulsive interactions reduce the driving force. Attractive interactions promote clusters of sites to be filled, i.e. the adjacent sites require less energy to fill.

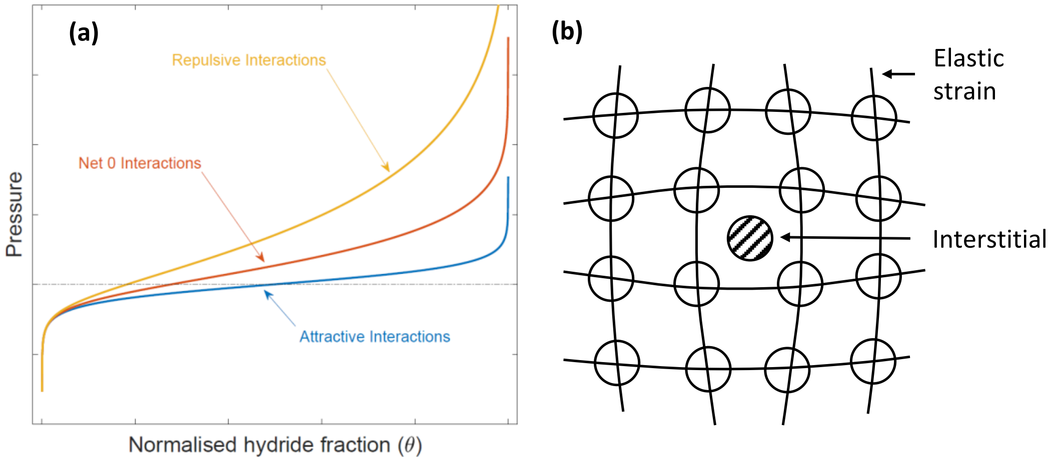

Figure 4.20: (a) Summary of the type of interactions as taken from the Lattice Gas Model. When the interaction energy is positive, the interactions are attractive, and when negative, they are repulsive. (b) Elastic strain representation of an interstitial

For Mg-MgH$_2$, equilibrium experiments at conditions of interest (330-400°C) result in a flat plateau. This indicates attractive interactions. As small aliquots are used, so that there is a small ΔP rise and therefore a small ΔT, there will be negligible site de-activation. This is shown as (1) in figure 4.21. But if a non-isothermal kinetic experiment is performed in such a way the interactions remain attractive, (approximately below 360°C and 25 bar for magnesium spheres @ 26 μm) the pressure curve $P_B \approx P_{eq}$ and the uptake curve is shown in blue in the bottom left graph of figure 4.21.

When the temperature and pressure is further increased, the H-H interactions start to become more complex and influential. The SAM:DR extension includes point defects. One of the characteristics of point defects is the localised disruption on the metal sub-lattice, where the bonds are elastically strained (as shown in figure 4.20b). The SAM:DR extension assumed Frenkel defects, however this may be a simplification. Either way, the end effect of including P_D could represent the reaction front being ‘effectively’ constrained and so repulsive interactions start to appear. As such, pressure is added to the reaction front with the resultant effect being a sloping plateau as shown by (2) in figure 4.21. Further, the end capacity is also reduced, because as the bound pressure approaches the gas pressure faster, the reaction front hits equilibrium sooner leaving un-reacted reactant leftover. This, when viewed using an electron microscope, can give the appearance of a

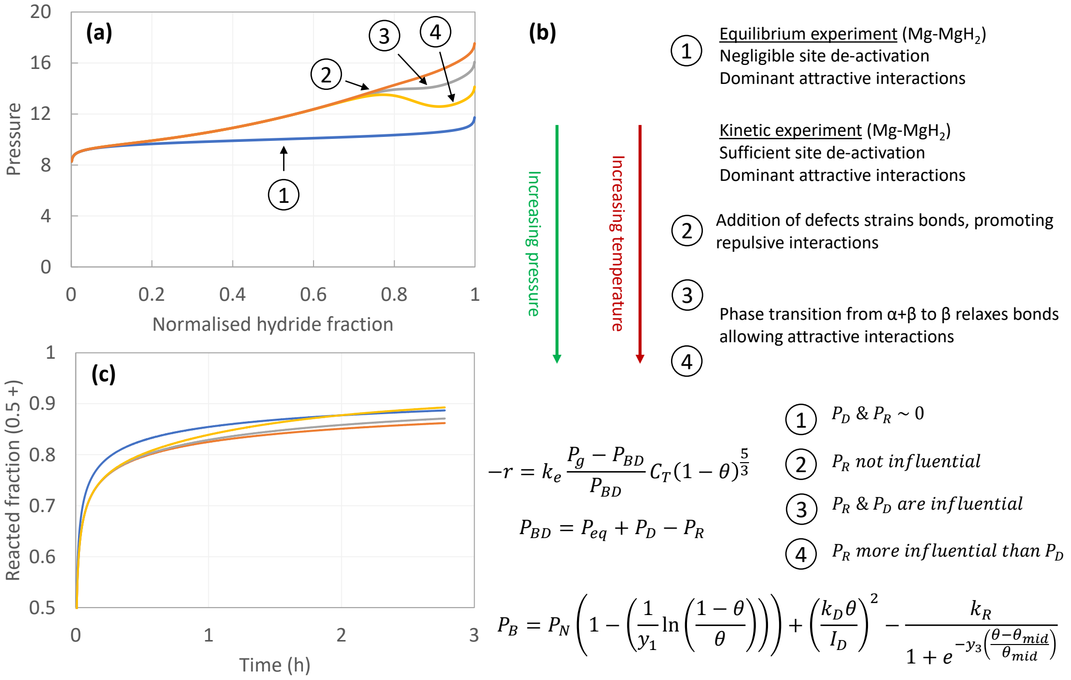

Figure 4.21: (a) Varying bound defect pressure (P_{BD}) curves considering P_D and P_R. (b) Explanations and equations outlined for each scenario. (c) The theoretical isothermal uptake curves at a fixed k_e and P_g, but varying P_D and P_R.

hydride 'crust/encasing shell', which has logically led researchers to indicate that the rate limiting factor is the diffusion length. However, as illustrated by the potential influence of strain, this could be a misconception.

Another characteristic of these bond interactions is not only can they be strained, but also relax. This is where the term relaxation pressure (P_R) comes from. It is re-iterated that this behaviour was developed empirically based on modelling a linear reacted fraction profile at high reacted fractions. The inclusion of P_R to P_D is shown by (3) and (4) in figure 4.21. It is assumed that the phase transition from $\alpha + \beta$ to β phase causes a change in the lattice structure. This change further complicates the bond interactions, in which the bonds can relax and the pressure curve is reduced at high reacted fractions, resulting in a secondary plateau. This is shown by (3) in figure 4.21, where both P_R and P_D have similar influence. If however, P_R becomes more influential than P_D, then the isothermal pressure curve dips further (4), resulting in a longer linear profile as shown by the yellow line in figure 4.21, and a higher capacity. This corresponds to our experimental data, as hydrogenation at 380°C & 24 bar resulted in a lower capacity than at 400°C & 32 bar.

The P_R and P_D driving force are assumed to be primarily governed through a temperature driving force (Arrhenius style expression). Mathematically, it is possible for k_R to be more sensitive to temperature than k_D, or visa versa, which is primarily achieved through the pre-exponential factor. From observation, the analysis of the results suggest that k_D onsets sooner than k_R, but k_R becomes more influential as the temperature and pressure are increased for Mg to MgH_2 between 330-400°C.

4.6.4.5 Relationship to dehydrogenation

Another piece of evidence that suggests strain is important, over the H diffusion length, is the observation that the dehydrogenation reaction rate is dependent on the previous hydrogenation conditions (see figure 5.1). For the dehydrogenation rate to be influenced by the previous hydrogenation run, there must have been a physical change to the hydride, which is stable, as the dehydrogenation can occur some time after the hydrogenation. When comparing strain (and in effect H-H interactions) to H diffusion length being the limiting factor in this context, the inclusion of strain + relaxation demonstrates a compelling angle when attempting to explain this phenomenon. This is expanded on in chapter 5.

4.6.4.6 Methodology to determine the kinetics

With the defect + relaxation optional extension applied to the SAM, there is now a more complex procedure to determine the kinetic parameters. As usual, kinetic data is gathered at varying temperatures and pressures of interest. When using the Site Availability Model, then either $\frac{3}{2}\left(\left[\frac{1}{1-\theta}\right]^{\frac{2}{3}}-1\right) = k_e\sigma_s t$ (including shrinking core) or $-ln(1-\theta) = k_e\sigma_s t$ (no shrinking core) is used. The maximum hydride fraction (x_m) is a regression parameter, where $\sigma_s = 0.5$ is assumed when finding A_e and E_e.

If linear least squares on the integrated rate equations fail, the rate law is not suitable. If they partially fit for some cases, then the bond interactions might be strong. Solving the differential equations (e.g. FEM) should then be attempted to explore bond strain before dis-regarding this model. The equation for P_B ($P_B = P_{eq}$) is obtained from PCI data:

$$P_{eq} = exp\left(\frac{\Delta_R H}{RT} - \frac{\Delta_R S}{R}\right)\left(1 - \frac{1}{y_1} ln\left(\frac{1-\theta}{\theta}\right)\right) \tag{4.81}$$

Further from equilibrium scenarios require determining P_{BD}, i.e.

$$P_{BD} = P_N\left(1 - \frac{1}{y_1} ln\left(\frac{1-\theta}{\theta}\right)\right) + \left(\frac{k_D \theta}{I_D}\right)^2 + \frac{k_R}{1 + exp\left(-y_3 \frac{(\theta - \theta_{mid})}{\theta_{mid}}\right)} \tag{4.82}$$

With $P_N = exp\left(\frac{\Delta_R H}{RT} - \frac{\Delta_R S}{R}\right)$. The parameters to find are I_D, A_D, E_D, (within k_D) A_R, E_R, (within k_R) y_3 and θ_{mid}. I_D in theory can be determined from the PCI. The deviation from stoichiometry (δ) is taken from the β phase, ($MH_{1\pm\delta}$) with y axis used for the pressure. This is plotted at the different temperatures tested. One does not get the whole plot and equation 4.83 is used.

$$\frac{P_{eq}}{P_0\left(\delta = 0\right)} = 1 + \frac{\delta^2 \pm \delta\sqrt{\delta^2 + 4\, I_D^2}}{2\, I_D^2} \tag{4.83}$$

A_D, E_D, A_R, E_R, y_3 and θ_{mid} are determined through regression to experimental data, typically with a small sample over a range of temperatures and pressures of interest. Then, these values are used to model larger samples. If COMSOL is used, the optimisation module is recommended.

4.6.4.7 The number of parameters

One of the criticisms of the SAM:DR, is the large number of parameters, in which the parameters could be losing physical significance. However, the site availability term is trying to represent the following, site availability = effects of site de-activation + effect of strained bonds from defects - effect of relaxed bonds from lattice re-arrangement. Although there are areas for improvement, the inclusion of P_D and P_R has managed to achieve reasonable fits at far from equilibrium conditions for the Mg-MgH_2 system, a first for this system. It is speculated that this could be common for materials that can accommodate a high amount of hydrogen, due to the potential for significant H-H interactions.

4.7 Hydrogenation chapter summary

This chapter has covered the hydrogenation kinetics of Mg through the development of the Site Availability Model (SAM). This model is based on a surface reaction expanding on Langmuir's assumptions from the Molecular Adsorption Model. The surface is assumed a sphere, where solid phase effects, represented by the site availability are an important characteristic. The elements of the site availability are discussed, from the phenomenon of site de-activation, the equilibrium behaviour represented by P_B, and the complex behaviour of the H-H interactions, inducing strain on the bonds, expressed by P_D and P_R.

The SAM challenges the long held belief that the rate determining step is the diffusion of hydrogen through hydride layer. One of the criticisms with this view is that diffusion mechanisms are not a strong function of pressure. It is clear that after attempting to model magnesium hydrogenation at far from equilibrium for many months, the kinetics change is a strong function of temperature and pressure, especially when entering into the 380-400°C region. Further, the encasing shell mechanism (diffusion based) did not give the linear shape at high hydride fractions, however pseudo steady state was assumed. The only way that was found to represent the linear shape, within the confines of this model, was through the application of P_D and P_R.

Adding one last piece of evidence, the next chapter will outline how the dehydrogenation of MgH_2 is influenced by the conditions of Mg hydrogenation. It is unlikely how a diffusion based mechanism could clarify this, however the inclusion of defects, altering the characteristics of the hydride, could offer an explanation.

Chapter 5

Dehydrogenation kinetics

In this chapter, the dehydrogenation kinetics of magnesium hydride are explored. Experimental data is compared to existing models, and an expansion to the Site Availability Model (SAM) is derived for the dehydrogenation reaction. The theory is outlined and then applied to experimental data.

5.1 Experimental results

Magnesium hydride dehydrogenation experimental data was gathered alongside the hydrogenation experiments, using the same magnesium sample and Sievert's apparatus (chapter 3). From analysing figure 5.1, the concentration profile is an upside down s-shape, thus the highest reaction rate is at the mid-point. In addition, it is clear that the weight percent (wt%) removal profile is influenced by the previous hydrogenation conditions. For example, focusing on the experiments at 360°C, the total reaction time reduces as the hydrogenation initial gas pressure is increased, even though the dehydrogenation conditions are identical. A dehydrogenation after a hydrogenation PCI resulted in the fastest reaction profile at a given operating temperature. Also, it is clear that as the initial temperature rises, the reaction rate increases, where the reaction rate is more sensitive to temperature than pressure.

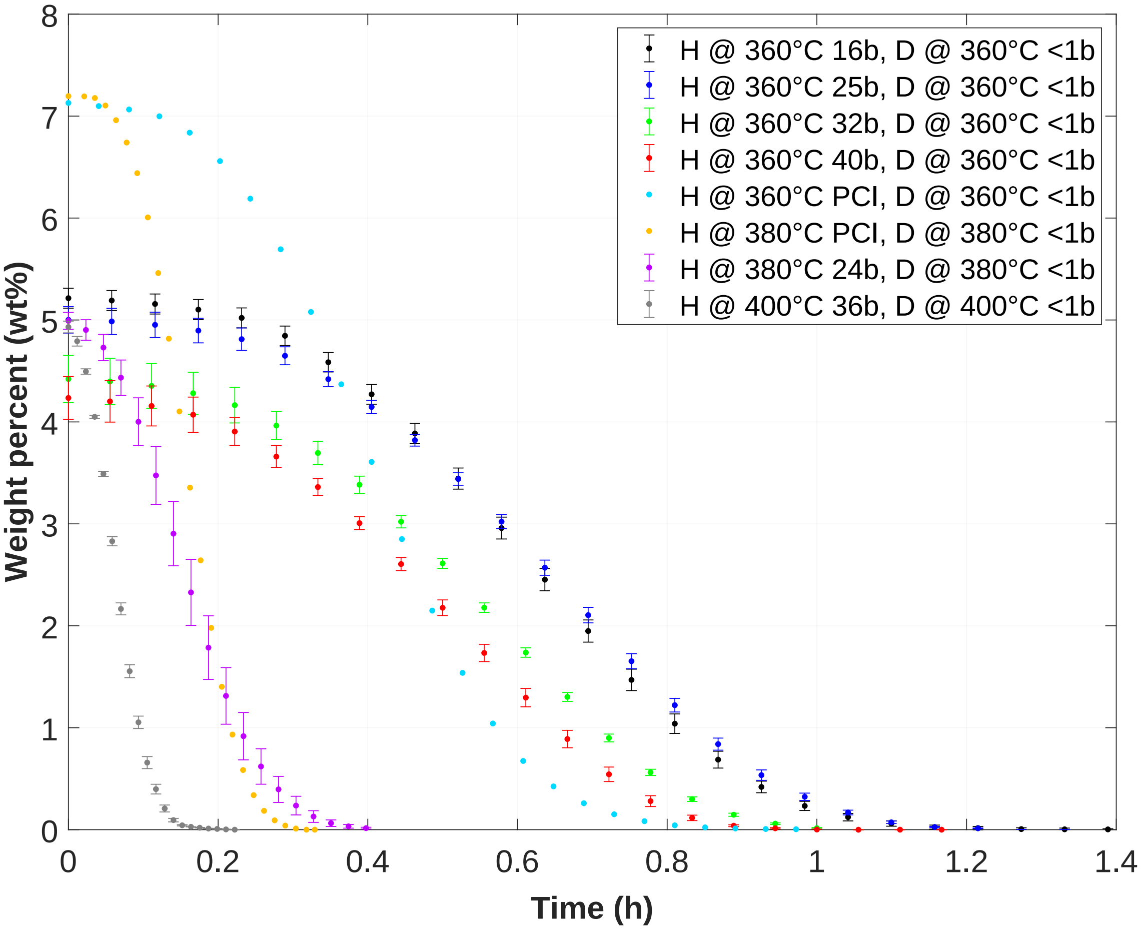

Figure 5.1: Experimental dehydrogenation data of MgH_2 into Mg at varying temperatures and $<$ 1 bar. "H" indicates the previous hydrogenation conditions and likewise "D" shows the conditions for dehydrogenation. The pressure is the initial gas pressure, and PCI is a pressure-composition-isotherm. For example, a PCI was performed at 380°C (over two weeks), and then dehydrogenated at 380°C and $<$ 1 bar.

5.2 Analysing previous rate laws

5.2.1 Chaise, Rango & Marty equation

The results of the Euler method to solve the ordinary differential equation by Chaise, Rango & Marty, are shown in figure 5.2a. Isothermal conditions were assumed for this analysis to determine the feasibility. For the equation to yield a reasonable result, the value of the frequency factor was altered from $A = 1 \text{ x } 10^{10}$ (as stated in their paper [12]) to $A = 7 \text{ x } 10^{7}$, and the activation energy to 130.5 kJ/mol. This could be due to their research experimenting with MgH_2 compacts, and the experimental data in thesis uses MgH_2 with no additives. Furthermore, Chaise et al. only focused on the first 20 minutes of the reaction, which resembles the initial part of the sigmoidal shape (figure 5.2a). A rate law that can represent the whole reaction is desirable.

5.2.2 Mayer, Groll & Supper equation

The results of the Mayer, Groll and Supper equation is shown in figure 5.2a. For this analysis, $E = 172$ kJ/mol and A $= 4.5 \text{ x } 10^{11}$ s^{-1} [75]. The main issue with this rate law is that the shape of the curve is fundamentally different to the experimental data, thus it is clear magnesium hydride dehydrogenation does not follow a first order based mechanism.

5.2.3 Sestak-Berggren equation

Figure 5.2b illustrates some of the experimental data using the Sestak-Berggren equation. An activation energy of 172 kJ mol^{-1} and frequency factor $= 4.5 \text{ x } 10^{11}$ s^{-1} was used to calculate κ_1, where $\kappa_1 = 0.00289$ s^{-1} at 360°C and 0.02 s^{-1} at 400°C (κ_1 is equivalent to rate constant k from the Arrhenius equation). κ_2 and κ_3 are regression parameters. It can be observed that the dehydrogenation for 360°C at 16 & 40 bar gave reasonably similar values of κ_2 and κ_3. However, when applied to dehydrogenation from an isotherm data, κ_2 and κ_3 changed. In addition, when applied to the conditions at 400°C, κ_2 and κ_3 changed again with no discernible trend. This demonstrates the complexity of magnesium hydride dehydrogenation kinetics. One of the key purposes of finding a sufficient model is one that provides confidence to the engineer when designing a reactor at scale. The variations in κ_2 and κ_3 do not provide this confidence.

5.2.4 JMAK Equation

Figure 5.2c shows the result of applying the Johnson–Mehl–Avrami–Kolmogorov (JMAK) equation on dehydrogenation experimental data after a 360°C and 16 bar initial gas pressure hydrogenation run. From initial observation, an Avrami equation where $n = 2.5$ shows a reasonable fit. However, strictly the value of n should be an integer, representing the type of dimensional growth. Other drawbacks of the Avrami equations are that it does not offer identification of the rate limiting step and taking logarithmic values of an integrated rate law masks disagreements between experimental data and theoretical models [24].

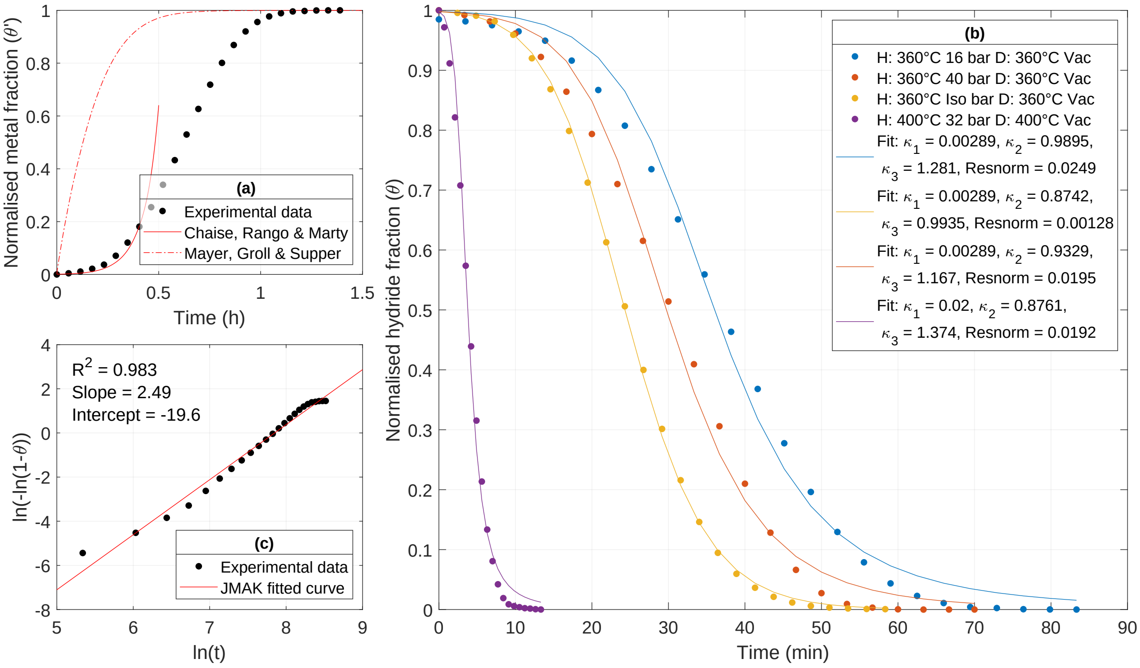

Figure 5.2: (a) Experimental data from a 360°C, initial 16 bar gas pressure sorption run, to a 360°C initial temperature, < 1 bar, dehydrogenation run (b) Selection of dehydrogenation experiments collected on a Sievert's apparatus tested using the Sestak-Berggren equation (c) JMAK equation applied to 360°C 16 bar hydrogenation, to a 360°C, < 1 bar run

As the current rate laws available in the literature have not satisfactory modelled magnesium hydride dehydrogenation at all the conditions tested, and provided a model with intensive characteristics, an extension was developed based on the Site Availability Model (SAM).

5.3 Theory

5.3.1 General mechanism

The Site Availabiliy Model (SAM) has been modified and applied to hydride decomposition based on the reaction mechanism shown below.

Step 1

$$\mathbf{H}\cdot\mathbf{M}+\mathbf{M}\rightarrow\mathbf{M}\cdot\cdot\mathbf{H}\cdot\cdot\mathbf{M}$$

Step 2

$$\mathbf{H}\cdot\mathbf{M}+\mathbf{M}\cdot\cdot\mathbf{H}\cdot\cdot\mathbf{M}\rightarrow H_2+3\mathbf{M}$$

Overall

$$2\mathbf{H}\cdot\mathbf{M}\rightarrow 2\mathbf{M}+H_2$$

Where $\mathbf{H}\cdot\mathbf{M}$ is a bound/normal site, $\mathbf{M}\cdot\cdot\mathbf{H}\cdot\cdot\mathbf{M}$ is a “hypothetical” transition state and $\mathbf{M}$ is a free site needed for a reaction to occur. In this mechanism, a bound $\mathbf{H}$ requires an adjacent free site to ‘jump to’ and form a shared complex. Another adjacent bound $\mathbf{H}$ then associates with the transition complex to form a gaseous hydrogen molecule.

Over the duration of the reaction, the number of free sites increases, so the reaction rate would initially start low, steadily increase as more free sites become available, reach its peak, and then tail off as the hydride depletes. This will resemble a sigmoidal shape, and be akin to an auto-catalytic reaction, where the free sites play the role of the auto-catalyst. The above reaction mechanism is new to this thesis, however an explanation of a generic auto-catalytic reaction can be found in [43].

Adopting the assumptions of the site availiability, it is assumed that any potential available site has a probability of being available/unavailable, where the probability of a free site being available is assumed to be represented by the ratio of available sites to ones that are unavailable. The driving force is the difference between the bound pressure (P_B) and gas pressure (P). The bound defect pressure considers the potential free sites introduced through defects under previous hydrogenation conditions. An unavailable site is related to the bound pressure. Figure 5.3 illustrates this. This is because an unavailable site is one that has returned to the metal state and is now assumed to have the extrinsic defect (caused by the hydrogen) removed. Therefore, the desorption site availability σ_D can be approximated as,

$$\sigma_D \approx \frac{\text{Available sites}}{\text{Unavailable sites}} \approx \frac{P_{BD} - P_g}{P_B} \ngtr 1 \tag{5.1}$$

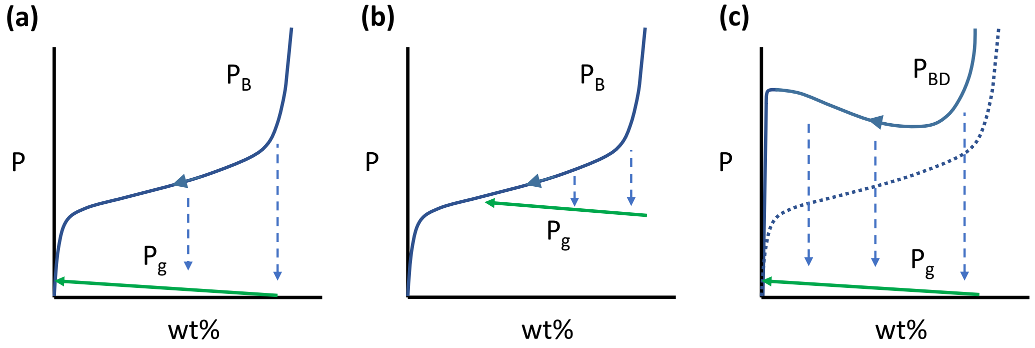

Figure 5.3: Three general scenarios of dehydrogenation within a Sievert's apparatus. (a) Far from equilibrium conditions, i.e. lowest pressure possible, giving mostly complete conversion. Dehydrogenation after an isothermal hydrogenation. (b) Likewise dehydrogenation at close to equilibrium after an isothermal hydrogenation. Results in incomplete conversion. (c) Proposed scenario whereby the prior hydrogenation had defects added.

If there are negligible formation of defects, then $P_{BD} = P_B$. If step 1 is assumed to be rate determining, the rate of hydrogen association depends on the concentration of bound sites, adjacent available/free sites that are directly exposed to the surface/gas interface, where the energy barrier can be overcome, and the desorption site availability. An inclusion of a dimensionless pressure term into the dehydrogenation reaction rate is not novel (see [54, 80]) but the application of the site availability concept and inclusion of defect pressure is new to this thesis. Therefore, the overall surface rate equation becomes:

$$-r''_{H\cdot M} = \frac{k''}{C_T} C_{H\cdot M} C_M \sigma_D \tag{5.2}$$

Where $r''_{H\cdot M}$ (mol m^{-2} s^{-1}) is the reaction rate in surface terms, and k$''$ can be considered an effective velocity constant of the reaction front (units m s^{-1}). Including a mole balance where the total concentration of sites is the sum of unbound and bound sites, the total site concentration is,

$$C_T = C_{H \cdot M} + C_M \tag{5.3}$$

Where the total concentration (C_T) is calculated from the capacity (at operating conditions). For example, the capacity could be 70% of 7.66wt% of a 'm' mass of sample. Substituting equation 5.3 in 5.2 gives the surface rate law based on an auto-catalytic reaction (ACR) including the site availability (σ_D),

$$-r''_{H \cdot M} = \frac{k''}{C_T} C_{H \cdot M}(C_T - C_M)\sigma_D \tag{5.4}$$

5.3.2 Shrinking core

Applying the shrinking core methodology (see Levenspiel [43]), if this reaction happens at the surface of a sphere, which is being depleted,

$$-\frac{RSA}{4\pi R_c^2} \cdot \frac{dN_{H \cdot M}}{dt} = \frac{k'' RSA}{C_T} C_{H \cdot M}(C_T - C_{H \cdot M})\sigma_D \tag{5.5}$$

where RSA is the (average) reactive surface area of a sphere, R_c is the radius of shrinking core and $N_{H \cdot M}$ is the moles of bound sites. If equation 5.5 is multiplied through by $\left(\frac{R_c}{R_0}\right)^2$ to express the rate equation in effective pellet volume form (denoted by removing " superscript). The units of $r_{H \cdot M}$ are (mol m^{-3} s^{-1}).

$$-r_{H \cdot M} = -\frac{RSA}{4\pi R_0^2} \cdot \frac{dN_{H \cdot M}}{dt} = \frac{k'' RSA}{C_T} C_{H \cdot M}(C_T - C_{H \cdot M}) \left(\frac{R_c}{R_0}\right)^2 \sigma_D \tag{5.6}$$

For the first case, it is assumed there is a sphere with an inward reaction front governed by the radius of the (shrinking) core R_c, or a **shrinking core mechanism,** which can be expressed as,

$$R_c = \left(\frac{C_{H \cdot M}}{C_T}\right)^{\frac{1}{3}} R_0 \tag{5.7}$$

Substitution of 5.7 into 5.6 to eliminate to R$_c$ and R$_0$ gives

$$-r_{H\cdot M} = \frac{k''RSA}{C_T} C_{H\cdot M}(C_T - C_{H\cdot M}) \left(\frac{C_{H\cdot M}}{C_T}\right)^{\frac{2}{3}} \sigma_D \tag{5.8}$$

Using the definition of the normalised hydride fraction $\theta = C_{H\cdot M}/C_T$,

$$-r_{H\cdot M} = \frac{k''RSA}{C_T} \theta C_T^2 (1-\theta)\theta^{\frac{2}{3}} \sigma_D \tag{5.9}$$

And simplifying with $k_{e_{H\cdot M}} = k''RSA/C_T$ gives the rate law in terms of concentration and site availability only,

$$\mathbf{-r_{H\cdot M} = k_{e_{H\cdot M}} C_T \sigma_D (1-\theta)\theta^{\frac{5}{3}}} \tag{5.10}$$

5.3.3 Including fragmentation

Equation 5.10 can be expanded by assuming that the dehydrogenation reaction causes the reactant to break up or fragment, incidentally, exposing more available surface and therefore increasing the reaction rate. The idea of fragmentation is novel to this thesis. To account for this, the radius of the shrinking core is converted to an effective shrinking radius R_{c_e}. Taking a step back to equation 5.6, if it is defined that $R_{c_e} = F\,R_c$ and R_c is replace with R_{c_e} (so R_c/R_0 becomes FR_c/R_0), and apply subsequent methodology as before, this gives,

$$-r_{H\cdot M} = k_{e_{H\cdot M}} C_T \sigma_D (1-\theta)\theta^{\frac{5}{3}} F^2 \tag{5.11}$$

in equation 5.11, F is the fragmentation factor. This pseudo representation of fragmentation is an estimation of a particle fragmenting as the reaction progresses, revealing more active surface. This increased surface area could be interpreted by the equivalent surface area of a sphere related through the effective particle radius. A generic transient change in R_{c_e} compared to R_c is shown in figure 5.4.

To represent fragmentation in dimensionless terms, it is assumed zero/first order and the rate

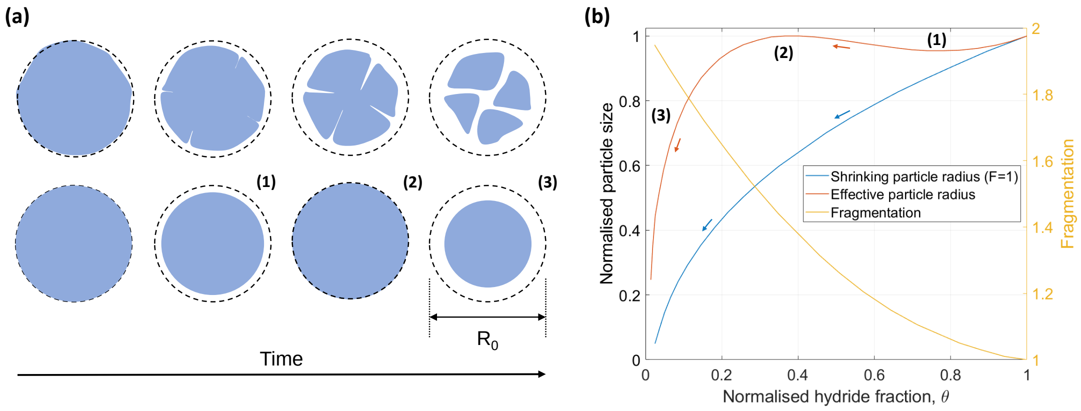

Figure 5.4: (a) Illustration of a particle fragmenting as the reaction occurs and the subsequent approximation using an effective particle radius. (b) Comparison between the effective particle radius R_{c_e} and unfragmented radius R_c as the reaction progresses.

of formation of F is proportional to the normalised metal fraction (θ').

$$\frac{dF}{d\theta'} = k_F \tag{5.12}$$

$$\frac{dF}{d\theta'} = k_F\theta' \tag{5.13}$$

Integrating from 1 to F, 0 to θ and substitute for the normalised hydride fraction, $\theta' = 1 - \theta$ gives,

$$F = k_F(1-\theta) + 1 \tag{5.14}$$

$$F = k_F(1-\theta)^2 + 1 \tag{5.15}$$

And substituting into equation 5.11,

$$-\mathbf{r_{H\cdot M}} = \mathbf{k_{e_{H\cdot M}}}(\mathbf{1}-\theta)\theta^{\frac{5}{3}}\sigma_{\mathbf{D}}(\mathbf{k_F}(\mathbf{1}-\theta)+\mathbf{1})^{\mathbf{2}} \tag{5.16}$$

$$-\mathbf{r_{H\cdot M}} = \mathbf{k_{e_{H\cdot M}}}(\mathbf{1}-\theta)\theta^{\frac{5}{3}}\sigma_{\mathbf{D}}(\mathbf{k_F}(\mathbf{1}-\theta)^{\mathbf{2}}+\mathbf{1})^{\mathbf{2}} \tag{5.17}$$

These two equations are the end result that includes an auto catalytic reaction at a spherical particle surface (whereby the reaction starts at the outer core with an inward reaction front), the concept of site availability and a particle fragmenting.

5.3.4 Expanding core

If an **expanding core mechanism** is adopted (new to this thesis based on altering the boundary conditions within the shrinking core method), whereby the reaction starts from $R_c = 0$ and then completes at $R_c = R_0$, as illustrated in figure 5.5b, then the normalised metal fraction (θ') can be expressed as,

$$\theta' = \frac{C_M}{C_T} = \frac{\frac{4}{3}\pi R_c^3}{\frac{4}{3}\pi R_0^3} = \left(\frac{R_c}{R_0}\right)^3 \tag{5.18}$$

In practice, the magnesium starts from an initial start point, e.g. $C_{M_0} = 0.05$. Regarding the rate law, an auto-catalytic reaction including site availability is still assumed, except the rate law is expressed as a rate of formation of metal sites, with the reaction occurring at the radius core R_c,

$$\frac{RSA}{4\pi R_c^2} \cdot \frac{dN_M}{dt} = \frac{k''RSA}{C_T} C_M (C_T - C_M)\sigma_D \tag{5.19}$$

Again, multiply both sides by $(R_c/R_0)^2$ and substitute $\theta' = C_M/C_T$ to give equation 5.20. If first order fragmentation is included, this produces equation 5.21.

$$\mathbf{r_M = k_{e_M} C_T \sigma_D (1 - \theta')(\theta')^{5/3}} \tag{5.20}$$

$$\mathbf{r_M = k_{e_M} C_T \sigma_D (1 - \theta')(\theta')^{5/3} (k_F (\theta')^2 + 1)^2} \tag{5.21}$$

This is the end result with an auto-catalytic surface reaction of a spherical pellet with an outward reaction front with the inclusion of site availability and fragmentation.

If the ACR occurred whereby the surface does not shrink in relation to the initial particle size (i.e. $R_c/R_0) \approx 1$), and no fragmentation, then dehydrogenation rate equation simplifies to equation

$$\mathbf{-r_{H\cdot M} = k_{e_{H\cdot M}} C_T \sigma_D (1 - \theta)\theta} \tag{5.22}$$

Which is essentially a straight forward auto-catalytic reaction including the site availability.

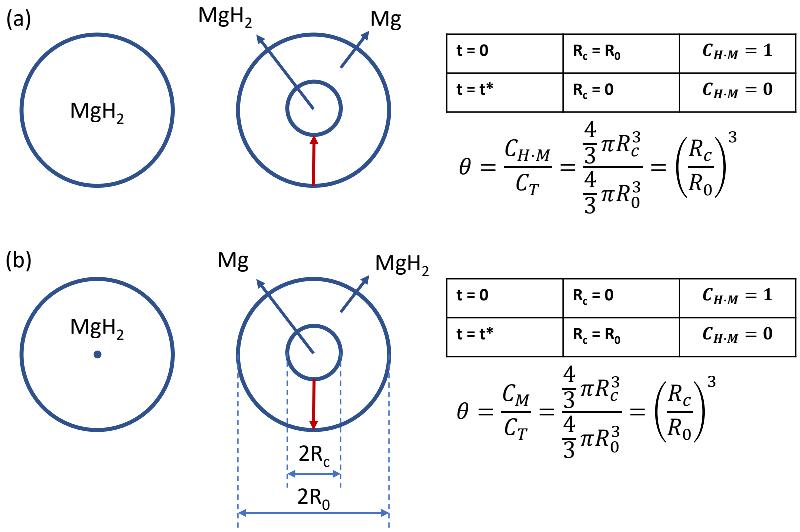

Figure 5.5: (a) Representation of a "shrinking" core. Reaction starts at the shell and proceeds inwards. Thus, concentration of $C_{H\cdot M}$ = core radius. (b) Representation of an "expanding core". Reaction starts at the centre and proceeds outwards.

5.3.5 Summary of rate equations

In summary, all the dehydrogenation rate laws derived are listed below with abbreviations, units mol m^{-3} s^{-1} and suitable for input into COMSOL. For recap $r = dC/dt$, θ = normalised hydride fraction and θ' = normalised metal fraction.

$$SAM : ACR \quad -r_{H\cdot M} = k_{e_{H\cdot M}} C_T \sigma_D (1-\theta)\theta \tag{5.23}$$

$$SAM : ACR : SC \quad -r_{H\cdot M} = k_{e_{H\cdot M}} C_T \sigma_D (1-\theta)\theta^{\frac{5}{3}} \tag{5.24}$$

$$SAM : ACR : SC : F_0 \quad -r_{H\cdot M} = k_{e_{H\cdot M}} C_T \sigma_D (1-\theta)\theta^{\frac{5}{3}}(k_F(1-\theta)+1)^2 \tag{5.25}$$

$$SAM : ACR : SC : F_1 \quad -r_{H\cdot M} = k_{e_{H\cdot M}} C_T \sigma_D (1-\theta)\theta^{\frac{5}{3}}(k_F(1-\theta)^2+1)^2 \tag{5.26}$$

$$SAM : ACR : EC \quad r_M = k_{e_M} C_T \sigma_D (1-\theta')(\theta')^{5/3} \tag{5.27}$$

$$SAM : ACR : EC : F_1 \quad r_M = k_{e_M} C_T \sigma_D (1-\theta')(\theta')^{5/3}(k_F(\theta')^2+1)^2 \tag{5.28}$$

Figure 5.6 illustrates the isothermal reaction profile of the derived rate laws. One can see the expanding core is slow to start and finishes quickly, essentially a mirror of the shrinking core, whereas inclusion of fragmentation increases the reaction rate at the middle to latter sections. Figure 5.7 shows an illustration of the SAM:ACR:SC:F rate law.

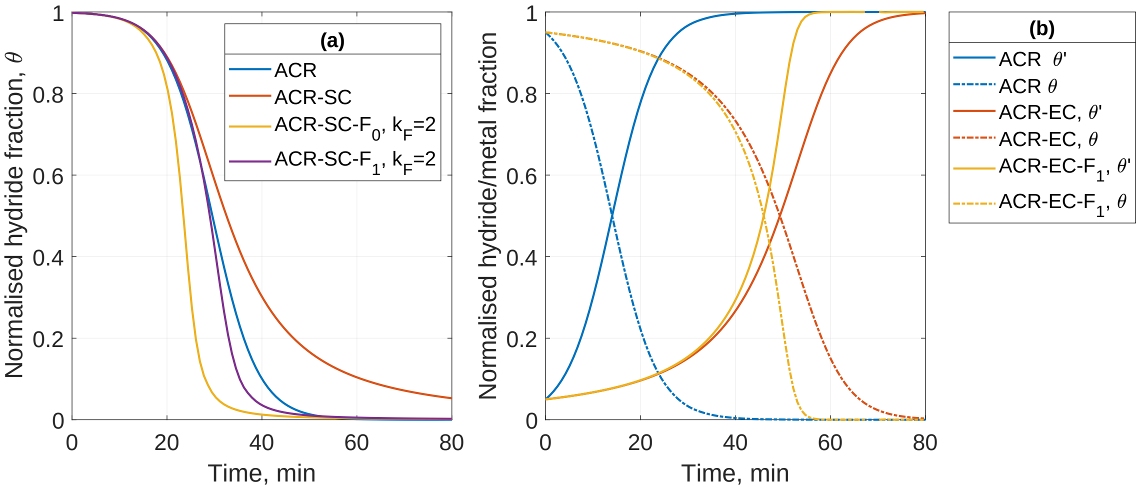

Figure 5.6: Illustration of the derived rate dehydrogenation rate laws at isothermal conditions and a constant site availability. Solved using ode45 in Matlab. (a) Reaction profile of ACR with shrinking core. $k = 0.007$, $\sigma = 0.5$ and $C_{H\cdot M_0} = 0.998$ (b) Reaction profile of ACR with expanding core, $k = 0.007$, $\sigma = 0.5$ and $C_{M_0} = 0.05$.

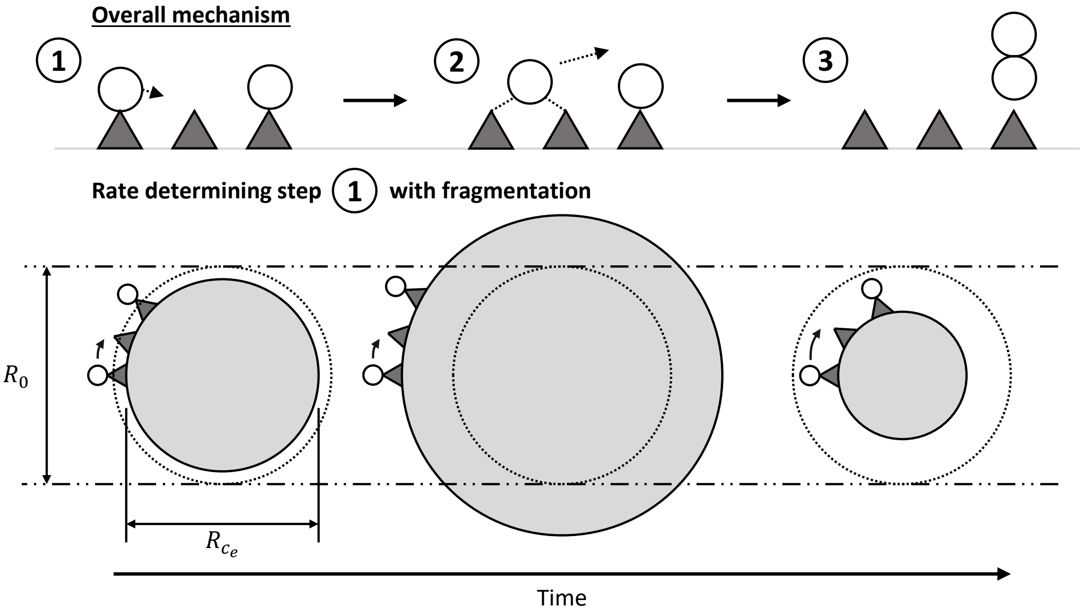

Figure 5.7: The SAM:ACR:SC:F rate equation illustrated using triangles (metal sites) and circles (hydrogen). Shown is the illustration of the effective particle radius changing with time based on step 1 being the rate determining step, thus showing that a shrinking core + fragmentation is an effective expanding core for the majority of the reaction.

Table 5.1: Table outlining unique work within this thesis for the hydrogenation model and previous literature used

Category	Auto-catalytic reaction	Site Availability	Shrinking core	Fragmentation	Expanding core
Previous work	Generic explanation of an auto-catalytic reaction is shown in (Levenspiel)	Dimensionless pressure term used in the reaction rate (Groll, Ron, Nasrallah)	Shrinking core reaction mechanisms are common models for solid particle reactions. (Levenspiel).	No previous literature used.	Much of the expanding core method is synonymous with the shrinking core. (Levenspiel)
New to this thesis	Application of an auto-catalytic reaction to site theory. Developed a reaction mechanism to reflect this.	Allocated alternative meaning to the dimensionless pressure term – site availability. Added the potential effect of defect pressure when dehydrogenating.	Combined the shrinking core to an auto-catalytic reaction mechanism.	Positioned the idea of fragmentation within the particle radius, to create an effective particle radius. Found that if fragmentation is paired with shrinking core, an effective expanding core is achieved for the key part of the reaction.	Altering the boundary conditions to create an outward reaction front (metal expands into hydride). Combined with fragmentation for completeness.

5.3.6 Analysing an ACR reaction

It also useful to scrutinise an auto-catalytic reaction mechanism. With the following general reaction $\mathbf{A} + \mathbf{B} \rightarrow \mathbf{B} + \mathbf{B}$, whereby reaction with **B** is required to produce more **B**, the rate law is

$$-r_A = k_A C_A C_B$$

where component **B** acts as the catalysing reactant. A low initial concentration of 'catalysing' reactant (C_B) gives a sigmoidal shape. Whereas, a high initial concentration of 'catalysing' reactant tends the profile to first order reaction shape. Also, the same effect would occur if the reaction rate coefficient (k) was higher (i.e. lower activation energy) with a moderate increase in C_B, as shown in figure 5.8. Therefore, applying this site theory, if C_B is the fraction of free sites required for a reaction to occur, then having a higher initial fraction of free sites and/or a lower activation energy (catalyst) will push the reaction profile to a first order shape. For instance, our data using Mg spheres only gave sigmoidal shape curves. Gambini et al. also tested a MgH_2 based system and their data was sigmoidal (even though they used first order to model their data) [29]. Likewise, data from Floriano et al. displayed a similar trajectory for bare MgH_2 but a first order shape with Nb based additives, in line with the theory of an auto-catalytic reaction [27]. Further, Cui et al. also added suitable additives to Mg, namely Ti, Nb, V, Co, Mo and Ni, and all reaction profiles exhibited a first order shape [17].

5.3.7 Kissinger method

As mentioned in the background section, the activation energy E and pre-exponential factor A can be determined through the solving the mole balance differential equation and regressing the variables to experimental data. However, according to the SAM, these methods would depend on how accurate the site availability is being modelled.

One way to work around this is to utilise the Kissinger method, via dehydrogenation under argon using differential scanning calorimetry (DSC). Separate batches of the same sample are heated under several heating rates (ι) while the peak temperature (T_m) is recorded at each heating

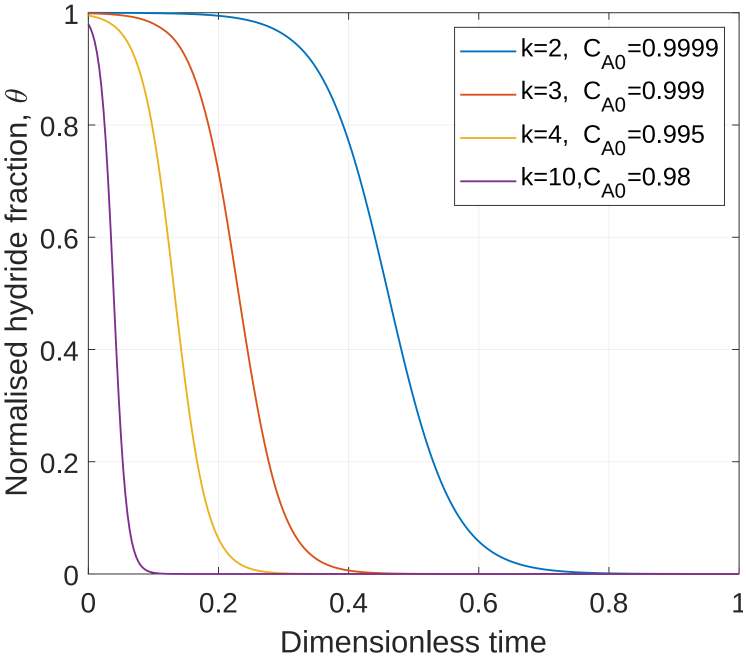

Figure 5.8: Change in auto-catalytic reaction profile with varying initial catalysing reactant, $C_{B0} = (1 - C_{A0})$ and rate constant (k). Graph generated from rate equation $-r_A = k_A C_A (C_T - C_A)$, where $C_T = 1$.

rate. The peak is the point of constant conversion.

The derivation of the original Kissinger method assumes a first order reaction. Thus, the derived dehydrogenation models need to be applied to the Kissinger method to determine the modified Kissinger equation. For completeness, the original Kissinger equation is re-derived [9] to then apply it to the metal hydride dehydrogenation reaction mechanism.

As the normalised hydride fraction is defined as $\theta = C_{H \cdot M}/C_T$, then the rate of disappearance of θ (dehydrogenation) for f(θ) being 'some function of θ' can be described as,

$$-\frac{d\theta}{dt} = kf(\theta)$$

Where "k" is the proportionality constant governed by the Arrhenius equation $k = Aexp(-E/RT)$. Partial differentiation with respect to time,

$$\frac{d}{dt}\left(\frac{d\theta}{dt}\right) = Aexp\left(-\frac{E}{RT}\right) \cdot \frac{d\theta}{dt} + Af(\theta) \cdot \frac{d}{dt}\left(exp\left(-\frac{E}{RT}\right)\right) \tag{5.29}$$

By defining $\iota = dT/dt$ (the heating rate) and using the chain rule,

$$\frac{d}{dt}\left(exp\left(-\frac{E}{RT}\right)\right) = \frac{d}{dT}\left(exp\left(-\frac{E}{RT}\right)\right)\cdot\frac{d}{dT} = \frac{E\iota}{RT^2}exp\left(-\frac{E}{RT}\right) \tag{5.30}$$

At the peak T = T$_p$ and $-\frac{d}{dt}\left(\frac{d\theta}{dt}\right) = 0$ therefore,

$$0 = \frac{d}{dt}\left(f(\theta)\right) + f(\theta)\cdot\frac{E\iota}{RT_p^2} \tag{5.31}$$

Defining $f'(\theta) = \frac{d}{d\theta}(f(\theta))$, then $\frac{d}{dt}(f(\theta)) = f'(\theta)\cdot\frac{d\theta}{dt}$

$$0 = Aexp\left(-\frac{E}{RT_p}\right)f'(\theta) + \frac{E\iota}{RT_p^2} \tag{5.32}$$

Rearranging for ι/T_p^2 and taking the natural logarithm gives the following equation.

$$ln\left(\frac{\iota}{T_p^2}\right) = ln\left(\frac{AR}{E}\right) + ln(|f'(\theta)|) - \frac{E}{RT_p} \tag{5.33}$$

From a plot of $ln(\iota/T_p^2)$ against $1/T_p$ the gradient, irrespective of the model chosen, is always $-E/R$. Note, for the SAM, to remove the features of the site availability, the hydrogenation should be held at close to equilibrium conditions, while the subsequent dehydrogenation should be under an inert gas, such as Argon. Then, the site availability is close to unity, ($\sigma_D = (P_{BD} - P_g)/P_B \approx P_B/P_B = 1$) and therefore enabling a straightforward differentiation of $f(\theta)$. The calculation of the pre-exponential factor through the y-intercept would change slightly depending on the model, where table 5.2 outlines the varying $ln(f'(\theta))$ at an assumed peak position of θ. The calculation of A would be,

$$A = \frac{E}{R}(exp(slope) - |f'(\theta)|) \tag{5.34}$$

As the slope is usually between 10-20 for dehydrogenation of a hydride, the $exp(slope)$ and the multiplication of E/R governs the size of the exponential factor, essentially meaning $|f'(\theta)|$ is negligible. Thus, it is a safe assumption to use the Kissinger method based on a first order reaction (equation 5.33) to determine E and A, which then can be applied to the SAM for modelling the reaction kinetics.

$$ln\left(\frac{\iota}{T_p^2}\right) = ln\left(\frac{AR}{E}\right) - \frac{E}{RT_p} \tag{5.35}$$

Further, as mentioned previously, the SAM assumes an effective rate constant (k_e) as,

$$k_e = A_e exp\left(-\frac{E_e}{RT}\right) \tag{5.36}$$

Then the determined values of A_e and E_e from the Kissinger method used within the SAM are expressed in rudimentary effective terms, so account for the change in surface area through an average number.

Table 5.2: Outline of reaction mechanisms applied to the Kissinger method (a) is the SAM where the reduction of a sphere is included within the rate equation. (b) If $(R_c/R_0)^2 \approx 1$, the rate law simplifies by dropping the order from 5/3 to 1.

Model	$f(\theta)$	$f'(\theta)$	$ln(\lvert f'(\theta)\rvert$
1st order	$\theta\sigma_D$	1	0
(a) SAM:ACR:SC	$\theta^{\frac{5}{3}}(1-\theta)\sigma_D$	$\frac{5}{3}\theta^{\frac{2}{3}} - \frac{8}{3}\theta^{\frac{5}{3}}$	-1.6 ($\theta \approx 0.5$)
(b) SAM:ACR	$\theta(1-\theta)\sigma_D$	$1-2\theta$	-3.9 ($\theta \approx 0.49$)

5.4 Simulation results

The methodology of the modelling procedure was to apply each rate equation to all experimental conditions, where the goal was to find a rate equation that satisfied all magnesium dehydrogenation profiles. The best performing rate equation is shown in this section, alongside other rate laws that help demonstrate why it is the most effective.

5.4.1 Auto catalytic reaction - ACR

The first equation tested was the straight ACR (equation 5.23), without a shrinking surface or site availability. The results are shown in figure 5.10b and d. The porous matrix thermal conductivity (λ_p) was fixed at 2 W m^{-1} K^{-1} with the initial concentration of free sites ($C_{H\cdot M_0}$) and maximum hydride fraction (x_m) altered to give the best fit. The applicability of the ACR is not the best as x_m was not fixed and was allowed to "float" in order to improve the R^2 value. This on many occasions resulted in a different value of x_m compared to the experiment.

At 360°C, the SAM:ACR rate law is suitable except for the isotherm case. At 380°C and 400°C the SAM:ACR rate law lost significance, again exhibiting a poor fit for the 380°C isotherm run. An auto-catalytic reaction mechanism has represented the s-shaped profile sufficiently, but the SAM:ACR would reduce in effectiveness as the sample sizes become large, due to temperature gradients.

5.4.2 Auto catalytic reaction, shrinking core – SAM:ACR:SC

The results of the SAM:ACR:SC rate law (equation 5.24) is shown in figure 5.10b and d, where the parameters $\lambda_p = 2$ W m^{-1} K^{-1}, E_e and A_e were the same as in the SAM:ACR case. It is evident that the fit worsens. As the inclusion of a shrinking core and site availability add resistance to the reaction rate, the total reaction time increases. This provides additional evidence a simple shrinking core mechanism is not ideal for magnesium hydride dehydrogenation. However, as the reaction is a function of pressure, a pressure term must be included within the rate law. As the pressure term, or site availability, is assumed to occur at the surface reaction front, a representation of the surface is required, if the SAM is to be used.

5.4.3 Auto catalytic reaction, expanding core – SAM:ACR:EC

As such, the next rate law includes an expanding core, or SAM:ACR:EC (equation 5.27). From figure 5.9, the reacted fraction profile greatly depends on the initial condition. If it is assumed that the hydride fraction at time = 0 is 0.68 (determined from experimental data), then the metal fraction is 0.32. However, it is apparent that when using this initial condition, the graph trajectory is incorrect (figure 5.9a). If the initial metal fraction is decreased to 0.09, a s-shape is apparent with the latter part of the experimental data sufficiently modelled, but the initial part is clearly unsatisfactory (figure 5.9b).

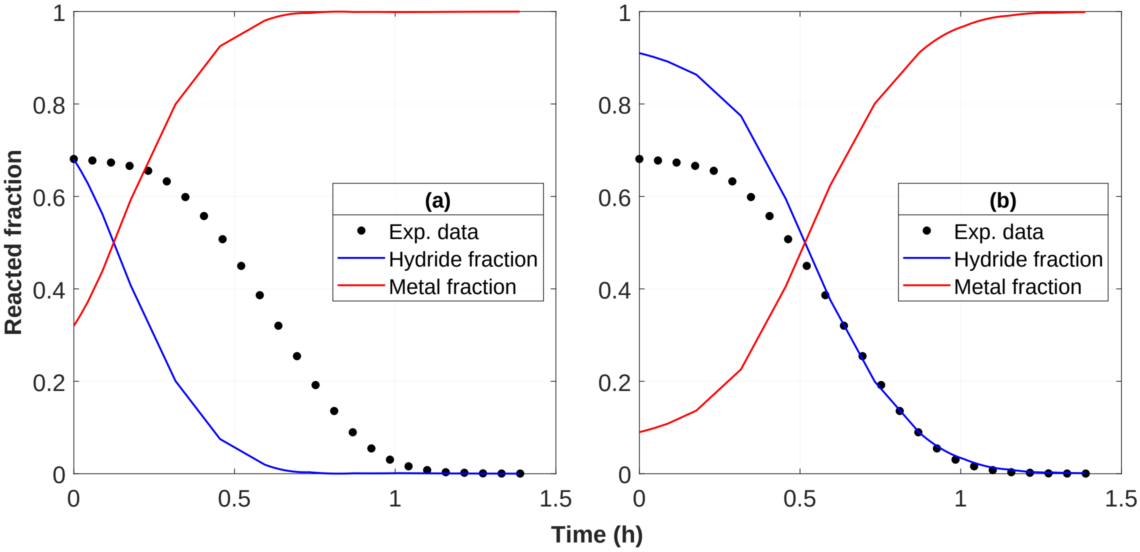

Figure 5.9: Simulations using the SAM:ACR:EC. Dehydrogenation at initial conditions of 360°C and < 1 bar, after a 360°C and 16 bar hydrogenation run. (a) Initial metal fraction = 0.32. (b) Initial metal fraction = 0.09

The problem with the initial portion (in figure 5.9b) may be due to the way the experimental data is collected. The initial metal fraction is 0.32 but not 100% of it is available for reacting. The rate equation is dependent on the available metal surface, and that is unknown. Hence, when the initial condition is lowered to 0.09, the fit improves in the latter half as more of the available sites are at the surface, in relation to the leftover volume. Another approach was attempted, where the experimental data was normalised, however this then means the initial metal fraction was small ($\approx$

0.01), and this caused the expanding core case to be too slow. Also, it does not solve the problem of how to determine the initial metal fraction available for reaction. Therefore, as the experimental data is collected on a volume basis, a rate law that can be smoothly applied to data is desirable.

5.4.4 Including fragmentation

As a representation of the surface over time is essential, and the expanding core has issues with the initial conditions (this includes expanding core with fragmentation SAM:AC:EC:F), fragmentation is introduced with a shrinking core. As such, the SAM:ACR:SC:F models (equation 5.25 and 5.26) were tested. Table 5.3 shows the parameter values used within these scenarios. As before, A_e and E_e were 4.5×10^{11} and 172 kJ mol^{-1} respectively. Figure 5.10b and d shows the results of these rate equations. It is evident that the SAM:AC:SC:F is effective for all scenarios tested, where the $R^2 > 0.99$ for all cases. A first order fragmentation works best for kinetics (n=2, first order) while for PCI's, n=1 (zero order) fits sufficiently. In this model, the site availability is represented by the van't Hoff equation, which simplifies the model and makes it much faster to solve.

Table 5.3: Key model parameters used for the ACR:SC:F. λ_p = porous matrix thermal conductivity, $C_{H \cdot M_0} = C_T \times const$ = constant used to determine initial condition.

Parameter	**360°C**					**380°C**		**400°C**
Initial sorption gas pressure (bar)	16	25	32	40	PCI	24	PCI	36
Equivalent over-pressure	1	2	3	4	n/a	1	n/a	1
λ_p	2	2	2	2	2	2	2	2
$C_{H \cdot M_0} = C_T \times const$	0.998	0.9985	0.9985	0.999	0.995	0.994	0.995	0.994
Max. hydride fraction, x_m	0.68	0.653	0.578	0.526	0.93	0.65	0.939	0.644
Fragmentation order, n	2	2	2	2	1	2	1	2
Fragmentation rate constant, k_F	1	1	1.4	1.8	2	1	3	4
Average bed T, T_{av} (K)	631.57	631.62	631.77	631.82	630.56	648.43	646.40	666.10

Assuming that the A_e and E_e is verified through DSC Kissinger plots, ΔH and ΔS are determined through PCI experiments, and the required thermophysical properties are measured through a suitable apparatus, therefore the parameters for the SAM:ACR:SC:F model are $const$, k_F, x_m and n. As n is fixed to either 1 or 2, and x_m is determined from experimental data, then there are two regression parameters: $const$ and k_F. As only two additional parameters are needed across a broad range of conditions, the SAM:ACR:SC:F is an effective model for MgH_2 dehydrogenation.

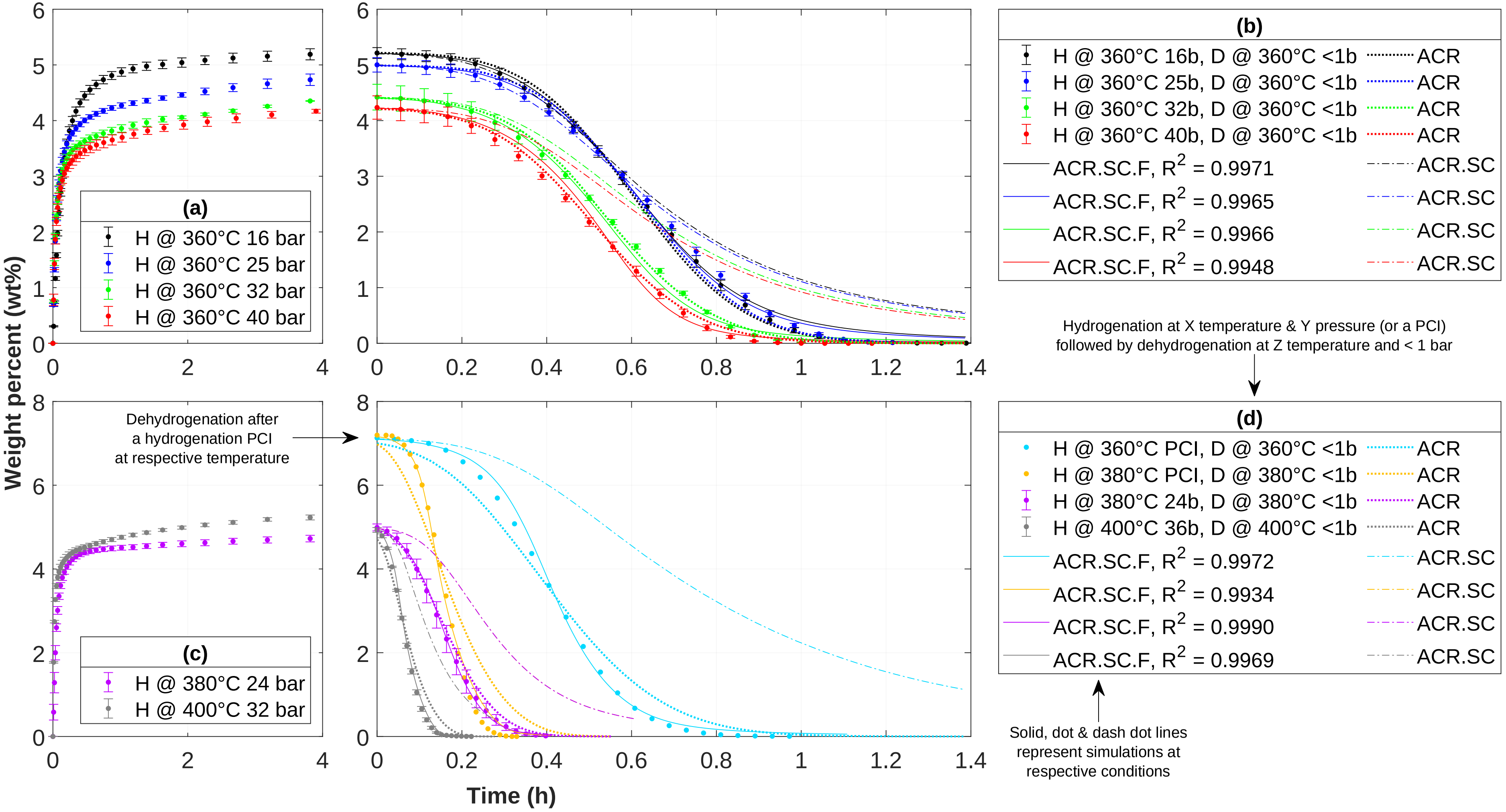

Figure 5.10: (a) and (c) Hydrogenation experimental data prior to the dehydrogenation run. (b) and (d) The SAM:ACR, SAM:ACR:SC, and SAM:ACR:SC:F tested against dehydrogenation experimental data collected on a Sievert's apparatus.

5.5 Discussion

5.5.1 Accuracy of the site availability

The accuracy of the site availability (σ_D) depends on the accuracy of all the site availability parameters, P_{BD}, P_g and P_B. Assuming P_g is represented by experimental data, then the level of accuracy for P_{BD} and P_B is required.

5.5.1.1 Considering bound pressure

For the SAM:ACR:SC:F cases above, if a scenario is considered where there are no defects ($P_{BD} \approx P_B$) so $\sigma_D = P_B - P_g/P_B$, then P_B can be represented through equation 4.6 or the van't Hoff equation (i.e. $P_B \approx P_{eq}$). This assumption ($P_B \approx P_{eq}$) was checked using the SAM:ACR:SC:F case at 360°C, 380°C and 400°C for one pressure condition using the van't Hoff equation or equation 4.6, where it was found the change was minimal. In other words, using the simpler van't Hoff equation to represent P_B for the SAM:ACR:SC:F is satisfactory for magnesium hydride dehydrogenation. However, this simplification might not be suitable for a material with a significant sloping plateau.

5.5.1.2 Considering bound defect pressure

If the bound defect pressure (P_{BD}) is inserted into σ_D, the site availability driving force can be increased. From the hydrogenation model, the non-isothermal P_{BD} profile is calculated at each time step, which can be extracted as a data file and imported into the dehydrogenation model. This method has an issue however, whereby the P_{BD} curve needs to change with a change in temperature based on the van't Hoff equation (i.e. site de-activation).

A empirical modification to the hydrogenation model allows for an input of the isothermal P_{BD} profile. In the SAM:EM hydrogenation model, $P_{BD} = \Omega \times P_B$, where Ω is a polynomial being a f(θ). In the dehydrogenation model, the addition of Ω causes a sloping plateau and thus a higher site availability driving force. This is not the non-isothermal P_{BD} curve but it is better than no representation of defects. The result of this is shown in figure 5.11, using the SAM:ACR:SC:F_0

rate law incorporating P_{BD}, where the values of k_F and $const$ are reduced to accommodate the effect of P_{BD}. The parameter Ω was represented by a 6th order polynomial and it is clear that the P_{BD} does not end (hydrogenation) and start (dehydrogenation) at the same place. This is due to inaccuracies in evaluating x_m and $const$.

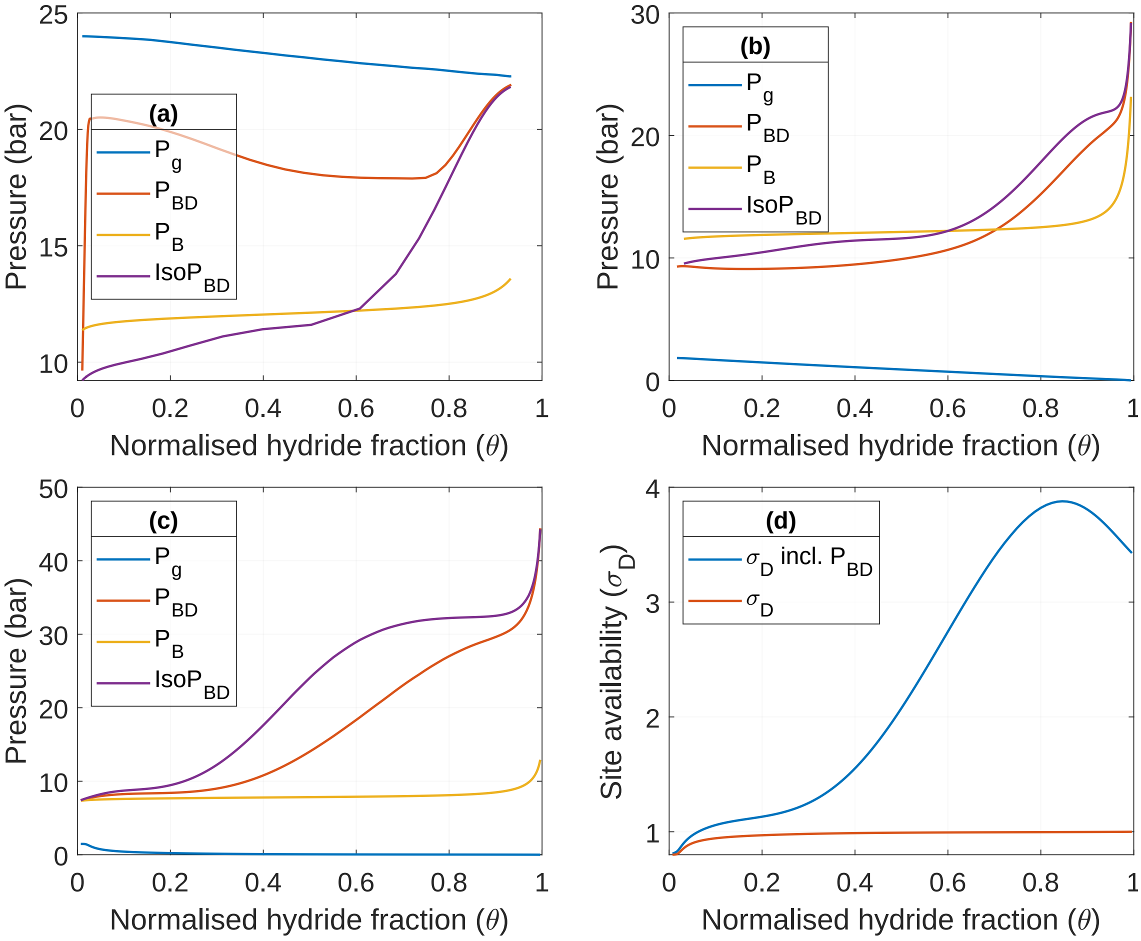

Figure 5.11: (a) and (b) Hydrogenation and dehydrogenation pressure curves at initial temperature and pressure of 380°C and 24 bar respectively. For each case the (kinetic) driving force is between the gas pressure P_g and bound defect pressure P_{BD}. (c) Dehydrogenation pressure curves at initial conditions 360°C 40 bar. (d) Site availability curves at initial conditions 360°C 40 bar, with and without P_{BD}.

5.5.1.3 The site availability limit

For the over-pressure $= 1$ case in figure 5.11a and b, the site availability does not rise above one (for most of the reaction). However, at a higher over-pressure experiment, such as at 360°C and 40 bar (figure 5.11c and d), the site availability does go above one. Using the rate law SAM:ACR:SC:F_0 and incorporating P_{BD}, the fit is very poor (the P_g line is not straight), where for a significant part of the reaction, the site availability is consistently above 2. As the model does not fit when σ_D >1, this indicates that the condition σ_D should not be above one holds true. If it is assumed that this assumption is true, then the addition of P_{BD} is not needed in this case. This is due to the dehydrogenation experiment operating with the largest possible pressure difference, thus maximum site availability driving force is achieved for most of the reaction when using $(P_B - P_g)/P_B$ instead of $(P_{BD} - P_g)/P_B$, where $P_B \approx P_{eq}$. If $(P_{BD} - P_g)/P_B$ was used and the term was capped at 1, then the difference between $(P_B - P_g)/P_B$ and $(P_{BD} - P_g)/P_B$ at 360°C and 40 bar would be a faster driving force between $\theta = 0.1$ - 0.3.

5.5.1.4 Influence of fragmentation on site availability

As both F and P_{BD}'s inclusion to σ_D increase the reaction rate, it is reasonable to suggest that an increase in k_F could increase the influence of F outside its original intention, i.e. cover the effects of σ_D. Figure 5.12 shows that fragmentation correlates with temperature and pressure, or an increase in reaction rate increases fragmentation, which is logical. As there is slight variation allowed in k_F to achieve a reasonable fit, combined with the limited experimental data available, it is difficult to pinpoint whether the relationship is linear/logarithmic etc. However, it is evident F is a $f(T, P)$.

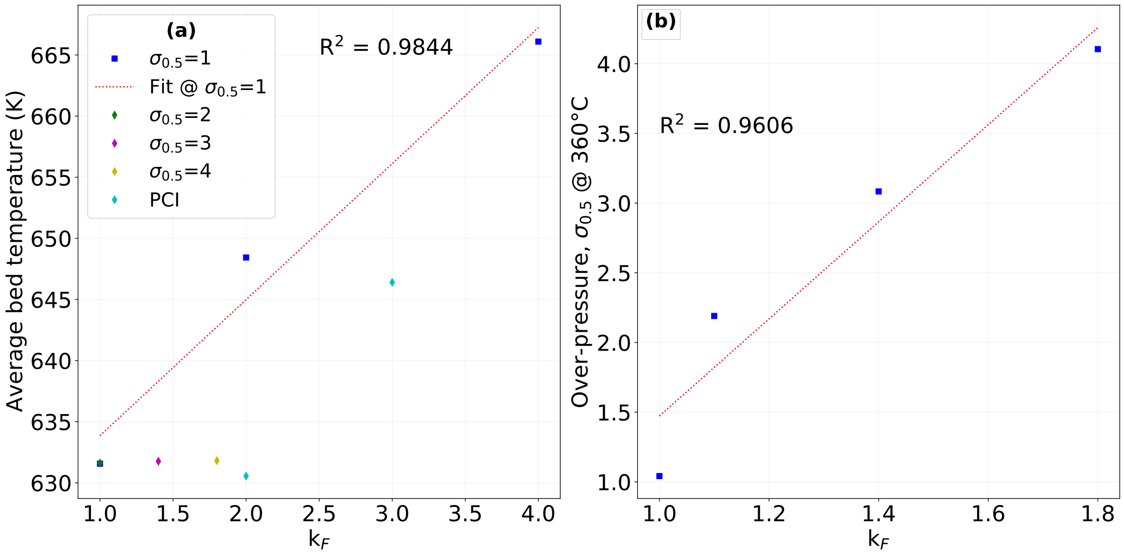

Figure 5.12: (a) Calculated average temperature of whole reaction and value of k_F used for all dehydrogenation cases (by varying over-pressure $\sigma_{0.5}$). (b) Over-pressure conditions (hydrogenation) versus the k_F values at 360°C.

5.5.2 Shrinking or expanding core

As discussed in the literature review, there is physical evidence of magnesium growing outwards into the hydride, which indicates an expanding core. Further, when the SAM:ACR:SC (shrinking core only) was applied to the experimental data, the fit was poor especially at low wt%.

Within the expanding core model, as the reaction progresses, the surface area increases as the metal core grows. Whereas, in the shrinking core, the reverse occurs. However, if fragmentation is included alongside a shrinking core, then the shrinking surface area of the core is countered by the increasing surface area caused by a fragmenting particle. As such, the surface area profile in the expanding core case can exhibit a similar profile using a combined shrinking core and fragmentation model (e.g. an effective expanding core).

Although the initial conditions for a SAM:ACR:SC:F enable easier application to dehydrogenation experimental data, there are issues with it. For example, the SAM:ACR:SC:F is based on the normalised hydride fraction. As it was simplified that $C_T = C_M + C_{H \cdot M}$, and $C_T = C_{ref} x_m$ then the maximum hydride fraction (x_m) is empirically accounting for $C_{H \cdot M}(Unavailable)$, as explained previously. If there was 5wt% uptake out of a reference 7.66wt% for MgH_2, then $x_m = 5/7.66 = 0.65$. Further, the initial condition of $C_{H \cdot M}(t = 0) = C_T \times const$; if $const = 0.99$ then 99% of 0.65 is free to react at time $= 0$, which is most likely not true. Although this is inaccurate, it allows the model to be applied to weight percent experimental data, which is in the form commonly expressed.

5.6 Dehydrogenation kinetics chapter summary

In this chapter, the Site Availability Model (SAM) has been applied to MgH_2 dehydrogenation. The model expands on the site availability assumption, where the rate determining step is through an auto catalytic reaction (ACR). The auto-catalyst are adjacent free (metal) sites, where the reaction is assumed to occur at a spherical surface with the possibility for the particle to fragment and reveal more active surface, represented through an effective particle radius. These collated ideas produce the SAM:ACR:SC:F, which represented MgH_2 dehydrogenation sufficiently at initial conditions < 1 bar between 360°C - 400°C.

In addition, the dehydrogenation overall completion time is dependent on the previous conditions the sample was hydrogenated at, with dehydrogenation from hydrogenation PCI's and high over-pressures delivering the shortest completion time. Further, as the rate equation is based on a surface reaction front, this indicates that the surface plays an integral role in the reaction rate.

Chapter 6

Large lab-scale reactor

6.1 Introduction

This chapter discusses the results of a 154 g helical flow double pipe reactor filled with magnesium spheres. The aim was to collect good quality data to which it could be modelled using the Site Availability Model (SAM) described in previous sections, effectively validating the model.

To cycle magnesium hydride using hot oil as the heat transfer fluid (HTF), the reactor first requires activation. This was achieved using OMEGA heating tape. Tests with the reactor filled with sand were heated using heating tape to ascertain a sufficient arrangement, which achieved a suitable temperature distribution across the reactor during activation.

The reactor was then filled with 26 μm magnesium spheres and activated by cycling 25 times under hydrogen using heating tape at 380°C and 13-14 barg. Once transferred to the hot oil circuit, the reactor was cycled under hydrogen 13 times with hot oil at 300°C and 12 barg. In this chapter, the experimental and simulation results are presented and discussed.

6.2 Experimental results

6.2.1 Uniform temperature profile tests

The use of heating tape can cause difficulty in reaching temperature uniformity, hence the need for these tests. Experiments were performed whereby 500 μm sieved sand was heated and left to reach steady state. The aims were:

- reaching uniform temperature along the reactor centre-line.
- determine the heat losses of this system and find a sufficient insulation arrangement.

Figure 6.1 shows the position of the centre-line, and the crosses indicate the positions at which a temperature readings occurred. This was achieved by sliding a type K thermocouple into the respective position.

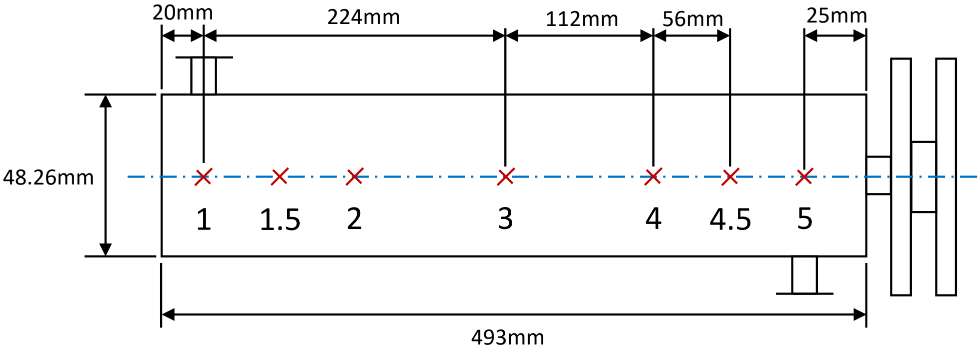

Figure 6.1: Test reactor showing approximate positions at where temperature was recorded

6.2.1.1 Configuration progress for activation

There were four tests in total where different insulation jacket and heating tape/rope arrangements were tested. The results of the tests are shown in figure 6.3 and the progress of the configurations in figure 6.2. A heating rope was included around the flange area to counter it acting as a heat sink, with the heating tape also concentrated near the flange end. In-between the jackets and reactor, loose quartz wool insulation was was packed in as tight as possible to help further minimise heat losses. The test 4 configuration resulted in a maximum temperature distribution of 10°C from the reactor centre point (3). This configuration was used during the activation experiments.

Test	Information	Pictures
1	Tape: temperature controlled position 3. Three insulation jackets used surrounding reactor, extra jacket as base. Loose sand at flange end.	
2	Tape: controlled position 3. Filled sand to flange end and Plugged tight with five 1 mm ENG fins. Extra jacket used on top. Added 2 extra thermocouples at position 1 and 5 between tape and jackets to monitor heat loss.	
3	Tape: controlled position 3. Added rope heater on flange. Rope: controlled (set point (SP) same as tape). Moved tape to concentrate at flange end.	
4	Same configuration as test 3. Tape: controlled position 3. Rope: controlled (SP above tape). Added loose insulation.	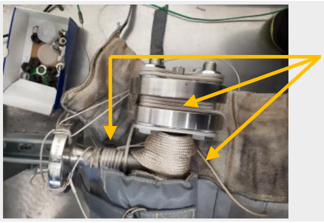 Areas loose quartz wool inserted

Figure 6.2: Progression of the insulation/heating arrangement for activation.

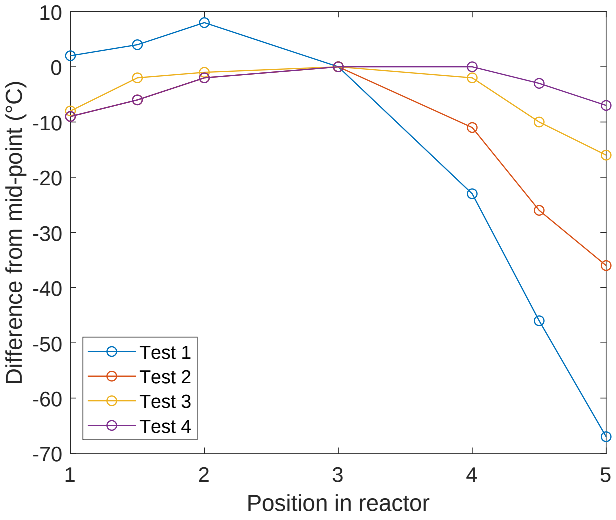

Figure 6.3: Illustration of the temperature difference from the reactor centre position.

6.2.2 Bed activation

6.2.2.1 Cycling

Figure 6.4 shows the activation results for the 154g magnesium reactor. The reactor was cycled 25 times with a full cycle taking 6.5 hours. However, the first hydrogenation was 24 hours. Dehydrogenation was performed in the morning, and hydrogenation in the afternoon, thus leaving the reactor at set temperature (≈ 380°C) in the hydride state overnight to minimise sintering. The heat input through the heating tape and rope was governed by the temperature set point and a typical temperature profile is shown in the next section.

For both hydrogenation and dehydrogenation, the capacity reached sufficient activation by the third run, and each subsequent run, followed a similar concentration profile. Run 15 had a slightly different profile as the regulator was changed to a higher pressure (16 barg). It was reduced back for later runs. After activation, approximately 7 wt% was achieved.

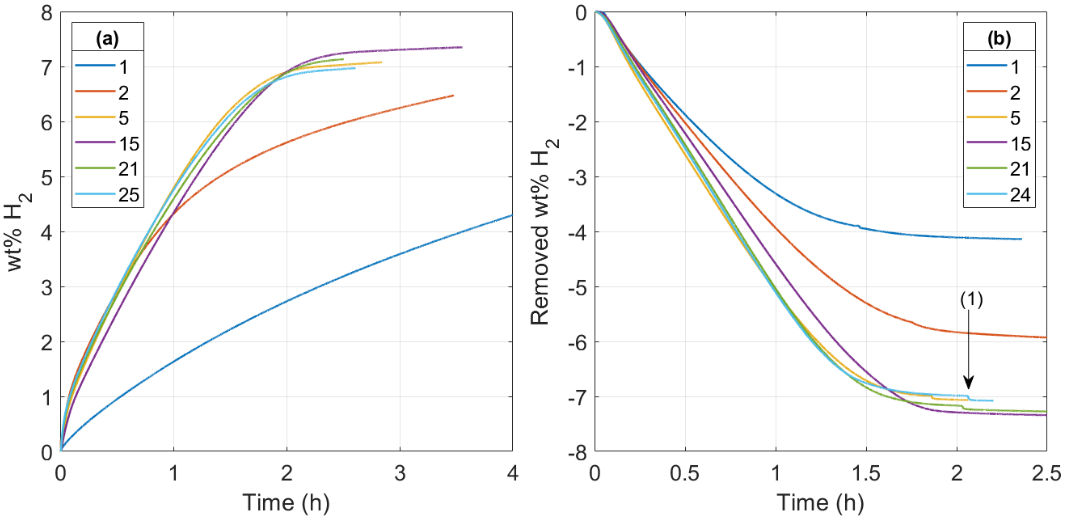

Figure 6.4: (a) Activation hydrogenation runs @ ≈ 380°C initial conditions and 25-26 barg. (b) Activation dehydrogenation runs @ ≈ 380°C initial conditions and 13-14 barg in reactor section and < -0.5 barg in manifold. (1) Discontinuity caused by opening vacuum line too suddenly.

6.2.2.2 Analysing run 006

Figure 6.5 shows the uptake and temperature results of the activation run 006. From figure 6.5a (hydrogenation) the reaction profile is different to common reaction profiles (such as first order). The reaction proceeds fast initially ($\Diamond_1$), enters into a linear trajectory for approximately an hour ($\Diamond_2$), and then tails off as the reactant depletes ($\Diamond_3$). Further, it is apparent that the linear increase in H_2 weight percent (wt%) correlates reasonably well with a constant TR3-TC2 (centre sensor) ($\Diamond_4$). This gives additional evidence that the rate determining mechanism for the majority of the reaction is centred around the rate removal of heat transfer, as discussed in the hydrogenation literature review and described by site de-activation within the site availability model (SAM). In addition, from the van't Hoff equation, the plateau at 420°C is 27 bar, which is the operating gas pressure. This provides further evidence that the bound pressure (P_B) approaches the gas pressure (P_g), causing the reaction rate to decrease ($\Diamond_5$), physically represented by site de-activation. There is also an increase in bed temperature on average by approximately 20°C. This may have been higher with improved insulation.

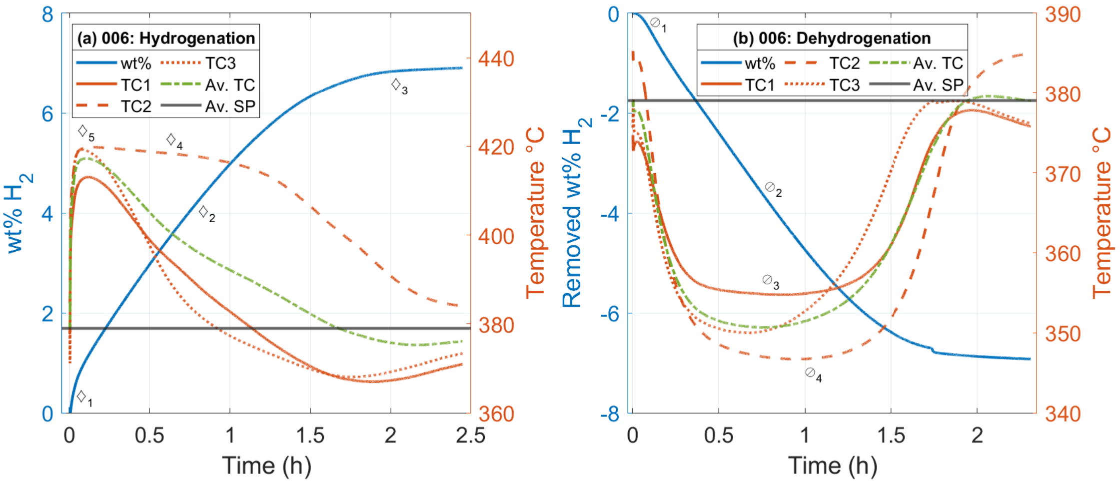

Figure 6.5: Hydrogenation and dehydrogenation reaction profiles of activation run 006. Temperature profiles are also shown. wt% = weight percent. TR3-TC1 = Farthest from hydrogen entry. TR3-TC2 = Middle. TR3-TC3 = Closest to hydrogen entry. SP = Set point. Av. = average. (a) Initial conditions 380°C and 26 barg. (b) Initial conditions 380°C and 13.5 barg.

With the dehydrogenation reaction profile (figure 6.5b), it begins with a sigmoid profile ($\oslash_1$), but then transitions to a linear removal profile ($\oslash_2$). The evidence of a sigmoid profile is further demonstrated through the inverted "top hat" temperature profile ($\oslash_3$), where the reaction peak is in the sigmoid centrepoint, as opposed to an initial temperature spike (for hydrogenation). Again, the linear removed wt% profile can be attributed to site de-activation, as TR3-TC2 shows a fairly constant temperature between 0.4 and 1.25 hours ($\oslash_4$). On average, there is a temperature drop of approximately 25°C for dehydrogenation. This data demonstrates 380°C is a good operating temperature for a MgH_2 TCES.

6.2.3 Bed cycling with hot oil

After activation, the hot oil circuit was commissioned. Unfortunately, this proved more challenging than expected and then with further delay due to COVID-19, there was around 6-8 months between activation and hot oil operation. The reactor was left in the metal state, and heated and cooled many times as the hot oil circuit was tested for leaks. This inadvertently may have influenced capacity. Once the system was leak tight, the reactor was cycled without insulation to try and re-activate the sample. The results from figure 6.6a suggest that approximately 85% re-activation had occurred. The Tool Temp TT-390 heater runs on Marlotherm SH, with a maximum operating temperature of 360°C. However, when leak testing, the loop experienced cavitation at the hot oil bypass valve above 310°C and less than 6 nl/min. Therefore, hot oil tests were performed at 302°C and 6 nl/min.

The insulation was installed from run 8 on-wards. The results of runs 10, 11, 12 and 13 are shown in figure 6.6. At 300°C and 9-14 barg, the hydrogenation achieved 5 wt% after 2.5 hours, and dehydrogenation took between 25-30 hours. The gas pressures are shown in figure 6.6b, where the initial drop in pressure is due to filling the reactor void volume, and the initial surge of hydrogen reacting.

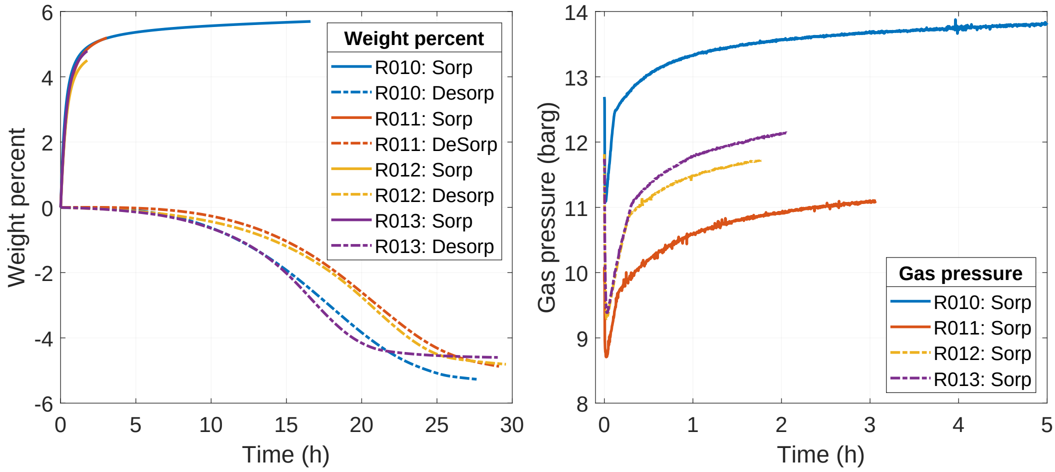

Figure 6.6: Experimental data of the 154 g magnesium reactor operating under hot oil at 300°C and 9-14 barg. (a) Weight percent data, both hydrogenation and dehydrogenation. (b) Gas pressure measured at transducer closest to reactor.

6.2.3.1 Run 011: Concentration and temperature

Figure 6.7 shows the temperature, pressure and concentration results of run 011 for both hydrogenation (9 to 11 barg) and dehydrogenation (-0.7 to -0.5 barg) at 302°C. The hydrogenation temperature spike (figure 6.7b) is not as high as expected. This may be due to the combination of: a low operating temperature, heat losses, entry of room temperature hydrogen into the bed, relatively high convective heat transfer coefficient, and incomplete re-activation. As the dehydrogenation has a slower reaction rate, it is no surprise that there was no change in bed temperature. The heat transfer fluid (HTF) IN and OUT sensors were attached as pipe surface thermocouples instead of being submerged within the fluid. As such, even though insulation surrounded them, the readings were lower than the bed temperatures. Unfortunately, due to the combination of low operating temperatures, high HTF flow rate, and surface HTF sensors, there was no observable change in the HTF temperature for both hydrogenation and dehydrogenation.

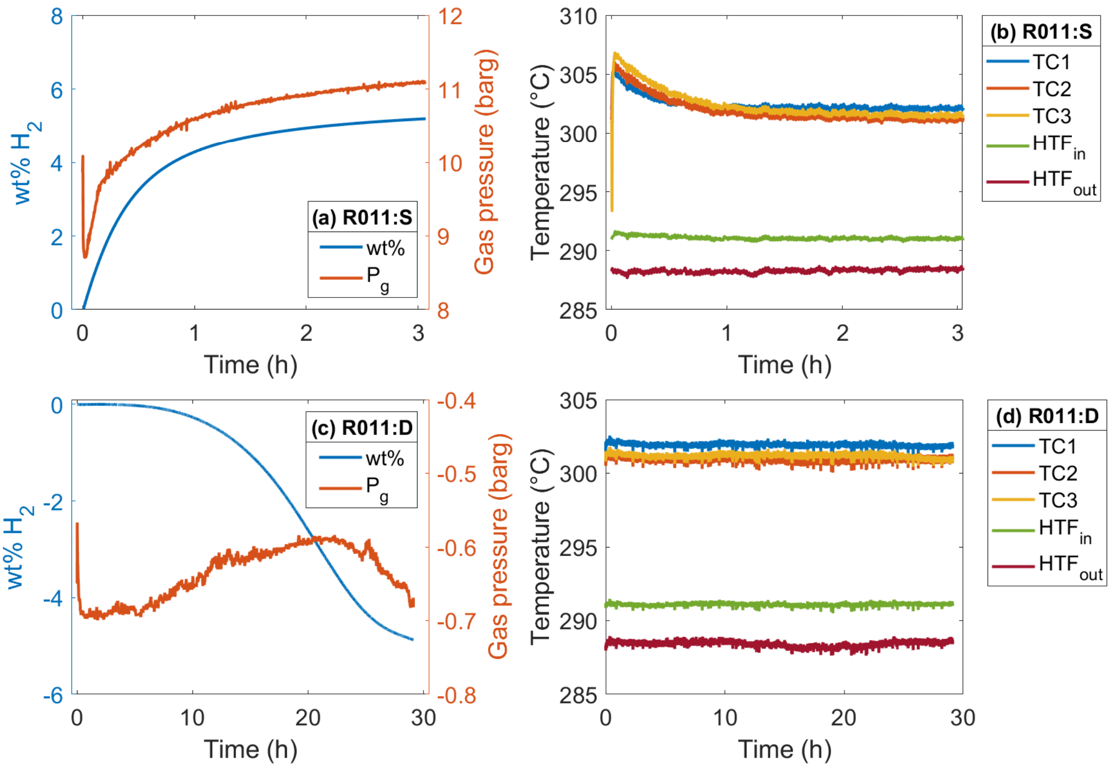

Figure 6.7: (a) Hydrogenation run 011. (b) Dehydrogenation run 011. (c) Hydrogenation temperature profiles (HTF = heat transfer fluid TR3-TC1 = Bed sensor closest to HTF$_{in}$, TR3-TC2 = Centre bed sensor, TR3-TC3 = Bed sensor cloest to HTF$_{out}$) (d) Dehydrogenation temperature profiles.

6.3 Experimental discussion

6.3.1 Activation

6.3.1.1 Accuracy of concentration measurements

It was found that during experiments, there were some design and operational issues that influenced the accuracy of the concentration measurements (through the flow meter).

For hydrogenation, at time = 0, the reactor was at ≈ -0.5 barg prior to gas entry. When the valve was opened, the system needed time to equalise, however the reaction was also progressing. This volume of gas was subtracted when the capacity was calculated, but it was estimated over a period of time. This estimation can influence the end capacity by approximately 0.1 - 0.5 wt%. If the reaction is fast (it is at 380°C), then this is problematic for hydrogenation, as the initial temperature spike is at the beginning. For future design, this problem can be mitigated with suitable valve positioning (close to reactor) and valve automation, such that the valve position is regulated to equalise quickly and then proceed at operating pressure.

For dehydrogenation, the reactor is isolated as the manifold is evacuated first. In this system, the pressure equalised to ≈ -0.5 barg quickly as the manifold was larger than the reactor void volume. Further, as magnesium hydride dehydrogenation does not exhibit an initial temperature spike, the surge effect on capacity (experienced with hydrogenation) is not encountered. Within this system, issues came from having to manually switch from vent to the vacuum pump, and operating within the flow meter range. I.e. the initial pressure equalisation would cause flow through the meter to reach above its limit of 25 nl/min, thus recording incorrect a flow rate. Again, these problems can be addressed with valve automation and flow meter switching, if needed.

6.3.2 Reactors in series

Due to outlet HTF temperature potentially only increasing by a small amount, reactors could be positioned in series. This allows, for example, a system of 30 reactors, to have 3 sets of 10 reactors with a $\Delta T_{HTF} = 10$°C for a total 100°C target. Each reactor would require its own gas pressure control and a customised material for the temperature range, suitable from both a thermodynamic and kinetic standpoint.

6.3.3 Reactor choice

Reviewing the shell & tube design, there is a disadvantage with powder positioned within the tubes, due to the smaller amount of material in a given volume. On the other hand, it allows for more effective heat transfer, which may be necessary for powders, where a small increase in radius can dramatically increase the conductive resistance (as shown in figure 4.15b).

The other disadvantage of a positioning powder within the shell (outside the tubes) is that it would be harder from a mechanical design perspective to handle daily large pressure swings (in this case up to 35 bar to 0.1 bar). Powder positioned within the tubes can handle the pressure swings more effectively.

The pressure swing becomes more important as the vessel gets larger. If the HTF was chosen to be gas (such as helium for a 720°C CSP receiver loop) then the low heat transfer coefficient will require a large heat transfer area to meet the required outlet HTF temperature. This will likely mean a very long reactor. Due to necessity in handling daily pressure swings, and a high overall heat transfer coefficient, a shell and tube reactor seems most viable.

6.3.4 Lessons learnt

6.3.4.1 Thermal oil

Thermal oil is a excellent heat transfer fluid (HTF) once working, but it is intricate to get operational. Contact the supplier of the fluid for parts, construction and insulation materials, good pipework design practice (such as minimal fittings), and commissioning procedures (such as gasket tightening procedure). Thermal oil regularly operates above the flash point and thus a circuit should be designed so no air build up occurs. Thermal oil has a lifetime, and if constantly operating (24 hours a day), regular tests are required (every 6 months) to indicate when the oil needs replacing/diluting to reduce light ends (light hydrocarbon gases and liquids). In addition, thermal oil is usually designed to operate for long periods at operating temperature, so it is recommended to design the system to operate continuously.

6.3.4.2 State of charge

With metal hydride thermal energy stores, the state of charge (SoC) can be reduced if not handled correctly. With magnesium hydride, leaving it in the metal state for long periods at temperature can damage its capacity. As such, metal hydride beds should be left for long periods in the discharged state (hydride) or partially charged, to increase longevity.

6.3.4.3 Activation

For the 154g reactor, activation was performed using electrical heating tape. Due to the non-uniformity in temperature during the hot oil experiments, it should be possible to activate the sample using the thermal oil (HTF), making the overall process simpler.

6.3.4.4 Thermocouples

To get good measurements of the HTF at entry and exit of a reactor, sensors are recommended to be placed within the fluid, instead of being attached as pipe surface thermocouples. Regarding reactor bed thermocouples, a multi-point thermocouple assembly is recommended over multiple single thermocouples fed through the same fitting. Although single thermocouples are cheaper, assembly can cause these sensors to move unintentionally from the planned position. In addition, it is recommended to have a separate port for hydrogen transit and reactor thermocouples.

6.4 Simulation results and discussion

6.4.1 Activation: hydrogenation

6.4.1.1 Methodology

The SAM:DR and SAM rate equations were used for the hydrogenation activation run 006, where the parameters determined in chapter (4) were inserted (e.g. A_e and E_e). The total internal reactor volume was used for concentration, and section 3.3.2 shows the geometry, boundary conditions and useful data regarding these simulations. The wire pitch was changed (either 6 or 39) as a variable for the thermal resistance in the radial direction.

6.4.1.2 Results and discussion

With appropriate thermal resistance (6 wires), both rate laws (SAM and SAM:DR) give good fits. From figure 6.8a, the SAM with thermal resistance at 6 wires exhibited the best fit ($R^2 = 0.9957$). Whereas, from figure 6.8b, the SAM:DR extension from first glance appears to represent the temperature descent more sufficiently. However, as heat losses would heavily influence this trajectory, it is not possible from figure 6.8b to definitively confirm which model exhibits the optimum fit. This is evident from observing the experimental average temperature (an average of TR3-TC1, TR3-TC2 and TR3-TC3 as shown in figure 3.8), where the bed temperature goes below 380°C as the heater could not transfer heat fast enough, and the heat losses lowered the curve past the set point.

The modelling also suggests that the activation tests were heat transfer limited. This is apparent from observing the significant change in uptake when switching the wire pitch from 6 to 39. Changes to the uptake profile between SAM:DR and SAM were small. As such, is it difficult to determine which rate law is more effective, as the differences could have been covered by the error in representing thermal resistance "effectively" through wire pitch.

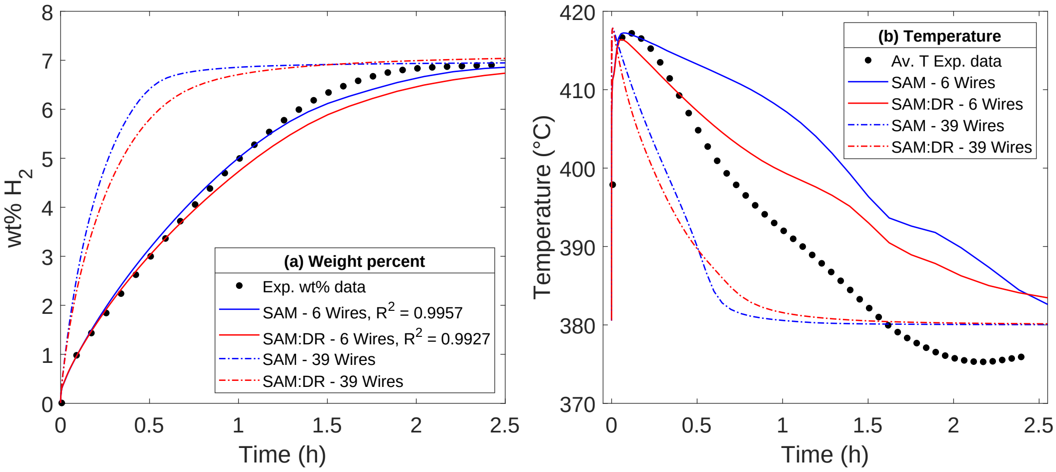

Figure 6.8: SAM and SAM:DR models for activation run 006. 2 thermal resistance scenarios based on 6 wires and 39 wires. (a) Weight percent chart, (b) temperature chart. Av. T = average temperature

6.4.2 Activation: dehydrogenation

6.4.2.1 Methodology

The boundary condition was set at 380°C & the maximum hydride fraction was $x_m = 0.925$. The geometry, and other parameter listed in the hydrogenation methodology were used (e.g. metal mass, internal volume) & the parameters used within SAM:ACR:SC:F were taken from the chapter 5, i.e. for A_e, E_e and k_F. Again, both scenarios of varying wire pitch (6 and 39) were tested.

6.4.2.2 Results and discussion

Figure 6.9 shows the COMSOL results against the experimental data. The best fit occurred when the wire pitch = 6, the same for hydrogenation. This provides confidence that the "effective" thermal resistance parameter through varying wire pitch has worked well. The wt% removal profile at "Wire 6" shows a similar shape to the experimental data. With the temperature curve, the overall shape is similar, except the modelled temperature is lower. This could be due to the heating tape receiving a signal to transfer more heat to counteract the endothermic reaction, and the net heat transferred is greater than the constant boundary temperature provides (in the model), hence a lower experimental peak temperature. In general however, the SAM:ACF:F model has sufficiently modelled the dehydrogenation reaction at 380°C with an $\mathrm{R}^2 = 0.9941$.

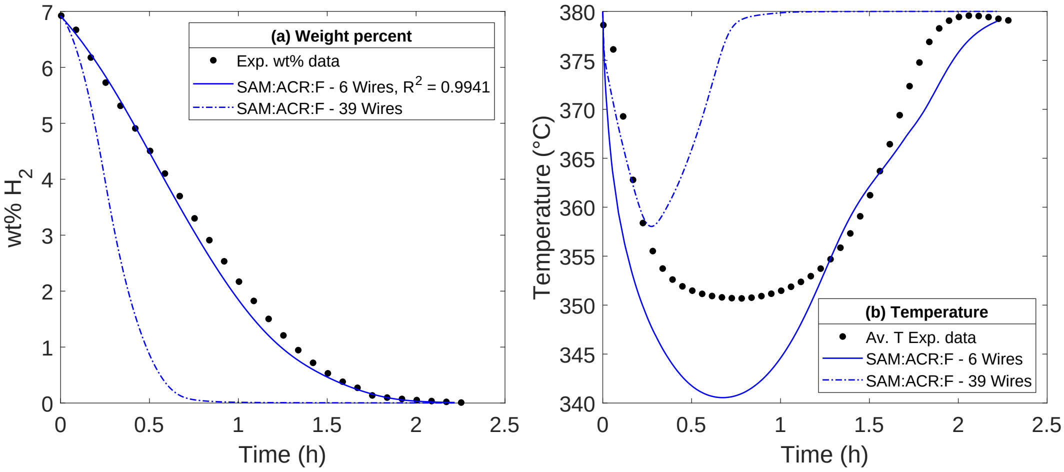

Figure 6.9: Activation run 006: SAM ACR-SC-F at the 2 thermal resistances used in hydrogenation. Initial conditions, 380°C and vacuum conditions.

6.4.3 Hot oil: hydrogenation & dehydrogenation. Run 011

6.4.3.1 Methodology

The bulk of the hot oil simulation methodology (geometry, boundary conditions, equations) is shown in section 3.3.3 of the experimental methods chapter. Again, parameters determined previously in the SAM, SAM:DR and SAM:ACR:SC:F models are unchanged (e.g. A_e, E_e etc.), with the reactor volume being used to calculate concentration. The initial temperature was set at 302°C and the gas pressure was imported experimental data.

6.4.3.2 Results and discussion

For the hydrogenation run, the SAM:DR model exhibited a superior fit than the original SAM model, as shown in figure 6.10a. Although the trajectory is not entirely correct, a R^2 of 0.9898 has been achieved using the SAM:DR model. As the bed may have not been fully re-activated, this could have influenced the kinetics and therefore the concentration (hydride fraction) curve. Figure 6.10b shows the results of the dehydrogenation simulation. Using the SAM:ACR:SC:F, a fit of $R^2 = 0.9941$ has been achieved using $k_F = 1$ and $C_{H \cdot M_0} = (0.9995)C_T$. The value of 0.9995 is different than the values regressed within chapter 5 (around 0.995). This shows the reaction was slower than the small sample, again this may have been influenced by the bed not being fully re-activated.

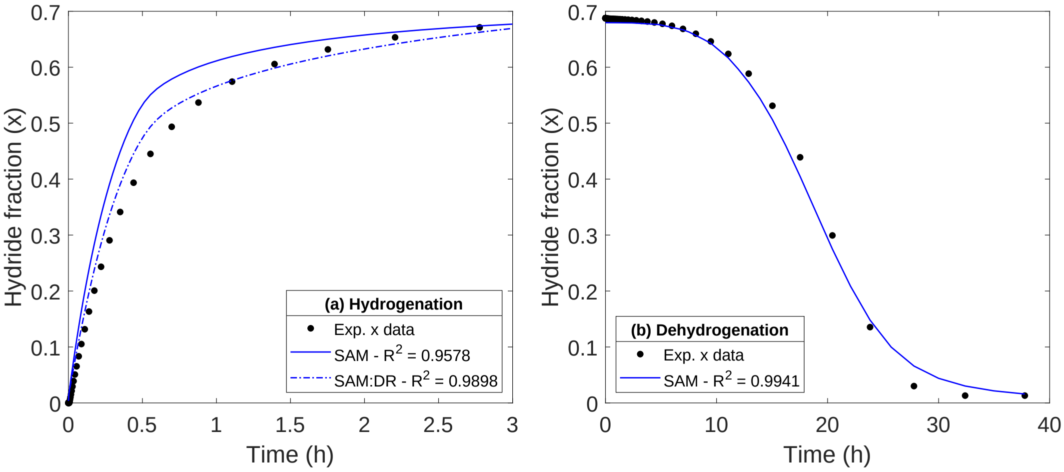

Figure 6.10: (a) Hydrogenation of run 011. SAM: $x_m = 0.82$, SAM:DR $x_m = 0.9$ (b) Dehydrogenation of run 011. SAM:ACR:SC:F $x_m = 0.68$, 'const' $= 0.9995$, $k_F = 1$

6.4.4 Simulated hot oil operation at 330°C

Applying the SAM for hydrogenation and the SAM:ACR:SC:F model for dehydrogenation, an initial temperature of 330°C, an over-pressure of 1 for hydrogenation, a pressure of 1 bar for dehydrogenation, and an maximum hydride fraction of 0.67, gives the results shown in figure 6.11.

At 330°C, metal hydrogenation is faster than magnesium hydride dehydrogenation, where hydrogenation resulted in an average bed peak difference of 30°C, while dehydrogenation only had a 10°C decrease. The hydrogenation peak can be increased with increasing the gas pressure, however dehydrogenation requires a higher operating temperature to give a larger average bed temperature reduction. Analysing the rate constant and equilibrium pressure for this sample, shows that the thermodynamics, forward and backward rate are acceptable $\geq$ 360°C.

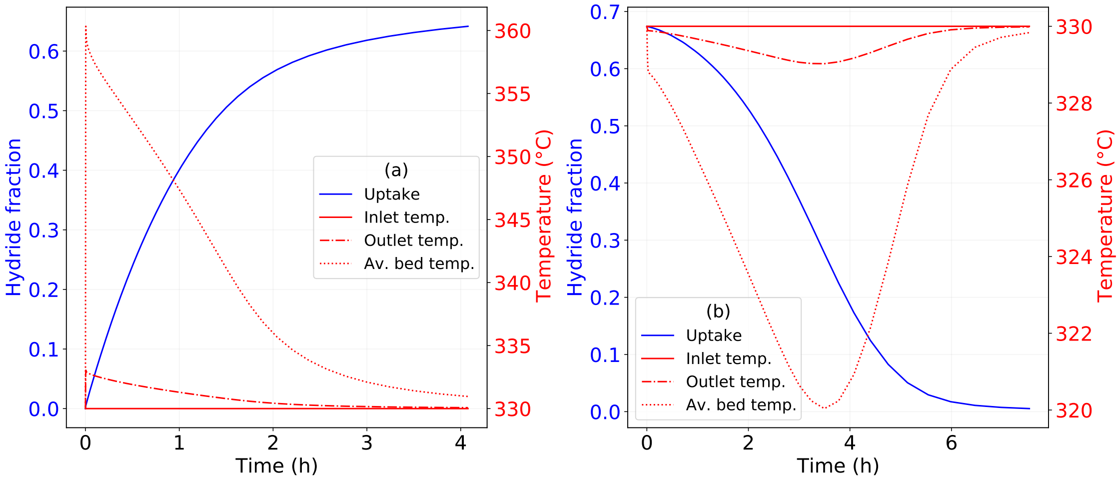

Figure 6.11: Simulated large lab-scale reactor at 330°C with Marlotherm SH as the heat transfer fluid. (a) Hydrogenation at one over-pressure, (b) Dehydrogenation at one bar.

6.4.5 Using the gas pressure for reactor control

Increasing the over-pressure during hydrogenation can in theory enable a higher outlet HTF temperature, as the bed can get hotter. The simulations suggest that the gas pressure can be modified to encourage a flat outlet temperature profile for an adequate time period (up to 30 minutes). Figure 6.12a shows an example of this.

If the HTF flow rate (and thus heat transfer coefficient) is increased to improve heat transfer, then there is a lower bed temperature and then a lower outlet HTF temperature (figure 6.12b). Therefore, there is a zone (to which the engineer aims to), where there is a sufficient gain in HTF ($T_{out} - T_{in}$), a large enough overall heat transfer coefficient (U) and heat transfer area (A) to transfer thermal energy to the HTF, while keeping the reaction rate at an appreciable rate so reaction completion is not too slow or fast, but with gas pressure control and some site de-activation to hold a sufficiently hot bed temperature for a reasonable time period, enabling a constant HTF outlet temperature and useful work from the fluid.

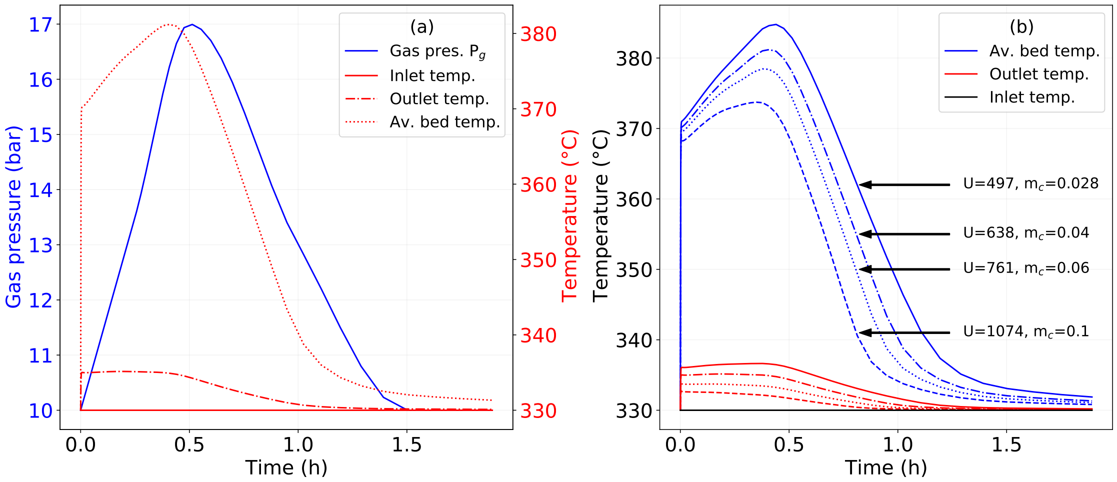

Figure 6.12: (a) Simulation @ 330°C and one over-pressure with a varied gas pressure causing a constant outlet temperature for 30 minutes. (b) Effect of the outlet temperature with variation in heat transfer coefficient (U) and mass coolant flow rate (m_c).

6.4.6 5kg test scale model

A multi-tube reactor with a single inner tube and outer annulus has been modelled to test the SAM at larger scale. With radius 30 mm and length 2 m, including 40 5mm steel lateral fins and a bulk density of 1000 kg m^{-3}, the total magnesium capacity = 5 kg. The initial temperature = 400°C, constant gas pressure of 25 bar, an assumed coolant flow rate of 0.03 kg/s and convective heat transfer coefficient of 250 W m^{-2} K^{-1}. The results are shown in figure 6.13, where the model and method applying a heat transfer coefficient at the boundary has been successful, showing a $\Delta T > 5$°C of the HTF for up to 8 hours.

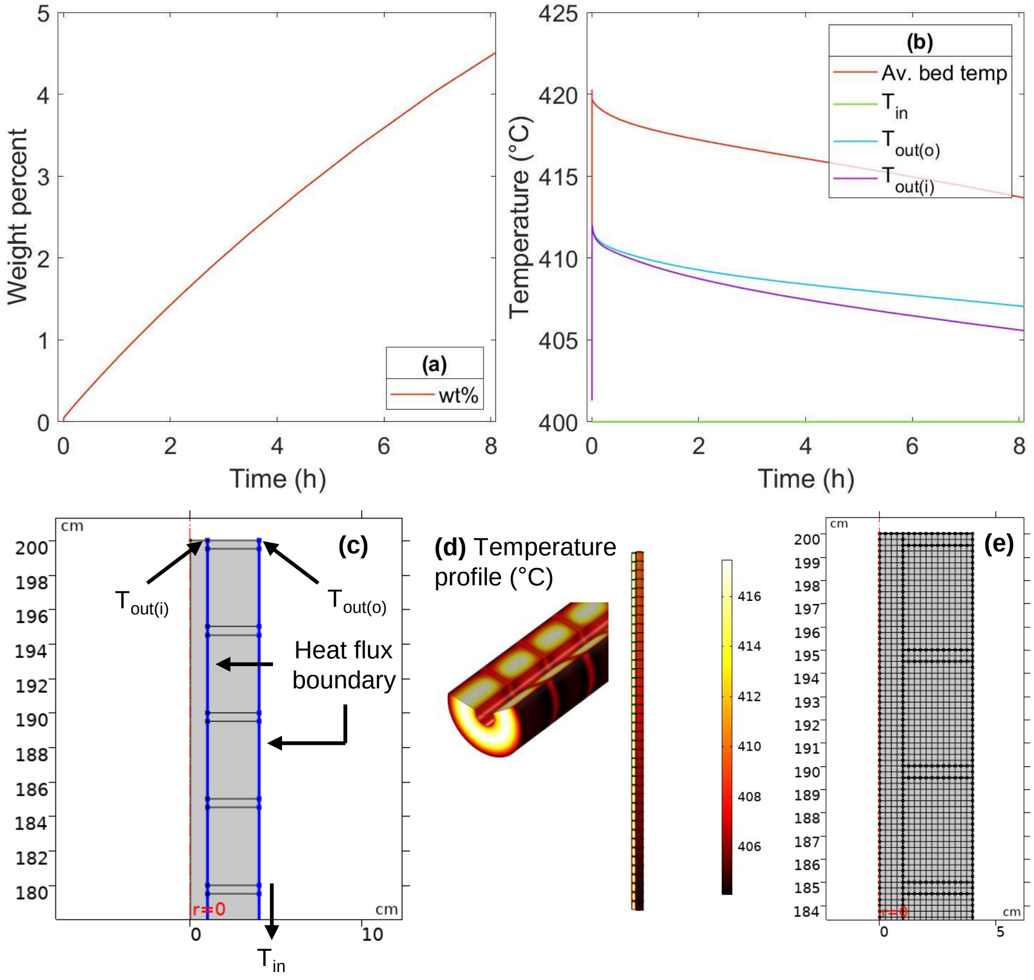

Figure 6.13: (a) Weight percent profile up to 8 hours. (b) Temperature profile up to 8 hours. (c) Illustration of the additional inner tube and subsequent additional heat flux boundary (d) Temperature profile at 8.8 hours (e) Mapped mesh used: number of vertex elements = 164, number of boundary elements = 3380.

6.4.6.1 Control scheme

The phenomenon of site de-activation can in theory be used to control the reaction rate. In figure 6.14, a simplified control scheme is illustrated with reactor pressure control. The 3-way control valve acts as the pivot between hydrogenation and dehydrogenation.

In hydrogenation mode, the control valve is controlled by the desired pressure downstream, which is also twinned to the temperature sensors within the reactor and HTF. Thus, if a higher HTF ΔT is required, more pressure is introduced, and likewise, if the rate needs reducing, then the gas pressure can be pinched towards the bound pressure governed by the van't Hoff equation, and determined through the temperature readings. If defects/phase changes do impose higher bound pressures then the additional defect pressure should be included. Tight control is necessary, because if the gas pressure is decreased too much, then the reactor is pushed into dehydrogenation conditions. The same concept applies for dehydrogenation but in reverse.

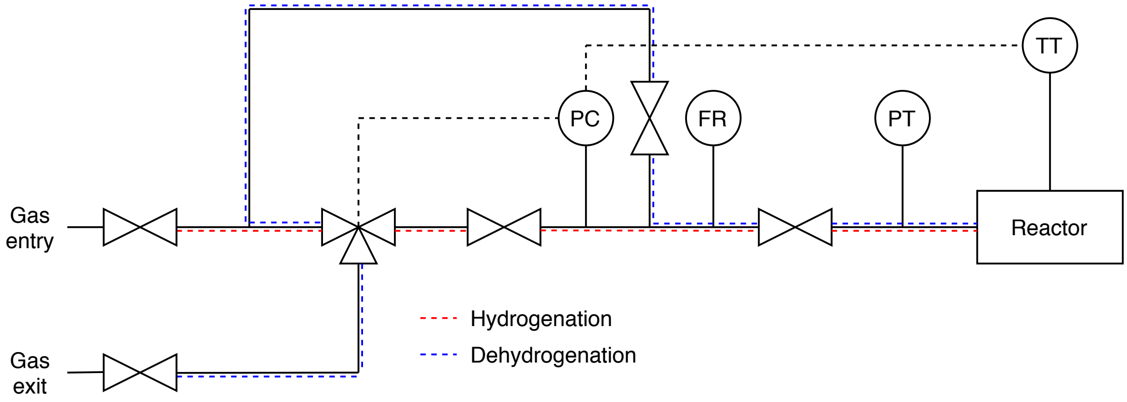

Figure 6.14: Simplified control scheme for proposed single reactor operation under pressure control. PC - pressure control. FR - flow recorder. PT - pressure transmitter. TT - temperature transmitter.

6.5 Importance of bulk density

From the current reactor designs in the literature review (section 2.5.2), Bogdanovic et al. noted the importance of bulk density. To gain better understanding, calculations have been performed here to assess this at commercial scale. Two reactors are compared, the shell & tube, and jacketed vessel. As from figure 6.15, the shell & tube case requires around 60 reactors to provide 7 hours of energy storage for approximately 1000 MWh_{th} capacity. Whereas a jacketed vessel, would require approximately half as many at the same bulk density of 1.3 g cm^{-3}. Note that using a bulk density of 0.75 g cm^{-3}, such as used in Bogdanovic et al's paper, approximately 50 reactors are required. This demonstrates the need for finding an optimum bulk density. The assumptions are:

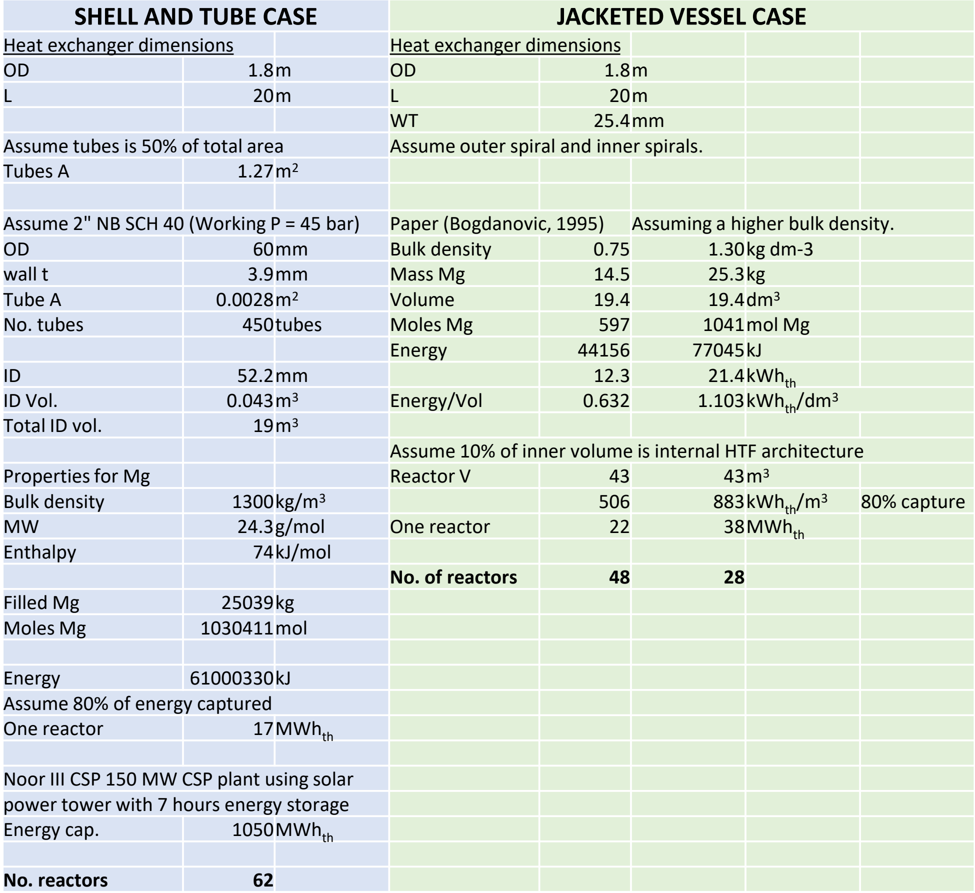

SHELL AND TUBE CASE		
Heat exchanger dimensions		
OD	1.8	m
L	20	m
Assume tubes is 50% of total area		
Tubes A	1.27	m^2
Assume 2" NB SCH 40 (Working P = 45 bar)		
OD	60	mm
wall t	3.9	mm
Tube A	0.0028	m^2
No. tubes	450	tubes
ID	52.2	mm
ID Vol.	0.043	m^3
Total ID vol.	19	m^3
Properties for Mg		
Bulk density	1300	kg/m^3
MW	24.3	g/mol
Enthalpy	74	kJ/mol
Filled Mg	25039	kg
Moles Mg	1030411	mol
Energy	61000330	kJ
Assume 80% of energy captured		
One reactor	17	MWh_{th}
Noor III CSP 150 MW CSP plant using solar power tower with 7 hours energy storage		
Energy cap.	1050	MWh_{th}
No. reactors	**62**	

JACKETED VESSEL CASE				
Heat exchanger dimensions				
OD	1.8	m		
L	20	m		
WT	25.4	mm		
Assume outer spiral and inner spirals.				
Paper (Bogdanovic, 1995)		Assuming a higher bulk density.		
Bulk density	0.75	1.30	kg dm-3	
Mass Mg	14.5	25.3	kg	
Volume	19.4	19.4	dm^3	
Moles Mg	597	1041	mol Mg	
Energy	44156	77045	kJ	
	12.3	21.4	kWh_{th}	
Energy/Vol	0.632	1.103	kWh_{th}/dm^3	
Assume 10% of inner volume is internal HTF architecture				
Reactor V	43	43	m^3	
	506	883	kWh_{th}/m^3	80% capture
One reactor	22	38	MWh_{th}	
No. of reactors	**48**	**28**		

Figure 6.15: Calculations to determine rough number of reactors required in order to meet 7 hour energy storage at the state of the art Noor III CSP 150 MW CSP plant in Morocco.

1. The reactors are nominal bore (NB) of 1.8m and length 20m with the volume assumed as a cylinder.

2. For the shell & tube case, the tubes are assumed 50% of the cross section area, with 2" NB tubes at schedule 40. The bulk density is assumed as 1.3 kg m^{-3} where 80% of the enthalpy of reaction is captured.

3. For the jacketed vessel case, the data is ratio-ed from the reactor detailed in Bogdanovic et al's paper [11]. A wall thickness of 25.4 mm is assumed. Again 80% energy capture is

assumed and that 10% of the inner volume is occupied for internal HTF architecture.

4. In both cases, the Noor III CSP 150 MW CSP plant is compared to. This plant is the third part of the Ouarzazate Solar Power Station based in Morocco.

In either case, it is also clear that metal hydride thermo-chemical energy storage is suitable as a MWh energy storage. For example, a proposed parabolic trough 100 MW plant in the Middle East is to have a monthly energy generated variation from 10 GWh (November) to 40 GWh (June) [73]. To account for just 20 GWh would require approximately 600 reactors. And within this, hydrogen storage tanks have not been considered. Therefore, although metal hydride thermo-chemical energy storage has the theoretical capability to be seasonal, it is limited by the engineering.

6.6 Large lab-scale chapter summary

A 154 g magnesium large lab-scale reactor was successfully activated using electrical heating tape at 380°C over 25 cycles. After, the reactor was cycled 13 times using thermal oil as the heat transfer fluid (HTF). The sample was sufficiently re-activated ($\approx 85\%$) so results could be attained. Although full re-activation was not achieved, thus the temperature results were not ideal, the concentration results could be modelled.

In this regard, the SAM, SAM:DR and SAM:ACR:SC:F were successful in representing the kinetics when the reactor was run under HTF and when activated using heating tape. As best to my knowledge, this is the first time a magnesium hydride system has been successfully validated at this scale under both HTF or electrical heating. Further, control scheme improvements are proposed and the bulk density has been highlighted as an important parameter in reducing the number of reactors at large scale.

Chapter 7

Conclusion

7.1 Modelling magnesium hydrogenation kinetics

Current models for representing magnesium hydrogenation vary in approach, with some including a dimensionless pressure term (2.3.2), others with diffusion controlling or nucleation & growth mechanisms (2.3.1), or a shrinking core (2.2.2.4). Many models combine the mechanisms above. These current models for magnesium hydrogenation were tested on kinetic experiments collected on a Sievert's apparatus. It was found these models do not represent the kinetics at conditions of practical interest (4.2).

As such, a new model framework was developed to represent magnesium hydrogenation. This blended previous work with novel ideas, encapsulated within the Site Availability Model (SAM). The foundation of the framework was based on site theory by the work of Langmuir (2.2.2) and the incorporation of a shrinking core 4.3.6. Site theory was applied to the dimensionless pressure term, giving the "site availability term" and the "site availability driving force" (4.3.3). This foundation was used as a base to build upon. From this, extensions were developed to the SAM, these are: SAM:ES, SAM:D+ES, SAM:EM (4.4) and the SAM:DR extension (4.3.8).

The most promising model was the Site Availability Model including the defects plus relaxation theory (SAM:DR), where the magnesium hydrogenation kinetics were successfully modelled at temperatures 330-400°C and pressures 8-40 bar (4.6.3). This is a first for this system, as best to my knowledge.

The main conclusions from the SAM:DR extension are covered here. When the conditions drift further from equilibrium and at higher temperatures, the site availability term starts to heavily influence the reaction rate. As such, it is proposed the site availability is accounting for the complex interactions between the hydrogen in the lattice, where these interactions can alter the site availability driving force. The addition of hydrogen can introduce defects into the lattice, which strains the bonds around the defective site. This is equivalent to adjacent sites being made unavailable, and the site availability driving force being reduced. Countering bond straining, it is further proposed that the bonds can be also be relaxed/re-organised, which is assumed to occur during the phase transition from the co-existence phase, to the hydride phase. This relaxation reduces the effective pressure of the reaction front, resulting in a linear uptake profile at high weight percent and potential improvement in capacity. It can be concluded that both the addition of bond strain (resulting in non-stoichiometry) and bond relaxation are a function of temperature and pressure. The modelling suggests for the Mg-MgH_2 system, the onset of defects occurs sooner than bond relaxation, but the bond relaxation starts to influence greater than the defect generation at higher temperatures and pressures ($\approx \geq$ 360°C @ 32 bar) and starts to dominate around 380°C ($\approx$ @ 24 bar). In effect, the bonds straining and relaxing may be related to the hydrogen interactions, where straining induces repulsive interactions and relaxation, promotes attractive interactions. See section 4.6.4 for more.

The site availability appears to be an important and governing concept that is incorporated within the surface resistance; this provides counter evidence to the common claim that the rate determining step is the internal diffusion of dissociated hydrogen through the hydride layer (4.3.6). As the SAM model is based on a surface reaction front (4.3.5), then application of the SAM suggests that the surface area is a critical component in determining the kinetic performance of a magnesium hydrogenation reaction.

7.2 Modelling magnesium hydride dehydrogenation kinetics

Metal hydride dehydrogenation kinetics have been less developed than the hydrogenation reaction. Applying rate laws from literature on gathered magnesium dehydrogenation data, the best fit model was the Sestak-Berggren model (5.2.3). However, this is an empirical model, so may have exhibit problems when transferring to large scale. Other models also either incorrectly/omit important physical phenomena, whether that be the observation that the reaction rate can be heat transfer controlled (5.2.4), or the sigmoidal weight percent profile is not represented (5.2.2).

Therefore, the Site Availability Model (SAM) was used as a framework to develop models for magnesium hydride dehydrogenation kinetics. Theory, such as an auto-catalytic reaction, a shrinking core or an expanding core and particle fragmentation were introduced (5.3). The most successful model for magnesium hydride dehydrogenation kinetics was the SAM:ACR:SC:F - the Site Availability Model incorporating an auto-catalytic reaction (ACR), shrinking core (SC) and particle fragmentation (F). This model represented the dehydrogenation of MgH_2 at all the conditions for practical purposes - dehydrogenation $<$ 1 bar at temperatures from 360°C - 400°C from hydrogenation conditions 360°C - 400°C @ 8 - 32 bar (5.4.4).

An auto-catalytic reaction switches from a sigmoidal shape to a first order shape with an increase in rate constant (k) or auto-catalyst concentration, where the addition of dopants (e.g. Ti, Nb, Cr) may be linked to this profile change (5.3.6). In addition, fragmentation is a function of temperature and pressure, where it is included with a shrinking core mechanism, resulting in an effective expanding core. The SAM:ACR:SC:F was checked for use using the Kissinger method, and it was found that there was negligible difference when determining the activation energy and pre-exponential factor through either assuming a first order or SAM:ACR:SC:F rate law (5.3.7).

From experimental data, the dehydrogenation of MgH_2 is dependent on the previous magnesium hydrogenation conditions, where the fastest dehydrogenation occurred after a PCI, then followed by high pressure hydrogenation. This provides evidence to suggest defects play a role, as the dehydrogenation site availability driving force (SA-DF) is increased due to higher bound pressure (imposed by the defects) during hydrogenation (5.1).

7.3 Large lab-scale reactor

A 154g lab-scale reactor was filled with 26 μm magnesium spheres where heat was supplied both by electrical tape or heat transfer fluid (Marlotherm SH). The aim was to test models developed in the previous chapters at larger scale.

Using 26 μm magnesium spheres, the 154 g sample activated in a similar fashion to the activation of a 0.2 g sample. The 154 g reactor successfully recovered capacity during activation and maintained its capacity to the 25th cycle, where the 154 g sample exhibited a similar de/hydrogenation temperature profile to the 0.2 g sample (6.2.2).

The SAM and SAM:DR hydrogenation models and the SAM:ACR:SC:F dehydrogenation model successfully modelled the activation experiments, resulting in $R^2 = 0.99$ for both hydrogenation and dehydrogenation (6.4.1 and 6.4.2). When the reactor was run using thermal oil, the SAM, SAM:DR and SAM:ACR:SC:F again were successful in representing the kinetics (hydrogenation and dehydrogenation $R^2 = 0.99$) (6.2.3). This indicates that these models show good intensive characteristics and are suitable for large scale magnesium hydride reactors.

It can be concluded that through simulations, that when a HTF was included, the change in gas pressure (P_g) can be used to deliver a constant outlet HTF temperature for a significant time period (6.4.5). With a reduction in HTF flow rate, and therefore a reduction in heat transfer coefficient, the HTF absorbed more thermal energy, thus delivering a hotter outlet HTF (6.4.5). The phenomenon of site de-activation can be utilised for reactor control, whereby the gas flow rate is regulated by a pressure controller coupled to the temperature readings in the reactor (6.4.6.1).

A shell and tube design appears to be the most effective metal hydride TCES, where further work is required on the finding an optimum bulk density (6.5).

7.4 Future work

In this thesis, understanding in the design of a metal hydride TCES has been developed through the implementation of the Site Availability Model (SAM). Although the focus was on coupling a TCES to CSP, another opportunity has emerged with the coupling of thermal energy storage to agile ammonia synthesis. Figure 7.1 details a potential position of a TCES unit when linked to an ammonia synthesis reactor. Introducing a thermal battery in a green ammonia plant, which typically operates under transient conditions, will improve efficiency and plant performance. As ammonia synthesis operates from 380 - 500°C, magnesium hydride is a suitable candidate, where the task is develop a TCES for this system and determine the viability.

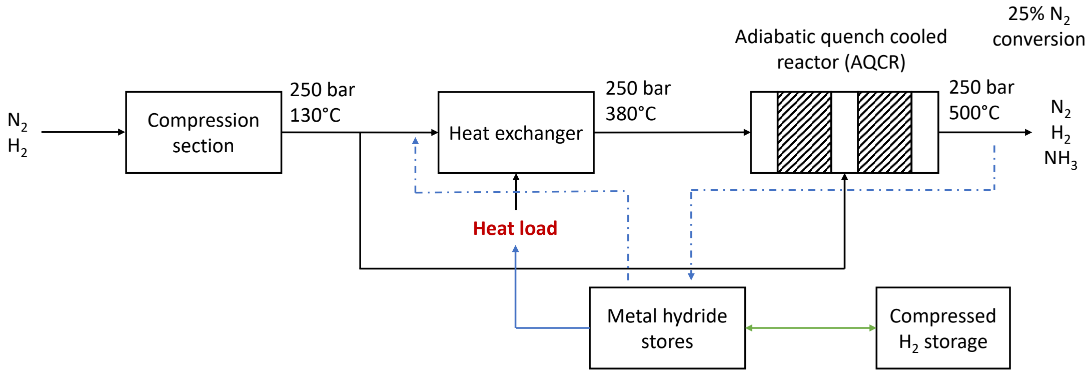

Figure 7.1: Useful work extracted downstream of the AQCR to charge the TCES, with delivery before the reactor pre-heater. Shown is a simplified two stage adiabatic quench cooled reactor (AQCR). Conditions and conversion from [40].

References

[1] Marcus Adams et al. "Modelling a kinetic deviation of the magnesium hydrogenation reaction at conditions close to equilibrium". In: *International Journal of Hydrogen Energy* (May 2019). ISSN: 0360-3199. DOI: `10.1016/J.IJHYDENE.2019.04.036`. URL: `https://www.sciencedirect.com/science/article/pii/S0360319919314272`.

[2] R.K. Ahluwalia. "Sodium alanate hydrogen storage system for automotive fuel cells". In: *International Journal of Hydrogen Energy* 32.9 (June 2007), pp. 1251–1261. ISSN: 0360-3199. DOI: `10.1016/J.IJHYDENE.2006.07.027`. URL: `https://www.sciencedirect.com/science/article/pii/S0360319906003661`.

[3] Rene Albert, Robert Urbanczyk, and Michael Felderhoff. "Thermal conductivity measurements of magnesium hydride powder beds under operating conditions for heat storage applications". In: *International Journal of Hydrogen Energy* 44.55 (Nov. 2019), pp. 29273–29281. ISSN: 0360-3199. DOI: `10.1016/J.IJHYDENE.2019.01.218`. URL: `https://www.sciencedirect.com/science/article/pii/S0360319919303994`.

[4] Jullian Ambrose. *Covid-19 crisis will wipe out demand for fossil fuels, says IEA*. 2020. URL: `https://www.theguardian.com/business/2020/apr/30/covid-19-crisis-demand-fossil-fuels-iea-renewable-electricity`.

[5] Mélvin Avrami. "Kinetics of phase change. I: General theory". In: *The Journal of Chemical Physics* 7.12 (1939), pp. 1103–1112. ISSN: 00219606. DOI: `10.1063/1.1750380`. URL: `http://scitation.aip.org/content/aip/journal/jcp/7/12/10.1063/1.1750380%5Cnhttp://scitation.aip.org/deliver/fulltext/aip/journal/jcp/7/12/1.1750380.pdf;jsessionid=77n8rt14s5smr.x-aip-live-03?itemId=/content/aip/journal/jcp/7/12/10.1063/1.1750380&mimeType=`.

[6] Zewei Bao et al. "Simulation studies on heat and mass transfer in high-temperature magnesium hydride reactors". In: *Applied Energy* 112 (2013), pp. 1181–1189. ISSN: 03062619. DOI: `10.1016/j.apenergy.2013.04.053`.

[7] Zewei Bao et al. "Three-dimensional modeling and sensitivity analysis of multi-tubular metal hydride reactors". In: *Applied Thermal Engineering* 52.1 (2013), pp. 97–108. ISSN: 13594311. DOI: `10.1016/j.applthermaleng.2012.11.023`. URL: `http://dx.doi.org/10.1016/j.applthermaleng.2012.11.023`.

[8] Gagik Barkhordarian, Thomas Klassen, and Rüdiger Bormann. "Kinetic investigation of the effect of milling time on the hydrogen sorption reaction of magnesium catalyzed with different Nb2O 5 contents". In: *Journal of Alloys and Compounds* 407.1-2 (2006), pp. 249–255. DOI: `10.1016/j.jallcom.2005.05.037`.

[9] Roger L. Blaine and Homer E. Kissinger. “Homer Kissinger and the Kissinger equation”. In: *Thermochimica Acta* 540 (July 2012), pp. 1–6. ISSN: 0040-6031. DOI: `10.1016/J.TCA.2012.04.008`. URL: `https://www.sciencedirect.com/science/article/pii/S0040603112001633`.

[10] Tina Block and Martin Schmücker. “Metal oxides for thermochemical energy storage: A comparison of several metal oxide systems”. In: *Solar Energy* 126 (Mar. 2016), pp. 195–207. ISSN: 0038-092X. DOI: `10.1016/J.SOLENER.2015.12.032`. URL: `https://www.sciencedirect.com/science/article/pii/S0038092X15007057?via%3Dihub`.

[11] Borislav Bogdanović et al. “Thermodynamic investigation of the magnesium–hydrogen system”. In: *Journal of Alloys and Compounds* 282.1-2 (Jan. 1999), pp. 84–92. ISSN: 09258388. DOI: `10.1016/S0925-8388(98)00829-9`. URL: `http://linkinghub.elsevier.com/retrieve/pii/S0925838898008299`.

[12] A. Chaise et al. “Experimental and numerical study of a magnesium hydride tank”. In: *International Journal of Hydrogen Energy* 35.12 (2010), pp. 6311–6322. ISSN: 03603199. DOI: `10.1016/j.ijhydene.2010.03.057`. URL: `http://dx.doi.org/10.1016/j.ijhydene.2010.03.057`.

[13] Royal Society of Chemistry. *Periodic Table - Magnesium.* 2017. URL: `http://www.rsc.org/periodic-table/element/12/magnesium`.

[14] Kuo-chih Chou and Kuangdi Xu. “A new model for hydriding and dehydriding reactions in intermetallics”. In: *Intermetallics* 15.5-6 (2007), pp. 767–777. DOI: `10.1016/j.intermet.2006.10.004`.

[15] COMSOL. *The Finite Element Method (FEM).* 2017. URL: `https://www.comsol.com/multiphysics/finite-element-method`.

[16] Claudio Corgnale et al. “Screening analysis of metal hydride based thermal energy storage systems for concentrating solar power plants”. In: *Renewable and Sustainable Energy Reviews* 38 (2014), pp. 821–833. DOI: `10.1016/j.rser.2014.07.049`. URL: `http://dx.doi.org/10.1016/j.rser.2014.07.049`.

[17] Jie Cui et al. “Mg-TM (TM: Ti, Nb, V, Co, Mo or Ni) core-shell like nanostructures: Synthesis, hydrogen storage performance and catalytic mechanism”. In: *Journal of Materials Chemistry A* 2.25 (2014), pp. 9645–9655. ISSN: 20507496. DOI: `10.1039/c4ta00221k`.

[18] D. Dong et al. “Thermal optimisation of metal hydride reactors for thermal energy storage applications”. In: *Sustainable Energy & Fuels* 1.8 (2017), pp. 1820–1829. ISSN: 2398-4902. DOI: `10.1039/c7se00316a`.

[19] Rebecca Dunn, Keith Lovegrove, and Greg Burgess. “A review of ammonia-based thermochemical energy storage for concentrating solar power”. In: *Proceedings of the IEEE* 100.2 (2012), pp. 391–400. ISSN: 00189219. DOI: `10.1109/JPROC.2011.2166529`.

[20] J Eckert. “Relationships governing the grain size of nanocrystalline metals and alloys”. In: *Nanostructured Materials* 6.1 (1995), pp. 413–416. ISSN: 0965-9773. DOI: `https://doi.org/10.1016/0965-9773(95)00084-4`. URL: `http://www.sciencedirect.com/science/article/pii/0965977395000844`.

[21] EERE. *Thermal Storage R&D for CSP Systems.* 2019. URL: `https://www.energy.gov/eere/solar/thermal-storage-rd-csp-systems`.

[22] Anas El Maakoul et al. “Numerical design and investigation of heat transfer enhancement and performance for an annulus with continuous helical baffles in a double-pipe heat exchanger”. In: *Energy Conversion and Management* 133 (Feb. 2017), pp. 76–86. ISSN: 0196-8904. DOI: `10.1016/J.ENCONMAN.2016.12.002`. URL: `https://www.sciencedirect.com/science/article/pii/S0196890416310780`.

[23] EngineersEdge. *Standard Pipe Schedules Pipe Sizes Chart Table.* 2021. URL: `https://www.engineersedge.com/pipe_schedules.htm`.

[24] E. Evard, I. Gabis, and V.A. Yartys. “Kinetics of hydrogen evolution from MgH2: Experimental studies, mechanism and modelling”. In: *International Journal of Hydrogen Energy* 35.17 (Sept. 2010), pp. 9060–9069. ISSN: 0360-3199. DOI: `10.1016/J.IJHYDENE.2010.05.092`. URL: `https://www.sciencedirect.com/science/article/pii/S0360319910010621`.

[25] Penghui Feng et al. “Optimal design methodology of metal hydride reactors for thermochemical heat storage”. In: *Energy Conversion and Management* 174.August (2018), pp. 239–247. ISSN: 01968904. DOI: `10.1016/j.enconman.2018.08.043`. URL: `https://doi.org/10.1016/j.enconman.2018.08.043`.

[26] Ted B. Flanagan. *Kinetics of Hydrogen Absorption and Desorption.* Vol. 2. International Association for Hydrogen Energy, 1978, pp. 135–150. DOI: `10.1016/b978-0-08-022715-3.50019-9`. URL: `http://dx.doi.org/10.1016/B978-0-08-022715-3.50019-9`.

[27] R. Floriano et al. “Iron and niobium based additives in magnesium hydride: Microstructure and hydrogen storage properties”. In: *International Journal of Hydrogen Energy* 42.10 (Mar. 2017), pp. 6810–6819. ISSN: 0360-3199. DOI: `10.1016/J.IJHYDENE.2016.11.117`. URL: `https://www.sciencedirect.com/science/article/pii/S036031991633405X`.

[28] H. Scott Fogler. *Elements of Chemical Reaction Engineering.* 5th. Prentice Hall, 2016, p. 992. ISBN: 81-203-2234-7. DOI: `10.1016/0009-2509(87)80130-6`.

[29] Marco Gambini et al. “High temperature metal hydrides for energy systems Part A: Numerical model validation and calibration”. In: *International Journal of Hydrogen Energy* 42.25 (June 2017), pp. 16195–16202. ISSN: 0360-3199. DOI: `10.1016/J.IJHYDENE.2017.05.062`. URL: `https://www.sciencedirect.com/science/article/pii/S0360319917319286`.

[30] Norbert Gérard and Shuichiro Ono. “Hydride formation and decomposition kinetics”. In: *Hydrogen in Intermetallic Compounds II.* Springer, 1992, pp. 165–195. ISBN: 978-3-540-54668-9. DOI: `https://doi.org/10.1007/3-540-54668-5{\_}11`.

[31] R. Grau-Crespo et al. “Thermodynamics of hydrogen vacancies in MgH2 from first-principles calculations and grand-canonical statistical mechanics”. In: *Physical Review B - Condensed Matter and Materials Physics* (2009). ISSN: 10980121. DOI: `10.1103/PhysRevB.80.174117`.

[32] D.N. Harries et al. “Concentrating Solar Thermal Heat Storage Using Metal Hydrides”. In: *Proceedings of the IEEE* 100.2 (2012), pp. 539–549. DOI: `10.1109/JPROC.2011.2158509`. URL: `http://ieeexplore.ieee.org/ielx5/5/6132586/05955063.pdf?tp=&arnumber=5955063&isnumber=6132586%5Cnhttp://ieeexplore.ieee.org/xpls/abs_all.jsp?arnumber=5955063&tag=1`.

[33] Kai Herbrig et al. “Hydrogen storage systems based on hydride–graphite composites: computer simulation and experimental validation”. In: *International Journal of Hydrogen Energy* 38.17 (June 2013), pp. 7026–7036. ISSN: 03603199. DOI: `10.1016/j.ijhydene.2013.03.104`. URL: `http://linkinghub.elsevier.com/retrieve/pii/S0360319913007441`.

[34] IEA. *Concentrating Solar Power.* 2020. URL: `https://www.iea.org/reports/concentrating-solar-power-csp`.

[35] IEA. *Key World Energy Statistics.* Tech. rep. International Energy Agency, 2019. DOI: `10.1016/B978-0-12-409548-9.00927-1`.

[36] IEA. *Solar - Key findings.* 2020. URL: `https://www.iea.org/fuels-and-technologies/solar`.

[37] Abdelmajid Jemni, Sassi Ben Nasrallah, and Jilani Lamloumi. "Experimental and theoretical study of a metal-hydrogen reactor". In: *International Journal of Hydrogen Energy* 24.7 (1999), pp. 631–644. ISSN: 03603199. DOI: `10.1016/S0360-3199(98)00117-7`.

[38] AK Jena and MC Chaturvedi. *Phase Transformations in Materials.* Prentice Hall, 1992, pp. 243–247. ISBN: ISBN 0-13-663055-3.

[39] Stephen T. Kelly et al. "Kinetic limitations of the Mg2Si system for reversible hydrogen storage". In: *Nanotechnology* 20.20 (2009). ISSN: 09574484. DOI: `10.1088/0957-4484/20/20/204017`.

[40] Mohammad Hasan Khademi and Reyhaneh Sadat Sabbaghi. "Comparison between three types of ammonia synthesis reactor configurations in terms of cooling methods". In: *Chemical Engineering Research and Design* 128 (2017), pp. 306–317. ISSN: 02638762. DOI: `10.1016/j.cherd.2017.10.021`. URL: `http://dx.doi.org/10.1016/j.cherd.2017.10.021`.

[41] Vamsi Kukkapalli and Sunwoo Kim. "Optimization of Internal Cooling Fins for Metal Hydride Reactors". In: *Energies* 9.6 (2016), p. 447. ISSN: 1996-1073. DOI: `10.3390/en9060447`.

[42] E.W. Lemmon and M.O. McLinden. *NIST Standard Reference Database 23: NIST Reference Fluid Thermodynamic and Transport Properties.* Gaithersburg, 2001.

[43] Octave Levenspiel. *Chemical reaction engineering.* 3rd. John Wiley & Sons, 1999. ISBN: 047125424X. DOI: `10.1016/0009-2509(64)85017-X`.

[44] Morten B. Ley et al. "Development of hydrogen storage tank systems based on complex metal hydrides". In: *Materials (Basel)* 8.9 (2015), pp. 5891–5921. DOI: `10.3390/ma8095280`.

[45] George Libowitz. *The Solid-State Chemistry of Binary Metal Hydrides.* 1st. W.A. Benjamin, 1965.

[46] Ming Liu et al. "Review on concentrating solar power plants and new developments in high temperature thermal energy storage technologies". In: *Renewable and Sustainable Energy Reviews* 53 (2016), pp. 1411–1432. ISSN: 1364-0321. DOI: `https://doi.org/10.1016/j.rser.2015.09.026`. URL: `http://www.sciencedirect.com/science/article/pii/S136403211500996X`.

[47] Cayetano Lopez. "Technology Roadmap, Solar Thermal Electricity Plants". In: *From Physics to Daily Life: Applications in Informatics, Energy, and Environment* (2014), pp. 119–140. ISSN: 03014215. DOI: `10.1002/9783527687039.ch06`.

[48] Keith Lovegrove and Wes Stein. "1 - Introduction to concentrating solar power (CSP) technology". In: *Concentrating Solar Power Technology.* Woodhead Publishing, 2012, pp. 17–64. ISBN: 9781845697693. DOI: `10.1533/9780857096173.1.91`.

[49] Jun Lu et al. "Hydrogen Storage Properties of Nanosized MgH2-0.1TiH2 prepared by Ultrahigh-Energy - High-Pressure Milling". In: *Journal of the American Chemical Society* 131.14 (2009), pp. 15843–15852. DOI: `10.1021/ja906340u`.

[50] Joshua W. Makepeace et al. "Ammonia decomposition catalysis using non-stoichiometric lithium imide". In: *Chemical Science* (2015). ISSN: 20416539. DOI: `10.1039/c5sc00205b`.

[51] Kandavel Manickam et al. "Future perspectives of thermal energy storage with metal hydrides". In: *International Journal of Hydrogen Energy* 44.15 (Mar. 2019), pp. 7738–7745. ISSN: 0360-3199. DOI: `10.1016/J.IJHYDENE.2018.12.011`. URL: `https://www.sciencedirect.com/science/article/pii/S0360319918339144`.

[52] Philippe Marty et al. "Numerical simulation of heat and mass transfer during the absorption of hydrogen in a magnesium hydride". In: *Energy Conversion and Management* 47.20 (2006), pp. 3632–3643. ISSN: 01968904. DOI: `10.1016/j.enconman.2006.03.014`.

[53] Richard I Masel. *Principles of adsorption and reaction on solid surfaces.* 1st. John Wiley & Sons, 1996. ISBN: 0-471-30392-5.

[54] U. Mayer, M. Groll, and W. Supper. "Heat and mass transfer in metal hydride reaction beds: Experimental and theoretical results". In: *Journal of the Less Common Metals* 131.1 (1987), pp. 235–244. ISSN: 00225088. DOI: `10.1016/0022-5088(87)90523-6`.

[55] Mark Mehos et al. *Concentrating Solar Power Gen3 Demonstration Roadmap.* Tech. rep. January. National Renewable Energy Laboratory, 2017, pp. 1–140. DOI: `10.2172/1338899`. URL: `https://www.nrel.gov/docs/fy17osti/67464.pdf%0Ahttp://www.nrel.gov/docs/fy17osti/67464.pdf`.

[56] Mark Mehos et al. "On the Path to SunShot: Advancing Concentrating Solar Power Technology, Performance, and Dispatchability". In: *SunShot* (2016), pp. 1–66. ISSN: 1557170X. DOI: `10.1016/B978-0-08-087872-0.00319-X`. URL: `http://www.nrel.gov/docs/fy16osti/65688.pdf`.

[57] S. Mellouli et al. "Hydrogen storage in metal hydride tanks equipped with metal foam heat exchanger". In: *International Journal of Hydrogen Energy* 34.23 (Dec. 2009), pp. 9393–9401. ISSN: 0360-3199. DOI: `10.1016/J.IJHYDENE.2009.09.043`. URL: `https://www.sciencedirect.com/science/article/pii/S0360319909014827`.

[58] Merck. *Magnesium hydride - hydrogen storage grade.* 2018. URL: `https://www.sigmaaldrich.com/catalog/product/aldrich/683043?lang=en&region=GB`.

[59] M. H. Mintz and J. Bloch. "A kinetic model for hydrogen-metal reactions controlled by a phase transformation step". In: *The Journal of Chemical Physics* 78.11 (1983), pp. 6569–6578. ISSN: 00219606. DOI: `10.1063/1.444705`.

[60] Moshe H. Mintz and J. Bloch. "Evaluation of the kinetics and mechanisms of hybriding reactions". In: *Progress in Solid State Chemistry* 16.3 (1985), pp. 163–194. ISSN: 00796786. DOI: `10.1016/0079-6786(85)90004-4`.

[61] Moshe H. Mintz and Yehuda Zeiri. "Hydriding kinetics of powders". In: *Journal of Alloys and Compounds* 216.2 (1994), pp. 159–175. DOI: `10.1016/0925-8388(94)01269-N`.

[62] Priyen C. Mistry et al. "Evolution of catalyst coated atomised magnesium spheres. An alternative thermal storage medium for concentrated solar power applications". In: *International Journal of Hydrogen Energy* 42.47 (2017), pp. 28453–28463. ISSN: 0360-3199. DOI: `10.1016/j.ijhydene.2017.09.095`. URL: `https://doi.org/10.1016/j.ijhydene.2017.09.095`.

[63] Caitlin Murphy et al. *The Potential Role of Concentrating Solar Power within the Context of DOE's 2030 Solar Cost Targets.* Tech. rep. January. National Renewable Energy Laboratory, 2019. URL: `https://www.nrel.gov/docs/fy19osti/71912.pdf.`.

[64] S.Ben Nasrallah and A. Jemni. "Heat and mass transfer models in metal-hydrogen reactor". In: *International Journal of Hydrogen Energy* 22.1 (1997), pp. 67–76. DOI: `10.1016/S0360-3199(96)00039-0`.

[65] M Nitsche and R.O Gbadamosi. *Heat Exchanger Design Guide.* Butterworth-Heinemann, 2016, pp. 1–19. ISBN: 9780128037645. DOI: `https://doi.org/10.1016/B978-0-12-803764-5.00001-8`.

[66] NYU Spatial Data Repository. *Maps and data through NYU.* 2019. URL: `https://geo.nyu.edu`.

[67] A Palacios et al. "Thermal energy storage technologies for concentrated solar power – A review from a materials perspective". In: *Renewable Energy* 156 (2020), pp. 1244–1265. ISSN: 0960-1481. DOI: `https://doi.org/10.1016/j.renene.2019.10.127`. URL: `http://www.sciencedirect.com/science/article/pii/S0960148119316258`.

[68] P. Pardo et al. "A review on high temperature thermochemical heat energy storage". In: *Renewable and Sustainable Energy Reviews* 32 (2014), pp. 591–610. DOI: `10.1016/j.rser.2013.12.014`. URL: `http://dx.doi.org/10.1016/j.rser.2013.12.014`.

[69] L. Pasquini et al. "Hydride destabilization in core-shell nanoparticles". In: *International Journal of Hydrogen Energy* 39.5 (2014), pp. 2115–2123. ISSN: 03603199. DOI: `10.1016/j.ijhydene.2013.11.085`. URL: `http://dx.doi.org/10.1016/j.ijhydene.2013.11.085`.

[70] L. Pasquini et al. "Metal-hydride transformation kinetics in Mg nanoparticles". In: *Applied Physics Letters* 94.4 (2009). ISSN: 00036951. DOI: `10.1063/1.3077186`.

[71] Sharad D. Patil and M. Ram Gopal. "Analysis of a metal hydride reactor for hydrogen storage". In: *International Journal of Hydrogen Energy* 38.2 (2013), pp. 942–951. ISSN: 03603199. DOI: `10.1016/j.ijhydene.2012.10.031`. URL: `http://dx.doi.org/10.1016/j.ijhydene.2012.10.031`.

[72] Antonio Perejón et al. "Magnesium hydride for energy storage applications: The kinetics of dehydrogenation under different working conditions". In: *Journal of Alloys and Compounds* 681 (Oct. 2016), pp. 571–579. ISSN: 0925-8388. DOI: `10.1016/J.JALLCOM.2016.04.191`. URL: `https://www.sciencedirect.com/science/article/pii/S0925838816310519#bib20%20https://www.sciencedirect.com/science/article/pii/S0925838816310519`.

[73] R. P. Praveen et al. "Performance analysis and optimization of a parabolic trough solar power plant in the middle east region". In: *Energies* (2018). ISSN: 19961073. DOI: `10.3390/en11040741`.

[74] Cristina Prieto et al. "Review of technology: Thermochemical energy storage for concentrated solar power plants". In: *Renewable and Sustainable Energy Reviews* 60 (July 2016), pp. 909–929. ISSN: 1364-0321. DOI: `10.1016/J.RSER.2015.12.364`. URL: `https://www.sciencedirect.com/science/article/pii/S1364032116001830`.

[75] Mistry Priyen. "Coated Metal Hydrides for Stationary Energy Storage Applications". PhD thesis. University of Nottingham, 2016.

[76] Petr Ptáček, Tomáš Opravil, and František Šoukal. “A Brief Introduction to the History of Chemical Kinetics”. In: *Introducing the Effective Mass of Activated Complex and the Discussion on the Wave Function of this Instanton.* 1st. IntechOpen, 2018. DOI: `10.5772/intechopen.78704`. URL: `https://www.intechopen.com/books/introducing-the-effective-mass-of-activated-complex-and-the-discussion-on-the-wave-function-of-this-instanton/a-brief-introduction-to-the-history-of-chemical-kinetics`.

[77] James R. Welty et al. *Fundamentals of momentum, heat and mass transfer.* 5th. John Wiley & Sons, 1970. ISBN: 9780470128688. DOI: `10.1016/0017-9310(70)90063-3`. URL: `http://linkinghub.elsevier.com/retrieve/pii/0017931070900633`.

[78] Gregg Radtke et al. “Size effects on the hydrogen storage properties of nanostructured metal hydrides : A review”. In: *International Journal of Energy Research* (2007). ISSN: 0363907X. DOI: `10.1002/er`.

[79] Pablo del Río, Cristina Peñasco, and Pere Mir-Artigues. “An overview of drivers and barriers to concentrated solar power in the European Union”. In: *Renewable and Sustainable Energy Reviews* 81.June 2016 (2018), pp. 1019–1029. DOI: `10.1016/j.rser.2017.06.038`. URL: `http://dx.doi.org/10.1016/j.rser.2017.06.038`.

[80] M. Ron. “The normalized pressure dependence method for the evaluation of kinetic rates of metal hydride formation/decomposition”. In: *Journal of Alloys and Compounds* 283.1-2 (Feb. 1999), pp. 178–191. ISSN: 0925-8388. DOI: `10.1016/S0925-8388(98)00859-7`. URL: `https://www.sciencedirect.com/science/article/pii/S0925838898008597`.

[81] Françoise Rouquerol, J Rouquerol, and K. S. W. Sing. *Adsorption by Powders and Porous Solids.* 1st. Elsevier Science & Technology, 1998. ISBN: 9781493301850.

[82] Charles N. Satterfield. *Heterogeneous Catalysis in industrial Practice.* 2nd. McGraw Hill, 1980. ISBN: 1-57524-002-5. DOI: `TP156.C35S27`.

[83] Holly Shaftel, Randal Jackson, and Susan Callery. *Climate Change: How Do We Know?* 2019. URL: `https://climate.nasa.gov/evidence/`.

[84] Drew A. Sheppard and Craig E. Buckley. “The potential of metal hydrides paired with compressed hydrogen as thermal energy storage for concentrating solar power plants”. In: *International Journal of Hydrogen Energy* 44.18 (Apr. 2019), pp. 9143–9163. ISSN: 0360-3199. DOI: `10.1016/J.IJHYDENE.2019.01.271`. URL: `https://www.sciencedirect.com/science/article/pii/S0360319919304550`.

[85] K. S. W. Sing. “Reporting physisorption data for gas/solid systems with special reference to the determination of surface area and porosity (Provisional)”. In: *Pure and Applied Chemistry* 54.11 (1982). DOI: `10.1351/pac198254112201`. URL: `https://www.degruyter.com/view/j/pac.1982.54.issue-11/pac198254112201/pac198254112201.xml`.

[86] R. K. Sinnott. *Coulson and Richardson's Chemical Engineering Volume 6 - Chemical Engineering Design.* 4th. Butterworth-Heinemann, 2005. DOI: `10.1016/b978-0-08-041865-0.50014-3`.

[87] Solargis. *Solar resource maps.* 2019. URL: `https://solargis.com/maps-and-gis-data/download`.

[88] A. Souahlia et al. “Experimental study of metal hydride-based hydrogen storage tank at constant supply pressure”. In: *International Journal of Hydrogen Energy* 39.14 (May 2014), pp. 7365–7372. ISSN: 0360-3199. DOI: `10.1016/J.IJHYDENE.2014.02.121`. URL: `https://www.sciencedirect.com/science/article/pii/S0360319914005199`.

[89] J. F Stampfer, C. E Holley, and J. F Suttle. “The Magnesium-Hydrogen System”. In: *Journal of the American Chemical Society* 82.14 (1960), pp. 3504–3508. DOI: `10.1021/ja01499a006`.

[90] Richard A Swalin. *Thermodynamics of Solids*. 2nd. Wiley, 1962. ISBN: 0471838535.

[91] Terry M. Tritt. *Thermal Conductivity - Theory, Properties, and Applications*. 1st ed. Springer US, 2004. ISBN: 978-0-387-26017-4. DOI: `10.1007/b136496`. URL: `https://www.springer.com/gp/book/9780306483271`.

[92] R. Urbanczyk et al. “Development of a heat storage demonstration unit on the basis of Mg2FeH6 as heat storage material and molten salt as heat transfer media”. In: *International Journal of Hydrogen Energy* 42.19 (May 2017), pp. 13818–13826. ISSN: 0360-3199. DOI: `10.1016/J.IJHYDENE.2017.02.160`. URL: `https://www.sciencedirect.com/science/article/pii/S0360319917307309`.

[93] John J. Vajo et al. “Altering hydrogen storage properties by hydride destabilization through alloy formation: LiH and MgH 2 destabilized with Si”. In: *Journal of Physical Chemistry B* 108.37 (2004), pp. 13977–13983. ISSN: 15206106. DOI: `10.1021/jp040060h`.

[94] Gavin S. Walker et al. “Destabilisation of magnesium hydride by germanium as a new potential multicomponent hydrogen storage system”. In: *Chemical Communications* 47 (2011), pp. 8001–8003. DOI: `10.1039/c0cc03425h`.

[95] Patrick A. Ward et al. “Technical challenges and future direction for high-efficiency metal hydride thermal energy storage systems”. In: *Applied Physics A* 122.4 (2016), p. 462. DOI: `10.1007/s00339-016-9909-x`. URL: `http://link.springer.com/10.1007/s00339-016-9909-x%20http://dx.doi.org/10.1007/s00339-016-9909-x`.

[96] WHO. *7 million premature deaths annually linked to air pollution*. 2014. URL: `https://www.who.int/mediacentre/news/releases/2014/air-pollution/en/`.

[97] V. A. Yartys et al. “Magnesium based materials for hydrogen based energy storage: Past, present and future”. In: *International Journal of Hydrogen Energy* 44.15 (2019), pp. 7809–7859. ISSN: 03603199. DOI: `10.1016/j.ijhydene.2018.12.212`.

[98] Chengshang Zhou et al. “Thermodynamic Destabilization of Magnesium Hydride Using Mg- Based Solid Solution Alloys”. In: *The Journal of Physical Chemistry* 118.22 (2014), pp. 11526–11535. DOI: `10.1021/jp501306w`.

[99] D. Zhou et al. “Thermal Energy Storage, Technology Brief”. In: *SpringerReference* 92.January (2013), p. 24. ISSN: 03062619. DOI: `10.1007/SpringerReference{\_}7300`. URL: `http://www.springerreference.com/index/doi/10.1007/SpringerReference_7300`.

[100] Andreas Züttel. “Materials for hydrogen storage”. In: *Materials Today* 6.9 (Sept. 2003), pp. 24–33. ISSN: 1369-7021. DOI: `10.1016/S1369-7021(03)00922-2`. URL: `https://www.sciencedirect.com/science/article/pii/S1369702103009222`.

Appendix A

Appendix

A.1 Sievert's apparatus generic information

This section details the standard technique concerning the Sievert's apparatus. The purpose of a Sievert's apparatus is to track the reaction of a sample, typically a metal hydride, by monitoring the change in pressure within the system. A basic setup of a Sievert's is shown in figure A.1. The red box indicates the reference volume (V_{ref}) and the sample volume (V_{cell}) as shown in green. A pressure transducer (PT) records the pressure of the system.

A.1.1 Fundamentals of Sievert's

As uptake will be calculated via the real gas equation, and the compressibility is a function of temperature, there must be a temperature profile representation of the system. To simplify the calculations, the reference/manifold (V_{ref}) volume is maintained at isothermal conditions. This enables a simple calculation for the moles of gas within the reference volume,

$$N_{ref} = \frac{P_{ref} V_{ref}}{Z(P_{ref}, T_{ref}) R T_{ref}} \tag{A.1}$$

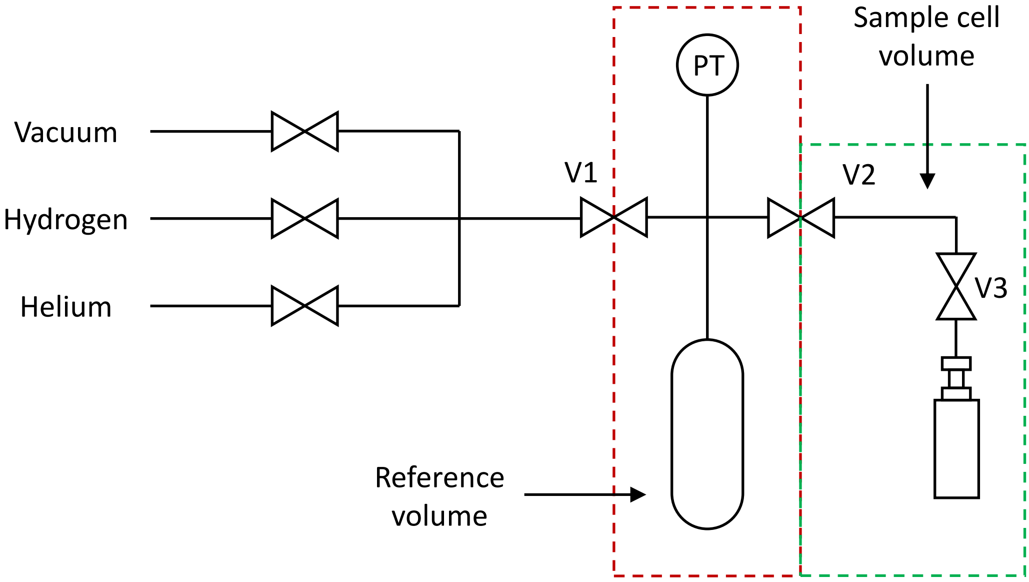

Figure A.1: Essential components of a Sievert's apparatus. PT = pressure transducer, V = valves, with the sample cell volume (V_{cell}) in the green box and the reference volume (V_{ref}) in the red box. V1 and V2 control the reference volume, with V3 used to disconnect/connect the sample cell.

Where the compressibility $Z(P_{ref}, T_{ref})$ is a function of the manifold pressure P_{ref} and temperature T_{ref}. To first achieve this, V_{ref} must be calibrated. The calibration test involves the pressure being measured in the reference volume only (initial - 1) and then measured once the valve to the sample cell has been opened (final - 2). As the moles of gas remains the same after the valve is opened, the new system pressure P_{sys} can be related to N_{ref} by,

$$N_{ref} = \frac{P_{sys}V_{ref}}{Z(P_{sys}, T_{ref})RT_{ref}} + \frac{P_{sys}V_{cell}}{Z(P_{sys}, T_{cell})RT_{cell}} \tag{A.2}$$

As the calibration is done at room temperature, typically with an inert gas such as helium, then $T_{cell} = T_{ref}$. Also, if the pressure before and after is measured with several varying additions of known volume, denoted V_{ex} then,

$$N_{ref} = \rho_1 V_{ref} = (V_{cell} - V_{ex})\rho_2 + \rho_2 V_{ref} \tag{A.3}$$

and upon rearranging this gives,

$$V_{ex} = -V_{ref}\frac{\rho_1 - \rho_2}{\rho_2} + V_{cell} \tag{A.4}$$

Thus, a plot of V_{ex} and $(\rho_1/\rho_2 - 1)$ will determine the reference and cell volumes at operating/room temperature. The densities are calculated from the molar volume $(\hat{V})$ that can be approximated by a suitable equation of state, such as the Virial equation (up to the third coefficient),

$$Z = \frac{P\hat{V}}{RT} = A + \frac{B}{\hat{V}} + \frac{C}{\hat{V}^2} \tag{A.5}$$

A is typically 1 and B and C are constants which vary depending on the gas and temperature. The coefficients are available online from the NIST database[1]. The molar volume can be calculated numerically or algebraically. Demonstrating an example of an algebraic solution; if $\Xi = RT/P$ then equation A.5 can be rearranged to form a cubic equation.

$$0 = \Xi + \frac{B\Xi}{\hat{V}} + \frac{C}{\hat{V}^2} - \hat{V} \tag{A.6}$$

$$0 = -\hat{V}^3 + \Xi\hat{V}^2 + B\Xi\hat{V} + C\Xi \tag{A.7}$$

If equation A.7 is reduced to a depressed cubic by stating that $\gamma + \Xi/3 = \hat{V}$, this gives A.8.

$$\gamma^3 + (p)(\gamma) + q = 0 \tag{A.8}$$

Using Cardano's method, the following formulas for p and q are,

$$p = \frac{3ac - b^2}{3a^2} = -B\Xi - \frac{\Xi^2}{3} \quad \therefore \qquad \varphi = \frac{p}{3} = -\frac{\Xi^2}{9} - \frac{\Xi B}{3} \tag{A.9}$$

$$q = \frac{2b^3 - 9abc + 27a^2d}{27a^3} = -\frac{2\Xi^3}{27} - \frac{B\Xi^2}{3} - C\Xi \quad \therefore \qquad \varpi = -\frac{q}{2} = -\frac{\Xi^2 B}{6} + \frac{\Xi C}{2} + \frac{\Xi^3}{27} \tag{A.10}$$

---

[1] https://www.nist.gov/pml/sensor-science/fluid-metrology/database-thermophysical-properties-gases-used-semiconductor-9

where Γ can be defined as,

$$\Gamma = \left(-\frac{q}{2} + \left(\frac{q^2}{4} + \frac{p^3}{27}\right)^{1/2}\right)^{1/3} + \left(-\frac{q}{2} - \left(\frac{q^2}{4} + \frac{p^3}{27}\right)^{1/2}\right)^{1/3}$$
$$= \left(\varpi + \left(\varpi^2 + \varphi^3\right)^{1/2}\right)^{1/3} + \left(\varpi - \left(\varpi^2 + \varphi^3\right)^{1/2}\right)^{1/3} = W + Z$$

which enables $\hat{V}$ to be determined from the previous definition.

$$\hat{V} = \frac{\Xi}{3} + \Gamma = \frac{\Xi}{3} + W + Z \tag{A.11}$$

The key equations for calculating the molar volume are summarised below,

$$\hat{V} = \frac{\Xi}{3} + W + Z \qquad \Xi = \frac{RT}{P} \tag{A.12}$$
$$Z = \left(\varpi - \left(\varpi^2 + \varphi^3\right)^{1/2}\right)^{1/3} \qquad W = \left(\varpi + \left(\varpi^2 + \varphi^3\right)^{1/2}\right)^{1/3} \tag{A.13}$$
$$\varpi = \frac{\Xi^2 B}{6} + \frac{\Xi C}{2} + \frac{\Xi^3}{27} \qquad \varphi = -\frac{\Xi^2}{9} - \frac{\Xi B}{3} \tag{A.14}$$

If experiments are run at a different temperature to the manifold/reference temperature, the temperature gradient from sample to reference volume must be considered. The method used for the manual Sievert's is the equivalent volume method [94]. Using equation A.2, if V_{cell}/T_{cell} is replaced with $V^e_{cell}(T_{cell})/T_{Ref}$, where V^e_{cell} is the effective sample cell volume,

$$N_{ref} = \frac{P_{sys}V_{ref}}{Z(P_{sys}, T_{ref})RT_{ref}} + \frac{P_{sys}V^e_{cell}}{Z(P_{sys}, T_{cell})RT_{ref}} \tag{A.15}$$

And upon rearranging,

$$V^e_{cell} = Z(P_{sys}, T_{cell})\left[\frac{N_{ref}RT_{ref}}{P_{sys}} - \frac{V_{ref}}{Z(P_{sys}, T_{ref})}\right] \tag{A.16}$$

As V^e_{cell} is a function of the sample cell temperature ($V^e_{cell} = f(T_{cell})$), a calibration must be performed at each temperature of operation. As the system pressure is a function of the reference and cell temperature, the effective volume will be expressed by the changes in pressure. Equation

A.16 is the equivalent volume method, and is reliable if the reference temperature fluctuation remains within 1°C. [94]

A.1.2 Hydrogenation kinetic

To calculate the hydrogen uptake, if the moles "lost from the manifold" from step 1 to step 2 is,

$$N_1 = N_{ref} - N_0 = N_{ref} - \frac{P^0_{sys}}{R}\left(\frac{V^e_{cell}(T_{cell})}{Z(P^0_{sys}, T_s)T_{ref}} + \frac{V_{ref}}{Z(P^0_{sys}, T_s)T_{ref}}\right) \tag{A.17}$$

And the second step difference is,

$$N_2 = N_0 - N_1 = N_0 - \frac{P^1_{sys}}{R}\left(\frac{V^e_{cell}(T_{cell})}{Z(P^1_{sys}, T_s)T_{ref}} + \frac{V_{ref}}{Z(P^1_{sys}, T_s)T_{ref}}\right) \tag{A.18}$$

This enables an equation based in terms of "i" steps; a generic equation for the mole difference at each step.

$$N_i = N_{i-2} - N_{i-1} = N_{i-2} - \frac{P^{i-1}_{sys}}{R}\left(\frac{V^e_{cell}(T_{cell})}{Z(P^{i-1}_{sys}, T_s)T_{ref}} + \frac{V_{ref}}{Z(P^{i-1}_{sys}, T_s)T_{ref}}\right) \tag{A.19}$$

But at $i = 1$, $N_{i-2} = N_{ref}$. The total uptake over time would be the accumulation of the differences as the reaction progresses. From knowing this, the weight percent can be calculated by,

$$wt\% = \frac{NM_{H_2}}{NM_{H_2} + m_s} \tag{A.20}$$

where M_{H_2} is the molecular weight of H_2 and m_s is the sample mass.

A.1.3 Hydrogenation Isotherm

Calculation of a sorption isotherm is slightly different to a kinetic run as the pressure is increased by small aliquots. When the gas pressure is above the equilibrium pressure ($P_{sys} > P_{eq}$) the hydrogenation reaction occurs. This causes a reduction in the gas pressure. Over time, P_{sys} approaches P_{eq} and eventually reaches equilibrium. This pressure is then recorded.

As not all the gas reacted with the metal in the previous aliquot, this excess must be accounted for (N_{cell}) when determining the uptake over the next and subsequent aliquots.

$$\sum(N_{ref} - N_{reacted} + N_{cell}) \tag{A.21}$$

$$n_{cell} = \frac{P_{sys} V^{e}_{cell}}{Z(P_{sys}, T_{cell}) R T_{ref}} \tag{A.22}$$

The amount of moles reacted ($n_{reacted}$) is based on equation A.19 above and n_{cell} is 0 at the first aliquot as there is no excess.

A.1.4 Dehydrogenation kinetic

For dehydrogenation kinetics, the focus is on the amount of hydrogen released into a fixed volume over time. Evacuate the reference volume, then open the sample valve. Pressure will build up in the combined volumes. A larger reference volume is required to maintain a lower gas pressure at the end of the reaction.

A plot of the kinetics using the Sievert's technique can be determined by calculating the difference between the end moles of gas in the combined volumes and the accumulation of moles in the combined volumes within over time, minus the initial gas remaining in the sample cell. Thus, the hydrogen weight percent can be expressed as,

$$wt\% = \frac{N_j M_{H_2}}{m_s + N_j M_{H_2}} - \sum_{i=1}^{i=j} \left(\frac{N_j M_{H_2}}{m_s + N_j M_{H_2}} \right) - N_{cell} M_{H_2} \tag{A.23}$$

where this data set starts at $i = 1$ and finishes at the j^{th} data point. M_{H_2} is the molecular weight of H_2 while m_s is the mass of metal/sample with no hydrogen.

A.2 Flow based calculations

A.2.1 Flow through meter

The flow meter records the flow of gas in nL/min. The moles of gas would equate to the area under the respective section, estimated via the trapezoidal rule, and suitable use of the gas law (see figure A.2). Therefore, the normal volume of gas between t_i and t_{i-1}, V_N (nL) is,

$$V_N = \text{Area of trapezium} = \frac{(\dot{V}_1 - 0 + \dot{V}_2 - 0)}{2(t_2 - t_1)} = \frac{(\dot{V}_{i-1} + \dot{V}_i)}{2(t_i - t_{i-1})} \tag{A.24}$$

where $\dot{V}$ is the volumetric flow rate (nL s^{-1}) and t is time (s). This is shown in figure A.2. Thus, measuring flow with a suitable acquisition rate will yield an approximation of moles of gas passing through the meter across each time step (see figure A.2).

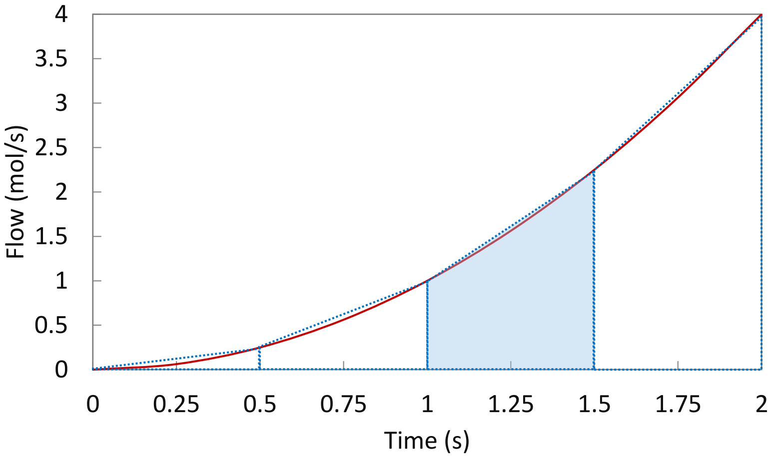

Figure A.2: Illustration of the trapezoidal rule on a flow rate profile with time. RED = flow rate profile. BLUE = Breaking up the profile into trapezoidal sections.

A.2.2 Hydrogenation flow calculations

For hydrogenation, the calculation takes into account the initial moles in V_1 before experiments start (i=0) and the excess/leftover in the system as reaction progresses ($V_1 + V_2$). These volumes are shown in a flow diagram (figure A.3). The moles within V_1 was calculated by the real gas equation, where it is assumed V_1 is at a constant temperature. V_2 is calculated by the equivalent volume method at the working temperature.

For first time step (i=1) = (Initial gas in V_1 at i=0) - (flow through meter) + (excess in system [V_1+V_2])

$$N_1 = \left(\frac{P_{sys}^{i=0} V_1}{Z_1 R T_1}\right) - \left(\frac{P_N^1 V_N^1}{Z_N R T_N}\right) + \left(\frac{P_{sys}^1 V_2}{Z_2 R T_2} + \frac{P_{sys}^1 V_1}{Z_1 R T_1}\right) \tag{A.25}$$

With Z = compressibility, R = universal gas constant J mol^{-1} K^{-1}, P = pressure (bar), T = temperature (K), subscript sys = system pressure, and subscript N = normal conditions. For each subsequent step,

Moles between t_i and t_{i-1} = Gas leftover - flow through meter + excess in system.

$$N_i \text{ (after i=1)} = \left(\frac{P_{sys}^{i-1} V_2}{Z_2 R T_2} + \frac{P_{sys}^{i-1} V_1}{Z_1 R T_1}\right) - \left(\frac{P_N^i V_N^i}{Z_N R T_N}\right) + \left(\frac{P_{sys}^i V_2}{Z_2 R T_2} + \frac{P_{sys}^i V_1}{Z_1 R T_1}\right) \tag{A.26}$$

The accumulation of moles, N_j, finishes at completion time t^*,

$$\sum_{j=i}^{t^*} N_j = N_i + N_{i-1} \tag{A.27}$$

which can be converted to hydrogen weight percent,

$$wt\%_{H_2} = \frac{N_j M_{H_2}}{m_s + m_{H_2}} \times 100 \tag{A.28}$$

where m_{H_2} = theoretical maximum mass of hydrogen the sample can hold & m_s = sample mass.

A.2.3 Dehydrogenation flow calculations

The dehydrogenation calculations involve subtracting the initial mass of gas in the reactor volume (i=0) and then converting the accumulated gas through the volumetric flow meter to removed hydrogen weight percent. The moles in reactor volume is,

$$\left(\frac{P_{sys}^{i=0}V_2}{Z_2RT_2}\right) \tag{A.29}$$

With the accumulation of moles over time being,

$$\sum_{j=i}^{t^*} N_j = \left(\frac{P_N^i V_N^i}{Z_N RT_N}\right) - \left(\frac{P_{sys}^{i=0}V_2}{Z_2RT_2}\right) \tag{A.30}$$

The moles can be converted to hydrogen weight percent removed by using,

$$-wt\%_{H_2} = -\left(\frac{N_j M_{H_2}}{m_s + m_{H_2}} \times 100\right) \tag{A.31}$$

The calculation for subtracting the initial moles for hydrogenation and dehydrogenation can be improved by staggering the removal over a period of time steps instead of a single time step. For these calculations, it was removed over a single time step.

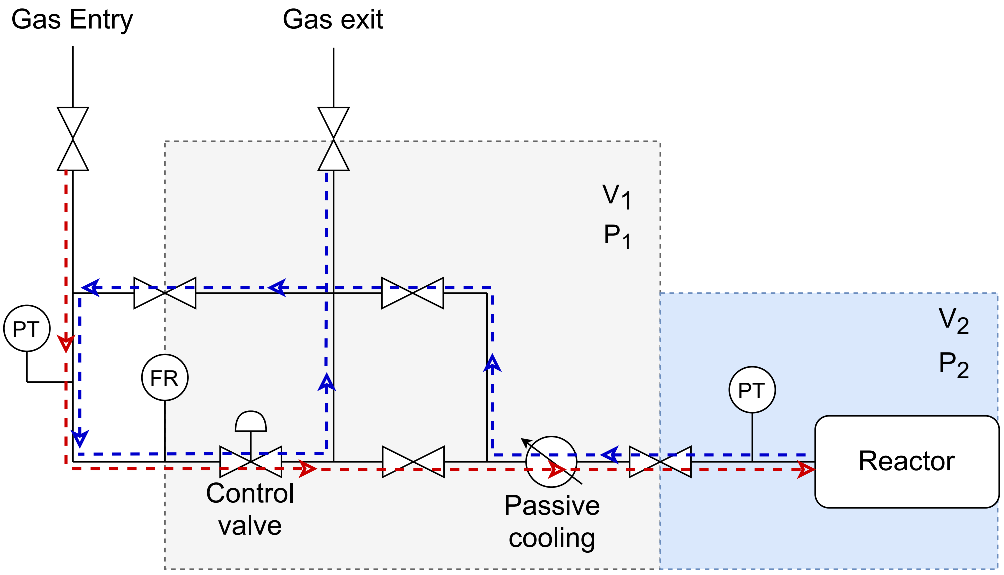

Figure A.3: Simplified diagram for flow control into the reactor. RED – hydrogenation. BLUE – Dehydrogenation.

A.3 COMSOL - simulation methods

A.3.1 Partial differential equations

In general, differential equations describe the change in a system. A partial differential equation (PDE) expresses that law in space and time. In many systems, variables do not just vary in time but also in space, thus it would be more accurate to use a PDE. For example, heat transfer within the solid can be expressed mathematically as a PDE. Knowing that there must be a conservation of energy, the change in energy accumulation (i.e. change in T) = Amount generated by the heat source. Following [15],

For an ordinary differential equation (ODE):

$$\rho c_p \frac{dT}{dt} = g(T, t)$$

This ODE relates the change in temperature with time being balanced by a heat source (g). Providing initial conditions allows the formulation of an analytical solutions.

For a PDE:

$$\rho c_p \frac{\partial T}{\partial t} + \nabla \cdot Q = g(T, t, \mathbf{x})$$

If variations in space need to be included, this can be achieved by spatial variables $\mathbf{x} = (x, y, z)$. Here $Q = (Q_x, Q_y, Q_z)$ is included, which is the heat flux vector and

$$\nabla \cdot Q = \frac{(\partial Q_x)}{\partial x} + \frac{(\partial Q_y)}{\partial y} + \frac{(\partial Q_z)}{\partial z}$$

$\nabla \cdot Q$ is the divergence of Q describing the variation of heat flux along spatial coordinates, expressed using the Cartesian coordinate system. At low to medium temperatures, heat flux in a solid is essentially conduction, which is described by Fourier's law. The law states,

$$Q = -\lambda \nabla T \rightarrow Q = \left(-\lambda \frac{\partial Q_x}{\partial x} + -\lambda \frac{\partial Q_y}{\partial y} + -\lambda \frac{\partial Q_z}{\partial z} \right)$$

where λ is the thermal conductivity. If the system was different, such as at high temperature or a flow was introduced, other components can be added, like radiative heat flux, or advection. Due to the large number of independent variables, (x, y, z, t) changing with T, solving a PDE using an analytical method would be difficult or impossible.

A.3.2 Finite element method

Due to the difficulty of solving PDEs analytically, a solution can be found by constructing approximations of the PDEs through discretisations methods. These discretisation methods can be solved using numerical methods, therefore the solution is an approximation of the real solution to the PDEs. The finite element method (FEM) is a type of numerical method. COMSOL is a commercial software package that uses the finite element method to solve these type of problems.

The FEM aims to find an approximate solution that is comprised of basis functions (ψ_i) multiplied by coefficients (u_i), and summed. For example, $u = f(T)$, then an approximate function of "u", u_h, can be written as

$$u \approx u_h$$

where

$$u_h = \sum_i u_i \psi_i$$

Thus, the approximate function u_h is the combination of the basis functions (ψ_i) with coefficients (u_i). Figure A.4 describes how "u" can be discretised in a 1D problem, illustrating one advantage of the FEM by varying the distribution in finite elements to improve u_h. Another advantage is the choice of basis function. In figure A.4, linear basis functions are used, but a higher order basis function could also be adopted. [15]

Figure A.5 is an overall flowchart of the finite element process shown as a visual, and in comparison, the procedure followed by the user interacting with COMSOL's graphical user interface. The graphic is summarised from COMSOL's blog on the finite element method, where heat transfer in a solid is used an example [15]. In short, the strong form of an equation is modified into the weak form, which allows discretisation via the approximation $u_h = \sum_i u_i \psi_i$. Further imposing boundary conditions allows the creation of a system of equations in the form $\mathbf{ZT}_h = \mathbf{b}$, which can be solved for $\mathbf{T}_h$.

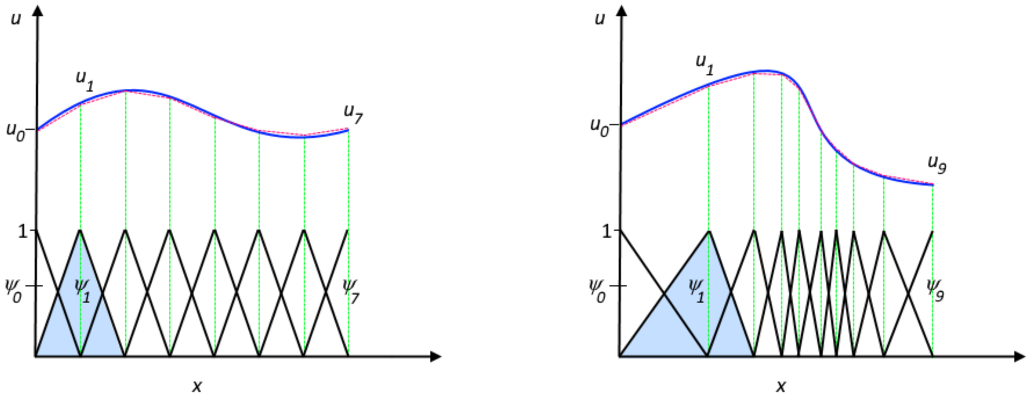

(a) There are seven finite elements with a value of 1 and 0 at the respective nodes, with the coefficients starting at 0 and ending at 7.

(b) Here the elements have been re-distributed to better approximate u_h at the steeper gradient, resulting in 9 elements.

Figure A.4: Function "u" in blue and the approximated function "u_h" in dashed red. u_h is a combination of linear basis functions ψ_i. Graphs taken from [15]

A.3.2.1 Comparing approximate solutions

An important element of FEM is the error estimate to compare approximate solutions, where the error is

$$\text{Error} = u - u_h$$

A simple method for comparing approximate solutions is through mesh convergence. In an ideal scenario, an increase in mesh density causes the approximation to approach the actual solution. In practice however, achieving a very fine mesh may be problematic, thus it is usual practice to use the finest mesh possible. [15]

Another straightforward approach on COMSOL is through an adapted mesh. After the first approximate solution has been computed, an adaptive mesh step is enabled, meaning the second computation makes the mesh denser, at local places where the error is large. This refined mesh further reduces the error. [15] For all simulations, the adapted mesh option is used.

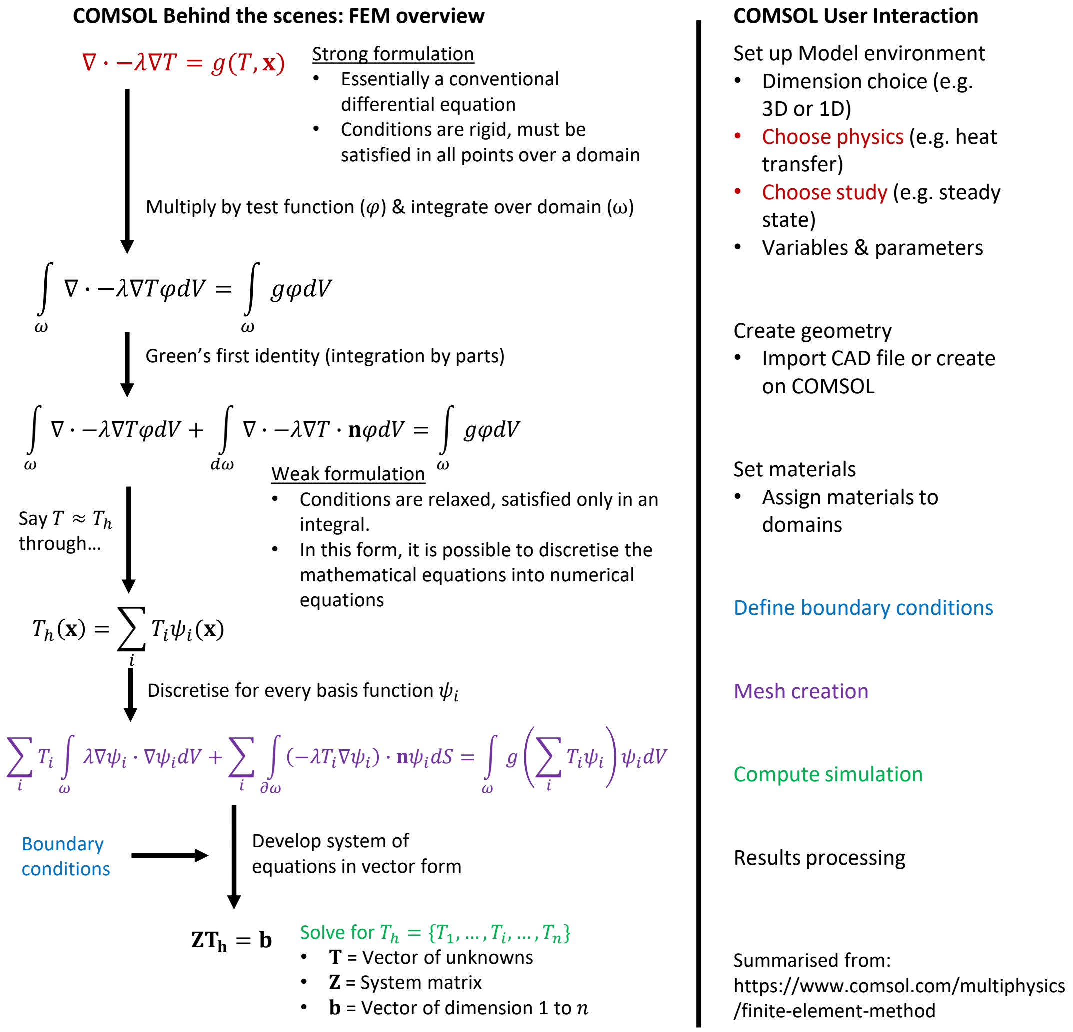

Figure A.5: A summary graphic of the finite element method employed by commercial software package COMSOL and the procedure followed by the user using the graphical user interface (GUI). Parts in the same colour correspond to the same stage between the COMSOL program (behind the scenes) and the GUI (user interaction) [15]

A.3.3 Using reaction rate in COMSOL

The reaction rate term (r_A) used is positioned within the "Dilute species transport" physics option in COMSOL. Dilute species means that one component (such as a carrier gas) dominates the momentum. [15] The equations are considered at unsteady state conditions (transient conditions). The template is:

$$\frac{\partial C_A}{\partial t} + \nabla \cdot (-D_A \nabla C_A) + \mathbf{u} \cdot \nabla C_A = r_A \tag{A.32}$$

- C_A = Concentration of component A [mol/m^3].

- D_A = Diffusion coefficient of component A [$\mathrm{m^2/s}$].
- $\mathbf{u}$ = The velocity field term indicating the average velocity of all A molecules [m/s].
- r_A = This is a source or sink term, which is a chemical reaction in this thesis [mol $\mathrm{m^{-3}}$ $\mathrm{s^{-1}}$].

A.3.4 Applying an energy balance

The exothermic heat source term, Q [W $\mathrm{m^{-3}}$] by convention is negative and given by:

$$Q = -r_A \Delta_r H$$

Where $\Delta_r H$ = enthalpy of reaction [J $\mathrm{mol^{-1}}$]. For non-isothermal design, an energy balance is required. This can be added via a "Heat Transfer" physics option in COMSOL. The unsteady state equation template for heat transfer within porous media is:

$$(\rho c_p)_e \frac{\partial T}{\partial t} + \rho_A c_{p_B} \mathbf{u} \cdot \nabla T + \nabla \cdot (-\lambda_e \nabla T) = Q \tag{A.33}$$

- c_{p_B} = specific heat capacity of fluid **B** [J $\mathrm{kg^{-1}}$ $\mathrm{K^{-1}}$]
- ρ_B = Density of **B** [kg $\mathrm{m^{-3}}$]
- $(\rho c_p)_e = (1 - \epsilon_b)\rho_p c_{p_p} + \epsilon_b \rho_B c_{p_B}$

  $(\rho c_p)_e$ is the volumetric heat capacity. Subscript p is the porous matrix, in this case the metal + metal hydride. Subscript **B** is for fluid component **B**. ϵ_b is the bed porosity.
- $\lambda_e = (1 - \epsilon_b)\lambda_p + \epsilon_b \lambda_B$

  This expression is a weighted arithmetic mean and is suitable for heat conduction of the solid and fluid occurring in parallel. λ_e is the effective thermal conductivity. As the thermal conductivity of the porous matrix is assumed constant, λ_e is essentially constant (although λ_B does change it slightly).
- $\mathbf{u}$ = velocity field either by an analytic expression or a COMSOL "Fluid flow interface". A common interface for fluid through powder is via the Darcy velocity.

A.3.5 Parameters, variables and mesh

This section discusses application of the rate equations into COMSOL through the parameters and variables interfaces, and the respective meshes used. Figure A.6 shows the meshes for the large lab scale reactor. A mapped mesh is chosen for simulations using thermal oil due to simple rectangular shapes, resulting in shorter compute times. Whereas the activation simulations used a free triangular mesh. This is mainly due to intersection between the copper wire and solid wall. A localised dense mesh (at * in figure A.6) was required to compensate for circular wire shape. As the thermal resistance is modified by the number of crossing, it is arguable a simpler cube could have replaced the circle, allowing adoption of a mapped mesh.

Figure A.7 shows the mesh, parameters and variables used for the Sievert's experiments and the large lab-scale reactor for both the SAM and SAM:DR (hydrogenation) models. Gas pressure experimental data was input through "Definitions" tab –> "Interpolation" function. The units do not match for the SAM:DR hence the "unit syntax error" (yellow font) due to P_R being normalised, the computation is un-affected.

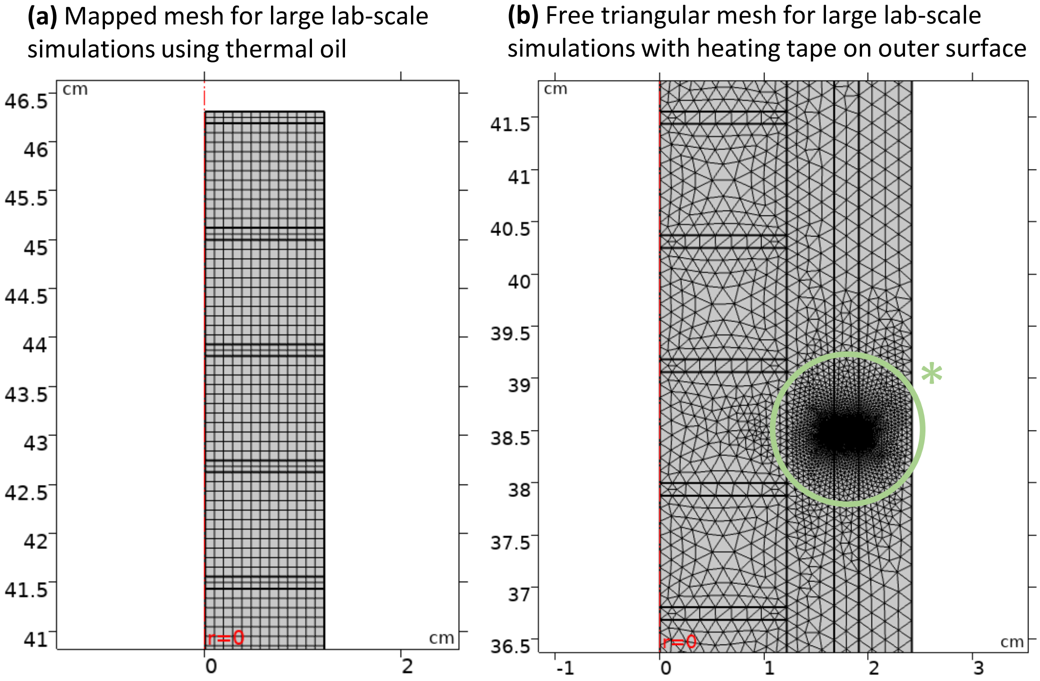

Figure A.6: (a) Mesh used for SAM and SAM:DR models when simulating the large lab-scale reactor with thermal oil. (b) Mesh used for activation simulations.

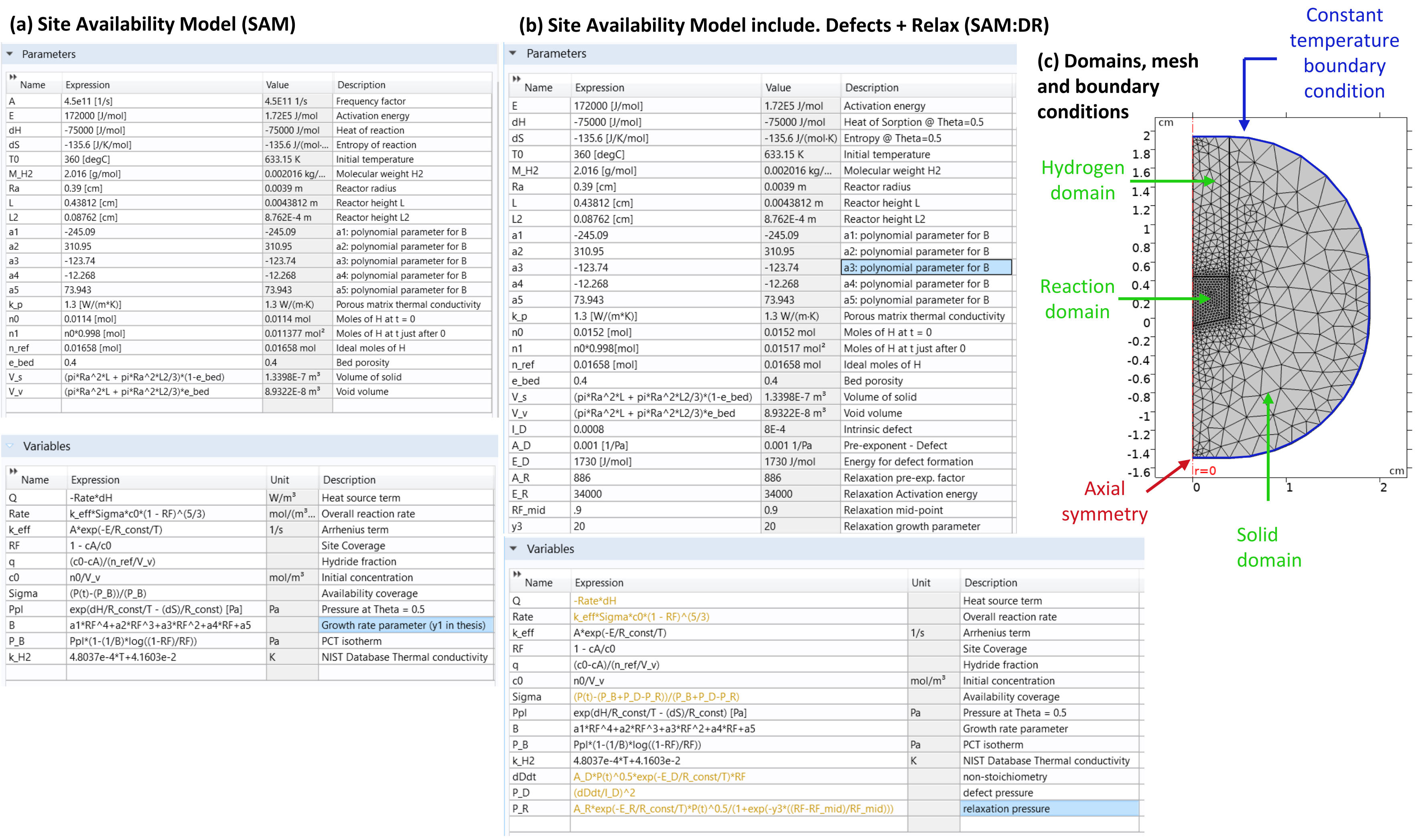

(a) Site Availability Model (SAM)

Parameters

Name	Expression	Value	Description
A	4.5e11 [1/s]	4.5E11 1/s	Frequency factor
E	172000 [J/mol]	1.72E5 J/mol	Activation energy
dH	-75000 [J/mol]	-75000 J/mol	Heat of reaction
dS	-135.6 [J/K/mol]	-135.6 J/(mol·...	Entropy of reaction
T0	360 [degC]	633.15 K	Initial temperature
M_H2	2.016 [g/mol]	0.002016 kg/...	Molecular weight H2
Ra	0.39 [cm]	0.0039 m	Reactor radius
L	0.43812 [cm]	0.0043812 m	Reactor height L
L2	0.08762 [cm]	8.762E-4 m	Reactor height L2
a1	-245.09	-245.09	a1: polynomial parameter for B
a2	310.95	310.95	a2: polynomial parameter for B
a3	-123.74	-123.74	a3: polynomial parameter for B
a4	-12.268	-12.268	a4: polynomial parameter for B
a5	73.943	73.943	a5: polynomial parameter for B
k_p	1.3 [W/(m*K)]	1.3 W/(m·K)	Porous matrix thermal conductivity
n0	0.0114 [mol]	0.0114 mol	Moles of H at t = 0
n1	n0*0.998 [mol]	0.011377 mol²	Moles of H at t just after 0
n_ref	0.01658 [mol]	0.01658 mol	Ideal moles of H
e_bed	0.4	0.4	Bed porosity
V_s	(pi*Ra^2*L + pi*Ra^2*L2/3)*(1-e_bed)	1.3398E-7 m³	Volume of solid
V_v	(pi*Ra^2*L + pi*Ra^2*L2/3)*e_bed	8.9322E-8 m³	Void volume

Variables

Name	Expression	Unit	Description
Q	-Rate*dH	W/m³	Heat source term
Rate	k_eff*Sigma*c0*(1 - RF)^(5/3)	mol/(m³...	Overall reaction rate
k_eff	A*exp(-E/R_const/T)	1/s	Arrhenius term
RF	1 - cA/c0		Site Coverage
q	(c0-cA)/(n_ref/V_v)		Hydride fraction
c0	n0/V_v	mol/m³	Initial concentration
Sigma	(P(t)-(P_B))/(P_B)		Availability coverage
Ppl	exp(dH/R_const/T - (dS)/R_const) [Pa]	Pa	Pressure at Theta = 0.5
B	a1*RF^4+a2*RF^3+a3*RF^2+a4*RF+a5		Growth rate parameter (y1 in thesis)
P_B	Ppl*(1-(1/B)*log((1-RF)/RF))	Pa	PCT isotherm
k_H2	4.8037e-4*T+4.1603e-2	K	NIST Database Thermal conductivity

(b) Site Availability Model include. Defects + Relax (SAM:DR)

Parameters

Name	Expression	Value	Description
E	172000 [J/mol]	1.72E5 J/mol	Activation energy
dH	-75000 [J/mol]	-75000 J/mol	Heat of Sorption @ Theta=0.5
dS	-135.6 [J/K/mol]	-135.6 J/(mol·K)	Entropy @ Theta=0.5
T0	360 [degC]	633.15 K	Initial temperature
M_H2	2.016 [g/mol]	0.002016 kg/...	Molecular weight H2
Ra	0.39 [cm]	0.0039 m	Reactor radius
L	0.43812 [cm]	0.0043812 m	Reactor height L
L2	0.08762 [cm]	8.762E-4 m	Reactor height L2
a1	-245.09	-245.09	a1: polynomial parameter for B
a2	310.95	310.95	a2: polynomial parameter for B
a3	-123.74	-123.74	a3: polynomial parameter for B
a4	-12.268	-12.268	a4: polynomial parameter for B
a5	73.943	73.943	a5: polynomial parameter for B
k_p	1.3 [W/(m*K)]	1.3 W/(m·K)	Porous matrix thermal conductivity
n0	0.0152 [mol]	0.0152 mol	Moles of H at t = 0
n1	n0*0.998[mol]	0.01517 mol²	Moles of H at t just after 0
n_ref	0.01658 [mol]	0.01658 mol	Ideal moles of H
e_bed	0.4	0.4	Bed porosity
V_s	(pi*Ra^2*L + pi*Ra^2*L2/3)*(1-e_bed)	1.3398E-7 m³	Volume of solid
V_v	(pi*Ra^2*L + pi*Ra^2*L2/3)*e_bed	8.9322E-8 m³	Void volume
I_D	0.0008	8E-4	Intrinsic defect
A_D	0.001 [1/Pa]	0.001 1/Pa	Pre-exponent - Defect
E_D	1730 [J/mol]	1730 J/mol	Energy for defect formation
A_R	886	886	Relaxation pre-exp. factor
E_R	34000	34000	Relaxation Activation energy
RF_mid	.9	0.9	Relaxation mid-point
y3	20	20	Relaxation growth parameter

Variables

Name	Expression	Unit	Description
Q	-Rate*dH		Heat source term
Rate	k_eff*Sigma*c0*(1 - RF)^(5/3)		Overall reaction rate
k_eff	A*exp(-E/R_const/T)	1/s	Arrhenius term
RF	1 - cA/c0		Site Coverage
q	(c0-cA)/(n_ref/V_v)		Hydride fraction
c0	n0/V_v	mol/m³	Initial concentration
Sigma	(P(t)-(P_B+P_D-P_R))/(P_B+P_D-P_R)		Availability coverage
Ppl	exp(dH/R_const/T - (dS)/R_const) [Pa]	Pa	Pressure at Theta = 0.5
B	a1*RF^4+a2*RF^3+a3*RF^2+a4*RF+a5		Growth rate parameter
P_B	Ppl*(1-(1/B)*log((1-RF)/RF))	Pa	PCT isotherm
k_H2	4.8037e-4*T+4.1603e-2	K	NIST Database Thermal conductivity
dDdt	A_D*P(t)^0.5*exp(-E_D/R_const/T)*RF		non-stoichiometry
P_D	(dDdt/I_D)^2		defect pressure
P_R	A_R*exp(-E_R/R_const/T)*P(t)^0.5/(1+exp(-y3*((RF-RF_mid)/RF_mid)))		relaxation pressure

Figure A.7: (a) Parameters and variables for the Site Availability Model (SAM) for Sievert's. (b) Parameters and variables including defects and relaxation pressure for Sievert's. (c) The domains, mesh and boundary conditions for Sievert's experiments (0.2g) c_A and T = Dependent variables, $P(t)$ = Gas pressure.

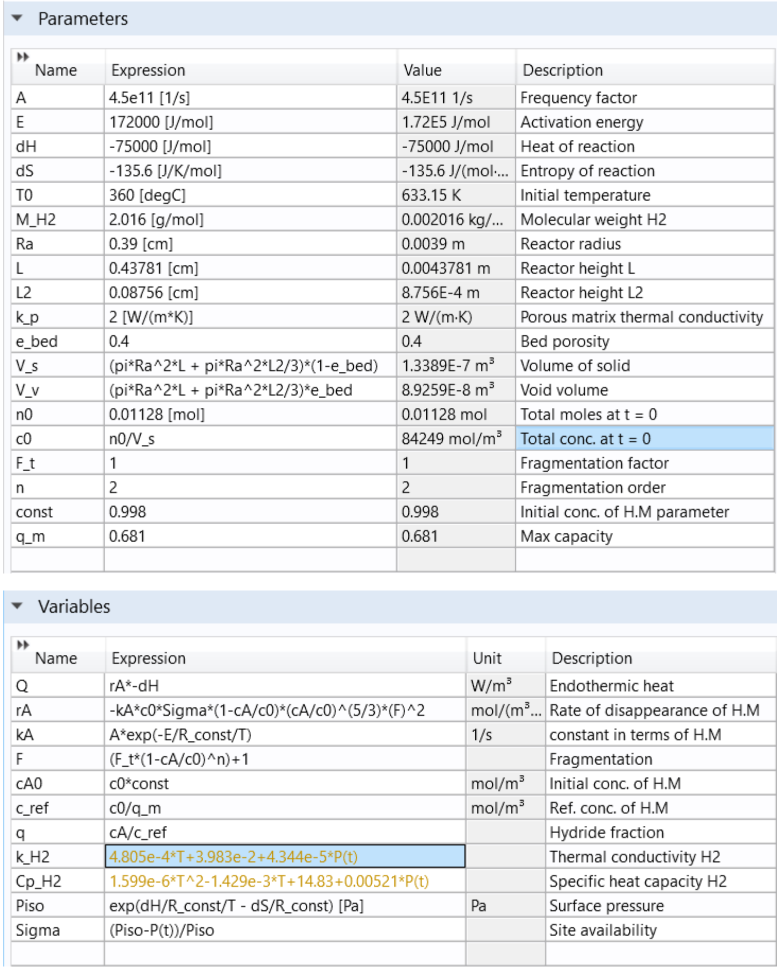

Parameters

Name	Expression	Value	Description
A	4.5e11 [1/s]	4.5E11 1/s	Frequency factor
E	172000 [J/mol]	1.72E5 J/mol	Activation energy
dH	-75000 [J/mol]	-75000 J/mol	Heat of reaction
dS	-135.6 [J/K/mol]	-135.6 J/(mol·...	Entropy of reaction
T0	360 [degC]	633.15 K	Initial temperature
M_H2	2.016 [g/mol]	0.002016 kg/...	Molecular weight H2
Ra	0.39 [cm]	0.0039 m	Reactor radius
L	0.43781 [cm]	0.0043781 m	Reactor height L
L2	0.08756 [cm]	8.756E-4 m	Reactor height L2
k_p	2 [W/(m*K)]	2 W/(m·K)	Porous matrix thermal conductivity
e_bed	0.4	0.4	Bed porosity
V_s	(pi*Ra^2*L + pi*Ra^2*L2/3)*(1-e_bed)	1.3389E-7 m^3	Volume of solid
V_v	(pi*Ra^2*L + pi*Ra^2*L2/3)*e_bed	8.9259E-8 m^3	Void volume
n0	0.01128 [mol]	0.01128 mol	Total moles at t = 0
c0	n0/V_s	84249 mol/m^3	Total conc. at t = 0
F_t	1	1	Fragmentation factor
n	2	2	Fragmentation order
const	0.998	0.998	Initial conc. of H.M parameter
q_m	0.681	0.681	Max capacity

Variables

Name	Expression	Unit	Description
Q	rA*-dH	W/m^3	Endothermic heat
rA	-kA*c0*Sigma*(1-cA/c0)*(cA/c0)^(5/3)*(F)^2	mol/(m^3...	Rate of disappearance of H.M
kA	A*exp(-E/R_const/T)	1/s	constant in terms of H.M
F	(F_t*(1-cA/c0)^n)+1		Fragmentation
cA0	c0*const	mol/m^3	Initial conc. of H.M
c_ref	c0/q_m	mol/m^3	Ref. conc. of H.M
q	cA/c_ref		Hydride fraction
k_H2	4.805e-4*T+3.983e-2+4.344e-5*P(t)		Thermal conductivity H2
Cp_H2	1.599e-6*T^2-1.429e-3*T+14.83+0.00521*P(t)		Specific heat capacity H2
Piso	exp(dH/R_const/T - dS/R_const) [Pa]	Pa	Surface pressure
Sigma	(Piso-P(t))/Piso		Site availability

Figure A.8: Parameters and variables for the SAM.ACR.SC.F model used for dehydrogenation models

A.4 Shrinking core derivations

This section shows the derivations of the shrinking core mechanisms shown in section 2.2.2.4 and figure 2.4.

A.4.1 Controlling: Diffusion through gas film

For the following reaction [43],

$$\mathbf{A}(\text{fluid}) + b\mathbf{B}(\text{solid}) \rightarrow \text{solid product} \tag{A.34}$$

If the diffusion through the (gas) film is controlling, the concentration driving force is the concentration of **A** in the gas phase (C_{A_g}) minus **A** at the outer surface ($C_{A_g} - C_{A_s}$). The concentration at the outer particle surface (C_{A_s}) is equal to the concentration at the core (C_{A_c}), as the product layer offers no resistance, therefore $C_{A_s} = C_{A_c} = 0$. The mole balance is,

$$\text{Rate of disappearance of } \mathbf{A}_{(g)} = \text{Diffusion through film}$$

$$-\frac{1}{4\pi R_0^2}\frac{dN_B}{dt} = -\frac{b}{4\pi R_0^2}\frac{dN_A}{dt} = bk_g(C_{A_g} - C_{A_s}) = bk_g C_{A_g} \tag{A.35}$$

Where k_g [m/s] is the mass transfer coefficient, N = moles, t = time and R_0 = total particle radius. Multiplying through the specific surface area (SSA) [m^{-1}] (based on the particle @ R_0) results in the rate equation being expressed in effective pellet volume (r_A) [mol m^{-3} s^{-1}], where the product ($k_g SSA$) is the effective mass transfer coefficient. We also substitute $C_{A_g} = C_T(1 - X_B)$ where C_T is the total concentration and X_B is the fraction of component **B** that is converted.

$$-\frac{bSSA}{4\pi R_0^2}\frac{dN_A}{dt} = -r_A = b(k_g SSA)C_T(1 - X_B) \tag{A.36}$$

The potency of the reaction rate is mainly dependent on the strength of the film, the concentration driving force and effective mass transfer area. Regarding the metal hydrogenation reaction, the influence of the gas film created by the hydrogen would most likely be minimal due to its light nature. Equation A.36 is in a form suitable for COMSOL multi-physics for a numerical solution. However, equation A.36 can be solved analytically by removing the variable moles of **A** (N_A). Conveniently, the change in N_A (dN_A) can be expressed in terms of un-reacted core radius R_c. As,

$$-dN_B = -bdN_A = -\rho_B dV = -\rho_B d\left(\frac{4}{3}\pi R_c^3\right) = -4\pi\rho_B R_c^2 dR_c \tag{A.37}$$

With ρ_B being density of solid component **B**. If this equation is substituted into A.35 and suitably integrated across the limits,

$$-\frac{\rho_B}{R_0^2}\int_{R_0}^{R_c} R_c^2 dR_c = bk_g C_{A_g}\int_0^t dt \tag{A.38}$$

Rearranging the following expression in terms of time (t),

$$t = \frac{\rho_B R}{3bk_g C_{A_g}} \left[1 - \frac{R_c}{R_0}^3 \right] \tag{A.39}$$

Denoting the time for a complete reaction as t^*, where $R_c = 0$, then

$$t^* = \frac{\rho_B R}{3bk_g C_{A_g}} \tag{A.40}$$

Combining to give t/t^*, and as $1 - X_B = (4/3\pi R_c^3)/(4/3\pi R_0^3)$, thus $1 - X_B = (R_c/R_0)^3$, then

$$\frac{t}{t^*} = X_B \ \ or \ \ kt = X_B \tag{A.41}$$

A.4.2 Controlling: Diffusion through product layer

When the product layer resistance controls the reaction rate, the diffusion through the product needs to be considered. As the reaction front progresses the core shrinks (this is an un-steady state process), and in turn the diffusion length increases. Therefore, it is assumed that the concentration gradient of **A** is constant (i.e. in steady state) over that distance. This is called the pseudo steady state approximation. [43] Thus, if the resistance through the product layer is controlling then,

Rate of disappearance of $\mathbf{A}_{(g)}$ = Diffusion through product (Fick's law)

Assuming one type of diffusion dominates, say Knudsen diffusion related by its effective diffusion coefficient D_e, then the mole balance is,

$$-\frac{dN_A}{dt} = 4\pi r^2 D_e \frac{dC_A}{dr} \tag{A.42}$$

Integrating from R_0 to R_c and from $C_{A_c} = 0$ to $C_{A_g} = C_{A_s}$ results in

$$-\frac{dN_A}{dt} \left(\frac{1}{R_c} - \frac{1}{R_0} \right) = 4\pi D_e C_{A_g} \tag{A.43}$$

Multiplying both sides by $1/R_0^2$ and RSA, and rearranging to give the reaction rate in terms of the effective pellet volume $(-r_A)$, where the reactive surface area (RSA) is the averaged reactive surface area over the course of reaction,

$$-\frac{dN_A}{dt}\frac{RSA}{4\pi R_0^2} = -r_A = \frac{D_e RSA C_{A_g}}{R_0}\frac{R_c}{R_0 - R_c} \tag{A.44}$$

As $1 - X_B = (4/3\pi R_c^3)/(4/3\pi R_0^3)$, thus $1 - X_B = (R_c/R_0)^3$, and substituting accordingly gives,

$$-\frac{dN_A}{dt}\frac{RSA}{4\pi R_0^2} = -r_A = \frac{D_e RSA C_T}{R_0}\frac{(1-X_B)^{5/3}}{1-(1-X_B)^{1/3}} = k_e C_T \frac{(1-X_B)^{5/3}}{1-(1-X_B)^{1/3}} \tag{A.45}$$

The reaction rate in this case is more complex, and interestingly also a function of the particle size, when expressed in this form. One could combine the effective diffusion coefficient, particle size and reactive surface area $(D_e RSA/R_0)$ to give an effective rate constant (k_e [1/s]). This equation is similar to equation A.50 except with the inclusion of $(1 - (1 - X_B)^{1/3})$ and a difference in k_e.

Again, equation A.45 is in a form suitable for COMSOL multi-physics for a numerical solution and equation A.43 can be solved analytically by removing the variable moles of **A** (N_A). Following the same process as before yields the following equation expressed in terms of dimensionless time,

$$\frac{t}{t^*} = 1 - 3\,(1 - X_B)^{\frac{2}{3}} + 2(1 - X_B) \tag{A.46}$$

With t* being,

$$t^* = \frac{\rho_B R_0^2}{6bD_e C_{A_g}} \tag{A.47}$$

This equation is the form $c + mx = y$, where the gradient is $1/t^*$ and passes through the origin. The gradient contains the constant D_e, the effective diffusion coefficient. The relationships and order of magnitude diffusion coefficients are shown in table A.1.

Table A.1: Diffusion coefficient relationships for gases, liquids and solids [28]. **A** = component **A**, **B** = component **B** and μ = viscosity.

Phase	Order of magnitude (m^2/s)	Temperature and pressure dependence
Gas (bulk)	10^{-5}	$D_{AB}(T_2, P_2) = D_{AB}(T_1, P_1)\frac{P_1}{P_2}\left(\frac{T_2}{T_1}\right)^{1.75}$
Gas (Knudsen)	10^{-6}	$D_A(T_2) = D_A(T_1)\left(\frac{T_2}{T_1}\right)^{1/2}$
Liquid	10^{-9}	$D_{AB}(T_2) = D_{AB}(T_1)\frac{\mu_1}{\mu_2}\left(\frac{T_2}{T_1}\right)$
Solid	10^{-13}	$D_{AB}(T_2) = D_{AB}(T_1)exp\left(\frac{E_D}{R}\left(\frac{T_2-T_1}{T_1T_2}\right)\right)$

A.4.3 Controlling: Surface chemical reaction

The last scenario covered is where the reaction at the surface of solid reactant **B** is rate determining [43]. Therefore, as the concentration of gas (C_{A_g}) is not affected by the gas film or resistance through the product layer, then it is constant until it reaches the reactant "**B**" available surface. Thus, the reaction rate is proportional to the reactive surface area (RSA) of **B**. As,

$$\text{Rate of disappearance of } \mathbf{A}_{(g)} = \text{Kinetics at surface core}$$

$$-\frac{b}{4\pi R_c^2}\frac{dN_A}{dt} = bk''C_{A_g} \tag{A.48}$$

Where k'' [m/s] is the velocity front constant. Multiplying both sides through $RSA \cdot \left(\frac{R_c}{R_0}\right)^2$

$$-\frac{bRSA}{4\pi R_c^2}\frac{dN_A}{dt}\left(\frac{R_c}{R_0}\right)^2 = -r_A = b(k''RSA)C_{A_g}\left(\frac{R_c}{R_0}\right)^2 \tag{A.49}$$

And substituting in $(1 - X_B) = (R_c/R_0)^3$ and $C_{A_g} = C_T(1 - X_B)$

$$-r_A = b(k''RSA)C_T(1 - X_B)(1 - X_B)^{\frac{1}{3}} = b(k''RSA)C_T(1 - X_B)^{\frac{5}{3}} \tag{A.50}$$

Equation A.50 is the rate law for when the reaction at the available surface of a sphere is controlling. The product of $k''RSA$ is the effective rate constant k_e with units mol m^{-3} s^{-1}. It can be seen that in this case, the increase in order would reduce the reaction rate, which would be expected as the shrinking available reactive surface would add resistance. If the same procedure is followed above (from equation A.48), this yields the integrated rate equation in terms of dimensionless time

(t/t^*), the following result is,

$$\frac{t}{t^*} = 1 - (1 - X_B)^{\frac{1}{3}} \tag{A.51}$$

Again, experimental data can be tested via equation A.51 with $1/t^*$ the gradient. Equation A.51 represents a chemical surface reaction control for a spherical geometry. The above analysis can be repeated for a cylinder geometry, where the reacted fractions are based on the volume of a cylinder,

$$1 - X_B = \frac{\pi R_c^2 L}{\pi R_0^2 L} = \left(\frac{R_c}{R_0}\right)^2 \tag{A.52}$$

And the reaction rate can be expressed as,

$$\frac{-b}{2\pi R_c L + 2\pi R_c^2} \frac{dN_B}{dt} = bk'' C_{A_g} \tag{A.53}$$

With R_c being the radius of the cylinder and L the length. Considering the pellet length L = 2 R_c,

$$\frac{-b}{6\pi R_c^2} \frac{dN_B}{dt} = bk'' C_{A_g} \tag{A.54}$$

The change in moles of B is related to the shrinking radius R_c,

$$-dN_B = -\rho_B dV = -\rho_B d(\pi R_c^2 L) = -\rho_B d(2\pi R_c^2) = -6\pi \rho_B R_c^2 dR_c \tag{A.55}$$

Substituting A.55 in A.54 and integrating from R_0 to R_c and $t = 0$ and $t = t$ and solving for dimensionless time (t/t^*) as before yields,

$$\frac{t}{t^*} = 1 - \frac{R_c}{R_0} = 1 - (1 - X_B)^{\frac{1}{2}} \tag{A.56}$$

In both equation A.51 and A.56 the rate constant is a strong function of temperature and governed by the Arrhenius equation. In addition, the resistances can be added together as the resistances are in series and exhibit a linear concentration profile.

$$t_{total} = t_{film} + t_{product} + t_{reaction}$$

Thus, the resistances can be combined into a single rate equation in the form: Rate = (Driving force)/(Resistance), which is in similar form to equation 4.24 within the SAM model [43].

$$-\frac{1}{4\pi R_c^2}\frac{dN_B}{dt} = \frac{bC_A}{\frac{1}{k_g} + \frac{R_0(R_0 - R_C)}{R_C D_e} + \frac{R_0^2}{R_C^2 k''}} \tag{A.57}$$

A.5 154g reactor calibration results

The 154g large lab-scale reactor and pipework up to V12 was calibrated by attaching to a Sievert's of known volume to determine this volume (segment marked RED in figure A.9. The reactor volume was determined as 288.6 ± 1.2 cm^3 @ 22°C (using $P_1V_1 = P_2V_2$). Using the known volume of RED, BLUE was then determined. In short hand, this is written as RED = BLUE. The other segments were found by,

1. RED = (to determine) BLUE
2. RED+BL = BROWN
3. RED+BL+BR = ORANGE
4. RED+BL+BR+OR = PURPLE
5. RED+BL+BR+OR+PU = GREEN

The results of the segment volumes are shown in table A.2. As the final result (GREEN) is the sum of the segments, the propagated uncertainty is $\delta R = \sqrt{RED^2 + BR^2 + OR^2 + PU^2 + GR^2} = 3.1$

The volume of the RED section at cell temperature was determined at 380°C. It was assumed all of RED was at this temperature. Using the equivalent sample cell method, and the manifold is all segments except RED, the effective reactor volume was found as 138.75 cm^3.

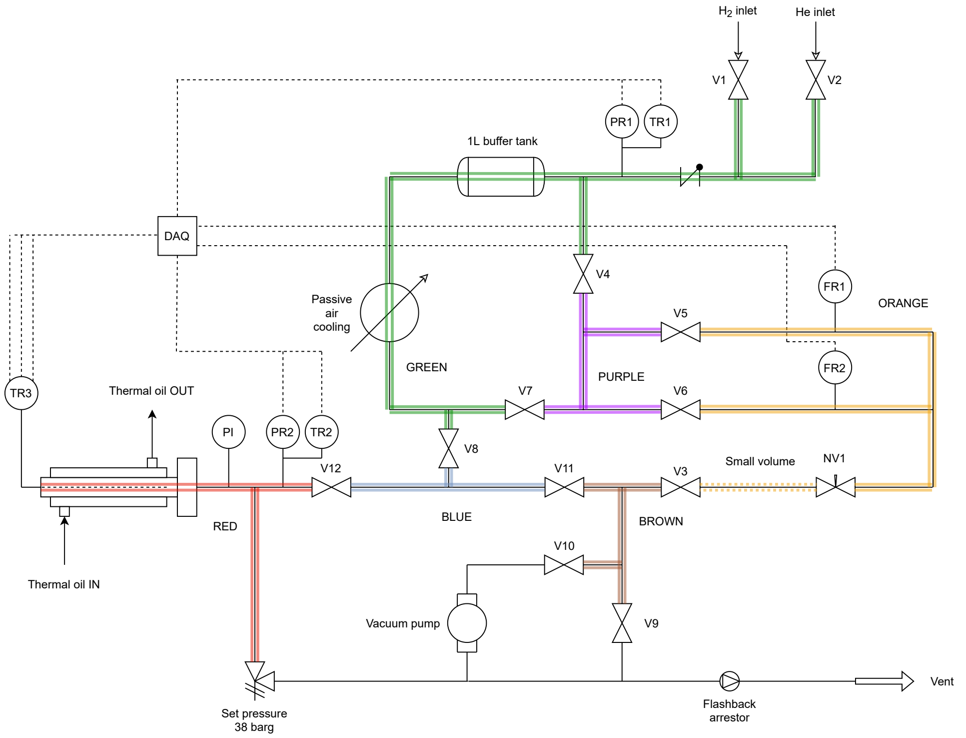

Figure A.9: Copied diagram of volume segments.

Table A.2: Calculated volumes for each segment and errors for each segment (1 standard deviation).

Segment	Volume (cm^3)	Std Err
RED	288.6	1.2
BLUE	51	0.05
BROWN	21.2	0.14
ORANGE	244.1	0.21
PURPLE	14.5	0.11
GREEN	1520	2.81

A.6 Connection assembly for 154g reactor

For $\frac{1}{4}$ - $\frac{1}{2}$" lines, typical VCR (copper/stainless steel) gaskets or Swagelok compression fittings are sufficient. A Change gasket (Flexitallic) was used for the reactor flange to the hydrogen circuit. As each cycle has a large pressure swing, the Change gasket was chosen. Flexitallic lubricant (Flex-Moly) was also used. The lubricant was applied to the thread and nut face seal, where the flange faces were cleaned with acetone before compressing the gasket. The gasket sealed first time with no issue applying a torque of 120 Nm (figure 3.8 shows typical placement of compression fitting and the change gasket used to seal the hydrogen line.).

The hot oil flanges were standard $\frac{1}{2}$” nominal bore, except the bypass valve which was a $\frac{3}{4}$” pipe. It was found that sealing the hot oil system was not straightforward. The operating temperature of the hot oil system is above the flash point (of 200°C). This means oxygen in surface contact with oil will ’flash’ and produce vapour, of which this vapour is carcinogenic.

The manufacturer of the oil was contacted (Global Heat Transfer). Further inspection indicated that two tee joints in the pipe circuit might be providing area for trapped air and constant vapour production. Figure A.11 shows the pipe layout with insulation fitted with the two tee joints removed. The consultant also recommended flange guards and spiral wound gaskets without an inner supporting ring. Also, the recommended tightening procedure was to apply a torque of 40 Nm at room temperature and then at increments of 100°C increments until operating temperature, allowing the rig to cool to room temperature before re-tightening. The hot oil circuit did not leak at 300°C with this approach.

Threaded fittings used graphite paste applied to the threading and tightened to no leak detection. For the inlet/outlet fittings, appropriate tightness resulted in two threads left visible on the male nut. The metal/metal face seals used a Swagelok SWOK lubricant paste applied to the thread and tightened until no leak detection. For future reference, the consultant at Global Therm recommended not using threaded or metal/metal face seal fittings in the future for Marlotherm SH. Figure A.10 shows the positions of the threaded, metal-metal and spiral wound gasket fittings for the 154g reactor.

Further, originally Rockwool insulation was purchased for this rig. It was also recommended to avoid use mineral wool (Rockwool) insulation. This insulation can absorb Marlotherm SH, creating a compound that can spontaneous combust at operating conditions. Foamglass insulation was recommended for this application and was installed by an independent contractor (a picture is shown in the appendix A.11). After installation, thermal losses were significantly reduced, and the hot oil circuit operated more efficiently.

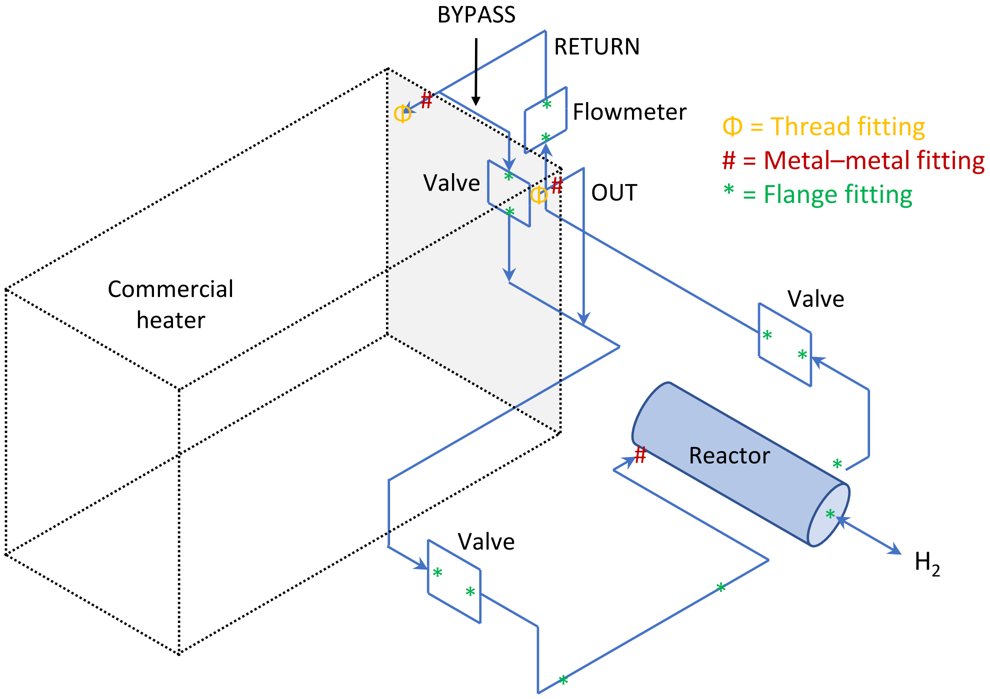

Figure A.10: Pipe layout diagram showing the positions of the different type of fittings used. Drawing is not to scale.

Figure A.11: Installed Foamglas insulation by contractor. 20mm thickness on pipes, double thickness on reactor.

A.7 Flow meter tests

The flow meters underwent calibration runs to improve the accuracy of the measurements. To test the flow meter, a known amount of gas was inserted into a known volume upstream of the flow meter. Then the gas was removed by the vent/vacuum pump. The results are shown in figure A.12 The initial spike shown in figure A.12 is the gradual opening of V5. The other spikes are either due to V5/NV1 being opened further or the vent closed, followed by the vacuum line opening (see figure A.9 for valve placements). If the meter is calibrated correctly, the total moles through the meter would equal the initial moles. A summary of the results are shown in table A.3. After three runs, it was clear a multiplication factor of 2.3 could be used to calibrate the data.

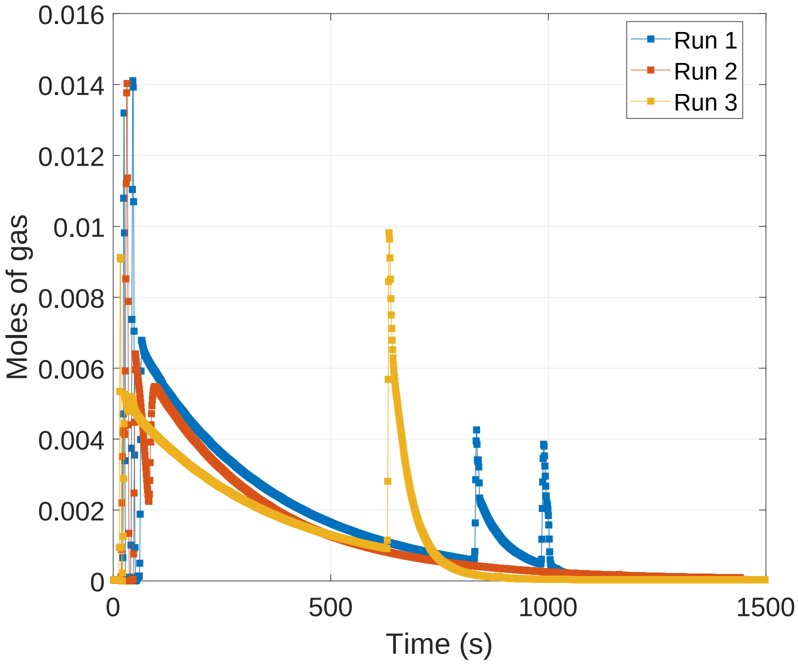

Figure A.12: Flow measurements from flow meter (converted to moles)

Table A.3: Summary of flow test calibration results for large lab scale rig.

Run	Initial moles	Initial pressure (bara)	Calculated total moles	Multiplication factor
1	0.99	16.0	2.27	2.28
2	0.82	13.3	1.87	2.27
3	0.83	13.4	1.90	2.28

A.8 Marlotherm SH properties

Table A.4: Thermo-physical properties of Marlotherm SH. Data used in the hot oil simulations.

Temperature		Density		Specific heat		Thermal conductivity		kinematic viscosity		Vapour pressure	
°C	°F	kg/m3	lb/ft3	kJ/kg K	Btu/lb °F	W/m/K	Btu/ft*hr°F	mm2/s	cSt	hPa	psi
0	32	1058	66	1.48	0.354	0.133	0.077	321	321	–	–
20	68	1044	65.2	1.55	0.37	0.131	0.076	47	47	–	–
40	104	1030	64.3	1.62	0.387	0.128	0.074	16.5	16.5	–	–
60	140	1016	63.4	1.7	0.406	0.125	0.072	8.1	8.1	–	–
80	176	1001	62.5	1.77	0.423	0.123	0.071	4.7	4.7	–	–
100	212	987	61.6	1.85	0.442	0.12	0.069	3.1	3.1	–	–
120	248	973	60.7	1.92	0.459	0.117	0.068	2.3	2.3	–	–
140	284	958	59.8	1.99	0.475	0.115	0.066	1.8	1.8	0.1	–
160	320	944	58.9	2.07	0.494	0.112	0.065	1.4	1.4	0.5	–
180	356	930	58.1	2.15	0.514	0.11	0.064	1.2	1.2	1.7	0.02
200	392	915	57.1	2.22	0.53	0.107	0.062	0.92	0.92	5	0.07
220	428	901	56.2	2.29	0.547	0.104	0.06	0.77	0.77	12	0.17
240	464	887	55.4	2.37	0.566	0.102	0.059	0.65	0.65	27	0.39
260	500	873	54.5	2.44	0.583	0.099	0.057	0.57	0.57	54	0.78
280	536	858	53.6	2.52	0.602	0.096	0.055	0.5	0.5	98	1.42
300	572	844	52.7	2.59	0.619	0.094	0.054	0.45	0.45	200	2.9
320	608	830	51.8	2.67	0.638	0.091	0.053	0.4	0.4	315	4.57
340	644	815	50.9	2.74	0.654	0.088	0.051	0.36	0.36	560	8.12
360	680	801	50	2.82	0.674	0.086	0.05	0.32	0.32	860	12.47

A.9 Depth Gauge

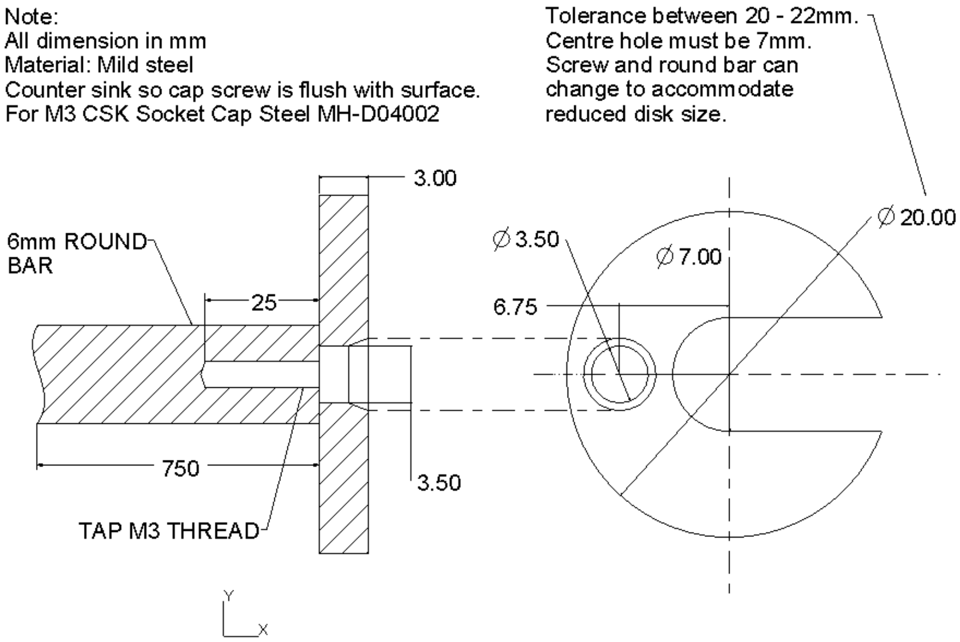

Figure A.13: Schematic of depth gauge used to position ENG fins into position.

A.10 Images of magnesium spheres

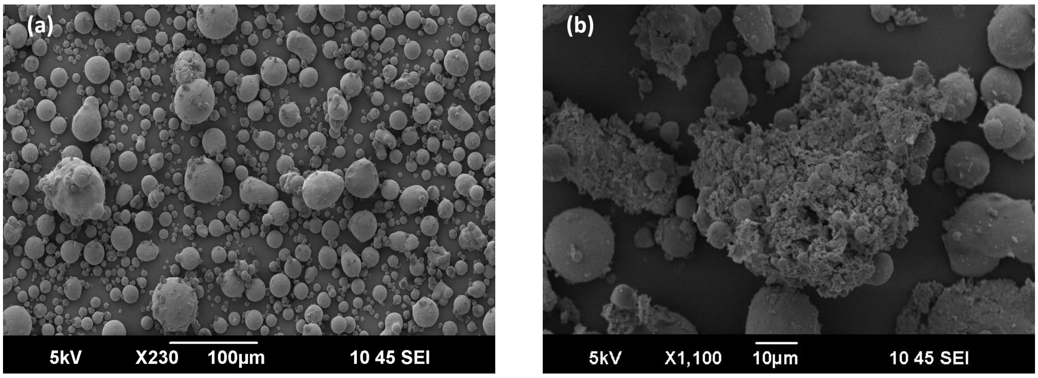

Figure A.14: Magnesium 26 μm spheres (average size) images taken using a scanning electron microscope (SEM) (a) Un-cycled Mg 26 μm purchased from SFM - FluorsidGroup Company. (b) Cycled particle next to un-cycled powder

A.11 Matlab code for Sestak-Berggren regression

Code for figure 5.2b. Best fit is based on a non-linear least squares method.

```
% Call experimental data and sort/remove NaN.
A = readtable('perejon_sanchez_eulers_method.csv');
xdata = rmmissing(A.time);
ydata = rmmissing(A.HF);

% Initial parameter guesses
k1 = 0.0065; % Rate constant
k2 = 1;
k3 = 5/3;
k4 = 0.5;
k0 = [k1;k2;k3;k4];
% Curve fit function for parameters. lb = lower bounds. ub = upper bounds.
% Output parameters in array kbest.
lb = [0.006,0.8,1,0];
ub = [0.008,1.2,2,1];
[kbest,resnorm,residual] = lsqcurvefit(@dy_dt,k0,xdata,ydata,lb,ub);

% Initiate graph and plot experimental data
axis tight
fig = gcf;
fig.Position = [20, 60, 850, 700];
plot(xdata/60,ydata,'o')
hold on

% Plot of best fit using parameters (kbest).
HF_0 = 0.998; % Initial conditions
% Rate of disappearance of HF (t=0 HF = 0.998, t=t* HF = 0)
dHF_dt = @(t,HF) -kbest(1) * (1-HF)^kbest(2) * HF^kbest(3) * kbest(4);
[t,HF] = ode45(dHF_dt,xdata,HF_0);
plot(t/60,HF)

% Plot extras
text(50,0.6,...
    sprintf('k1 = %.3g\nk2 = %.4g\nk3 = %.4g\nk4 = %.4g\nResidual = %.3g',...
    kbest(1),kbest(2),kbest(3),kbest(4),residual(end)),'FontSize',20)
text(50,0.8,'$-\frac{d\theta}{dt}=k_1(1-\theta)^{k_2}\theta^{k_3}k_4 $',...
    'Interpreter','Latex','FontSize',22)
xlabel('Time, min')
ylabel('Normalised hydride fraction')
legend('Experimental data','Fit','Location','Best')
hold off
ax = gca;
ax.YGrid = 'on';
ax.XGrid = 'on';
ax.GridAlpha = 0.075;
ax.FontSize = 20;

% Function to input k parameters into differential equation based on
% experimental xdata and initial condtions yfit_0 = 0.998.
function yfit = dy_dt(k,xdata)
k1 = k(1);
k2 = k(2);
k3 = k(3);
k4 = k(4);
yfit_0 = 0.998;
f = @(t,y) -k1 * (1-y)^k2 * y^k3 * k4;
[¬,yfit] = ode45(f,xdata,yfit_0);
end
```